University of Nottingham
UK | CHINA | MALAYSIA

Sustainable Aviation Fuels (SAF) Production. Process And Techno-Economic Assessment Modelling of Gas Fermentation with SCWG Heat Integration

Simon Emeka Agbo

A thesis
submitted to the University of Nottingham in fulfilment of the
requirement for the degree of Doctor of Philosophy
in
Chemical Engineering

May 2023

ABSTRACT

This dissertation investigates the potential of producing sustainable aviation fuel (SAF) through the integration of aerobic gas fermentation and supercritical water gasification of lignin-content, aiming to address increasing environmental challenges and energy supply uncertainties in the aviation industry. The industry currently accounts for 2% of global CO_2 emissions, a figure projected to rise due to increasing air traffic. Fuel makes up about 23% of operating costs, highlighting the need for an economically viable, environmentally friendly solution.

This study evaluates the feasibility of heat-integrating aerobic gas fermentation of H_2 and CO_2 with supercritical water gasification (SCWG) of black liquor for a proposed SAF plant in China, and SCWG of pot ale draft for a UK-based plant. A comprehensive techno-economic assessment (TEA) compares the production of SAF (C_{16} fractions) via three routes: acetaldehyde (C_2 heat-integrated) and isobutanol (C_4 non-heat and heat-integrated) pathways assessing their economic viability. The entire process scenarios are simulated in Aspen HYSYS v12 with the integration of Cell Designer, OptFlux, and Excel enabling the accurate modelling of the gas fermentation bioreactor. This methodology uniquely links systems biology to a typical chemical engineering process simulation.

The evaluation using various TEA methods shows that the C_2 heat-integrated SAF plant requires a total capital investment (TCI) of $101-$102 million, with annual fixed operating costs (FOC) around $6.42-$6.87 million and variable operating costs (VOC) of $1.76 million. Despite generating a net 160 GWh of electricity sold at $0.1085/kWh and 7.7 kt of SAF sold at $611/ton, this plant records a negative cumulative NPV of about -$3 million over a 25-year period. Break-even occurs at year 25 with electricity sold at $0.1120/kWh or at year 12 with SAF and electricity prices at $771/ton and $0.134/kWh, respectively. Comparatively, using the same black liquor in a steam-turbine powered electricity plant yields a $70 million NPV and breaks even within the initial 4 years.

For the proposed C_4 route-to-SAF plants, two crucial experiments were conducted to inform the modelling of the upgrading units. In the oligomerization of isobutene experiment, trimers (C_{12}) and tetramers (C_{16}) were identified as significant SAF fractions, constituting approximately 90% of the product distribution over the Amberlyst-35 catalyst. Optimal conditions for the highest yield of C_{12} and C_{16} were determined at 70°C. A residence time of 45 minutes was also recorded. The oligomerised isobutene product undergoes hydrogenation reaction. Results indicated that increasing the pressure to 20 bar with a 3:1 catalyst to substrate

ratio (1 wt.% Pd on Al_2O_3) significantly accelerated the reaction rate. Reducing the catalyst concentration to 1 wt.% Pd on Al_2O_3 and a 1:1 ratio showed a slightly reduced but notably faster reaction than initial low-pressure conditions. Data from the hydrogenation experiment were used for kinetic fitting modelling, revealing second-order kinetics for the hydrogenation reaction and determining the kinetic constant. Additionally, parsimonious flux balance analysis (pFBA) of gas fermentation in OptFlux helped determine the molar ratio H_2:CO_2 as (5:1) and CO_2:O_2 as (1:1), with key stoichiometric equations derived for modelling the bioreactor in ASPEN HYSYS. Oxygen transfer coefficients (K_{LA}) were also found to be 323.13 [1/h] and 329.72 [1/h] for C_4 heat-integrated and C_4 non-heat-integrated cases, respectively.

Results from the experiments and pFBA modelling informed the TEA of both C_4 cases. Investment estimations revealed that the C_4 heat-integrated route-to-SAF plant requires a total TCI of $117.35 million, compared to $66.31 million for the C_4 non-heat-integrated case. FOC were estimated at $7.35 million for the C_4 heat-integrated case, compared to $6.5 million for the C_4 non-heat-integrated case. VOC analysis showed that the C_4 heat-integrated process incurs lower costs due to the absence of a need for cooling water for the bioreactor, unlike the C_4 non-heat-integrated case, which incurs about 1.4 times higher costs. The C_4 heat-integrated plant generates a net 142.47 GWh/annum of electricity, while its counterpart generates 61.90 GWh/annum. Initially, the heat-integrated process shows a lower cumulative NPV (-$139.61 million) compared to the non-heat-integrated process (-$78.99 million) in the second year. However, over time, the cumulative NPV of the heat-integrated process increased to around $20 million by the 25th year, showing improved profitability whereas the non-heat-integrated case stayed at -$52.28M at the same point. Despite this, the C_4 heat-integrated has a longer payback period of 16 years, which might impact investor interest. To break even, the C_4 heat-integrated scenario requires an electricity selling price of $0.123/kWh, assuming a constant SAF price of $611/ton. Conversely, the non-heat-integrated scenario requires a much higher electricity price of $0.241/kWh to break even, representing a significant 95% increase in selling price. Break-even analysis shows the lowest required selling prices for SAF ($694.65/ton) and electricity (0.163 kWh/$) in the 12th year for the C_4 heat-integrated route. Monte Carlo simulations reveal uncertainties in NPV calculations. The C_4 heat-integrated case demonstrates a 69% likelihood of achieving a net cumulative NPV between $5 million and $65 million, with an 11% risk of loss. Initial IRR stands at 12% for the C_4 heat-integrated process at a $611/ton SAF price. Sensitivity analysis revealed that doubling the SAF price raises NPV by $65 million with a 16% IRR and a 10-year payback. Tripling the SAF price boosts NPV by $110 million,

achieving a 20% IRR and an 8-year payback, which is much higher when compared with the conventional electricity plant.

The proposed UK SAF mandate buy-out price (£2567/tonne) was introduced and utilized to determine the impact on the proposed SAF plants. For the C_4 heat-integrated route, NPV increases from $21 million to $210 million (based on $611/ton SAF), elevating IRR from 12% to 27% and reducing payback from 16 to 6 years. More so, implementing the buy-out price significantly improved the C_2 heat-integrated case with NPV reaching $110M from -$3M, IRR at 25%, and a shortened payback period to 7 years.

Overall, the heat-integrated approaches, especially the C_4 heat-integrated route-to-SAF, emerged as the most economically viable option for SAF production followed by the C_2-heat-integrated case. Outperforming both C_2 heat-integrated and C_4 non-heat-integrated scenarios, the C_4 heat-integrated route exhibited promising NPV and minimal selling price requirements. The insights generated seek to support the design, execution, and evaluation of policies that foster the growth of SAF, aiding the transition to a more sustainable aviation industry.

ACKNOWLEDGEMENT

The completion of this research has been an incredibly rewarding and fulfilling journey, and I am deeply grateful to the individuals and organizations who have helped me along the way.
First and foremost, I must express my deepest and most heartfelt gratitude to my wife, who has not only been my rock throughout this entire process but also my most enthusiastic cheerleader. There is a running joke between us that she was more eager for me to finish this PhD than I was – partly for my academic success, but mostly so she could reclaim the hours I have spent poring over research for some quality husband-wife time.
Her unwavering love and support have been a constant source of strength and motivation for me, even more so when she gave birth to our daughter, Amarachi, in the middle of the research. If there were a PhD for spousal support, she would have earned it with flying colours – along with a minor in patience for putting up with my endless ramblings about my research! I cannot thank her enough for all she has done and for being there for me every step of the way. She is my partner in life, and I am eternally grateful for her love and support.

I am also incredibly grateful to my supervisors, Prof. Alex Conradie and Dr. Buddhika Hewakandamby, for their guidance, support, and invaluable insights throughout the research. Their expertise and knowledge in the field have been instrumental in shaping the direction and outcome of this research. Their encouragement and support have been invaluable, and I am deeply indebted to them for their mentorship. They have been a source of inspiration and motivation throughout the process, and I am deeply grateful for their wisdom and guidance.

I would also like to extend my gratitude to my PhD sponsors, the Petroleum Technology Development Fund (PTDF) for their generous financial support, which has been instrumental in enabling this research. Their support has been invaluable and has allowed me to focus on my research and achieve my goals.

Lastly, I would like to express my sincerest and most profound gratitude to God for guiding me through this journey. His grace and blessings have been with me every step of the way, and I am forever grateful for his guidance and protection. This research is an accomplishment that I never thought possible, and I am eternally grateful to God for granting me the strength and determination to see it through.

DEDICATION

This research is dedicated to God Almighty, my wife, my daughter Amarachi-Ariana (and possibly future little scholars who will be inspired by this journey), and lastly, to my parents, who have always dreamed of the day they could proudly wear the titles "Mama Dokita" and "Papa Dokita". They have been my unwavering source of strength, encouragement, and inspiration. Without their love, support, and eager anticipation of becoming the beaming parents of a PhD holder, this journey would not have been possible.

TABLE OF CONTENTS

List of Figures

and third scenarios examine the effects of doubling and tripling the price, resulting in IRR of 16 % and 20 %, respectively.

Figure 7.13. Comparison of the NPV between a conventional renewable energy generation plant and the two heat-integrated cases at a buy-out price of £2567/tonne.

List of Tables

Abbreviations and Nomenclatures

2EHO– 2-ethyl-hexanol

AcH– Acetaldehyde

ADP– Adenosine Diphosphate

ASTM– American Society for Testing and Materials

ATJ– Alcohol to Jet

ATJ-SKA– Synthetic kerosene with aromatics

ATJ-SPK– Synthetic paraffinic kerosene

ATP– Adenosine Triphosphate

BtL– Biomass to Liquid

BuONa– Sodium tert-butoxide

C_{16}– Bio-jet blend

CBB– Calvin-Benson-Bassham Cycle

CDR– Cambridge Reactor Design

CH_4– Methane

CO– Carbon monoxide

CO_2– Carbon dioxide

CRI– Carbon Recycling International

CSTR– Continuous stirred tank reactor

DME– Dimethyl ether

ER– Equivalence ratio

ETC– Electron Transport Chain

FCI– Fixed Capital Investment

FFAs– Free fatty acids

FBA– Flux Balance Analysis

FOC– Fixed Operating Cost

FTS– Fischer-Tropsch Synthesis

GC– Gas Chromatography

GHG– Green House Gas

GMF– Garuda Maintenance Facility

GTL– Gas to Liquid

HEFA– Hydro-processed Esters and Fatty Acids

HHV– Higher Heating Value

HRJ– Hydro-processed renewable jet

HtL– Hydrothermal Liquefaction (HtL)

IATA– International Air Transport Association

ICAO– International Civil Aviation Organization

IEA– International Energy Agency

ISBL– Inside Battery Limit

KIV– 2-keto-isovalerate

MC– Moisture content

MEA– Monoethanolamine

MFC– Mass Flow Controller

MTBE– Methyl Tertiary Butyl Ether

MTG– Methanol to Gasoline

MTL– Methanol to Liquid

NADH– Nicotinamide Adenine Dinucleotide

NADPH– Nicotinamide Adenine Dinucleotide Phosphate

NPV– Net Present value

NREL– National Renewable Energy Laboratory

OLE DB– Object Linking and Embedding Database

OSBL– Outside battery Limit

pFBA– Parsimonious Flux Balance Analysis

PPP– Pentose phosphate pathway

RWGS– Reverse Water-Gas Shift Reaction

SAF– Sustainable aviation fuel

SBML– Systems Biology Markup Language

SCWG– Supercritical Water Gasification

scH2O– Supercritical Water

SKA– Synthetic Kerosene with Aromatics

SPK– Synthetic paraffinic Kerosene

TCA– Tricarboxylic acid

TEA– Techno-Economic Assessment

TCI– Total Capital Investment

TS– Towler and Sinnott

VOC– Variable operating cost

WGSR– Water-gas shift reaction

WHSV– Weight-hourly space velocity

XML– Extensible Markup Language

CHAPTER 1.

INTRODUCTION

Air transportation is a major source of global carbon dioxide (CO_2) emissions, contributing to around 2% of the overall emissions, as indicated by current estimations [1]. This figure is projected to increase in the coming years, as a result of a projected annual rise in traffic of 4.5% over the next two decades [2]. This increase in traffic is driven by the growth in global population, economic development, and an increase in the standard of living, which results in an increase in air travel. Furthermore, the International Air Transport Association (IATA) approximates that fuel makes up around 23% of operational expenses in the aviation industry. In 2018, the worldwide airline sector's fuel expenditure amounted to an estimated $180 billion, which represented approximately 23.5% of operating costs at a Brent crude oil price of $73.0 per barrel [3].

Additionally, the aviation industry faces challenges in terms of energy supply, as competition for oil products between different sectors, coupled with environmental considerations, continue to present obstacles. The increasing demand for oil and its derivatives, such as jet fuel, leads to an increase in prices and a decrease in availability. Furthermore, the environmental impact of the sector, including the emissions of CO_2 and other greenhouse gases, has been brought to the forefront of public and political attention, leading to a call for the reduction of emissions from the aviation sector.

One potential solution to these challenges is the production of renewable jet fuel, which can serve as a "drop-in" fuel and help to curb the sector's environmental impact. Lignin, a renewable carbon feedstock, offers great potential in this regard, as it is widely available in large quantities. Lignin is a complex polyphenolic polymer that is a secondary product of the pulp-paper sector, and it can be obtained from various lignocellulosic feedstocks such as wood, straw, and bagasse.

However, its complex structure requires a significant investment in pre-treatment to fully harness its potential. The complex structure of lignin makes it difficult to break down into simple sugars and other small molecules that can be used to produce biofuels. Therefore, a novel approach is required to break down lignin into simpler molecules that can be used to produce biofuels.

This research aims to model a novel approach to the sustainable production of SAF through the integration of endothermic supercritical water gasification (SCWG) of black liquor (BL) and exothermic gas fermentation via a heat pump. SCWG is a process that converts lignocellulosic biomass into a mixture of gases and liquids, including methane (CH_4), hydrogen (H_2), and carbon monoxide (CO), at high temperatures and pressures. The integration of SCWG with exothermic gas fermentation allows for the recovery of heat generated in the fermentation process, which can then be used to heat the SCWG process, thus increasing the overall efficiency of the system.

This integration technique opens up the potential of renewable feedstocks such as lignin by breaking down its complex structure into simple sugars and other small molecules that can be used to produce biofuels. The present research includes a comprehensive examination of the techno-economic feasibility and comparison of the two routes for the production of C_{16} (aviation drop-in) bio-jet. Specifically, the study evaluates the production of C_{16} biofuel via the C_2 route, utilizing acetaldehyde pathway as a building block, and the C_4 route, utilizing isobutanol production pathway as a building block. These routes are referred to as the C_2 and C_4 routes, respectively, throughout the study.

The chapter begins by providing an overview of the background and context of the study, including the current state of the aviation sector and the challenges it faces in terms of energy supply and emissions reduction. It then proceeds to examine the research problem, specifically the need for a sustainable and efficient method for the production of bio-jet fuel from lignin.

The research aims and objectives are then outlined, which include modelling a novel approach for the sustainable production of bio-jet fuel through heat integration of endothermic SCWG and exothermic gas fermentation, and conducting techno-economic assessments (TEA) and comparison studies for the production of C_{16} (aviation drop-in) via C_2 and C_4 routes.

The significance of the research is also discussed, highlighting the potential impact on the aviation sector and the environment. Harnessing lignin as a renewable feedstock for bio-jet production can greatly cut down the industry's reliance on fossil fuels and decrease its environmental impact. Additionally, the integration of SCWG and gas fermentation can improve the overall performance of the system and reduce the costs associated with the production of bio-jet fuel.

Finally, the limitations of the research are discussed, including the need for further research and development to optimize the process, as well as the need for large-scale implementation to fully realize the potential of this approach.

Overall, this research aims to provide a comprehensive and detailed study of a novel approach to sustainable and efficient bio-jet fuel production, which can help to address the long-term challenges faced by the aviation sector in terms of energy supply and emissions reduction.

1.1 Background

Most countries in the world have relied heavily on conventional petroleum-based fuels for transportation. But in recent times, due to certain factors and uncertainty surrounding the future security of the supply of fuels, especially pertaining to sustainability, more countries are looking for alternative fuels for the transportation sector. Projections indicate that energy usage within this industry may rise by 80% to 130% in the coming decades, leading to an increase in CO_2 emissions from transportation, ranging from 16% to 79% [4].

More so, over the past few decades, a substantial rise in atmospheric pollutant levels has been observed, particularly with regard to greenhouse gases, which largely contribute to climate change. Studies reveal that the effects of this phenomenon include, but are not limited to, the rapid melting of polar ice caps, modified weather patterns, and the disappearance of specific animal species. CO_2 has been acknowledged as the foremost greenhouse gas contributing to climate change[5], leading to the objective of curbing CO_2 emissions in the transport sector as a key driver for the expansion of biofuels [6].

Many countries have addressed this issue by implementing regulations and policies to promote research and development, as well as the commercialization of technologies that facilitate the creation of affordable, low-emission fuels. As an illustration, the European Union (EU) as per the Renewable Energy directive(RED II) has mandated its member countries to source 14% of all transportation fuel from renewable sources by 20 [7] [8].

By the year 2050, IEA expects biofuels to account for 27% of fuels within the transportation industry, mainly replacing aviation fuel [9]. In 2015, the United Nations introduced its Sustainable Development Goals, encompassing objectives such as sustainable industrialization and proactive measures to address climate change [5]. The growing focus on biofuels, derived from sources like plant-based materials and lignocellulosic biomass, has also been a result of this increased interest in sustainability [10]. To achieve these objectives, the chemical industry is shifting away from the use of conventional fossil fuels to reduce carbon emissions.

1.2 Challenges: The aviation sector.

Despite air transport accounting for only around 2% of global CO_2 emissions and 13% of transportation emissions at present [11] a 4.5% yearly growth in air traffic is anticipated over the forthcoming two decades [1].

Figure 1.1 shows the international aviation net CO_2 emission according to International Civil Aviation Organization (ICAO). The blue-shaded region illustrates the potential CO_2 reduction range achievable through advancements in aviation technology and procedures, while the orange line represents the ambitious target of a 2% yearly fuel efficiency improvement. Furthermore, the green-covered area highlights the discrepancy between the contributions of technological and procedural enhancements and ICAO's CO_2 emission reduction plan, commencing in 2020 [1].

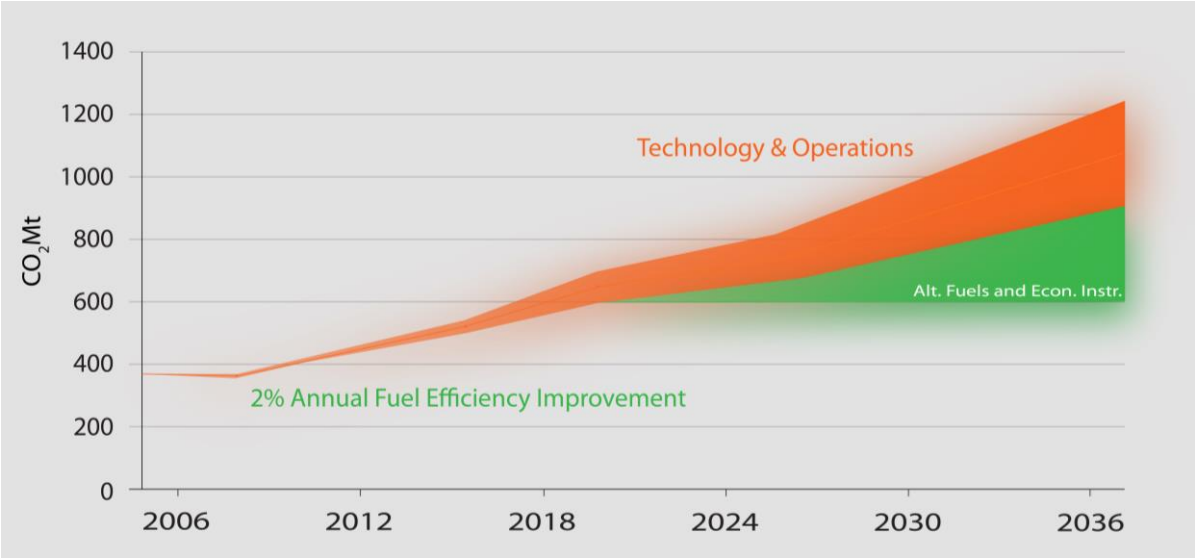

Figure 1.1. International aviation net CO_2 emissions [1].

Robert Boyd of IATA reveals that while it took 104 years for the first 70 billion travellers to fly, the following 70 billion will achieve this milestone in only two decades [12]. Also, the ICAO studies have indicated that air traffic doubles every 15 years and together with Garuda Maintenance Facility (GMF) they agreed that there is approximately 4.5% growth per annum [2]. According to Airbus, countries like India experienced a 20.17% annual growth in domestic air traffic between 2016 and 2018 [2]. This growth poses more and more environmental challenges which should not be overlooked. Figure 1.2 depicts the world's annual traffic using

RPK(Revenue Passenger Kilometres), common unit of measure in the aviation industry to evaluate passenger traffic.

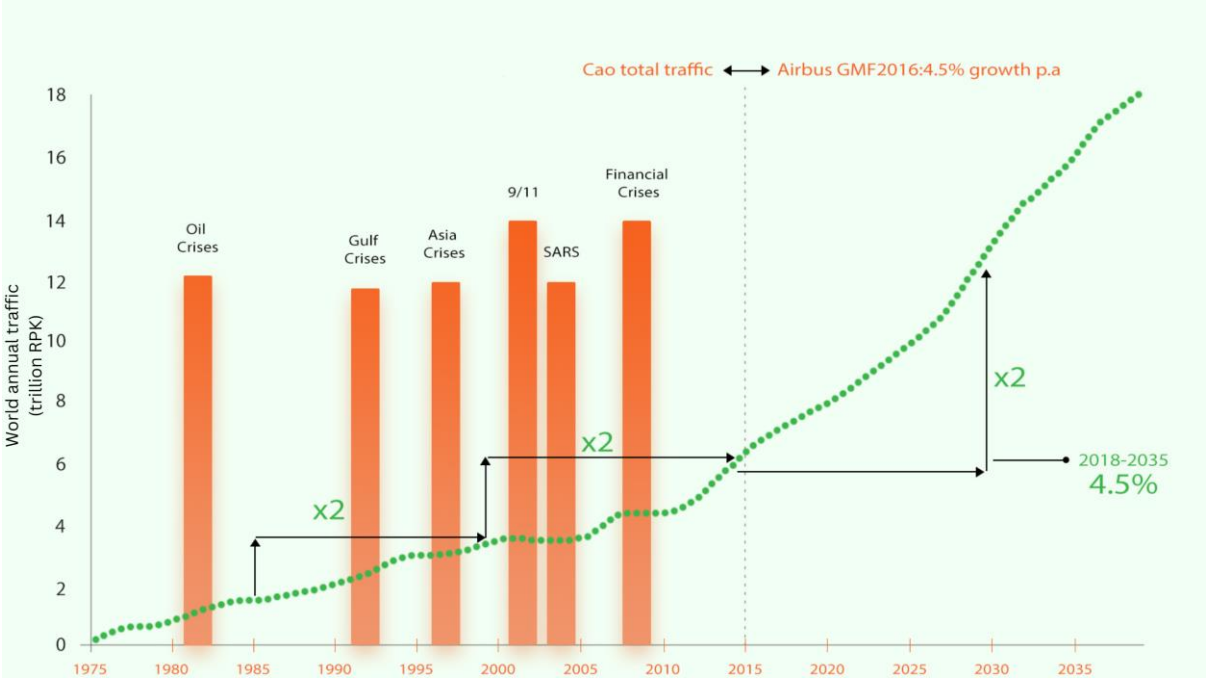

Figure 1.2.World annual traffic and projection [2].

In the aviation sector, according to IATA fuel consumes about 23% of the operating cost. In 2018 alone, the worldwide airline sector industry faced a fuel expenditure of approximately $180 billion, which constituted about 23.5% of operational costs, given the Brent crude oil price of $73.0 per barrel [3]. IATA predicted that in 2019 the fuel cost will be $200 billion, which will account for about 24.2% of operating expenses at $65 per barrel Brent [3]. In Figure 1.3, the cost of fuel is compared with the net profits between 2005 and 2019 [3]. Overall, it can be seen that a reduction on the fuel costs positively affects the net profits and vice versa.

Due to high dependence on the price of crude, the aviation sector and stakeholders are faced with the challenge of instability of crude oil price. These not only affect long-term planning and budgeting but also profitability. Figure 1.4 shows the high dependency of crude oil to the price of jet fuel. Despite the difficulties in bringing biofuels to market and making them competitive with traditional fuels, some experts believe that renewable jet fuels, derived from lignocellulosic feedstocks, have the potential to reduce reliance on a single energy source and mitigate the impact of fluctuating crude oil prices. Additionally, these alternative fuels may also help lower greenhouse gas emissions [13].

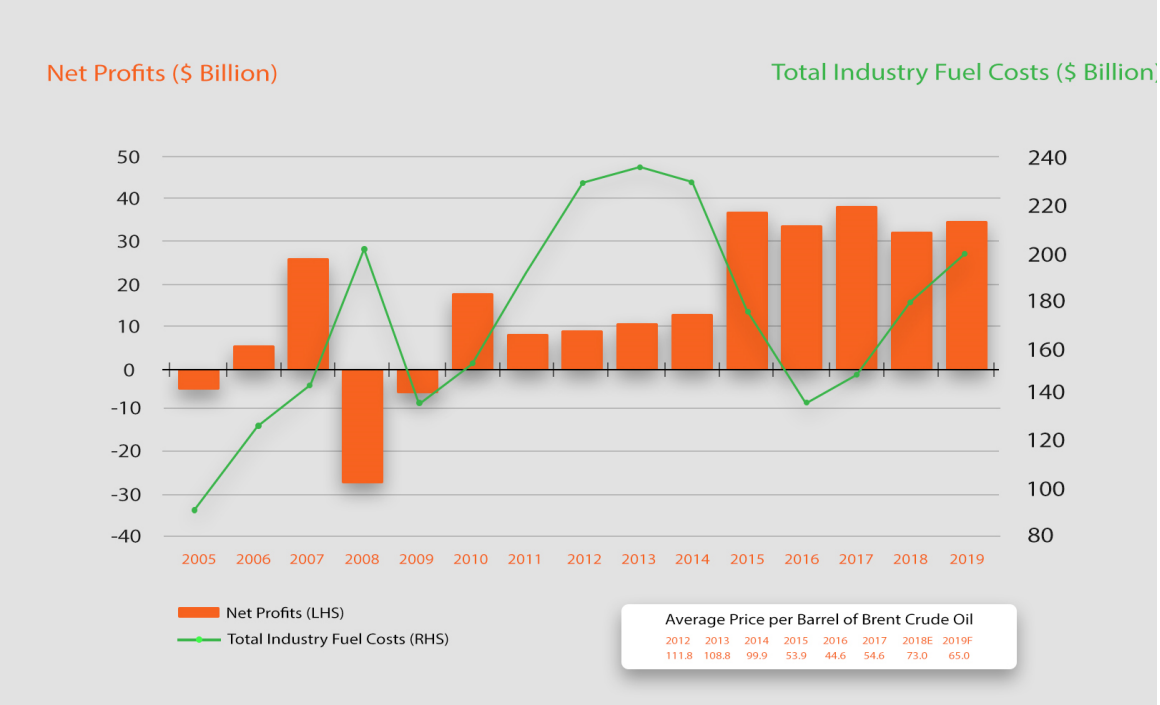

Figure 1.3. Aviation industry fuel cost and net profit [3].

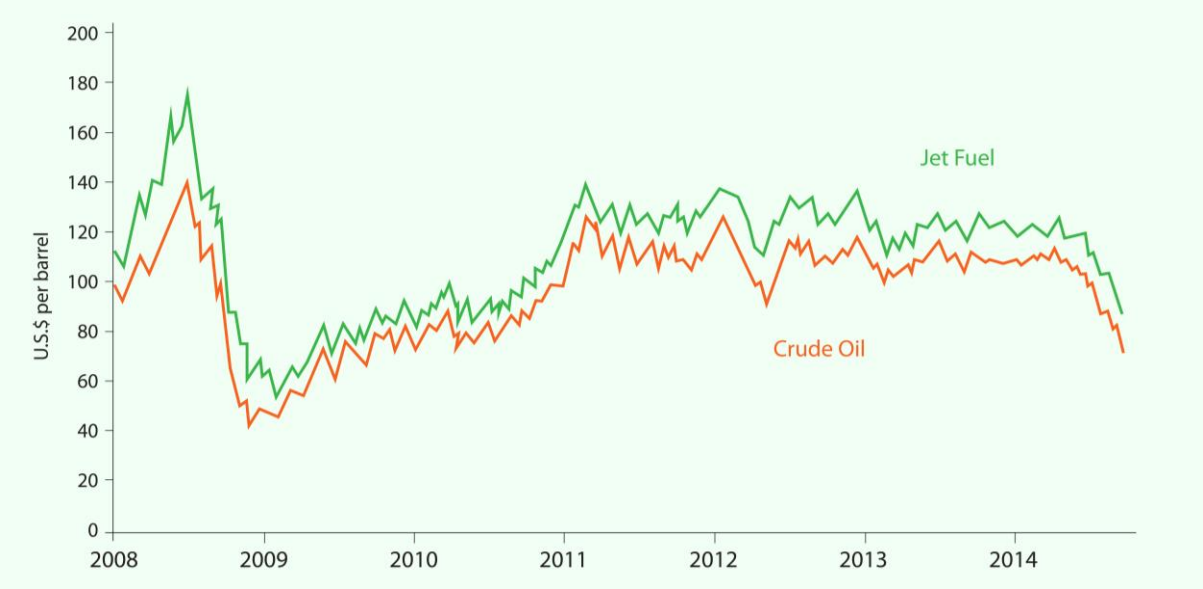

Figure 1.4. Dependence of jet fuel prices on the crude oil price [3].

These statistics show that the aviation sector has long-term challenges in energy supply due to competition for oil products between different sectors as well as environmental issues.

Thus, the production of SAF to serve as a drop-in fuel, is one of the ways to tackle the aforementioned challenges.

1.3 Research Problem and gap

While a significant number of studies have explored the production of biofuels, with a majority of them focusing on biodiesel and ethanol for the road sector, there has been comparatively less focus on the development of a production pathway for bio-jet fuels. According to our best knowledge, there has been little research conducted on the techno-economics of producing bio-jet fuel via gas fermentation, particularly when it comes to overcoming the technical challenges associated with transitioning from a laboratory or pilot phase to a full-scale commercial implementation [14]. Few TEA studies available have focused mainly on the hydro-processed fatty acid esters and fatty acids (HEFA) process, a process where feedstock availability competes with food [15][16][17][18][19]–[21].

While the technology for making first-generation biofuels like ethanol from corn is firmly established [22], there are still questions about their environmental, social, and economic sustainability, as well as their limited ability to address both the climate issue and energy security [23][22]. Furthermore, the use of corn or sugarcane as feedstocks for the HEFA process creates a direct competition with food [22] [24] [25]. As a result, the second generation of biofuel production technologies based on energy-rich lignocellulosic biomass becomes more attractive.

These carbon sources are readily available and inexpensive [26]. Generally, lignocellulosic biomass is predominantly composed of cellulose, hemicellulose, and lignin components. However, traditional fermentation methods face a significant challenge in effectively utilizing lignin, which accounts for approximately 40% of the biomass in biofuel production [27].

The Kraft process is a widely used industrial method for converting wood into pulp, which is a key raw material for the production of paper and various other wood-based products. The Kraft process in pulp mills produces a secondary product known as black liquor, which is abundant in lignin. To recycle pulping chemicals and produce steam, Tomlinson recovery boilers burn black liquor. Around 10 metric tons of diluted black liquor are generated per metric ton of pulp that has been dried by air [28].

The generated steam typically fulfils the electricity requirements for various processes. By expanding this steam via a turbine, electrical power is generated [29]. Consequently, today's Kraft mills have attained independence in both steam and electrical energy production [30]. Nevertheless, some studies indicate that there is still an opportunity to lower the energy use of mills by up to 40 percent [31]. Such measures will enable the utilization of a fraction of dilute black liquor for alternative revenue creation. The gasification of black liquor offers this alternative revenue creation possibility.

Gasification involves converting biomass into H_2, CO, CO_2, and CH_4 in a high-temperature condition with regulated quantities of O_2 and steam [32]. In the case of supercritical water gasification, a specific biomass conversion method, supercritical water (374°C and 22.1 MPa) serves as the primary agent. The primary distinction between supercritical water gasification (SCWG) and alternative thermochemical conversion approaches is the choice of gasification agent, which could be non-reactive gas, vapor or supercritical water [33]. SCWG offers an advantageous approach to gasifying moisture-rich biomass materials, yielding syngas composed of hydrogen (H_2) and carbon monoxide (CO). Unlike thermochemical gasification, which requires significant energy resources for converting biomass, gasification via supercritical water is more energy-saving, with no added requirement for biomass dehydration [34]. As a result, it possesses the capability of utilizing moist feedstocks like black liquor, which are commonly considered economically unviable for conventional gasification technologies [35]. More so, compared to conventional gasification, the SCWG process leads to a low amount of tar and coke formation which simplifies syngas purification [32]. Near the supercritical threshold, water is capable of producing ions that contribute to the decomposition of biomass elements[33]. Another benefit of biomass SCWG is the production of high-pressure hydrogen, which reduces energy expenditures related to compression in the storage process [36]. When it comes to syngas processing, the technology has been around and well explored especially for coal feedstocks. This also has been applied to syngas generated from renewable sources. Nonetheless, issues such stringent CO/H_2 ratios, high operating pressures/temperatures and gas contaminants associated with these still result to high operating costs [37]. Gas fermentation comes into the picture as a substitute technology for transforming syngas into valuable commodities thus addressing these inherent difficulties through high selectivity bio-transformations [37]. In gas fermentation, syngas is typically upgraded via fermentation. By modifying the metabolic pathways of microorganisms that can use CO_2 and H_2 as their only source of carbon and energy, gas fermentation enables the production of desired chemicals [38]. Gas fermentation can be either aerobic, occurring in the presence of oxygen, or anaerobic, in the absence of oxygen. Table 1.1 outlines a comparative analysis between these two modes of fermentation.

Anaerobic fermentation dominates the commercialisation of gas fermentation with companies such as LanzaTech pioneering the utilisation of CO off-gas from steel mill for ethanol production [39]. Anaerobic fermentation, while widely adopted for gas fermentation commercialization, presents some drawbacks. One significant limitation is the dependence on specific metabolic pathways, such as the Wood-Ljungdahl route, which restricts the range of

chemicals that can be produced. This narrow metabolic scope can be a hindrance when targeting a diverse array of valuable compounds.

Table 1.1. Comparison between Aerobic and Anaerobic gas fermentation [40].

Aspect	**Aerobic Fermentation**	**Anaerobic Fermentation**
Oxygen requirement	Requires oxygen	Does not require oxygen (occurs in absence of oxygen)
Occurrence	Occurs in the presence of oxygen	Occurs in the absence of oxygen
Efficiency	More efficient in producing adenosine triphosphate (ATP)	Less efficient in ATP production
End products	Carbon dioxide and water	Ethanol and carbon dioxide, or lactic acid, or other organic acids, alcohols, or gases
ATP production	Higher ATP production per glucose molecule. 38 per glucose molecule	Lower ATP production per glucose molecule. 2 per glucose molecule
Organism involved	Yeast, bacteria, fungi, plants, animals	Yeast, bacteria, some archaea
Examples	Cellular respiration in animals, plants	Lactic acid fermentation in muscles, alcoholic fermentation in yeast
Electron acceptor	Oxygen serves as the final electron acceptor	Various compounds serve as electron acceptors
Duration	Prolonged energy production	Short bursts of energy production
Efficiency of utilization	Efficient utilization of glucose for energy	Less efficient utilization of glucose for energy
Types	Krebs cycle (TCA cycle), electron transport chain (ETC)	Lactic acid fermentation, Alcoholic fermentation
TEA	Generally, aerobic processes are more complex and may require more infrastructure for oxygen supply.	Anaerobic processes may be simpler, potentially requiring less equipment and energy for oxygenation.

This is largely due to energy-related constraints associated with anaerobic CO_2 fixation [41]. Moreover, anaerobic fermentation often leads to the generation of low-value by-products, introducing complexities in downstream processing. The co-production of undesirable substances not only reduces the overall carbon effectiveness of the intended product but also necessitates intricate separation and purification procedures, contributing to increased operational costs [42].

Another drawback is the production of biogas, predominantly methane, as a by-product in anaerobic fermentation. While methane is a valuable energy source, its low market value compared to other chemicals can be a financial drawback. Furthermore, managing and utilizing biogas effectively can pose challenges in terms of storage, transportation, and infrastructure requirements, adding to the overall complexity and cost of the anaerobic fermentation process [43]. Additionally, anaerobic fermentation systems often face challenges related to the sensitivity of the microorganisms involved. Anaerobic microorganisms can be susceptible to variations in environmental conditions, including pH levels, temperature, and substrate composition. Maintaining optimal conditions for these microorganisms can be demanding, requiring precise control and monitoring to ensure consistent and efficient fermentation [43].

In contrast, aerobic cell factories, although facing challenges such as dependence on the energy-intensive Calvin-Benson-Bassham cycle (CBB), have the potential to produce more sophisticated chemicals, expanding the scope of renewable chemicals that can be generated [42], [44]. The heat generated in aerobic bioreactors necessitates significant cooling and the use of compressors and stainless-steel reactors, making aerobic fermentation more suitable for low-volume, high-value products [44]. These costs need to be reduced to exploit the full potential of aerobic fermentation through improved engineering design.

This study strategically selects aerobic gas fermentation technology for further exploration for SAF production, taking into consideration the limitations associated with anaerobic fermentation. The decision to focus on aerobic gas fermentation is motivated by its potential to overcome challenges related to metabolic pathway constraints, by-product generation, and microorganism sensitivity observed in anaerobic processes.

To address both the potential benefits and challenges of aerobic gas fermentation, this thesis will explore an innovative integration framework based on the recommendations of Bommareddy et al [45]. The study proposes that with the help of a heat pump, the integration framework harnesses low-temperature thermal energy generated during aerobic gas fermentation to support the high-temperature supercritical water gasification process. This method negates the necessity for bioreactor cooling. Furthermore, the system harnesses thermal

power released in the expansion of pressurized gas products through a turbo expander, enabling air compression without external energy dependence. This integrated approach seeks to improve the cost-efficiency of aerobic gas fermentation for generating valuable large-scale chemical compounds, with a particular focus on jet fuel blends.

In this work, Cupriavidus necator serves as the microbial cell factory in the aerobic gas fermentation experiment and simulation section. Cupriavidus necator is a type of bacteria that can grow by using CO_2 as the only carbon source. It is also important to highlight that in the gas fermentation process, hydrogen donates its electron, whereas oxygen acts as an electron acceptor. This will be covered in more detail in Chapter 5.

1.4 Research aims and objectives

Aim: To develop an integrated approach for SAF production via aerobic gas fermentation, combining systems biology and chemical engineering principles, to assess the economic viability and policy implications, with a focus on the C_2 (acetaldehyde) and C_4 (isobutanol) routes-to-SAF.

This aim is set to be achieved by the following objectives:

RO1: Perform an extensive literature review on current and emerging technologies involved in SAF production process routes.

RO2: Create a model with the help of Cell Designer and OptFlux representing the biochemical network of CO_2 and H_2 aerobic gas fermentation. Integrate this model to an ASPEN HYSYS bioreactor process simulation using generated yield and stoichiometry data.

RO3: Design a conceptual SAF plant showing the heat integration between SCWG and aerobic gas fermentation.

RO4: Conduct an experiment for the oligomerization of isobutene to ascertain the appropriate residence time and the ideal reaction temperature. These findings will inform the reactor process simulation in ASPEN HYSYS for the C_4 route.

RO5: Conduct a subsequent experiment involving the hydrogenation of oligomerised isobutene to produce SAF fractions. Utilize the experimental data to carry out a kinetic fitting via regression analyses to determine key reaction parameters to be used in process simulation.

RO6: Utilize ASPEN HYSYS for process simulation of conceptual SAF plants (C_2 route-to-SAF and C_4 route-to-SAF) incorporating aerobic gas fermentation modelling, isobutene oligomerisation and hydrogenation experimental data.

RO7: Conduct comprehensive TEA and comparative studies for both C_2 route-to-SAF and C_4 route-to-SAF.

RO8: Assess policy implications of producing SAF via proposed routes.

RO9: Provide recommendations for future research, focusing on areas where additional study is needed, and emphasize the significance of policy support and other incentives in promoting the development and adoption of SAF production technologies.

1.5 Significance

This research will add to the body of knowledge on the commercialization of biofuel production, specifically SAF, while also addressing the current lack of research in this area and providing real-world value to organisations involved in SAF production.

Furthermore, this research will aid in the achievement of the UN Sustainable Development Goals, which include Sustainable Industrialization and Climate Action [26].

1.6 Research Limitations

The scope of this work will not include process optimization of both process routes investigated. A measure of uncertainties was accounted for in the research via Monte Carlo simulation, however, comprehensive uncertainty studies were not carried out in this study. The TEA model used in this study includes a sensitivity analysis, which addressed the effects of only one variable at a time rather than a combination of variables. The simulation results are only reliable approximations subject to statistical errors. There are uncertainties involved in the kinetics and experimental data used in the simulations.

1.7 Thesis Structure

This research is organized into eight chapters, each covering a specific aspect of the study.

Figure 1.5 visually illustrates the interconnectedness of these chapters, providing a schematic representation of the logical progression and integration of experimental, gas fermentation modelling, and simulation data in the exploration of the proposed routes to SAF production.

In Chapter One, the research scope is outlined by introducing the context, which covers the objectives, questions, significance, and constraints of the study. This opening chapter delivers an overview of the issue being investigated and the goals of the research, preparing the ground for the chapters that follow.

In Chapter Two, an extensive examination of the existing body of literature regarding SAF production is conducted. This section offers an in-depth understanding of the present state of research in this domain, emphasizing crucial pathways and advancements within the field.

In Chapter Three, the focus shifts to the evaluation of a conceptual process overview and ASPEN HYSYS simulation of the C_2 route-to-SAF gas fermentation with heat integration of supercritical water gasification for SAF production. This chapter presents the results from the process simulation and a TEA modelling approach was conducted to be used throughout this study. Finally, the economic feasibility of the C_2 route-to-SAF approach was assessed and presented.

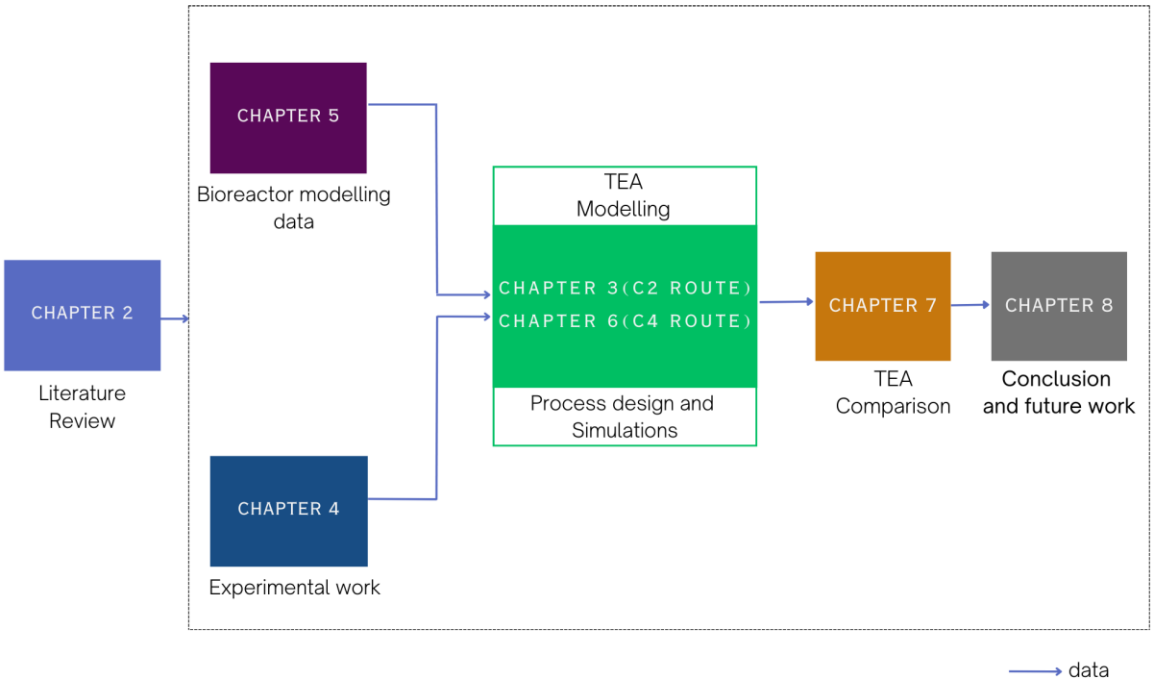

Figure 1.5. Thesis structure Flowchart - A visual guide showing how each chapter connects in the overall journey of the research.

In Chapter Four, C_4 route-to-SAF production is considered. Isobutene oligomerisation and hydrogenation reaction are key operational units of this pathway. The experimental data from isobutene (C_4 route) oligomerisation and subsequent hydrogenation reactions which was conducted is presented, along with results and discussions. The kinetic fittings for the hydrogenation reaction is carried out and presented, which ultimately informs the TEA of the C_4 route-to-SAF process.

In Chapter Five, the focus is on aerobic gas fermentation, a crucial component of SAF production through the C_2 and C_4 routes. The chapter discusses the theoretical foundations of gas fermentation and evaluates its role in biofuel production. The gas fermentation of CO_2 and H_2 is modelled and simulated using OptFlux and Cell Designer to determine key reaction stoichiometry, via flux balance analysis (FBA), needed for ASPEN HYSYS conversion reactor (aerobic gas fermentation). These results ultimately help inform the TEA of the C_4 route-to-SAF process.

In Chapter Six, the experimental and modelling data from both Chapter Four and Five are integrated to conduct a conceptual process design and ASPEN HYSYS simulation of the C_4 route-to-SAF production. Heat and non-heat integrated routes are investigated.

In Chapter Seven, the comparison of C_2 (heat-integrated case) and C_4 (non-heat and heat-integrated cases) is conducted to assess the economic feasibility. The C_4 heat integrated process was favoured and further examination carried out, most notably, the implication of policy support measures such as the UK buy-out price.

In Chapter Eight, a conclusion of the thesis is presented, summarizing the key findings and contributions of the research. This chapter also includes further recommendations for future research, highlighting areas where additional study is needed and emphasizing the importance of policy support to enhance the economic viability of the proposed SAF plant.

Overall, the research is structured in a logical and coherent manner, moving from an overview of the problem and existing literature to a detailed examination of the specific research objectives, and culminating in a comparison and recommendations for future work. The research incorporates various aspects such as price modelling, experimental data, biochemical modelling, and case studies to provide a well-informed and balanced perspective on SAF production via the C_2 and C_4 routes.

1.8 Thesis methodology

As can be seen in Figure 1.6, this thesis methodology closely aligns with the overall structure of the thesis and is underpinned by a thoughtful selection of simulation and modelling tools. Commencing with the design of the plant and the establishment of a process flow for the C_2 and C_4 routes to SAF, ASPEN HYSYS was selected for its robust capabilities in simulating

various plant processes. Its versatility is particularly advantageous for providing a comprehensive overview of the envisioned chemical processes. More so, it is widely supported and applied in the Chemical industry.

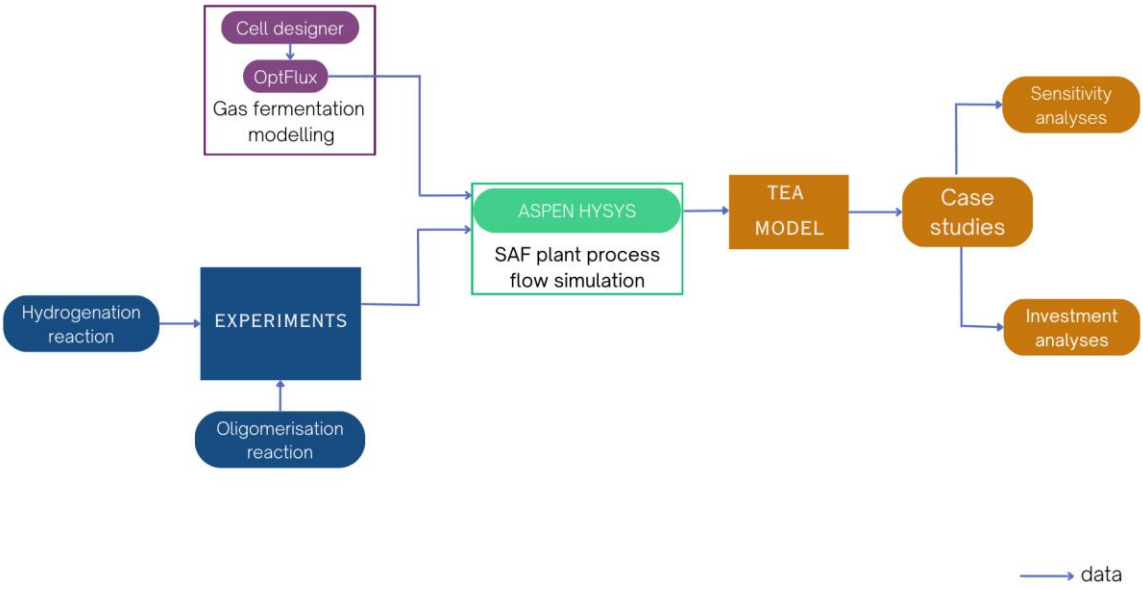

Figure 1.6. Schematic overview of methodology used in this thesis.

However, recognizing the inherent limitations of ASPEN HYSYS in effectively simulating intricate biological processes such as gas fermentation, two additional software tools, namely Cell Designer and OptFlux, were incorporated into the methodology.

Cell Designer was employed to visualize and represent potential biochemical reactions and pathways involved in the gas fermentation of H_2 and CO_2. This software's capability to encapsulate complex biochemical networks, including pathways like glycolysis and the Krebs Cycle, was instrumental. The information stored in Cell Designer's biochemical network modelling was then converted into an Extensible Markup Language (XML) file. This file was subsequently introduced into OptFlux software, which specializes in FBA. This dual software approach was chosen to bridge the gap left by ASPEN HYSYS, ensuring a more accurate representation of the biological processes in the gas fermentation stage. The resulting output plays a crucial role in determining the stoichiometry of the bioreaction to be incorporated into the bioreactor, modeled as a conversion reactor in ASPEN HYSYS. This is a key contribution because systems biology has been uniquely linked to a typical chemical engineering process simulation through the stoichiometry of gas fermentation.

For the proposed C_4 route-to-SAF, experiments were conducted namely the oligomerization of isobutene and subsequent hydrogenation of the oligomerized fractions (dimer, trimers, and tetramers). These experiments were introduced into the HYSYS simulation to provide real-world data for sizing reactors and determining key operating conditions such as temperature, pressure, reaction rates and residence time. The rationale behind these experiments lies in their practical significance. They serve not only to validate the theoretical models but also to refine the simulation inputs and enhance the accuracy of the HYSYS model. This iterative approach, combining experimental data with simulation, ensures a robust and reliable foundation for subsequent analyses and assessments within the overall methodology.

The mass and energy balance data obtained from ASPEN HYSYS simulations were further employed in TEA modeling. This encompassed comparative studies, sensitivity analyses, and investment analyses of all the proposed processes.

CHAPTER 2.

LITERATURE REVIEW

2.1 Jet fuel

Jet fuel consists of a complex blend of C_8–C_{17} hydrocarbons primarily derived from the kerosene or light components of oil refining. Jet fuel composition is subject to variation based on the origin of the crude and the specific production process implemented [46]. The composition mainly consists of paraffin, cycloalkanes, and aromatic collections, with only trace amounts of olefins. Aromatics, which make up under a quarter, are non-saturated ring-shaped hydrocarbons containing single or multiple six-carbon rings. Due to their shortage of hydrogen, they have a high energy density per unit volume but a lower energy density per unit mass compared to paraffin with the same carbon chain length. Jet fuel comprises of hetero atoms, which are hydrocarbon compounds derived from petroleum that has oxygen, nitrogen, and sulfur. Present in minute amounts, these elements influence the fuel's resistance to oxidation and lubricating properties. Sulphur also exists as thiols, mercaptans, aromatic sulfur compounds, and several other sulfur-rich compounds in jet fuel. The current specification sets a limit on the total sulfur content, capping it at three thousand parts per million [47]. Baun et al, in their work, estimated that between 35%–100% of global jet fuel demand could be provided by biofuel by 2050 [48]. ASTM (American Society for Testing and Materials) is an institution that creates and disseminates collaborative, consensus-driven technical standards applicable to an extensive array of substances, goods, processes, and offerings. The specifications for aviation fuels that comprise synthesized hydrocarbons and are suitable for use in turbine-powered aircraft engines are outlined in Table 2.1 [49]. The global aerospace sector uses roughly 1.6 billion barrels of traditional jet fuel annually [50]. In 2015, over 781 million metric tons of CO_2 were produced by air travel, accounting for 2% of all human-caused CO_2 emissions worldwide [51]. In recent times, there has been a huge interest from the aviation sector to contribute to the global goal of reducing the Greenhouse effect. Apart from reducing the greenhouse effect, another serious concern for the aviation industry is the price volatility of conventional jet fuel [52]. Consequently, the idea of using renewable-based jet fuel has attracted significant attention, and airlines such as British Airways, have been actively involved in the initial stages of aviation biofuel advancements by partnering with manufacturers in the biofuels industry [53].

Table 2.1. Comprehensive specification of synthetic hydrocarbon-based aircraft engine fuels.

PROPERTY		**Jet A or Jet A-1**
COMPOSITION		
Acidity, total mg KOH/g	Max	0.1
Aromatics: One of the following requirements shall be met:		
1. Aromatics, volume per cent	Max	25
2. Aromatics, volume per cent	Max	26.5
Sulfur, mercaptan mass per cent	Max	0.003
Sulfur, total mass per cent	Max	0.3
VOLATILITY		
Distillation		
Distillation temperature, °C:		
10 % recovered, temperature (T10)	Max	205
50 % recovered, temperature (T50)		report
90 % recovered, temperature (T90)		report
Final boiling point, temperature	Max	300
Distillation residue per cent	Max	1.5
Distillation loss, per cent	Max	1.5
Flashpoint, °C	Min	38
Density at 15 °C, kg/m3		775 to 840
FLUIDITY		
Freezing point, °C	Max	—40 Jet A
		—47 Jet A-1
Viscosity —20 °C, mm2/sJ	Max	8
COMBUSTION		
Net heat of combustion, MJ/kg	Min	42.8
One of the following requirements shall be met:		
(1) Smoke point, mm, or	Min	25
(2) Smoke point, mm, and	Min	18

PROPERTY		**Jet A or Jet A-1**
Naphthalenes, volume, per cent	Max	3
CORROSION		
Copper strip, 2 h at 100 °C	Max	No. 1
THERMAL STABILITY		
2.5h at a controlled temperature of 260 °C, min		
Filter pressure drop, mm Hg	Max	25
Tube rating: One of the following requirements shall be met:		
(1) Annex A1 VTR, VTR colour code	Less than	3
		No peacock or abnormal colour deposits
(2) Annex A2 ITR or Annex A3 ETR, nm avg over an area of 2.5 mm2	Max	85
CONTAMINANTS		
Existent gum, mg/100 mL	Max	7
Micro-separometer, O Rating		
Without electrical conductivity additive	Min	85
With electrical conductivity additive	Min	70

By using an industrial processing plant, feedstock from biomass is converted and upgraded to a standardized fuel. Jet fuel must adhere to stringent composition standard that exceed those of road transport fuels. It demands high energy content, low friction, and cold flow properties as essential attributes. To achieve these specifications, bio-jet fuel is currently combined with conventional jet fuel sourced from fossil fuels as a drop-in fuel [53].

2.2 Review of different bio-jet production pathways

The production of bio-jet fuel has generated significant interest in the energy sector, as various companies have explored different pathways to utilize sustainable feedstock. In this context, ASTM International plays a crucial role in the aviation sector by developing and publishing technical standards that ensure safety, quality, and performance of materials, products, and processes, including those related to bio-jet fuel production and use. With participation from a diverse range of stakeholders, such as manufacturers, airlines, government agencies, and academia, ASTM fosters a collaborative environment to create comprehensive and up-to-date standards that support the adoption of sustainable aviation fuels and contribute to the industry's efforts in reducing its environmental footprint. Some pathways have been approved by the ASTM [49].

As of January 2017, only five pathways have been certified by the ASTM D7566 process [54]:

1. Hydro-processed Fermented Sugars to Synthetic Iso-Paraffins (HFS-SIP) from biochemical sugars, certified for up to 10% blending with conventional jet fuel.
2. Fischer-Tropsch Synthetic Paraffinic Kerosene with Aromatics (FT-SPK/A) from syngas, certified for up to 50% blending with conventional jet fuel.
3. Fischer-Tropsch Synthetic Paraffinic Kerosene (FT-SPK) from synthesis gas (syngas), certified for up to 50% blending with conventional jet fuel.
4. Hydro-processed fatty acid esters and fatty acids(HEFA), certified for up to 50% blending with conventional jet fuel.
5. Alcohol-to-Jet Synthetic Paraffinic Kerosene (ATJ-SPK) from isobutanol conversion, certified for up to 30% blending with conventional jet fuel.

The D7566 process has some other pathways awaiting certification [54]:

a. Aqueous Phase Reforming for Sugar Catalytic Conversion (APR-CCS): Transforming sugars into hydrogen and valuable chemicals through a catalytic process in an aqueous environment.
b. Lipids Catalytic Hydro-Thermolysis (CH): A thermochemical process utilizing catalysts to convert lipids into biofuel components, such as alkanes and oxygenates.
c. Bio-Crude Integration: Merging renewable bio-crude feedstocks with conventional crude oil processing techniques to produce sustainable fuels and chemicals.
d. Alcohol Intermediates Catalytic Upgrading (CATJ-SKA, Aromatic Synthetic Kerosene): A process to convert alcohol intermediates into synthetic kerosene with aromatic compounds, suitable for aviation fuel.

e. Ethanol Catalytic Upgrading (ATJ-SPK Expansion): Enhancing ethanol's properties through catalytic conversion, making it a viable alternative for aviation fuel.

Various biomass sources can be utilized for bio-jet fuel production, such as lignocellulosic biomass, triglycerides, sugar-based, and starchy feedstocks.

Figure 2.1 shows major pathways that have been identified for the production of SAF from biomass [55].

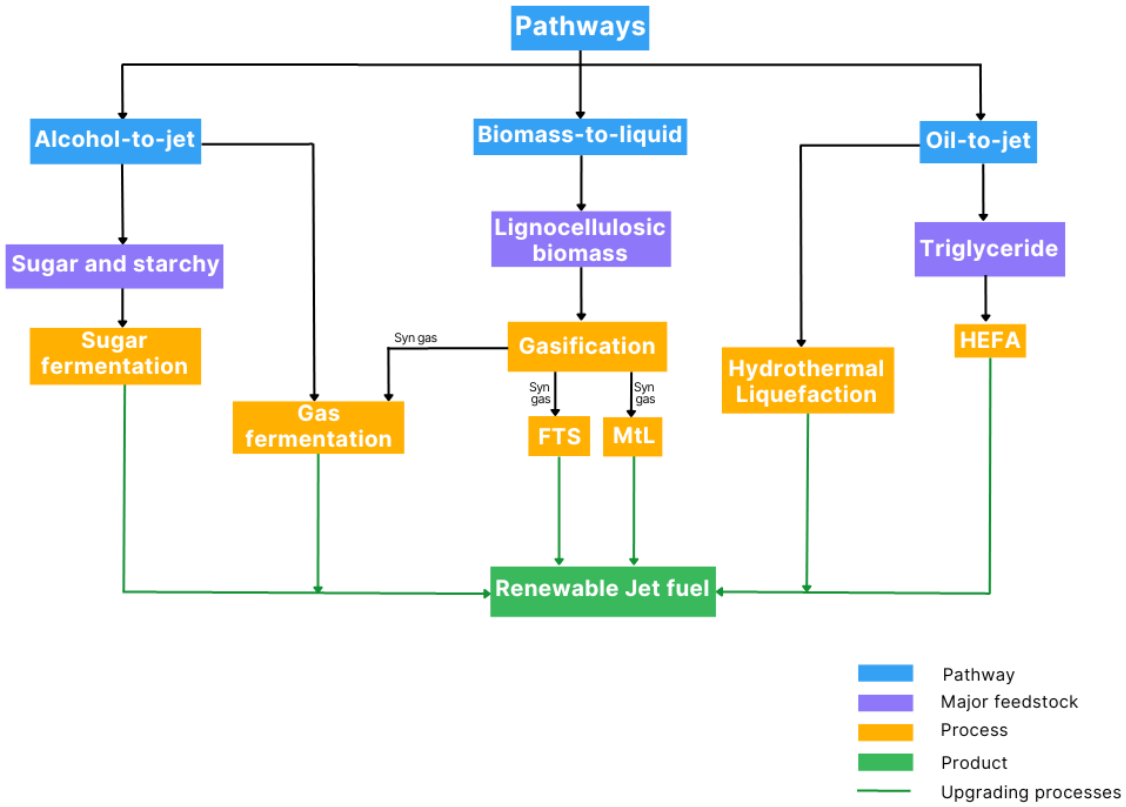

Figure 2.1. Major pathways identified for the production of renewable jet fuel.

The production methods for each of these depend on the specific renewable resource and can be categorized into three main pathways: hydro-processing for triglyceride-based feedstocks, thermochemical conversion for biomass, and the alcohol-to-jet process[56]. In order to minimize costs, it is crucial to select an appropriate production technique based on the availability and accessibility of raw materials. For instance, while lignocellulosic biomass may be a low-cost option, its multi-stage processing can drive up expenses. The cost and transportation of raw materials have a significant impact on the supply chain, ultimately influencing the overall feasibility of bio-jet fuel production [55].

2.3 Oil-to-jet

This pathway can also be referred to as hydro-processing and it primarily involves chemically transforming triglyceride-based raw materials via hydro-deoxygenation, hydro-isomerization, and hydrocracking to generate bio-jet fuel [57]. This conversion route typically comprises 3 methods: Hydro-processed Renewable Jet (HRJ), commonly referred to as Hydro-processed Esters and Fatty Acids (HEFA), a process that converts lipids from various sources into renewable jet fuel; Catalytic Hydro-Thermolysis, often called Hydrothermal Liquefaction (HtL), a technique that subjects biomass to high temperatures and pressures in a water-based environment with a catalyst to produce bio-oil; and pyrolysis, a method that employs heat in the absence of oxygen to decompose cellulosic biomass into valuable biofuels and other products [58].

2.3.1 Feedstock

The feedstock for HEFA and HtL conversion process includes oils from waste, plants, algae, vegetables, and pyrolysis oil. Jatropha oil, algae oils, and animal fats are all classified into non-edible oils. These feedstocks are triglyceride-based and can be used to produce biofuels [22]. Due to conflicts and competition in the food sector, the use of vegetable oil is usually not considered. Fats originating from animals are regarded as by-products of the livestock processing sector, while residual oils are derived from the culinary sector. Bio-oils resulting from pyrolysis can be used to produce biofuels by upgrading them. Plant oils like soybean, canola, rapeseed, palm oils and corn oils are becoming promising feedstock for this pathway. In 2014 alone, 1,450 metric tonnes of palm oil were consumed for biodiesel consumption in Europe [59]. Researchers have taken a keen interest in algae oil due to a variety of factors:

(1) less freshwater is required for its cultivation and use of different sources of water;

(2) it can be cultivated on non-arable land;

(3) hydrogen can be produced using microalgae;

(4) it leverages cost-effective nutrient sources like phosphorus and nitrogen from wastewater for growth;

(5) relatively little GHG emission in comparison with other feedstock [60][61][62].

Pyrolysis oil is also one of the main feedstocks in this conversion pathway. Despite its distinct nature compared to other oils, it is still possible to transform it into sustainable aviation fuel in a similar manner [63]. Another important point to take note of when processing oils is the level of fatty acid. A greater supply of hydrogen will be needed if the oil contains many unsaturated

fatty acids [64]. A list of some companies operating or planning to operate HEFA process is shown in Table 2.2.

Table 2.2. Industries currently operating or anticipating using HEFA method [65].

Project	**Location**	**Feedstock**	**Capacity (million gallons/yr)**	**Operation Year {anticipated}**
Emerald Biofuels	Gulf Coast	Fats, oils, and greases	91	{2025} [66]
Alt Air Fuels	Los Angeles, California	Fats, oils, and greases	40	2016
Neste	Rotterdam, Singapore and Finland	Crude palm oil (36%), waste oils and fats (64%)		2007
REG Synthetic Fuels	Geismar, Louisiana	Fats, oils, and greases	75	2014
Diamond Green Diesel	Norco, Louisiana	Fats, oils, and greases	150	2013
SG Preston	South Point, Ohio	Fats, oils, and greases	120	{2023}[67]
SG Preston	Logansport, Indiana	Fats, oils, and greases	120	{2023} [67]

As about 2017, the total operational capacity of HEFA facilities is about 4.3bln litres per year [65].

2.3.2 Process description

HEFA process hinges on the transformation of raw materials rich in triglycerides, utilizing processes such as hydrogenation, hydro-isomerization, and hydrocracking for bio-jet production In the first phase, the feedstock is transformed into elongated, linear hydrocarbon chains. This transformation typically involves the use of hydrogen and a catalyst, in an environment characterized by high temperature and pressure. The process often includes deoxygenation and decarbonylation reactions. The principal by-products generated from these reactions include CO, water, and CO_2 [68].

Hydro-processed renewable jet conversion has the highest maturity level because its processing is equivalent to conventional petroleum and the technology are already in existence for a long time. Hydrogenation is needed to achieve full saturation of the double bonds present in renewable lipid sources, which may have varying levels of unsaturation [69]. Furthermore, unsaturated fatty acids that are in a liquid state can be converted into their saturated forms through hydrogenation in the presence of a catalyst or by reacting with glycerides [69]. Alternatively, glycerides can be converted to Free Fatty Acids (FFAs) through thermal hydrolysis [70]. Triglyceride-rich oils and fats are transformed into FFAs and glycerol by treating the raw materials with water. The water's H^+ ion binds to the glycerol structure, generating one unit of glycerol, while the water's OH^- ion combines with the ester group, yielding three units free fatty acids To facilitate the dissolution of water into the oil phase, temperatures between 240°C and 270°C are necessary. Additionally, high pressure is essential to keep the reactants in their liquid state. Glycerol, a secondary product, has a wide range of uses in medical, industrial, and cosmetic applications. Although the high-energy demand associated with purifying glycerol increases the overall cost, however, the sale of glycerol may compensate for these expenses [71].

2.3.3 Review of scientific and technological progress

Honeywell company established a process for the production of bio-diesel, but later incorporated a selective cracking method to produce SAF [47]. Several commercial airline flights have used this jet fuel in a 50% blend [72]. However, a big disadvantage of this process is a high hydrogen consumption which negatively affects the cost and safety [73]. Bezergianni et al. examined three reactor temperatures with a specific pressure, liquid hourly space velocity (LHSV), and an H_2/oil ratio [74]. They found that increasing the temperature raised the conversion while the selectivity for jet fuel and a lighter hydrocarbon fraction remained less than 20%. Verma et al., investigated the hydro-processing of jatropha oil using sulfided

catalysts backed by a particular molecular sieve [75]. They conducted the study in a fixed-bed reactor with specific operating conditions. The researchers achieved a certain level of selectivity for aviation fuel in the liquid hydrocarbon product (with notable yields). The resulting jet fuel contained a percentage of aromatic components. The benefit of their findings is that the process required less hydrogen consumption. The production of aromatic components is crucial for blending SAF with conventional fossil jet fuel.

In a separate study, researchers utilized a Ni-Mo/γ-Al_2O_3 catalyst in two lab-scale reactors (structured and compact) for hydro-processing jatropha oil [76]. The outcomes were analysed to compare the selectivity for kerosene. The kerosene selectivity in both reactors was 8-25 times greater than that in a standard columnar bed reactor. This research illustrated that employing advanced apparatus which permits intensification, results in higher selectivity. This in turn has positive impacts on the cost of production.

Gutiérrez-Antonio et al. explored the energy integration of the hydro-treating process using sustainable feedstock as an eco-friendly alternative [77]. They compared the traditional method with the energy-optimized approach. They found that energy optimization reduced temperature-control requirements, but it necessitated additional equipment, leading to higher capital costs. As a result, the overall annual costs were minimally affected. Moreover, a significant reduction in CO_2 emissions was observed with energy optimization. In a follow-up study, Gutiérrez-Antonio et al. examined energy optimization and intensification in the separation area [78]. The primary impact was seen in the further reduction of CO_2 emissions.

Renewable jet fuel can also be produced by hydro-treating pyrolysis oil. Elliot et al. [79] determined that immediate processing of bio-oil in traditional hydro-processing approaches has often been ineffective [80], [81]. More so, fast pyrolysis can be used with a hydro-treating process which can diminish oxygen presence in bio-oil production, while decreasing hydrogen consumption [82].

Aulich et al. proposed a method for creating bio-jet fuel from medium-chain triglycerides and fatty acids (C_8-C_{14}) [83]. The process begins with the separation of fatty acids from the glycerol structure, which can be achieved through heat-based methods or hydro-treatment. Next, glycerol is removed, and the fatty acids also undergo oxygen and carbon dioxide removal process. The final steps involve isomerization and distillation to separate the resulting fractions. Although the liquid produced in this patent closely resembles jet fuel, it does not contain the full spectrum of hydrocarbons [84].

In another patented work by Bao et al., they authors presented a process for producing biomass-derived hydrocarbons, which can be pre-mixed with hydrocarbons. The process involves

treating the biomass with hydrogen in the presence of Ni or Mo catalysts to yield extended-chain hydrocarbons. The utilization of these catalysts allows for reduced processing temperatures in comparison to the higher temperatures demanded by cobalt-molybdenum catalysts [85].

In another review Huber et al examined the chemistry, catalysts, and obstacles involved in producing biofuel by transforming biomass obtained from feedstock in fluidized catalytic cracking and hydro-treating industrial plants [86]. Conversely, rapid pyrolysis optimizes oil production by heating pulverized feedstock for a short duration and subsequently cooling the produced vapours to yield bio-oil [87].

Ramirez Corredores et al, proposed integrating a bio-oil production system with a traditional oil processing facility [88]. Their concept involves jointly processing bio-oil and petroleum-derived streams, enabling the treatment of combined feed materials. This approach could be advantageous during the shift towards sustainable energy sources as petroleum resources are exhausted.

Parimi et al introduced a technique for developing a catalyst that can remove oxygen from bio-based feedstock to generate hydrocarbons [89]. The researchers tested a nano-coated metallic catalyst, with a base of palladium, backed by porous carbon material for jet fuel production. The reactions occurred at temperatures ranging from 250-360°C and a pressure of 69 bar. Finally, isomerization and cracking were carried out on the obtained hydrocarbons through a reactor. They found that the process can yield up to 80% of jet fuel by volume [90].

One study introduced a method for creating renewable jet fuel through hydro-processing renewable feedstock, which improved the cold properties of the resulting products [91]. The cold properties of the obtained hydrocarbons were improved; hydro-processing immediately follows the hydro-treating step. Meanwhile, another research team explored a series of processes from a bio-refinery perspective, resulting in biofuels including jet fuel-range hydrocarbons produced via hydro-treating and other upgrading techniques [92].

2.4 Alcohol-to-jet

Alcohol-to-jet (ATJ) production involves the conversion of various alcohols, such as ethanol or butanol, into jet fuel. This process is gaining attention due to its potential to produce SAF that can significantly reduce greenhouse gas emissions compared to traditional fossil fuels. This process can use various biomass feedstocks, such as sugarcane, corn grain, or switchgrass, to produce the alcohols through fermentation [93].

More so, syngas can undergo fermentation to produce liquid biofuels instead of upgrading the syngas catalytically. Daniell et al. suggested that cooled syngas from gasification could undergo fermentation through specific microorganisms to produce ethanol or butanol [94]. These combined alcohols, including ethanol and 2,3-butanediol, can be transformed into aviation fuel through ATJ technology, which incorporates hydrogenation, distillation, dehydration, and oligomerization processes. In 2012, Daniell et al. highlighted that the gas fermentation process demonstrated a total energy productivity of about 57 percent, surpassing the Fischer-Tropsch Synthesis (FTS), which reached a comparative total energy productivity of around 40 percent [94]. Many companies are exploring the use of lignocellulosic biomass to produce alcohol due to its sustainable nature. Emerging alternative fuels comprise artificial paraffinic kerosene (ATJ-SPK) and artificial kerosene containing aromatics (ATJ-SKA). These processes are modelled on established petrochemical industry techniques and do not necessitate external hydrogen or hydro-processing [1].

The LanzaTech technology, a biofuel conversion process, extracts bio-jet fuel from lignocellulosic biomass such as timber, woodland waste, and cereal crops. The process entails producing sugar from the biomass source before fermenting it. The resulting products encompass alternative hydrocarbon fuels like gasoline, diesel, and jet fuel. More so, LanzaTech's technology further captures waste gases with a high concentration of carbon monoxide, using them as energy providers in this innovative technique [58]. Figure 2.2 shows LanzaTech’s gas fermentation process for Jet fuel production. More so, Gevo Inc., through its technology research has developed a process to produce bio-jet fuel from isobutanol [95]. In this method, the resulting jet fuel consists of a mixture that combines 50% ATJ hydrocarbons, derived from isobutanol, with traditional JP-8 jet propellant. This process has been demonstrated in a bio-refinery plant located in Silsbee, Texas. Figure 2.3 depicts the Gevo technological process.

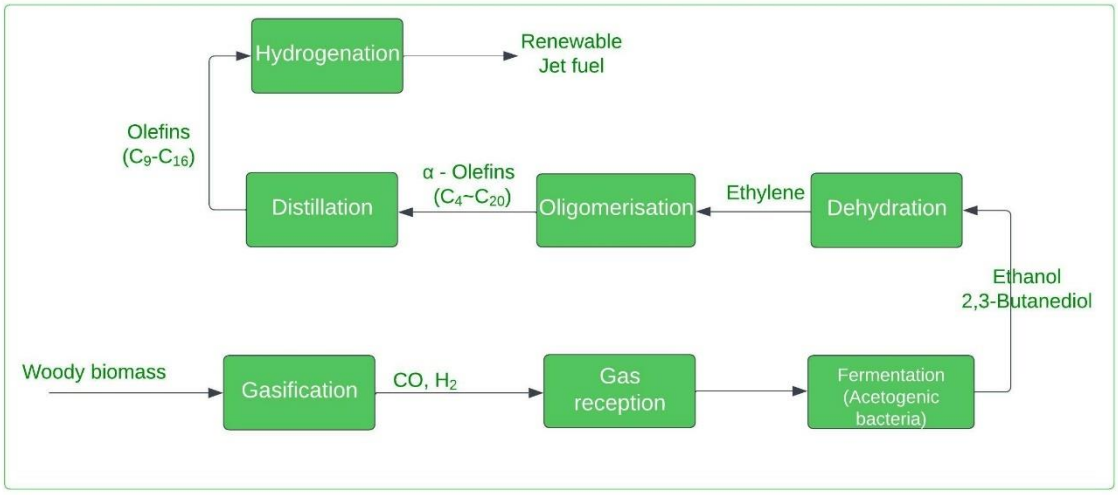

Figure 2.2. LanzaTech gas fermentation to bio-jet concept [95].

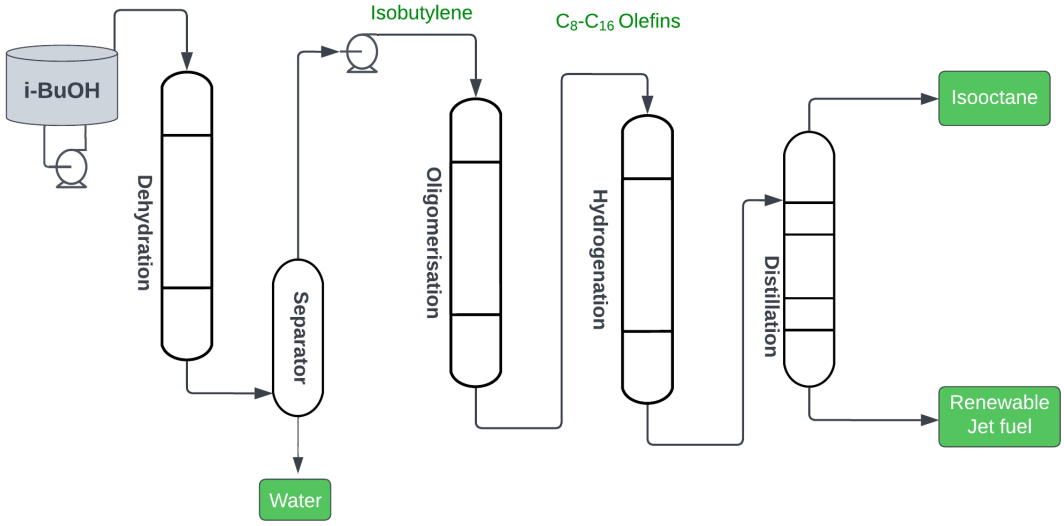

Figure 2.3. Gevo alcohol-to-jet (ATJ) process.

There are several methods for producing bio-alcohol [96],such as:

a) fermenting sugar using yeast or microorganisms;
b) hydrolysing starch followed by fermentation; and

c) fermenting or catalytically hydrogenating hydrolysed lignocellulosic feedstock or thermochemically converted materials (for instance syngas). Upgrades can be achieved through dehydration, oligomerization, and hydrogenation.

Several TEA studies of ATJ production shows that the cost and profitability of the process depend on several factors, such as the type and price of the feedstock, the conversion efficiency and yield of the alcohols and the jet fuel, the capital and operating costs of the plant, and the market prices of the products and co-products [97]. Among the three feedstocks considered, sugarcane has the lowest cost and risk, followed by corn grain and switchgrass. The breakeven price of ATJ jet fuel ranges from $0.96/L ($3.65/gal) for sugarcane to $1.38/L ($5.21/gal) for switchgrass [97].

The high cost of alcohol production is the primary obstacle to commercializing Alcohol-to-Jet fuels. One challenge with sugars and starches is that most feedstocks come from edible crops, which compete with human consumption. Additionally, the low output efficiency for alcohol production results in limited aviation fuel production.

2.5 Gas fermentation: Feedstocks for Gas Fermentation

2.5.1 Carbon dioxide (CO_2)

It is evident that employing CO_2-rich gases as the only source of carbon for microbial conversion presents an attractive option. High CO_2 concentration emissions are prevalent, originating from numerous human activities, including coal or gas power plant electricity generation, waste incineration facilities, and various fossil fuel-powered operations. However, CO_2 cannot supply enough metabolic energy to support microbial life by itself. Moreover, the carbon atom in CO_2 possesses its most oxidized redox state (+4), while carbon in biomass maintains a redox state close to zero. As a result, additional redox equivalents must be supplemented. However, these methods have been created using phototrophic organisms, which use sunshine to provide energy and reduce CO_2. Microorganisms that are involved include prokaryotic cyanobacteria and eukaryotic higher algae or microalgae. A few phototrophic fermentation systems are being researched and, at least in part, have already been applied on a large scale. This covers the creation of pigments, fatty biodiesel components, and

entire cells used as food additives. There has been a thorough examination of algal/cyanobacterial development systems elsewhere [98].

2.5.2 Carbon monoxide (CO)

Carbon monoxide, primarily produced through the incomplete combustion of organic materials or fossil carbon, is a distinct gaseous C_1 component. Unlike CO_2, a wide variety of microorganisms can utilize CO as their sole source of energy and carbon.

Growth rates on simple CO, on the other hand, are often relatively low, but the addition of H_2 considerably increases metabolic turnover (Diener et al., 2015). The off-gas is produced by several industrial processes and can be used. Examples include emissions gases from steel mills, the metal industry, refineries, and chemical facilities that produce gases with varying CO, H_2, and CO_2 compositions. Often, such gases are either flared or, more desirably, combusted for on-site energy production within the industrial facility.

An emerging potential gas resource is the synthesis gas generated through the thermal decomposition or conversion of biomass. This approach is gaining traction as a substitute for the direct fermentation of waste materials that are typically difficult to degrade and may necessitate significant pre-processing [100]. It is believed that nearly all organic waste materials can be repurposed into synthesis gas [101]. Consequently, this technique can utilize diverse feedstocks, including gasified organic substances from municipal solid waste, industrial refuse, biomass, and agricultural residues.

2.5.3 Methane gas

Methane is considered one of the most effective feedstocks for single-carbon gas compounds. This includes large volumes of natural gas that are currently flared or vented, as well as renewable sources from the breakdown of organic material without oxygen in biogas facilities and waste sites. Although methane production at individual sites is typically on a small scale, the sheer number of sites results in significant overall resources [102], [103]. Consequently, microbial transformations occur through a respiratory process that leverages oxygen or, with lower effectiveness, alternative electron receptors like nitrate or sulphate. Oxygen-dependent methane-consuming microbes can rely on methane as their exclusive energy and carbon source, allowing the production of various products such as protein from biomass, bio-based plastics, and bio-derived diesel fuel.

Section 2.5.4 to 2.5.9 will discuss the major pathways of biochemical reactions that occur in a typical aerobic gas fermentation of CO_2 and O_2.

2.5.4 Krebs cycle

The tricarboxylic acid (TCA) cycle, commonly known as the Krebs or citric acid cycle, is a central hub of cellular metabolism, playing a pivotal role in energy production through aerobic respiration. This metabolic pathway, powered by the breakdown of carbohydrates and lipids that generate acetyl coenzyme-A (acetyl-CoA), is essentially a biochemical mechanism where acetyl CoA's chemical energy is transferred to nicotinamide adenine dinucleotide (NADH) [104]. Located within the mitochondrial matrix, the TCA cycle operates in all oxygen-respiring organisms [105]. The overall reaction of the Krebs cycle is outlined below:

$$\text{Acetyl} - \text{CoA} + 3\text{NAD}^+ + \text{FAD} + 2\text{H}_2\text{O} + \text{ADP} + \text{P} \longrightarrow \text{CoA} - \text{SH} + 2\text{CO}_2 + \text{FADH}_2 + \text{ATP} + 3(\text{NADH} + \text{H}^+) \quad \text{Eqn 2.1[106]}$$

Acetyl-CoA, derived from carbohydrates, fats, and proteins, merges with oxaloacetate to launch the TCA cycle, forming citrate. This cyclic series of eight enzymatic reactions results in the production of high-energy molecules such as ATP, NADH, and FADH2. These molecules are channelled into the final stage of aerobic respiration, the electron transport chain, for further ATP synthesis. The cycle also releases CO_2 as a by-product. Figure 2.4 depicts a typical Kreb's Cycle.

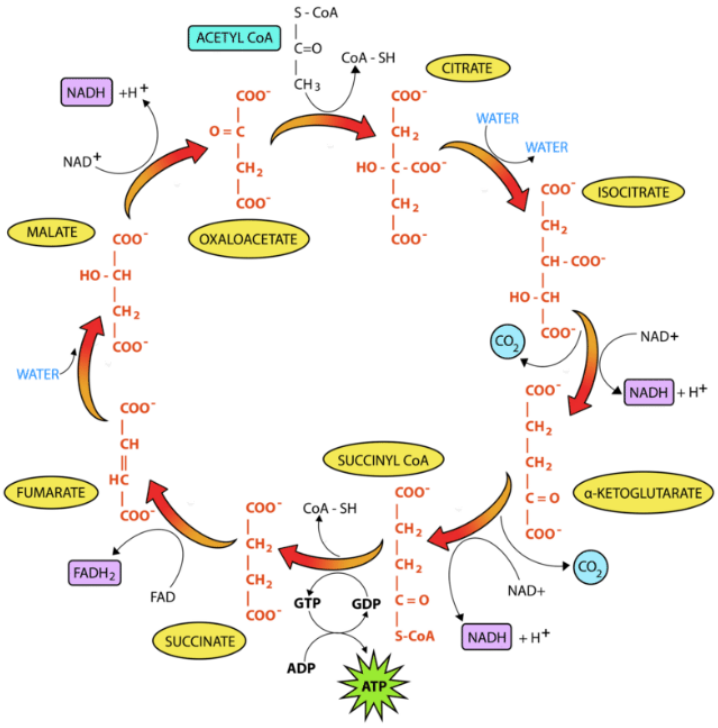

Figure 2.4. Typical Krebs Cycle.

Enzymatic Reactions of the Krebs Cycle:

1. Citrate Synthase: The cycle initiates with the condensation of acetyl-CoA and oxaloacetate to form citrate.
2. Aconitase: The citrate is subsequently isomerized to isocitrate via a cis-aconitate intermediate.
3. Isocitrate Dehydrogenase: Isocitrate undergoes dehydrogenation and decarboxylation by isocitrate dehydrogenase to yield alpha-ketoglutarate, CO_2, and NADH.
4. Alpha-Ketoglutarate Dehydrogenase Complex: Alpha-ketoglutarate is decarboxylated and oxidized by the alpha-ketoglutarate dehydrogenase complex to form succinyl-CoA, NADH, and CO_2.
5. Succinyl-CoA Synthetase: Succinyl-CoA is converted into succinate, generating a molecule of ATP via substrate-level phosphorylation.
6. Succinate Dehydrogenase: Succinate is oxidized to fumarate, with the reduction of flavin adenine dinucleotide (FAD) to flavin adenine dinucleotide (FADH2).
7. Fumarase: Fumarate is hydrated to form malate.
8. Malate Dehydrogenase: Malate is oxidized to regenerate oxaloacetate, producing NADH in the process.

2.5.5 Glycolysis

Glycolysis, a central metabolic pathway, involves the conversion of one molecule of glucose into two molecules of pyruvate. This process comprises ten enzyme-catalysed reactions, split into two primary stages: the preparatory phase (investment of energy) and the payoff phase (generation of energy).

Glycolysis is principally regulated at the steps driven by hexokinase, phosphofructokinase-1, and pyruvate kinase, as these are irreversible points in the pathway. These enzymes are influenced by multiple factors, including substrate availability, enzyme modification, and hormonal control. Glycolysis serves as the primary catabolic pathway for glucose, generating ATP, NADH, and metabolic intermediates for other pathways, such as the TCA cycle and the pentose phosphate pathway. Figure 2.5 shows a schematic depiction of glycolysis.

The enzymatic reactions of glycolysis proceed as follows:

- Step 1: Hexokinase/glucokinase uses ATP to phosphorylate glucose into glucose-6-phosphate.
- Step 2: Phospho-glucose isomerase converts glucose-6-phosphate into fructose-6-phosphate.
- Step 3: Phospho-fructokinase-1 initiates another phosphorylation step, changing fructose-6-phosphate to fructose-1,6-bisphosphate.
- Step 4: Aldolase splits fructose-1,6-bisphosphate into two three-carbon sugars: dihydroxyacetone phosphate and glyceraldehyde-3-phosphate.
- Step 5: Triosephosphate isomerase transforms dihydroxyacetone phosphate into glyceraldehyde-3-phosphate.
- Step 6: Glyceraldehyde-3-phosphate dehydrogenase oxidizes glyceraldehyde-3-phosphate into 1,3-bisphosphoglycerate.

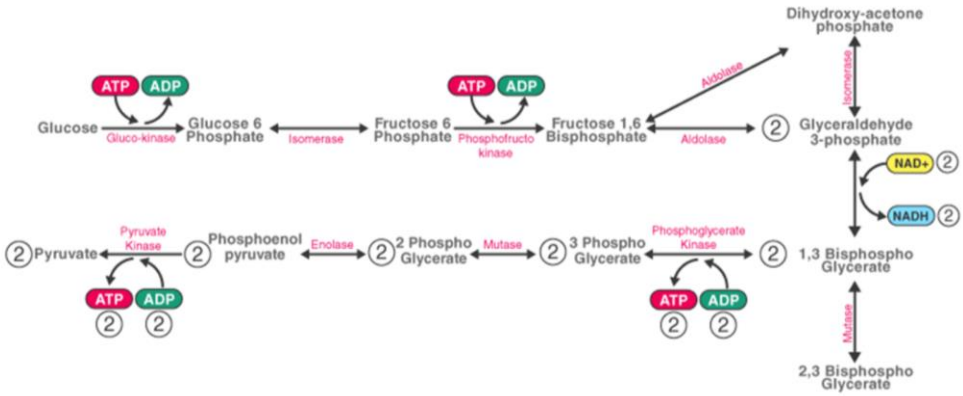

Figure 2.5. A typical pathway for Glycolysis.

- Step 7: Phosphoglycerate kinase transfers a phosphate group from 1,3-bisphosphoglycerate to Adenosine diphosphate (ADP), producing 3-phosphoglycerate and ATP.
- Step 8: Phosphoglycerate mutase rearranges 3-phosphoglycerate into 2-phosphoglycerate.
- Step 9: Enolase catalyses the dehydration of 2-phosphoglycerate, forming phosphoenolpyruvate
- Step 10: Pyruvate kinase generates another ATP by transferring a phosphate group from phosphoenolpyruvate to ADP, yielding pyruvate.

Glycolysis is mainly controlled at the stages involving hexokinase, phosphofructokinase-1, and pyruvate kinase, since these represent the non-reversible steps in the process. The regulation of these enzymes is achieved through various approaches, such as the availability of substrates,

allosteric modulation, and hormone-mediated regulation. Glycolysis serves as the central pathway in glucose catabolism, providing ATP, NADH, and metabolic intermediates for other pathways, such as the Krebs cycle and the Pentose Phosphate Pathway. It is also vital for cells in hypoxic or anaerobic conditions, as it can operate independently of oxygen.

2.5.6 The Pentose Phosphate Pathway

The Pentose phosphate pathway (PPP), also referred to as the hexose monophosphate shunt, is a significant metabolic pathway that runs parallel to glycolysis. It generates nicotinamide adenine dinucleotide phosphate (NADPH), vital for reductive biosynthetic reactions, and ribose-5-phosphate, a core component of nucleotides and nucleic acids. The PPP comprises two distinct stages: the oxidative and non-oxidative stages.

The PPP initiates with glucose-6-phosphate and concludes with ribose-5-phosphate production. This pathway also generates NADPH, a key component in the biosynthesis of fatty acids, steroids, and detoxification processes in the liver. Figure 2.6 shows a typical pathway for pentose phosphate pathway.

The principal regulatory point in the PPP is the first enzyme, glucose-6-phosphate dehydrogenase. This enzyme is allosterically activated by NADP+ and inhibited by NADPH, aligning the pathway's activity with the cell's requirements for NADPH and ribose-5-phosphate.

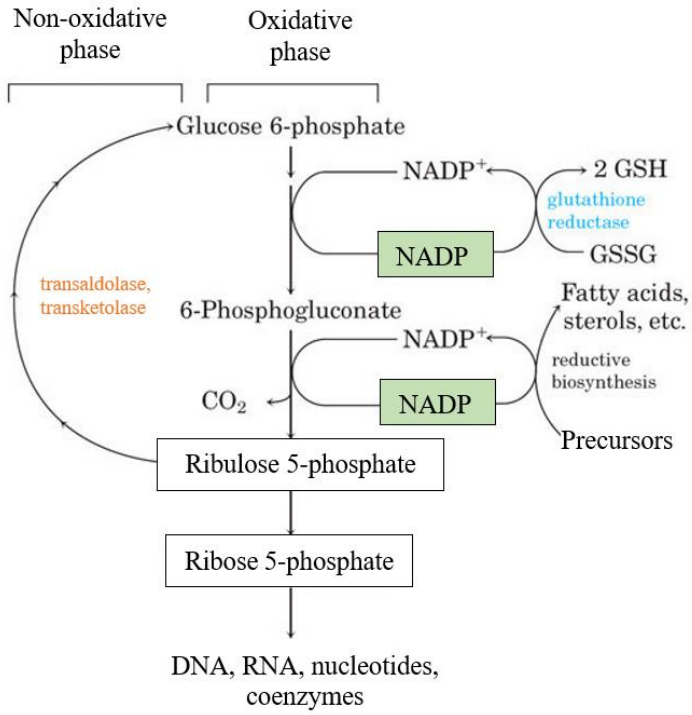

Figure 2.6. A typical pentose phosphate pathway.

The PPP plays an essential role in cellular biosynthetic processes by providing NADPH and ribose-5-phosphate. NADPH acts as a reducing agent in biosynthetic reactions and aids in neutralizing reactive oxygen species. Ribose-5-phosphate is fundamental for the synthesis of nucleotides and nucleic acids. The PPP also provides metabolic flexibility through the interconversion of sugars.

Enzymatic Reactions of the Pentose Phosphate Pathway

1. Glucose-6-Phosphate Dehydrogenase: Glucose-6-phosphate is oxidized to 6-phosphogluconolactone, with NADP+ reduced to NADPH.
2. 6-Phosphogluconolactonase: 6-Phosphogluconolactone is hydrolysed to 6-phosphogluconate.
3. 6-Phosphogluconate Dehydrogenase: 6-Phosphogluconate undergoes decarboxylation to produce ribulose-5-phosphate, CO2, and another molecule of NADPH.
4. Ribulose-5-phosphate Isomerase: Ribulose-5-phosphate is converted into ribose-5-phosphate in the non-oxidative phase.
5. Ribulose-5-phosphate Epimerase, Transketolase, and Trans-aldolase: These enzymes convert ribulose-5-phosphate into fructose-6-phosphate and glyceraldehyde-3-phosphate, which can be directed back into the glycolytic pathway or used for other metabolic processes.

The first enzyme in the PPP, glucose-6-phosphate dehydrogenase, serves as the primary control point. This enzyme is allosterically activated by NADP+ and suppressed by NADPH, enabling the cell to adjust to its requirements for NADPH and ribose-5-phosphate. The availability of the substrate, glucose-6-phosphate, also impacts the activity of this pathway.

The PPP is pivotal in cell anabolic activities, as it generates NADPH and ribose-5-phosphate. NADPH acts as a reductive agent in biosynthetic reactions, including the production of fatty acids, cholesterol, steroids, and also in counteracting reactive oxygen species. Ribose-5-phosphate is essential for nucleotide and nucleic acid formation. Additionally, the ability of the PPP to interchange sugars grants metabolic versatility to the cell.

2.5.7 Valine synthesis

Valine synthesis is a part of the biosynthesis of amino acids and involves several enzymatic reactions. Valine is one of the essential amino acids required by organisms for protein synthesis

and is synthesized via a series of steps from intermediates within the central metabolic pathways. Figure 2.7 shows the typical valine synthesis pathway [107].

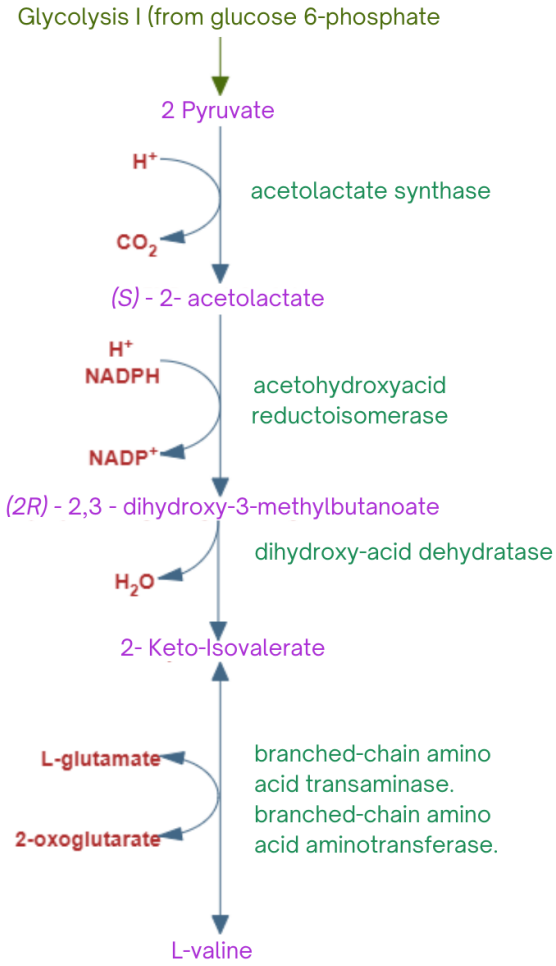

Figure 2.7. Typical valine synthesis pathway.

The steps involved in this are as follows:

Starting Precursors:

- The process begins with pyruvate, an intermediate from glycolysis, and α-keto-butyrate, derived from either threonine or from the catabolism of isoleucine.

Transamination:

- Pyruvate undergoes a transamination reaction, forming α-keto-butyrate, catalysed by a transaminase enzyme.

Formation of α-Isopropylmalate:

- α-Keto-butyrate then combines with acetyl-CoA to form α-isopropylmalate, a reaction catalysed by α-isopropylmalate synthase.

Conversion to β-Isopropylmalate:

- α-Isopropylmalate is further modified to β-isopropylmalate by an enzyme called α-isopropylmalate isomerase.

Formation of α-Keto-isovalerate:

- β-Isopropylmalate undergoes oxidative decarboxylation, resulting in the formation of α-keto-isovalerate, mediated by β-isopropylmalate dehydrogenase.

Conversion to Valine:

- α-Keto-isovalerate is finally converted into valine via a transamination reaction, involving the transfer of an amino group from glutamate, catalysed by a transaminase enzyme specific to valine synthesis.

2.5.8 Calvin cycle

The Calvin Cycle, also known as the Calvin-Benson Cycle, is a fundamental metabolic pathway occurring in the stroma of chloroplasts in plants, algae, and some bacteria. It's the second stage of photosynthesis and plays a crucial role in carbon fixation, converting CO_2 from the atmosphere into organic compounds, primarily sugars [108].

The cycle comprises a series of enzymatic reactions that can be categorized into three main stages: carbon fixation, reduction, and regeneration of RuBP (Ribulose-1,5-bisphosphate).

1. Carbon Fixation:
    - The cycle starts with the enzyme Rubisco (Ribulose-1,5-bisphosphate carboxylase/oxygenase) catalysing the fixation of atmospheric CO_2 by combining it with a five-carbon compound, Ribulose-1,5-bisphosphate (RuBP). This reaction leads to the formation of two molecules of 3-phosphoglycerate (3-PGA), which are three-carbon compounds.
2. Reduction:
    - ATP and NADPH, produced during the light-dependent reactions of photosynthesis, provide energy and electrons for the reduction of 3-PGA to glyceraldehyde-3-phosphate (G3P). This step requires ATP as an energy source and NADPH as a reducing agent.
    - For every three molecules of CO_2 fixed, six molecules of G3P are produced. Out of these, one molecule exits the cycle to be used for the synthesis of sugars and other organic molecules.

3. Regeneration of RuBP:
    - The remaining molecules of G3P undergo a series of enzymatic reactions, consuming ATP to regenerate RuBP. This regeneration step is essential for sustaining the Calvin Cycle and continuing carbon fixation.

The RuBP regenerated in this phase restarts the cycle, allowing for further carbon dioxide fixation to occur. The net reaction of the Calvin Cycle is the conversion of three molecules of CO_2 and nine molecules of ATP and six molecules of NADPH into one molecule of G3P, which can be used to synthesize glucose and other carbohydrates.

The Calvin Cycle operates continuously in the light-independent reactions of photosynthesis, functioning alongside the light-dependent reactions to produce organic molecules crucial for plant growth and serving as a primary mechanism for CO_2 assimilation in plants [108].

2.5.9 Electron transport chain (ETC)

The Electron Transport Chain (ETC) is a critical process occurring in the inner mitochondrial membrane of eukaryotic cells or the plasma membrane of prokaryotic cells (such as bacteria) during cellular respiration and is responsible for generating ATP, the cell's primary energy currency [109].

In cellular respiration, within the inner mitochondrial membrane, the ETC receives high-energy electrons from NADH and FADH2, generated during earlier stages of glycolysis and the citric acid cycle. These electrons move through a series of protein complexes—comprising NADH dehydrogenase, cytochrome bc1 complex, and cytochrome c oxidase—within the mitochondrial inner membrane.

As electrons travel through these complexes, they release energy. This energy is used by the complexes to actively transport protons (H^+) across the inner mitochondrial membrane, establishing an electrochemical gradient or proton motive force [109]. The movement of electrons through the complexes is facilitated by redox reactions, with oxygen acting as the final electron acceptor, ultimately combining with protons to form water.

The energy released during electron movement powers the pumping of protons into the intermembrane space, creating a concentration gradient. This gradient serves as a source of potential energy that drives the ATP synthase enzyme to catalyse the synthesis of ATP from ADP and inorganic phosphate. This process, known as chemiosmosis, exemplifies how the flow of electrons is tightly coupled with ATP production.

In photosynthesis, the ETC operates in the thylakoid membranes of chloroplasts. Here, the ETC is part of the light-dependent reactions, receiving high-energy electrons from chlorophyll

molecules excited by light. These electrons are then passed through a series of protein complexes, similar to those in cellular respiration, generating a proton gradient across the thylakoid membrane.

As in respiration, the proton gradient drives ATP synthesis by ATP synthase, facilitating the conversion of ADP and inorganic phosphate into ATP. Additionally, in photosynthesis, the ETC plays a crucial role in generating reducing power in the form of NADPH, essential for the Calvin Cycle—fuelling the conversion of CO_2 into organic compounds.

Both in cellular respiration and photosynthesis, the electron transport chain is pivotal in utilizing electron energy to generate ATP, meeting the energetic needs of the cell or providing the necessary reducing power for carbon fixation. This intricate process of electron movement and ATP synthesis highlights the remarkable efficiency and interconnectedness of cellular energy production.

2.6 Biomass-to-liquid (BtL)

Biomass-to-liquid (BtL) is one of the pathways that is used to convert biogas or syngas into biofuel. Biogas can be obtained via biomass as feedstock. Antal et al. emphasize that although biomass represents a sustainable resource, varying levels of carbon in different types of biomass can impact jet fuel production. For example, timber-based biomass has a carbon concentration ranging from 45% to 55%, while farming by-products display a broader span of carbon concentrations, between 40% and 60% [110]. The BtL process produces intermediate distillates, such as diesel and jet fuel "alternative" fuels, through the combined approach of gasification and the Fischer-Tropsch synthesis or Methanol-to-liquid (MtL) method [111].

2.6.1 Gasification

Gasification, a high-temperature heat-driven chemical reaction (occurring between 550°C and 1350°C), requires heat to transform biomass or similar carbon-rich materials into various gases. The resulting mixture typically comprises constituent gases such as CO, H_2, H_2O, N_2 and CH_4, along with impurities like carbon residues, solid waste, and other hydrocarbon by-products. There are different types of gasifiers employed in the industry. A range of gasifiers are utilized in the industry, which can be sorted by fuel interaction techniques, airflow direction, and bed types. Updraft, downdraft, and cross-draft configurations are examples of fixed bed gasification systems [112]. Gasifiers can be categorized into two main types: direct or partial oxidation gasifiers and indirect steam-blown gasifiers [113].

In an investigation conducted by NREL on indirect gasification, the gasification process is endothermic, and artificial olivine sand is heated and circulated to indirectly heat the biomass.

Steam is injected to fluidize the biomass within the gasifying chamber, and gasification takes place at 850°C. This process breaks down the biomass into a syngas mixture, chars and tars [113].

In the process of indirect gasification, the primary reaction entails the decomposition of biomass into gases, condensable materials, and char, which are considered by-products. The resulting gas composition in the gasifier is governed by several parameters, encompassing the makeup of the feedstock, the type of gasifier, the duration of residence time, and operational variables such as temperature and pressure. Moreover, the importance of gas-phase reactions, such as the water-gas shift, contributes to the determination of the gas mixture [114].

Four stages are involved in the gasification process: biomass drying, primary and secondary pyrolysis, product combustion, and the reduction of hydrogen, carbon dioxide, and water using char. The first kinetic models emphasized the de-volatilization of wood or cellulose, converting them into gases, char, tar and char [115]. However, coal gasification research has yielded important insights through the incorporation of mixed char reaction kinetics and transport processes [116].

Chopra and Jain's review highlights that downdraft gasifiers are typically appropriate for processing biomass fuel with moisture and ash content below 20% and 5%, respectively [117]. Numerous studies verify that downdraft gasification yields syngas with minimal tar content and offers simplicity and reliability. In such gasifiers, biomass travels alongside the gas, passing through drying, pyrolysis, oxidation, and reduction zones. The majority of gasifier models found in the literature lack a throat due to the intricate downdraft design and often feature air injection at the gasifier's top. In contrast, the majority of these models work in a steady state and assume the presence of stable zones.

C. Dejtrakulwonga et al., attempted to model the four zones of the downdraft gasifier in their study, focusing on the effect of moisture content and the air-to-fuel ratio [118]. They observed that an increase in moisture content led to an increase in the heights of the drying and pyrolysis zones, while the critical reduction zone decreased. Moreover, when the air-to-fuel proportion varied between 1.8 and 3, the critical height of the reduction zone slightly decreased.

In contrast, Ozgun Yucel et al., claim that in that these models often inaccurately assume reactions fully reach completion, particularly within the char reduction zone. They suggest that the gasification efficiency depends on various factors, such as the air-to-carbon ratio, solid residence time, and other kinetic elements. Therefore, equilibrium models tend to overestimate the yields of hydrogen and carbon monoxide while underestimating the output of carbon dioxide and other by-products, such as char and tar, especially at lower temperatures during

the gasification process [119]. Ozgun et al. presented a complete and validated model of the transient behaviour of a gasifier. Unlike other studies that used mini-scale lab equipment, they worked on a pilot-scale unit. The authors claimed that this approach provided an enhanced examination of operational circumstances, thermal dissipation, linkage and channelling, as well as issues related to measurement. The authors concluded that the model result was in line with experimental data, however, the throated gasifier presented some difficulties in modelling.

Since gasification is a thermochemical process, it is tagged as the safest way to extract the maximum energy from waste biomass. It is also said to be very efficient because it has the potential to reach complete oxidation of waste to produce valuable gases. It is also a very flexible and more reliable method to create synthetic gas from low-value feedstock production of high-value products and power.

2.6.2 Supercritical water gasification

Supercritical water gasification (SCWG) is a promising technology that harnesses the potential of biomass for the creation of renewable energy. As an innovative method, SCWG utilizes the distinct properties of water under supercritical conditions, specifically above its critical point (647 K, 22.1 MPa), to convert organic matter into valuable gaseous products [120]. The primary outputs of this process are hydrogen and carbon dioxide, with lesser amounts of carbon monoxide and methane.

Supercritical water, under certain conditions, displays interesting features that are usually seen in both gases and liquids. It has a low density, much like a gas, and a strong ability to dissolve substances, similar to a liquid. Moreover, supercritical water has a significant ion product of 10^{-2} mol^2 L^{-2}. These unique traits make supercritical water a great choice for carrying out chemical reactions, adding to its scientific value.

The biomass in the SCWG process undergoes various stages, including hydrolysis, dehydration, decarboxylation, and finally gasification. The gasification stage holds the most significance as it transforms the biomass into a gaseous mixture, predominantly containing H_2, CO_2, and lesser amounts of CH_4 and CO.

SCWG is fundamentally an exothermic process with its thermodynamics primarily driven by two crucial reactions: the water-gas shift reaction and the methane reforming reaction. The former involves a reaction between carbon monoxide and water, generating carbon dioxide and hydrogen, while the latter incorporates the reaction of methane with water, yielding carbon monoxide and hydrogen.

The kinetics of SCWG is multifaceted, influenced by a wide array of factors such as temperature, pressure, residence time, and the nature of the biomass feedstock. Increased temperatures and pressures tend to favour the gasification process, while an optimal residence time is necessary to ensure comprehensive conversion of the biomass.

Catalysts are indispensable in augmenting the efficiency of the SCWG process. By accelerating the reaction rate and shifting the reaction equilibrium towards the preferred products, catalysts play a critical role in the process [121]. Notable catalysts include noble metals such as ruthenium, palladium, and platinum, as well as base metals like nickel and cobalt. The selection of a catalyst is typically influenced by its activity, stability under supercritical conditions, and resistance to deactivation due to processes like coking and sintering.

Despite the promise of SCWG for biomass conversion, it still faces several technological hurdles. These include the development of catalysts that offer high performance and cost-effectiveness, the design of reactors capable of enduring high temperatures and pressures, and the management of waste products, especially carbon dioxide [122].

Moreover, there is a need to improve the commercial viability of SCWG. This can be achieved through integrated systems that couple SCWG with other biomass conversion technologies, thus allowing for a broader range of products and enhancing the overall process economics.

2.6.3 Methanol-to-liquid (MtL)

Methanol-to-jet is another pathway that has been also considered in recent times. Methanol serves as a flexible feedstock for the industrial chemical sector and represents a significant commodity, with yearly output of approximately 80 million tons in 2016 [123]. It can also be used in the production of methyl ethers like DME or even biodiesel. It has been a common thing to use methanol as gasoline blend stock [124]. Methanol can be produced from syngas which can be derived from sources like fossil fuels or carbonaceous materials. The process begins with the production of syngas, which can be obtained through various methods like steam reforming or partial oxidation of natural gas, or gasification of coal or biomass. The ratio of hydrogen to carbon monoxide in syngas is crucial for the subsequent methanol synthesis reaction. Usually, a catalyst such as Cu-ZnO-Al_2O_3 is used and the reactions are as follows [125].

$$CH_4 + H_2O \rightarrow CO + H_2 \qquad \text{Eqn 2.2}$$

Then, the next reaction is methanol synthesis:

$$CO_{(g)} + 2H_{2(g)} \rightarrow H_3COH \ \Delta H° - 31.6\ KJmol^{-1}$$ Eqn 2.3

Syngas, at the right composition, is fed into a methanol synthesis reactor containing a catalyst bed. This reaction is exothermic, releasing heat, and typically occurs under moderate temperatures and high pressures (around 50 to 100 bar) to favour methanol formation. A typical process can be seen in Figure 2.8 [126]. Recent research has shifted its focus toward enhancing catalysts that facilitate the conversion of CO_2 via introducing H_2, eliminating the need to produce CO through the reverse water-gas shift (RWGS) reaction [127].

$$CO_2 + 3H_{2(g)} \rightarrow H_3COH_{(l)} + H_2O \ \Delta H° - 137.8KJmol^{-1}$$ Eqn 2.4

Methanol is usually isolated from water through another process due to insolubility. Additionally, the reaction is highly exothermic, necessitating heat removal to maintain control over the process [126]. According to Porosoff et al., direct conversion of CO_2 often leads to many technical issues, particularly concerning the amount of required pressure which usually exceeds 30 MPa for a good reaction performance [128]. In contrast, Carbon Recycling International (CRI) operates an industrial-scale methanol manufacturing facility utilizing a CO_2 reaction, processed with hydrogen generated through electrolysis [129]. CRI has a facility in Iceland that has been in operation since 2012 and generates about 4000t of methanol per annum [129]. A different strategy currently under investigation involves the co-electrolysis of water and CO_2, which directly generates H_2 and CO as a promising technological option[130]. The methanol-to-gasoline (MTG) process is more prevalent and employs a specially engineered zeolite catalyst with dimensions that allow molecules within a hydrocarbon range(C1-C9) to exit. High octane gasoline is usually produced via this process due to the high amount of branched alkanes and aromatics. In this approach, methanol undergoes conversion to dimethyl ether (DME), which can function as an effective diesel fuel, through the reaction below [126].

$$2CH_3OH \rightarrow CH_3OCH_3 + H_2O$$ Eqn 2.5

Furthermore, the subsequent dehydration of dimethyl ether produces the desired hydrocarbon product. The reaction sequence is stated below:

$$CH_3OH \rightarrow -(CH_2) - n + H_2O$$ Eqn 2.6

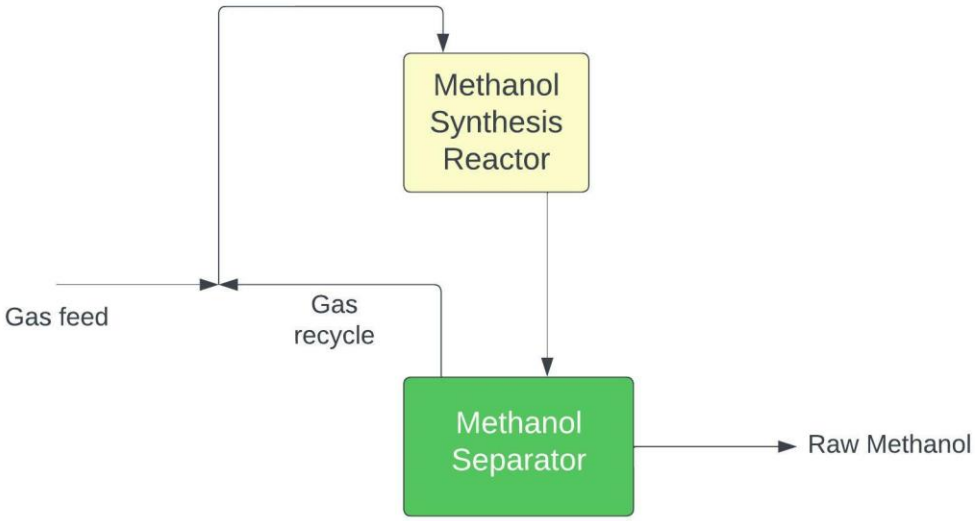

Figure 2.8. A typical process flow of Methanol synthesis [126].

Mobil has successfully implemented the transformation of methanol into intermediate-range fuels [131]. This process typically involves converting methanol into light olefins, which then undergo oligomerization, followed by minimal hydro-treatment and fractionation The evaluation of the resulting distillate fractions' properties indicates that certain aviation fuel and biodiesel specifications have been satisfied [132]. Mobil's conversion technique, which transforms methanol into distillate, holds the promise of producing 100% alternative synthetic fuel in compliance with the existing ASTM D7566 standard. Despite its potential, the process has not yet been commercialized, nor has it received ASTM approval.

2.6.4 Fischer-Tropsch Synthesis (FTS)

ASTM-approved bio-jet fuel production for commercial applications involves gasification and the FTS. The transformation of lignocellulosic biomass via gasification and FTS is illustrated in Figure 2.9. The process begins with the production of syngas via gasification, which is a mixture of hydrogen (H_2) and carbon monoxide (CO). Syngas is fed into the FT reactor, which contains a catalyst. The catalyst used in the FT process is typically based on metals like iron, cobalt, or nickel supported on inert materials such as alumina or silica. These catalysts facilitate the chemical reactions necessary to convert syngas into hydrocarbons. The FT reaction involves a series of complex chemical reactions where carbon monoxide and hydrogen molecules are rearranged and combined to form longer-chain hydrocarbons. These hydrocarbons can range from methane (CH_4) to high-molecular-weight waxes and can be

further processed into liquid fuels [111]. One of the significant advantages of the FT process is its ability to produce a wide range of hydrocarbons with varying chain lengths. Depending on the catalyst and reaction conditions, the process can yield light olefins, paraffins, and even waxes, which can be subsequently upgraded or refined into products such as diesel, gasoline, lubricants, and waxes. The mixture of hydrocarbons obtained from the FT process undergoes separation and refining steps to isolate and purify the desired end products. This refining may involve processes such as hydrotreating, distillation, and hydrocracking [111].

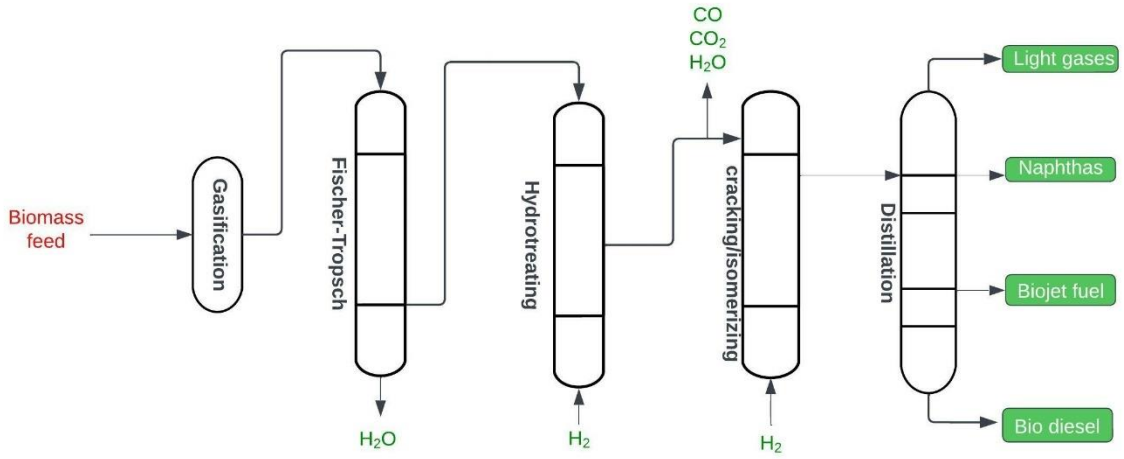

Figure 2.9. Lignocellulosic biomass conversion utilizing gasification and Fischer-Tropsch synthesis techniques [111].

According to Liu et al, a combination of pyrolysis, gasification, and FT synthesis presents an optimal approach for generating bio-jet fuel [133].

Europe's pioneering Green Sky project, a collaboration between British Airways and Solena, employs cutting-edge technology to transform waste materials into bio-jet fuel[1]. Relying on gasification techniques, the project aims to process about half a million tons of post-recycled waste into 120,000 tons of eco-friendly liquid fuels using Solena's innovation [134]. The selection of gasification methods varies based on feedstock attributes [135]. A crucial factor in this method is the relatively low bio-jet fuel yield, approximately 20%. Consequently, it is essential to monetize the resulting by-products for the process to be economically viable. Notably, FT fuels possess minimal sulphur and aromatic content compared to gasoline and diesel, resulting in reduced emissions when utilized in jet engines [48].

2.7 Technology and process selection for Thesis

2.7.1 Advantages of supercritical water gasification over conventional gasification

The selection of SCWG stems from its unique operational characteristics and environmental advantages, positioning it as a compelling choice for this thesis. Table 2.3 provides a summary of the comparison between SCWG and the conventional gasification.

Enhanced reaction rates and versatile operation

SCWG operates under high temperatures and pressures, leveraging the distinctive behaviour of supercritical water to enhance reaction rates. Its dual role as a solvent and catalyst facilitates efficient breakdown and accelerates chemical reactions. Compared to conventional methods, SCWG demonstrates superior speed and efficiency due to these characteristics, setting it apart as a technologically advanced and efficient process.

Versatility in biomass feedstocks

An inherent advantage of SCWG lies in its ability to process a wide array of biomass materials, including diverse sources like agricultural waste, animal by-products, algal biomass, and municipal solid waste. Traditional gasification techniques often struggle with these heterogeneous and moisture-rich feedstocks, requiring costly drying procedures. SCWG's tolerance to high water content eliminates the need for such preparatory steps, making it a practical choice for handling varied feedstock compositions.

Table 2.3. Comparison between SCWG and conventional gasification process [136], [137].

Criteria	**Supercritical water gasification (SCWG)**	**Conventional gasification**
Operating temperature	Above 374°C, at supercritical conditions	Typically around 700-1500°C
Pressure	Above 22.1 MPa (Critical pressure)	Varies, often lower
Feedstock	Can handle wet biomass without drying	Requires drying and size reduction
Heat source	Less external heat required	Relies on external heat sources

Criteria	Supercritical water gasification (SCWG)	Conventional gasification
Reaction speed	Faster due to supercritical conditions	Slower compared to SCWG
By-products	Fewer solid by-products	Can produce more solid residues
Water usage	Uses water as a reaction medium	Less water-intensive
Scale of application	Still in development for large-scale use	Established at industrial scales
Environmental impact	Potential for cleaner gasification	Emissions and residues may pose environmental concerns

Syngas enriched with hydrogen and environmental impact

SCWG produces a syngas with a high H_2 concentration. In a global shift towards cleaner energy sources, hydrogen's high energy content and carbon-neutral emissions profile make it increasingly valuable as a fuel. This stands in contrast to other gasification methods that yield syngas with lower hydrogen content and often result in the production of pollutants like tar, char, and particulate matter. SCWG's inherent solubilization capabilities and high operating temperatures significantly reduce the generation of these pollutants, aligning with environmental sustainability goals.

Energy conversion efficiency

One of SCWG's notable strengths is its enhanced energy conversion efficiency relative to other gasification methods. The inherently exothermic nature of the process, coupled with high reaction rates and comprehensive feedstock conversion, positions SCWG as a promising pathway for efficient energy conversion from biomass.

Limitations and Ongoing Development:

However, SCWG is not without its limitations. The technology demands high operating pressures and temperatures, leading to the requirement for specialized materials and complex

reactor designs, which may escalate operational costs. Additionally, while SCWG demonstrates promise, its scale of application is still in developmental stages for large-scale industrial implementation. The limitations in scalability and the need for further research and development to overcome engineering challenges remain critical areas of consideration.

In summary, the unique combination of superior operational efficiency, versatility in handling diverse feedstocks, minimal solid by-products, reduced environmental impact, and the potential as aerobic gas fermentation feed source, makes SCWG a compelling and relevant choice for exploration within the scope of this thesis.

2.7.2 Gas Fermentation: Benefits and Opportunities

The strategic selection of gas fermentation as the focal technology for SAF production in this thesis, is driven by its multifaceted advantages and its potential impact on the field. Table 2.4 shows an overview comparisons of existing SAF production pathways.

Gas fermentation, whether aerobic or anaerobic, stands out as a promising technology for transforming syngas into valuable commodities such as SAF, addressing inherent difficulties through high selectivity bio-transformations [37]. By modifying the metabolic pathways of microorganisms capable of utilizing CO_2 and H_2 as their sole source of carbon and energy, gas fermentation facilitates the production of desired chemicals.

Gas fermentation boasts a considerable edge over first-generation methods such as HEFA by enabling the utilization of feedstocks not derived from food sources, thus eliminating competition with food while ensuring plentiful feedstock supply for generating substantial quantities of renewable fuel. Additionally, when compared to alternative second-generation strategies, gas fermentation presents many process benefits in terms of feedstock adaptability and production cost-effectiveness. This method encompasses a broad array of feedstock choices, coupled with elevated levels of energy and carbon sequestration. Moreover, the process is characterized by growth possibilities, catalyst versatility, high selectivity, and robustness[138], [139].

More so, when compared to FT synthesis, a widely employed process involving the thermochemical conversion of syngas into liquid hydrocarbons utilizing cobalt or iron-based catalysts, gas fermentation demonstrates notable advantages. Similar to gas fermentation, this process commences with the gasification of biomass to produce syngas, which subsequently undergoes thorough purification and adjustments in its composition through an energy-demanding water-gas shift phase.

Table 2.4. Summary table for SAF production technologies comparison [144], [145].

SAF Production Pathway	Feedstock	Pros	Cons	Cost($/L)	GHG Emissions Savings	Environmental Impact	Scalability
FT	Lignocellulosic Biomass, MSW	- Can use various lignocellulosic biomass	- High capital cost - Low yield - High water and energy demand	$2 - $5	50-90%	Land use change, water consumption, air pollution	High
HEFA	Oil-seed crops	- Utilizes existing infrastructure - Can utilize waste oils - Can utilize microalgae	- Limited feedstock options (mostly oil-seed crops) - Challenges in scalability and cost -Competition with food	$2.5 - $4.5	50-80%	Land use change, water consumption, biodiversity loss	Moderate scalability
	Waste oils			$1.5 - $3.5	80-90%		Moderate scalability
	Microalgae			$4 - $30	60-90%		Limited scalability due to cultivation challenges
ATJ	Ethanol from biomass, biogas, MSW	- Can use diverse feedstocks like ethanol	- High energy input	$2 - $4	40-80%	Land use change, water consumption, air pollution	Moderate scalability
Gasification & FT	Biomass, MSW	- Versatile in accepting a wide range of feedstocks	- High capital and operational costs	Variable, potentially high	Depends on feedstock	Land use change, water consumption, air pollution	Limited scale due to cost
MTL	Lignocellulosic Biomass	- Can use lignocellulosic biomass	- High-cost and energy-intensive	$2 - $5	80-95%	Land use change, water consumption, air pollution	Moderate scalability
Power-to-liquid (PtL)	Renewable electricity, water, CO_2	Drop-in fuel, carbon-neutral, scalable, low land and water use	High cost, high energy demand, limited availability of CO_2, immature technology	$4 - $6	80-100%	Electricity source, CO_2 source, air pollution	High scalability

Once processed, the syngas is hydrocracked, leading to the formation of liquid fuels following the conversion into a blend of hydrocarbons via the FT process. Various complex models have been put forth to clarify the underlying principles of the FT process [140]–[142]. FT synthesis has experienced considerable advancements and is now extensively employed in South Africa for transforming coal into liquid fuels [142]. The FT process, much like gas fermentation, presents a critical benefit of feedstock flexibility. This advantage is made possible through the gasification stage, which enables the complete utilization of all components of the biomass, including the lignin part. However, when compared with gas fermentation, the FT process's catalysts are believed to exhibit constraints in terms of sturdiness, adaptability, and selectivity, potentially leading to a financial drawback for production [100].

Maintaining high syngas purity levels is essential to avoid catalyst contamination, as the presence of specific substances, such as sulphur or CO_2, can hinder or even permanently inactivate the catalysts employed [143]. Moreover, for optimal productivity, a consistent gas ratio within the syngas is often needed. For instance, catalysts used in the FT process that are derived from cobalt necessitate a steady hydrogen to carbon monoxide ratio, typically around the value of 2.15 [142]. Achieving this balance can be particularly challenging when dealing with an inconsistent feedstock like biomass or urban waste materials. Owing to these strict criteria, generating refined, optimally composed syngas constitutes about 65% of the operational expenses in a conventional FT facility [142].

In contrast, bio-catalysts can accommodate a diverse array of syngas ratio variations, removing the necessity for an additional gas shift reaction [146], and exhibit increased resilience to impurities in the syngas, thus requiring a more cost-effective gasification procedure [147]. As bio-catalysts demonstrate greater selectivity, gas fermentation yields are enhanced, and post-processing is simplified, leading to a decreased likelihood of unwanted by-products [100].

Regarding catalysts, the metal-based agents employed in the FT process can incur significant expenses [143]. More so, gas-consuming microorganisms can effectively regenerate by utilizing a portion of the supplied gas and inexpensive supplementary growth substrates.

Additionally, research comparing the two methods revealed that the FT process has an approximate relative energy conversion rate of 44%, while gas fermentation attains a near 57% relative energy conversion rate [100].

An alternative approach to biofuel production is the fermentation of biomass containing lignocellulose, a multi-stage biochemical process that involves pre-treatment, hydrolysis, and fermentation of biomass with lignocellulose to generate bioethanol. This method is often employed in processes like the ATJ process, where alcohols derived from biomass are

converted into SAF. However, the stubborn nature of biomass presents a major challenge for this method. The lignin component, which generally makes up a significant portion of the biomass (between 9-26%), is not readily processed by this type of fermentation. This is crucial because the lignin makes up 25 to 35 percent of the feedstock's energy content. This resource's carbohydrate component must first undergo a difficult and expensive pre-treatment step to separate the lignin from the cellulose and hemicellulose polymers, which must then undergo enzymatic hydrolysis to convert the polymers into fermentable sugars [146].

Pre-treatment methods for lignocellulosic biomass include mechanical processing such as grinding and exposure to radiation, in addition to chemical pre-processing approaches involving substances that promote oxidation and strong acids [148].

On the other hand, gas fermentation simplifies the process by bypassing many of these steps. The gasification method converts the entire raw material, encompassing both lignin and sugar-derived parts, into a fermentable synthesis gas [139]. This holistic transformation via gasification enables diverse resources to be processed using one technology, resulting in a fermentable gas product.

Anaerobic fermentation has dominated commercial gas fermentation, yet it presents limitations, including a narrow metabolic scope due to energy-related constraints associated with anaerobic CO_2 fixation [41]. The generation of low-value by-products and challenges in downstream processing are common in anaerobic fermentation [39] [42].

Comparatively, aerobic gas fermentation offers several advantages. Despite challenges associated with the energy-intensive Calvin-Benson-Bassham cycle, it has the potential to produce sophisticated chemicals, expanding the scope of renewable chemicals [42], [44]. As previously mentioned in section 1.7 , this study strategically selects aerobic gas fermentation for SAF production due to its potential to overcome limitations observed in anaerobic processes, such as metabolic pathway constraints, by-product generation, and microorganism sensitivity.

In summary, the strategic choice of exploring aerobic gas fermentation for SAF production within the scope of this thesis, is bolstered by its numerous advantages over anaerobic fermentation and other SAF production pathways. Its multifaceted benefits, adaptability, and efficiency position aerobic gas fermentation as a promising technology within the renewable fuel production landscape.

2.7.3 Case studies explored in thesis

In the context of aerobic gas fermentation of CO_2 and H_2, this thesis investigated the metabolic engineering of Cupriavidus necator for the production of two key intermediates for SAF synthesis, namely 2-ketoisovalerate and acetaldehyde. These intermediates hold significant promise in the synthesis of specific jet fuel blends, forming integral components within the broader SAF synthesis pathway.

The strategic selection of acetaldehyde (C_2H_4O) and 2-ketoisovalerate ($C_5H_8O_3$) as primary intermediates in this study resonates with their pivotal roles as metabolic intermediates essential for synthesizing a diverse array of value-added products via aerobic gas fermentation of CO_2 and H_2 [149]–[152]. These intermediates serve as precursors for many products, exemplified by their conversion into isobutanol, n-butyraldehyde, L-valine, acetoin (derived from 2-ketoisovalerate), ethanol, butanol, and acetone (derived from acetaldehyde) [150], [151], [153]. These products serve as essential building blocks, further upgradable to SAF via subsequent chemo-catalytic processes.

Cupriavidus necator is a representative hydrogen-oxidizing bacterium that has been widely studied and engineered for gas fermentation, as it can utilize CO_2 and H_2 as sole carbon and energy sources and produce a biodegradable polymer, polyhydroxybutyrate (PHB), as well as other compounds [152]. This bacterium has a well-developed genetic system and metabolic engineering tools that enable manipulation and optimization of carbon fixation and product formation pathways, underscoring its potential for advancing gas fermentation technology.

In this thesis, the microbial pathway involving acetaldehyde as an intermediate is denoted as the C_2 pathway or route for SAF production, attributed to its two-carbon composition. Conversely, the pathway featuring 2-ketoisovalerate as an intermediate is labelled the C_4 pathway or isobutanol route owing to its association with isobutanol production, characterized by its four-carbon atom structure.

In the C_2 route, CO_2 and H_2 are enzymatically transformed within Cupriavidus necator under optimal conditions that favour the production of acetaldehyde via pyruvic acid decarboxylation [154]. This process involves regulating the enzymatic activity, the carbon-to-hydrogen ratio, and other factors that influence the metabolic pathway toward acetaldehyde synthesis.

In the C_4 route, CO_2 and H_2 are converted to 2-ketoisovalerate and subsequent isobutanol production through a complex and coordinated series of enzymatic reactions within Cupriavidus necator. This process involves manipulating the availability of cofactors, the redox balance within the microbial cell, and the composition of the gas feed (CO_2 and H_2) to steer the metabolic flux towards the synthesis of 2-ketoisovalerate [150], [153], [155]. The

efficiency of this pathway might be influenced by factors like gas pressure, gas flow rate, and the specific metabolic engineering strategies employed to optimize Cupriavidus necator's pathways for 2-ketoisovalerate production.

The selection of these two intermediates is underpinned by their multifaceted technical advantages. They have favourable chemical properties, ease of extraction, scalability, and compatibility with downstream processing techniques that make them suitable candidates for the intricate SAF synthesis pathways. The synthesis of these intermediates from waste CO_2 and H_2 not only aligns with environmental sustainability goals but also demonstrates promise in CO_2 utilization and reduction of greenhouse gas emissions. The deliberate choice of acetaldehyde (C_2 route-to-SAF) and 2-ketoisovalerate (C_4 route-to-SAF) as intermediates of aerobic gas fermentation for SAF production within this investigation is rooted in their technical feasibility and their potential to revolutionize SAF production.

The forthcoming chapters will detail the proposed conceptual SAF plants corresponding to both the C_2 and C_4 routes, involving aerobic gas fermentation of CO_2 and H_2. For the C_2 route, assuming a plant location in China, the required CO_2 and H_2 will be sourced from the SCWG of black liquor. Conversely, the C_4 route-to-SAF, based on a plant in the UK, will utilize SCWG of pot ale draff for the same purpose.

Chapter 3 will focus on investigating the heat integration of the aerobic gas fermentation bioreactor with the SCWG of black liquor (modelled as guaiacol) for the C_2 route SAF plant. In contrast, Chapter 6 will delve into both non-heat-integrated and heat-integrated scenarios for the aerobic gas fermentation and the SCWG of pot ale draff (modelled as glycerol) in the C_4 route SAF plant. Additionally, TEA studies will comprehensively evaluate the three plant case scenarios.

CHAPTER 3.

PROCESS AND TEA MODEL OF SAF PRODUCTION VIA C_2 HEAT-INTEGRATED ROUTE

The C_2 route-to-SAF in this study refers to the utilization of acetaldehyde as the aerobic gas fermentation intermediate for SAF production.

In this chapter, a conceptual process approach for the production of SAF (C_{16} drop-in fuel) via the C_2 heat integrated route-to-SAF will be presented. This approach will encompass the integration of heat from the syngas production process using the SCWG of black liquor, followed by the implementation of a techno-economic analysis model to assess the economic feasibility of the proposed plant. The results and discussions stemming from the analysis will also be included in this chapter.

3.1 Process and TEA modelling methodology

In this work, the approach to modelling will be similar for both the C_2 (via acetaldehyde) and C_4 (via isobutanol) routes to jet fuel blends. The C_4 routes will be covered further down in Chapter 6.

The proposed C_2 route-to-SAF plant will make use of excess weak black liquor, which is a by-product generated from the Kraft and pulp mill processes. This weak black liquor will undergo supercritical gasification to produce the H_2 needed to be utilized in the aerobic gas fermentation bioreactor. To prevent reactor blockages and contaminations caused by salts in black liquor, [156] an assumption that the salt has been extracted before gasification was made in our model. Aerobic gas fermentation of CO_2 and H_2 will be utilized to produce the intermediate product for C_{16} production. A simplified C_2 route-to-SAF process flow for SCWG integration with gas fermentation is depicted in Figure 3.1. As can be seen in Figure 3.1, some other processes and reactions will be needed to upgrade the precursor to C_{16} jet fuel blend. These will be discussed in more details section 3.2.1 and 3.2.2.

In terms of the TEA calculation of the process, mass and energy balance from the simulation results will be utilized in the techno-economic assessment. First, three TEA methods will be evaluated and one of them will be taken forward for capital costs, fixed operating and variable costs estimations. The value or costing of black liquor was taken as the opportunity cost of combusting it for conventional electricity generation as opposed to utilizing (gasifying) it in

the proposed C_2 route SAF plant. This approach adopted, draws inspiration from the work of Rodgers et al. on the production of acetone and isopropanol [157].

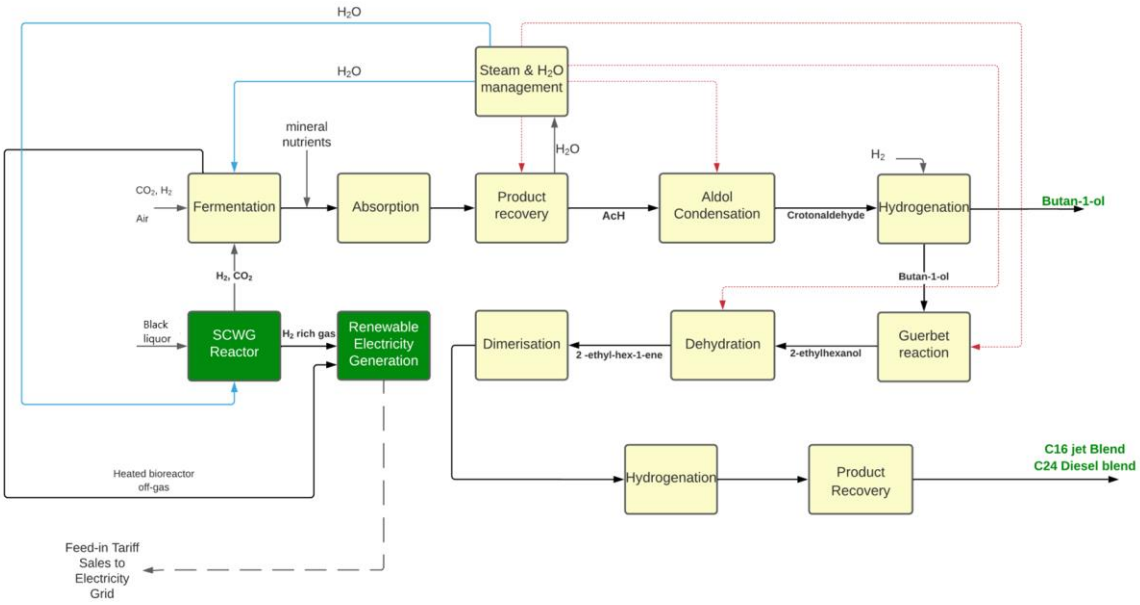

Figure 3.1. A simplified C_2 route SAF plant process flow showing SCWG of black liquor integration with the gas fermentation for the production of renewable C_{16} jet-fuel blend and C_{24} diesel blend.

Further down this chapter, the NPV of plant using the black liquor to produce conventional electricity will be compared to the NPV of an alternative use for gasification in the proposed SAF plant.

3.2 C_2 route heat-integrated process simulation overview

To calculate and determine the mass and energy balance of the C_2 heat-integrated plant, Aspen HYSYS v12 was used for rigorous process simulation. The bioreactor's fermentation experimental data from Bommeraddy et al work, was utilized in the HYSYS simulation [45]. Key parameters such as the O_2 transfer coefficient, reactor volume, number of bioreactor trains and gas uptakes were utilized in simulation of the aerobic gas fermentation of CO_2 and H_2. Table 3.1 shows the data from the gas fermentation experiment utilized in the simulation modelling [45]. Black liquor (BL) was modelled using guaiacol. This was adopted because the lignin concentration of BL was the closest to guaiacol [158].

Table 3.1. An overview of data from gas fermentation experiment utilized in ASPEN HYSYS process modelling.

Sources and sinks	**Unit**	**Value**
Bioreactors		
O_2 transfer coefficient	[1/h]	415
O_2 concentration in off-gas	[%] (mol/mol)	3.35
Vessel volume	[m3]	500
Number of bioreactor trains	[-]	4
Gas uptake rates		
O_2 concentration in off-gas	[mmol/(L·h)]	230
CO_2	[mmol/(L·h)]	125
H_2	[mmol/(L·h)]	1006
Biomass		
Growth rate	[h-1]	0.025
Dry Cell Weight with cell retention	[g/L]	21.5

Lowering the biomass concentration in black liquor through dilution prior to its introduction to the supercritical water gasification reactor enhances thermochemical disintegration and results in increased yields of H_2 and CO_2 [159].

A comprehensive process flow diagram of C_2 heat-integrated route which shows upstream and downstream processing can be seen in Figure 3.2 and Figure 3.3 respectively. This process flow was extensively modelled in ASPEN HYSYS including the heat integration with the help of an isopentane-carrying heat pump acting as the bridge between the exothermic gas fermentation operating at lower temperatures and the endothermic supercritical water gasification operating at higher temperature as detailed in [45]. Full details of the ASPEN HYSYS simulation process flow including the mass and energy balance can be seen in Appendix 1. A summary of the major operating units associated with the plant modelling is presented in Table 3.2.

Table 3.2. A summary of the different operating units associated with C_2 route heat-integrated plant modelling.

Plant division	Operating units	HYSYS package used
Preliminary processing of feed materials	Super critical water gas reactor, Combustion chamber and turbine, heat pump condenser and compressor	LKP
Gas fermentation	A centrifuge, pumps, seed bioreactors, and production bioreactors employed in the bioreactor system.	LKP
Product recovery	Acetaldehyde recovery, Water Stripper, dewatering columns, distillation columns	UNIFAC
Reaction sections	Aldol condensation reactor, Guerbet reaction reactor, crotonaldehyde hydrogenation reactor, Dehydrogenation reactor, dimerization reaction reactor,2-ethyl-hexene hydrogenation reactor	UNIFAC
Steam and water management	Vapour compressors, heat exchangers.	LKP

3.2.1 C_2 route-to-SAF upstream process simulation

Figure 3.2 illustrates the simulation process for the upstream process as modelled in ASPEN HYSYS. The Lee-Kesler-Plocker equation of state was utilized to represent the thermodynamic properties of the process fluids, chosen for its accuracy in modelling high-pressure gases [160]. The U-loop bioreactor (BC2-1) is modelled as a conversion reactor using CO_2 as the sole carbon source, H_2 as an electron donor, and O_2 as the electron acceptor. CO_2, H_2, air, and nutrient feed (BC2-2) are fed into the bioreactor's conversion reactor at 40°C. The exothermic reaction occurs at approximately 38.9°C and 390 kPa.

The bioreactor conversion reaction was modelled based on the following reaction:

$$a\ H_2 + b\ CO_2 + c\ O_2 + d\ NH_3 \rightarrow e\ C_3H_4O_3 + f\ H_2O + g\ DCW \qquad \text{Eqn 3.1}$$

Where $C_3H_4O_3$ represents Pyruvic acid, a, b, c, d, e, f, g correspond to 230.529, 39.820, 82.453, 1.684, 10.961, 208.093, 1.684 respectively. DCW(Dry cell Weight) of biomass – $C_{47.5248}H_{6.9307}N_{13.8614}O_{31.6832}$

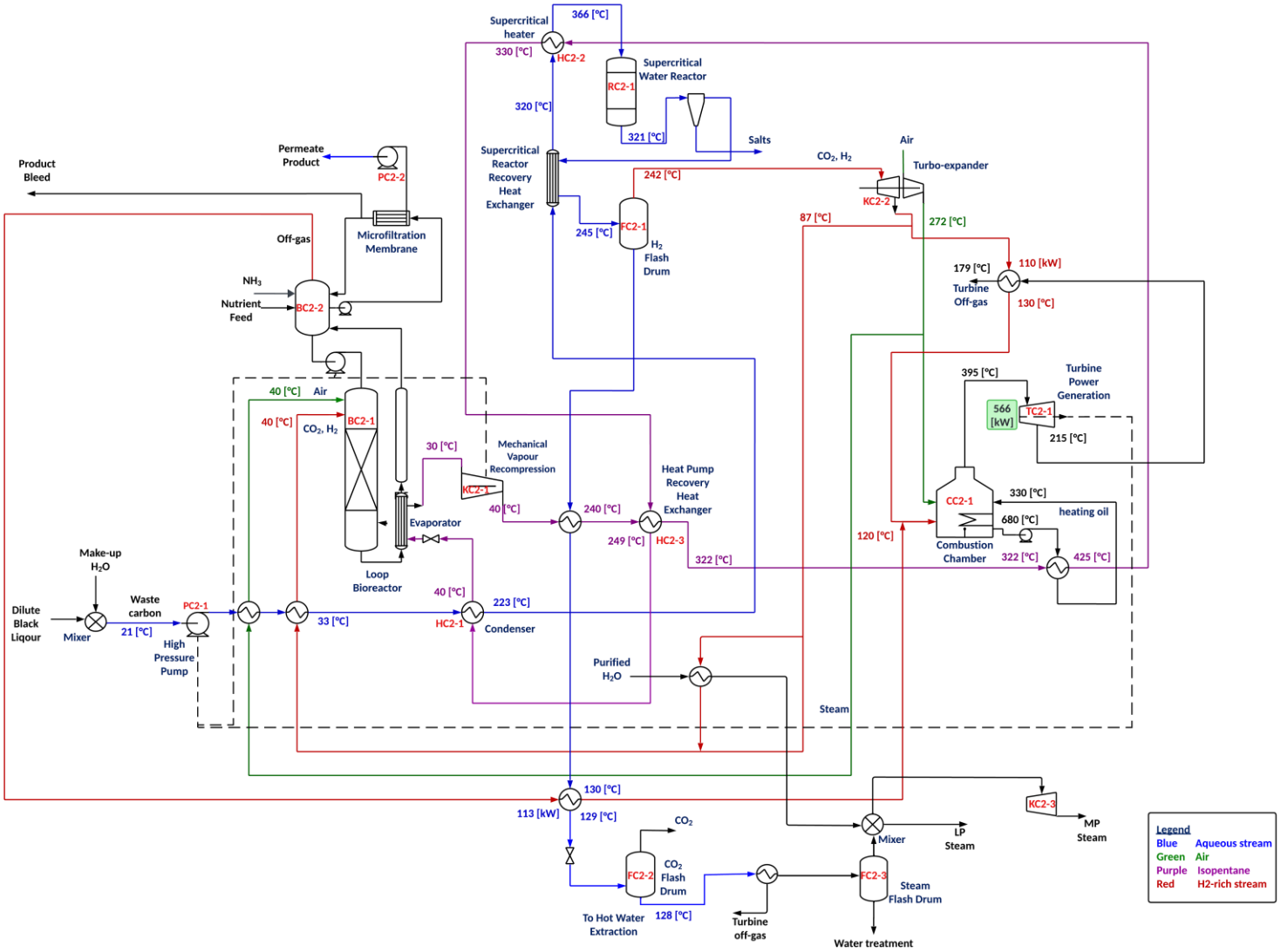

Figure 3.2. Conceptual upstream C_2 heat-integrated route-to-SAF process: Depicting the heat integration between SCWG of BL and the gas fermentation of CO_2 and H_2. Also showcases the generation of renewable electricity within the SAF plant.

This heat is then increased to approximately 366°C via a heat pump network for the SCWG reaction. The heat pump network, indicated by a purple line, uses isopentane as the carrier fluid. 9250 kgmole/h of isopentane with an absorbed temperature of 30°C is introduced into the mechanical vapour recompression pump (KC2-1). It is compressed to about 40°C and further heated to around 322°C through a series of heat exchangers, including the heat pump recovery heat exchanger (HC2-3). The iso-pentane stream passes through the supercritical heater (HC2-2) exiting at 330°C and is condensed via the condenser (HC2-1) to about 40°C.
Black liquor (at 23,725 kg/h), modelled as guaiacol, is diluted with 30,125 kg/h makeup water and passed through a high-pressure pump (PC2-1) operating at 24 MPa. This increases the pressure of the BL stream from 0.1 MPa to about 23 MPa. The stream is then heated up to about 373.5°C for the supercritical water gasification reaction in a series of heat exchangers, including the supercritical reactor recovery and heater exchanger. Plug flow reactor was adopted for the SCWG reactor's simulation, employing the Ni-catalysed kinetic rate constant suggested by DiLeo et al [161] within a pseudo-first-order framework.
The reaction modelled in the SCWG reactor is shown in equation 3.2 as follows:

$C_7H_8O_2 + 12\ H_2O \rightarrow 7\ CO_2 + 16\ H_2$ ΔH^o 394238 kJ/kgmole Eqn 3.2

Where $C_7H_8O_2$ represents guaiacol modelled as black liquor.

The product stream exits RC2-1 at a temperature of 321°C and passes through the Supercritical Reactor Recovery heat exchanger, where it cools down to 245°C. This stream, predominantly composed of H_2 and CO_2, is directed to the H_2 flash drum (FC2-1) where H_2 is separated. Some of the pressurized H_2-rich gas stream undergoes further expansion via the turbo-expander (KC2-2),generating additional electricity and also resulting in a significant drop in pressure and temperature of the gas stream. This H_2 stream is heated through the heat exchanger network before introduction into the combustion chamber (CC2-1). The combustion chamber, modelled as a conversion reactor, assumes total conversion of the H_2 and O_2 to H_2O. The product exits the combustion chamber at 1414°C and 0.39 MPa, then cooled to about 425°C, generating about 566 kW of electricity via the combustion turbine (TC2-1). This meets the plant's electricity requirements, and the surplus electricity produced is sold for additional income.
A portion of the H_2 gas produced in SCWG is recycled back to the bioreactor as gas fermentation feed. Additionally, the plant generates low and medium-pressure steam used for heat integration within the plant.

3.2.2 C_2 route-to-SAF downstream process simulation

Figure 3.3 shows the upgrading of the intermediate product derived from aerobic gas fermentation through a sequence of reaction and separation units utilized in the process.

From the top of the bioreactor, a permeate product containing mainly pyruvic acid, CO_2, H_2O, and carbon mass is sent via a pump (PC2-2) to a decarboxylation reactor (RC2-2), modelled as a plug-flow reactor in ASPEN HYSYS. This stream enters the reactor at 2396 kgmole/h. Decarboxylase enzymes activate when the solution is heated to about 85°C, leading to the conversion of pyruvic acid to acetaldehyde (AcH) [154]. The stream containing acetaldehyde, CO_2, H_2, and some unreacted pyruvic acid is introduced into the distillation column (DC2-1), where acetaldehyde, being more volatile, exits from the top. The top acetaldehyde stream is then cooled from 77°C to 35°C. The majority of the water is removed using a flash reboiler (FC2-4).

The acetaldehyde stream is further cooled from 77°C to 35°C, then enters the flash drum for the liquid product to recycle back into the reboiler. The acetaldehyde in the vapour phase is absorbed in the absorption column (DC2-2) and is stripped using furfural as the entrainer. Furfural is introduced at a flow rate of 304 kgmole/h at 30°C. The column, a 10-stage absorber, efficiently separates acetaldehyde for further processing. Acetaldehyde is easily separated due to its significant boiling point difference with furfural. Another column (DC2-4) is utilized to recover the furfural from the bottom, whereas acetaldehyde is collected as a distillate. The downcomer stream at 56.8°C from DC2-2 containing the mixture of AcH and NH_3 is sent to a distillation column (DC2-3) where AcH is separated. The top stream containing NH_3 is recycled back to the bioreactor as fermentation media. An aqueous stream from DC2-3 containing mostly AcH and water further undergoes distillation in column DC2-4. Acetaldehyde leaves from the top of DC2-3 and enters another reactor (RC2-3) where it undergoes aldol condensation to produce a solution containing mostly crotonaldehyde, which then goes to a flash drum to separate the permanent gases. RC2-3 was modelled as a plug-flow reactor, and the reaction occurred at 225°C. The equation as modelled in ASPEN HYSYS is as follows:

$$2\ C_2H_4O \rightarrow C_4H_6O + H_2O \qquad \Delta H^o\ -8312\ kJ/kgmole \qquad \text{Eqn 3.3}$$

Where C_2H_4O is AcH and C_4H_6O is crotonaldehyde.

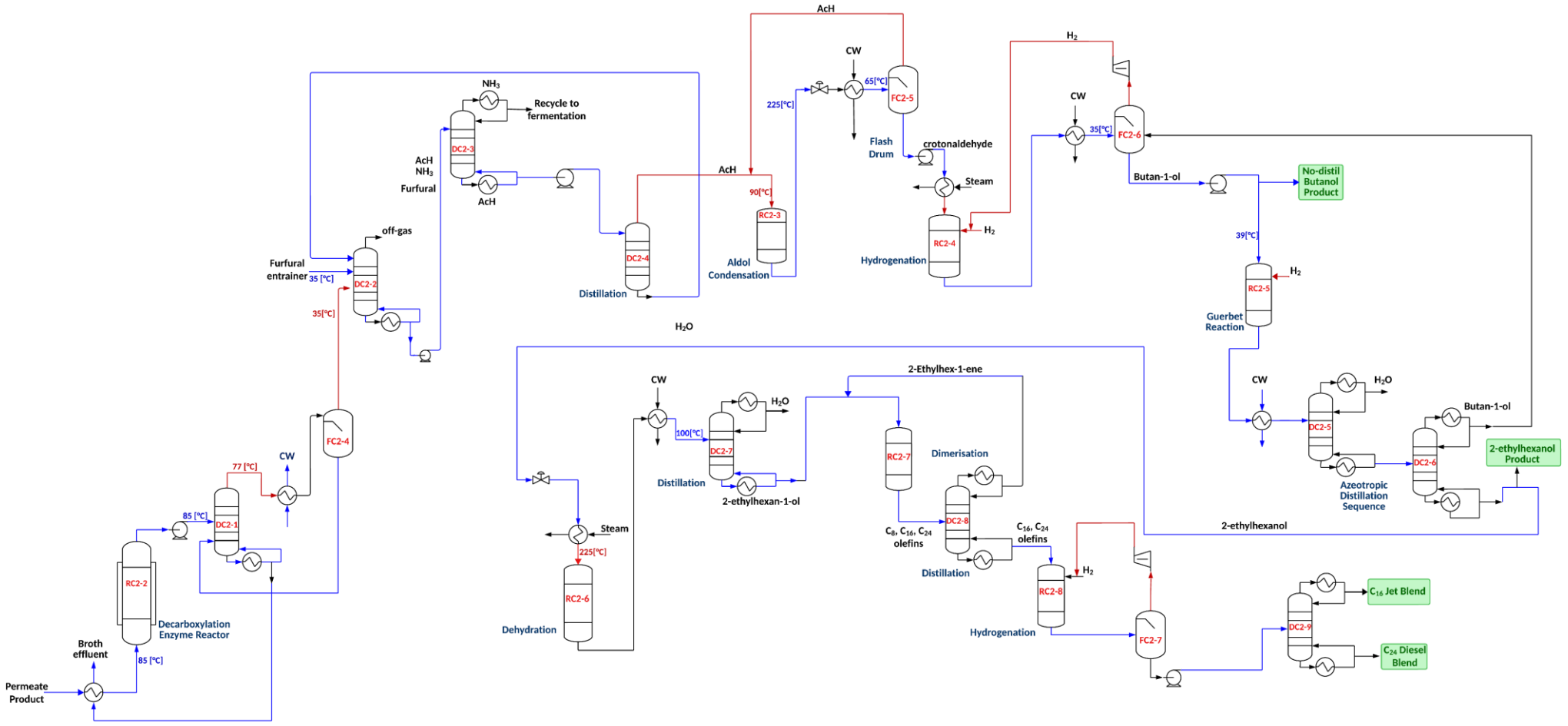

Figure 3.3. Conceptual downstream C_2 heat-integrated route-to-SAF process: showing the upgrading of aerobic gas fermentation product to C_{16} jet blend and C_{24} diesel blend.

The product stream leaves RC2-3 at 225°C and is cooled to about 65°C before introduction into a flash drum (FC2-5). Unreacted AcH from the top of FC2-5 is recycled back to the RC2-3 reactor. Further distillation, together with a decanter, is employed to separate water from crotonaldehyde. The water from the decanter is recycled, and the organic phase then moves to the second column where purer crotonaldehyde is recovered.

Next, a 99% pure crotonaldehyde undergoes a hydrogenation reaction in another reactor (RC2-4) to produce butan-1-ol. This reactor, also modelled as a plug-flow reactor in ASPEN HYSYS, operates at approximately 66°C. Excess hydrogen is removed from the solution via a flash drum (FC2-6), and pure butan-1-ol is then sent to another reactor (RC2-5) where it undergoes a Guerbet condensation reaction and subsequent azeotropic distillation (DC2-5 and DC2-6) to produce 2-ethyl-hexanol. The Guerbet reactor was modelled as a conversion reactor with a 57.9% conversion rate [162]. A fraction of the butan-1-ol is then recycled back to the FC2-6. 2-ethyl-hexanol is then dehydrated in another reactor (RC2-6) to produce a solution of 2-ethyl-hexene. This reactor, modelled as a plug-flow reactor, operates at 225°C. Water is removed via distillation (DC2-7), and purer 2-ethylhexene undergoes dimerization in DC2-8 to produce an olefin fraction of C8, C_{16}, and C_{24}. This stream is then sent to a distillation column (DC2-8) where the C_{16} and C_{24} fractions are separated, and the unreacted 2-ethylhexene and C8 fraction are recycled back to RC2-7. These olefin products (C_{16}, C_{24}) are then hydrogenated and subsequently distilled to obtain a pure C_{16} jet blend and C_{24} diesel blend.

3.2.3 Next best alternative use of black liquor

Just as previously stated, the next best alternative use for black liquor is for generating renewable electricity in the Kraft process [29]. Figure 3.4 illustrates the process flow of alternative use of black liquor for electricity production. The breakdown of the mass-energy balance can be found in Table A.6 located in Appendix 1, while the investment analysis details are available in Table A.24 within Appendix 4. The initial stage involves the collection of black liquor from the pulping process, encompassing both organic materials and chemicals with inherent energy content. Then BL is then concentrated with the help of the multi-effect evaporator. Subsequently, the concentrated BL is fed into a dedicated Tomlinson Recovery Boiler designed to operate under conditions of elevated temperature and pressure. Within this environment, the organic compounds present in the black liquor undergo combustion reactions, liberating heat energy. The heat generated from the combustion process is harnessed for the production of steam. This steam finds application within the paper mill for diverse processes, including but not limited to paper drying and the generation of additional electricity.

The high-pressure steam is then directed through a steam turbine, inducing its rotation and subsequently driving a generator. The turbine's mechanical energy conversion, in conjunction with the generator, transforms the kinetic energy of the steam into electrical energy.

The resultant electricity proves instrumental in powering the operational needs of the paper mill. Additionally, any surplus electricity generated has the potential to be fed back into the grid, contributing to broader energy distribution.

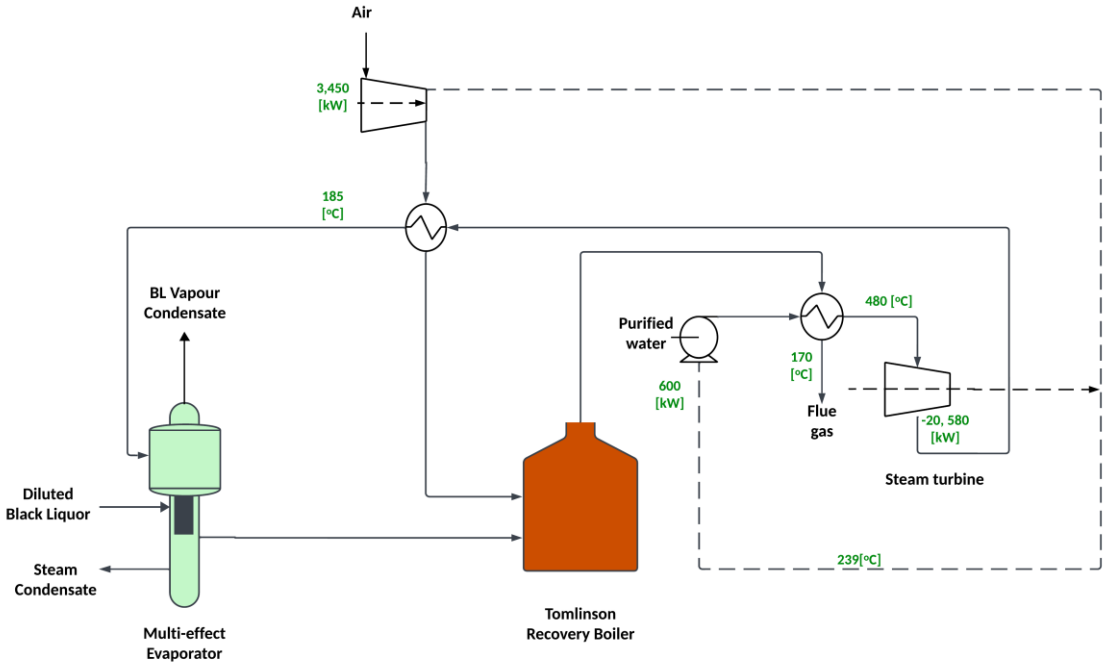

Figure 3.4. Production of electricity using black liquor [163].

3.2.4 Reaction kinetics used for the simulation

For the simulation of reactions in ASPEN HYSYS, especially in the downstream processing, various reaction kinetic data were sourced from different literature and papers where these experiments were conducted. These data were utilized to model the reactions especially in the plug-flow reactors. However, it is important to note that this approach presents a level of uncertainties that may affect the accuracy and reliability of the simulation results.

However, it is paramount to underscore the rigorous and meticulous process involved in curating these kinetic data. Extensive comparison among multiple scholarly papers and thorough cross-referencing with established literature were undertaken to ensure the selection of datasets. This approach seek to reduce the uncertainties in the reaction kinetic data and improve the quality of the simulation.

Simulation kinetic data sources

An aldol condensation is a reaction in which a base catalyses the formation of a β-hydroxy aldehyde (aldol) from two aldehydes by facilitating the nucleophilic addition of an enolate (derived from one aldehyde) to the carbonyl carbon of another aldehyde.

The kinetic model and parameters used for aldol condensation were taken from [164] as can be seen in Table 3.3. The rate and reaction equation are depicted by equation 3.4 and equation 3.3 respectively.

$$r = \frac{[d]_s \frac{k_1}{2} P_{AcH}}{1 + \frac{k_1}{2k_2} P_{AcH}} \qquad \text{Eqn 3.4}$$

The rate of acetaldehyde adsorption is denoted by k_1, and the rate of product desorption is represented by k_2, with $[d]_s$ indicating the number density of surface sites and P_{AcH} denoting the partial pressure of acetaldehyde.

Table 3.3. Rate parameters for aldol condensation reaction [164].

T(K)	**$[*]_0 k_1/2$ (mol kPa^{-1} m^{-2} s^{-1})**	**$k_1/2k_2$ (kPa^{-1})**	**Activation energy (kJmol^{-1})**	**catalyst**
553	1.9 x 10^{-8}	0.063	47	HAP

Crotonaldehyde, the main product of aldol condensation, undergoes a hydrogenation reaction to produce 1-butanol as the desired product.

The reaction is as follows:

$CH_3CH = CHCHO + 2H_2 \rightarrow C_4H_9OH$ ΔH^o -171300kJ/kgmole Eqn 3.5

In this work, the rate parameters used were taken from the experimental work of D.Jiang et al. as can be seen in Table 3.4 [165]. The rate expression shown in equation 3.6:

$$r = \frac{k_1 P_{H_2} P_{CRAL}}{1 + k_2 P_{H_2} + k_3 P_{CRAL} + k_4 P_{H_2} P_{CRAL}} \qquad \text{Eqn 3.6}$$

where r is the reaction rate, k_1, k_2, k_3, and k_4 are the rate constants, while P_{H_2} and P_{CRAL} are the partial pressures of hydrogen and crotonaldehyde, respectively.

$$k_1 = 1.45 \times 10^{11} \exp\left(\frac{-68.7}{RT}\right) \qquad \text{Eqn 3.7}$$

$$k_2 = 1.21 \times 10^{10} \exp\left(\frac{-68.7}{RT}\right) \qquad \text{Eqn 3.8}$$

$$k_3 = 1.41 \times 10^{10} \exp\left(\frac{-71.2}{RT}\right) \qquad \text{Eqn 3.9}$$

$k_4 = 1.21\times10^{10}\exp\left(\frac{-68.7}{RT}\right)$ Eqn 3.10

where R is the gas constant and T is the temperature in Kelvin.

Table 3.4. Rate parameters for Crotonaldehyde hydrogenation [165].

T(K)	Partial pressure P_{H_2}(kPa)	Rection order (n)	Activation energy (KJmol^{-1})	Catalyst
403	101.3	0.61	85.3	PdCu/AC

Butanol undergoes a Guerbet reaction to form 2-ethyl hexanol which is used to produce bio-jet fuel and renewable diesel via a dimerization reaction.

Xiaoxu et el. [166], determined that the Guerbet reaction can be characterized by a three-step reaction mechanism. The reaction commences with the dehydrogenation of n-butanol into n-butyraldehyde and hydrogen. Next, aldol condensation and dehydration of n-butyraldehyde produce 2-ethyl-2-hexenal and water. Finally, 2-ethyl-2-hexenal undergoes hydrogenation to form 2-ethylhexanol [166]. A schematic description of the reaction paths for the synthesis of 2-ethylhexanol Can be seen in Figure 3.5.

$$C_4H_{10}O \rightarrow C_4H_8O + H_2 \quad \text{Eqn 3.11}$$

$$2C_4H_8O \rightarrow C_8H_{14}O + H_2O \quad \text{Eqn 3.12}$$

$$C_8H_{14}O + 2H_2 \rightarrow C_8H_{18}O \quad \text{Eqn 3.13}$$

The following expressions show the kinetic equations for the reactions:

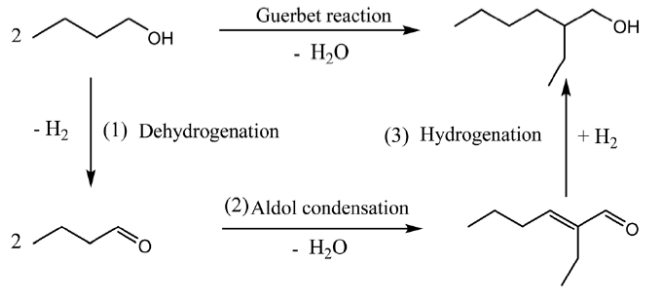

Figure 3.5. Schematic representation of the 2-ethylhexanol synthesis via n-butanol Guerbet condensation reaction.

These three-step reactions can be seen in equation 3.11 – 3.13 while equations 3.14 – 3.17 depicts the kinetic rate expressions utilized in the simulation. Table 3.5 shows the values of the parameters involved in the kinetic equations.

$$-\frac{dC_A}{dt} = A_1 \exp\left(\frac{-Ea_1}{RT}\right) C_A^{m_1} \quad \text{Eqn 3.14}$$

$$\frac{dC_B}{dt} = A_1 \exp\left(\frac{-Ea_1}{RT}\right) C_A^{m_1} - A_2 \exp\left(\frac{-Ea_2}{RT}\right) C_B^{m_2} \quad \text{Eqn 3.15}$$

$$\frac{dC_C}{dt} = A_2 \exp\left(\frac{-Ea_2}{RT}\right) C_B^{m_2} - A_3 \exp\left(\frac{-Ea_3}{RT}\right) C_C^{m_3} (0.5C_C + C_D + C_B)^{m_4} \quad \text{Eqn 3.16}$$

$$\frac{dC_D}{dt} = A_3 \exp\left(\frac{-Ea_3}{RT}\right) C_C^{m_3} (0.5C_C + C_D + C_B)^{m_4} \quad \text{Eqn 3.17}$$

Where A, B, C, and D correspond to n-butanol, n-butyraldehyde, 2-ethyl-2-hexenal and 2-ethyl-2-hexenal respectively.

Table 3.5. Estimated kinetic parameters for n-butanol Guerbet reaction [167].

Parameters	**Estimates**
A_1 ($Lkmol^{-1}min^{-1}$)	2.38×10^5
A_2($Lkmol^{-1}min^{-1}$)	2.55×10^5
A_3($Lkmol^{-1}min^{-1}$)	1.28×10^4
Ea_1 ($KJmol^{-1}$)	68.50
Ea_2 ($KJmol^{-1}$)	53.74
Ea_3 ($KJmol^{-1}$)	38.24
m_1	0.82
m_2	1.95
m_3	1.12
m_4	0.84

This study modelled the n-butanol Guerbet reaction as a conversion reaction with a 57.9% n-butanol conversion to 2-ethyl-hexanol based on the experimental data of Carlini et al. who used heterogeneous copper chromite and sodium tert-butoxide as catalysts [162]. Also, about 30% conversion of n-butanol is reported in the experimental works of Xiaoxu et el. [168] and Miller

et al. [169]. Experimental data and kinetic parameters that was used in modelling the dehydration of 2-ethylhexanol to 2-ethyl-1-hexene can be seen in Table 3.6 [170].

Table 3.6. Dehydration of 2-ethylhexanol to 2 ethyl-1-hexene.

T [°C]	**Space velocity [L·kgcat-1·h-1]**	**Conversion 2-ethylhexanol [%]**	**2-ethyl-1-hexene**
270	6	84	54
250	6	35.1	80.7

3.3 Economic assessment methodology utilised

The costing models will be used to guide all the TEAs presented in the thesis. A comparison of the three calculation methods using the C_2 heat-integrated process will be conducted, and the most suitable one will be selected for the subsequent TEA of the C_4 routes-to-SAF plants. For the C_2 heat-integrated route-to-SAF plant, China was assumed to be the location. The selection of China as the plant location for C_2 heat-integrated SAF plant stemmed from its status as the world's foremost producer and consumer of paper products. This positioning aligns with the abundance of black liquor production, a significant by-product within China's paper industrial landscape [171].

The estimation of major equipment for capital cost was carried out using Seider et al. models [172], while the mass and energy balance obtained from the rigorous process simulation was used to estimate the fixed and variable operating costs as well as the capital cost.

Turbo expander costing was adopted using [173].

3.3.1 Estimation of total capital investment (TCI)

Three distinct techniques were employed to compute the total capital investment (TCI) in this research, due to variations in the estimation approaches. This approach was adopted from the work of Rodgers et al [163]. Specifically, three techniques were employed: the NREL method, which is detailed in the 2011 NREL report [174]; Sinnott and Towler method, referred to as the TS method [175]; and the Hand method, which can be found in Sustainable Design Through Process Integration [176]. In order to determine the within plant boundary installation costs for all approaches, the cost of acquiring different plant machinery is factored in by an installation factor. The TS method utilizes a standard multiplier, while the other two methods apply installation factors tailored to the specific type of machinery. The costs of all machinery were

updated to reflect 2019 values using a cost index of 607.5 from Chemical Engineering Plant [177].Table 3.7 provides insights into the calculation basis for each of these methods used in the TEA studies.

Table 3.7. Capital cost estimation models used.

	Hand method	**NREL method**	**TS method**
Year basis	2019		
Year of production	8110 hours (bioreactor cycle time)		
Installation factor (multiplied by equipment cost) – Inside battery limits (ISBL)	Table A.17 (Appendix 4)	Table A.14 (Appendix 4)	Table A.16 (Appendix 4)
Outside battery limits (OSBL)	25% of ISBL	Table A.15 (Appendix 4)	30 % of ISBL
Contingency			10% of ISBL
Engineering and design costs			10% of ISBL
Commissioning costs	5% of ISBL		
Fixed capital investments (FCI)	ISBL + OSBL + Commissioning cost		ISBL + OSBL + Contingency + design and engineering
Working Capital	10% of FCI		
TCI	FCI + working capital		

NREL Method

The NREL method, tailored for renewable energy technologies, relies on the levelized cost of energy (LCOE) as a pivotal metric for TCI estimation. It factors in direct installation costs alongside supplementary expenses like warehouse fees, site development, piping, commissioning, and working capital. Although not directly computing TCI, these costs significantly shape the LCOE, offering a comprehensive financial perspective. This method allocates 5% of Inside Battery Limits (ISBL) to calculate the plant's commissioning cost. The fixed capital investment (FCI) combines ISBL, Outside Battery limits (OSBL), and commissioning costs.

Hand Method

In chemical engineering, the Hand method employs empirical factors ("hand factors") as multipliers for total process equipment (ISBL) and facility (OSBL) cost estimations. Drawing from historical data or industry-specific knowledge, it factors in commissioning costs and working capital for an efficient start-up phase. OSBL is computed as 25% of ISBL, while working capital stands at 10% of the FCI, thereby summing up to derive the TCI.

Towler and Sinnott Method (TS)

The TS approach integrates meticulous process design and economics for precise TCI estimation. It includes ISBL and OSBL costs, engineering expenses, and contingency charges. This method accounts for specific plant requirements in estimating ISBL costs and encompasses OSBL costs for utilities and infrastructure beyond plant boundaries. Engineering costs related to design, site remediation, and contingency charges are meticulously considered. Contingency costs account for 10% of ISBL, while OSBL is set at 30% of ISBL within this method.

3.3.2 Estimations of fixed operating costs (FOC)

Fixed Operating Costs (FOC) are crucial ongoing expenses necessary to maintain and operate a process plant. The fixed operating cost was calculated using three methods namely: NREL method [174], TS method [178] and Coulson & Richardson volume 6 [175] detailed in Table 3.8.

NREL Method

Labour, supervision, and overhead expenses are considered in the NREL method. It involves detailed salary computations for plant personnel, labour burden (90% of total salaries), maintenance costs (3% of ISBL), and property insurance (0.7% of FCI). However, it doesn't explicitly account for land rental, general plant overhead, and allocated environmental charges.

Coulson and Richardson Method

This comprehensive method encompasses labour, maintenance, utilities, insurance, administrative expenses, and safety measures for FOC estimation. Maintenance costs are set at 5% of ISBL and OSBL, while general plant overhead stands at 50% of operating labour costs. Property taxes account for 2% of ISBL and OSBL.

Table 3.8. Fixed operating costs estimation methods.

Parameters	NREL	TS	Coulson & Richardson
Operating Labour	The estimates for salaries in China for the roles of process operator, engineering, and maintenance were obtained from salaryexpert.com.	The salary estimates for China were sourced from salaryexpert.com. 3 process operators per shift 4 shift teams	The estimates for salaries in China for the roles of process operator, engineering, and maintenance were obtained from salaryexpert.com.
Supervisory Labour		25% of operating Labour	
Direct Salary Overhead	90% of Operating and Supervisory Labour	50% of Operating and Supervisory Labour	
Maintenance	3% of ISBL	3% of ISBL	5% of ISBL + OSBL (conventionally 5% FCI)
Property Taxes and Insurance	0.7% of FCI	1% of ISBL	2% of ISBL +OSBL (conventionally 2-3% FCI)
Rent of Land		1% of FCI	
Royalties			0% of FCI (conventionally 1% FCI)
General Plant Overhead		65% of Total Labour and Maintenance	50% of Operating Labour
Allocated Environmental Charges		1% of FCI	

Towler and Sinnott Method (TS)

The TS approach provides a systematic estimation for FOC related to process plants. It accounts for labour, maintenance, utilities, insurance, property taxes, administrative expenses, and safety measures. Supervisory labour stands at 25% of operating labour costs, and direct salary overhead is calculated as 50% of operating and supervisory labour costs.

3.3.3 Estimation of variable operating costs (VOC)

Variable costs required by the bio-jet fuel plant to run efficiently were calculated. Cooling water requirement [179], nutrients for fermentation, electricity [179], ammonia [180], furfural for product recovery [181] and hydrogen cost [182] for hydrogenation reactions are all the variable costs required for running the plant.

The calculation of variable operating costs originated from the expenses specified in Table 3.9, which were adjusted for annual inflation as specified in the table.

Table 3.9. Utility and consumable prices used in this study.

Item	**Prices**	**Unit**
Cooling water	0.73	[$/m^3]
Nutrients	0.75	[$/(m^3 media water)]
Electricity	0.06	[$/kWh]
Process water	0.53	[$/m^3]
Ammonia	250	[$/tonne]
Furfural	1000	[$/tonne]
Hydrogen cost	2	[$/kg]
Catalyst	Assumed negligible	-
Black liquor	0	[$/tonne]

The price of jet fuel was informed by Jet fuel's historic price which is depicted in Figure 3.6 [183]. For this TEA model, the average price of jet fuel between 2006-2019 was assumed as the long-term forecast. This is because the total average percentage change in price during this period is 0.27%.

Figure 3.6. Chart showing the historic price of jet fuel between the period 2006-2019. The average price for jet fuel during this period is $2.20 per US gallon [183].

The valuation of black liquor and any surplus electricity produced by the C_{16} facility in the renewable electricity project is determined using a long-term average price of 0.109 [$/kWh], which is in line with the biomass subsidy in China [184].

3.3.4 Investment analyses

The investment analyses were informed based on the calculations for TCI, FOC and VOC. The cost of black liquor is calculated based on its utility value, which is the net present value forgone from electricity generation. The parameters used in the investment analysis are specified in Table 3.10.

Table 3.10. Parameters used in evaluating the investment analysis.

Parameters	**Value**	**Additional information**
Construction period	2 years	
Plant salvage value	No value	
Linear depreciation	10 years	Straight line calculation
Plant life	25 years	
Annual inflation	2 %	
Corporation tax	25 %	Corporation tax in China
Discounted rate of return	10 %	BETO Biofuels TEA Database [185]
Annual operational hour	8810 hours	

The following shows the main calculations used to determine the NPV of the SAF plant putting into account mass and energy balance data obtained from the simulation.

Plant Income

Plant income (P_{inc}) was calculated using the following formula:

$$P_{inc} = (M_{FL} \times SP_{ker}) + (E_{prod} \times T_{op} \times SP_{elec}) \quad \text{Eqn 3.18}$$

Where

M_{FL} – Mass flow rate of SAF (taken from simulation mass balance)

SP_{ker} – Selling price of kerosene

E_{prod} – Amount of electricity generated(kW)

T_{op} – Operational time in a year

SP_{elec} – Selling Price of electricity

Depreciation

Depreciation was estimated using the following formula:

$$\text{Depreciation} = \frac{FCI}{Linear\ depreciation\ years} \quad \text{Eqn 3.19}$$

Where FCI denotes the fixed capital investment.

Corporation Tax

Corporation tax (C_{tax}) was taken as:

$$C_{tax} = (P_{inc} - VOC - FOC - Depreciation) \times tax\ (\%) \quad \text{Eqn 3.20}$$

Where VOC and FOC correspond to variable operating cost and fixed operating cost respectively.

Total Cash Flow (*CF_{total}*)

Overall plant's total cash flow was calculated using this formula below

$$CF_{total} = (P_{inc} - VOC - FOC - W_c - C_{tax}) \quad \text{Eqn 3.21}$$

Where W_c denotes the working capital of the plant.

Net Present Value(NPV)

The NPV of the plant was calculated using the formula below:

$$\text{NPV} = \frac{CF_{total}}{(1+discounted\ rate\ of\ return)^n} \quad \text{Eqn 3.22}$$

Where n represents project life year.

Cumulative NPV

$$\text{Cumulative NPV} = \sum NPV\ (Over\ the\ project's\ life) \quad \text{Eqn 3.23}$$

3.3.5 Sensitivity Analysis

Sensitivity analysis refers to the analytical process of exploring the impact of changes to input variables of a model on its output variables. The technique is utilized to ascertain the most significant input variables and assess their effect on desired output variables. One-factor-at-a time (OFAT) sensitivity analysis involves the manipulation of one input variable at a time, observing the impact on the output variable. Tornado diagrams exhibit the sensitivity of the output variable to alterations in each input variable.

OFAT sensitivity analysis was conducted to understand the impact of different variables on the cumulative NPV of the plant. The long-term average price of jet fuel, annual inflation rate,

FOC, VOC, electricity selling price, corporation tax, OSBL/ISBL and working capital parameters were adjusted up and down by ±20% from their predicted prices and current values. The results including the tornado diagram are presented in the result and discussion section below.

3.4 Results and Discussions

3.4.1 Calculations of major equipment sizing

The design and cost assessment of equipment for the C_2 heat-integrated SAF plant was achieved through a comprehensive approach leveraging ASPEN HYSYS simulations. The dimensions of the primary equipment were determined based on comprehensive mass and energy balance data acquired through the simulation. The simulation played a fundamental role in cost-evaluating key components like the SCWG reactor, heat exchangers, centrifugal compressor, and distillation tower. Incorporating simulation-derived specifics, each assessment meticulously integrated parameters, material characteristics, and operational insights crucial for precise cost estimations and optimal equipment design. This connection between the detailed methodologies and simulation-derived data not only underscored the depth of analyses but also highlighted the indispensable role of the simulation in informing both the TEA and the implementation of the plant's equipment.

For deeper insights into the mass and energy balance specifics utilized in equipment costing, please refer to Appendix 1. Detailed cost analysis of some major plant equipment is presented below.

SCWG reactor

The SCWG reactor cost was assumed to be a vertical pressure vessel and modelled in HYSYS as a vertical plug-flow reactor. The capital purchasing cost (C_P) of this reactor was taken from Seider et al [172].

$$C_P\ (f.o.b) = F_M.C_V + C_{PL} \qquad \text{Eqn 3.24}$$

Where:

$C_P\ (f.o.b)$ - Capital purchasing cost (free on board) [$US]

F_M - Materials of construction factor [-] (assumed as 3.7)

C_V - (f.o.b) purchase cost of the empty vessel (but including nozzles, manholes and supports) [$US]

C_{PL} - Added cost of purchasing platforms and ladders [$US]

For vertical vessels such as modelled for the SCWG reactor, C_v was calculated using the formula:

$$C_V = exp\{7.0132 + 0.18255[ln(W)] + 0.02297[ln(W)]^2\} \quad \text{Eqn 3.25}$$

Where W represents the Weight of the Vertical Pressure Vessel [lb], calculated based on various parameters like the inside diameter (Di), tan-tan length (L), average shell thickness (t_s), and density (ρ).

Moreover, the shell thickness (tp) to endure internal pressure at the top of the vessel was determined as per the equation:

$$t_p = [(P_d) \times (Di)] / [(2SE) - (1.2P_d)] \quad \text{Eqn 3.26}$$

Where P_d is the Internal Design gauge pressure, S represents the Maximum allowable stress of the shell material at the design temperature, and E signifies the fractional weld efficiency.

The maximum allowable stress is an estimation for stainless steel (construction material) using a low alloy steel (1% Cr and 0.5% Mo), in a non-corrosive environment, with a temperature range of 650 - 900°F.

The determination of P_d followed a detailed formula for calculation:

$$P_d = exp\{0.60608 + 0.91615[ln(P_o)] + 0.0015655[ln(P_o)]^2 \quad \text{Eqn 3.27}$$

P_d = Internal Design gauge pressure [psig]

P_o = Operating Pressure [psig]

The Di, L, and P_o were obtained from the HYSYS simulation data of the SCWG reactor, modelled as a vertical pressure plug-flow reactor, and used to estimate the CP (f.o.b).

Heat Exchangers

The costing for shell and tube heat exchanger types was based on assumptions of a fixed head design and computed using several factors like Pressure factor (F_P), Materials of construction factor (F_M), Tube length correction factor (F_L), and base capital purchase cost (C_B) at a CE index of 500. The CE index was adjusted for 2019 for accurate assessments.

The formulation for C_P *(f.o.b)* is expressed as:

$C_P\ (f.o.b) = F_P\ x\ F_M\ x\ F_L\ x\ C_B$ Eqn 3.28

Where:

C_P (*f.o.b*) denotes capital purchasing cost (free on board) [$US]

C_B represents base capital purchase cost [$US]

F_P, F_M, and F_L correspond to the pressure factor, materials of construction factor, and tube length correction factor, respectively.

The Chemical Engineering cost index (CE) for 2019 adjustments was derived from the ratio of the current Cost Index (2019) [CE] to the Base cost index (2006) [CE].

$F_M = a + (A/100)^b$ Eqn 3.29

F_M was computed using the coefficients *a* and *b* in the equation $F_M = a + (A/100)^b$, where *a* and *b* coefficients are assumed to be 1.75 and 0.13, respectively.

Additionally, F_P and C_B were determined as follows:

$F_P = 0.9803 + 0.018(P/100) + 0.0017(P/100)^2$ Eqn 3.30

P = Shell side pressure [psig] {*P* => 100 - 2000 psig}

$C_B = exp\{11.0545 - 0.9228[ln(A)] + 0.09861[ln(A)]^2\}$ Eqn 3.31

A = Outside tube surface area (ft^2)

The surface area of the heat exchangers was computed using data extracted from the heat exchanger simulation, which included the total duty, overall heat transfer coefficient, and Logarithmic Mean Temperature Difference (LMTD).

Centrifugal Compressor

A prevalent type of compressor due to its manageable nature, the centrifugal compressor was assumed to have an efficiency of 70-75%. The calculation of the capital purchasing cost integrated $C_p\ (f.o.b)$ integrated F_M, F_D and F_M considering the consumed Horsepower (P_c) obtained from ASPEN HYSYS simulation data.

$C_P = F_D\ x\ F_M\ x\ C_B$ Eqn 3.32

C_P (f.o.b) = Capital Purchasing Cost (free on board) [$US]

F_D = Driver Type Factor [-]

F_M = Materials of Construction Factor [-]

C_B = Base Cost (f.o.b) [$US]

$$C_B = exp\{7.5800 + 0.80[ln(P_c)]\} \quad \text{Eqn 3.33}$$

P_c = Consumed Horsepower [Hp]

Distillation Tower

The purchasing cost determination for the Distillation Tower relied on the vessel's weight (including the cylindrical shell and the two 2:1 elliptical heads) following the methodology established by Mulet et al [186].

The expression for Capital Purchasing Cost (CP) at f.o.b. is outlined as:

$$C_P\ (f.o.b) = (F_M\ x\ C_V) + C_{PL} + (V_P C_{PK} + C_{DR}) \quad \text{Eqn 3.34}$$

F_M - Materials of Construction Factor [-] taken as 1.7 for stainless steel 304

C_V - (f.o.b) purchase cost of the empty vessel (but including nozzles, manholes and supports) [$US]

C_{PL} - Added cost of purchasing platforms and ladders [$US]

V_P - Volume of packing [ft^3]

C_{PK} - Installed cost of the Packing [$US/$ft^3$]

C_{DR} - Installed cost of high-performance liquid distributors and redistributors required for obtaining satisfactory performance with packings [$US]

$V_P C_{PK} + C_{DR}$ - Added cost of purchasing structured packing [$US]

The determination of C_v *and* C_{PL} relies on the following calculations:

$$C_V = exp\{7.2756 + 0.18255[ln(W)] + 0.02297[ln(W)]^2\} \quad \text{Eqn 3.35}$$

where W represents the Weight of the Tower [lb]

$$C_{PL} = 300.9\ x\ [(Di)^{(0.63316)}]\ x\ [(L)^{(0.80161)}] \quad \text{Eqn 3.36}$$

where:

Di stands for the Inside Diameter of the Tower [ft]

L signifies the tan-tan length of the Tower [ft]

The determination of W involves the following formula:

$$W = \prod(Di + t_v)(L + 0.8Di)t_v\rho \quad \text{Eqn 3.37}$$

Where t_v is shell thickness

Variables such as the tower's diameter, operating temperature, length, and specific area, derived from simulation data, are pivotal in determining the comprehensive cost analysis of the towers used throughout the C_2 heat-integrated SAF plant simulation.

3.4.2 Production rate and yields of C_2 heat-integrated SAF Plant

The bioreactor conversion reactor within the C_2 heat-integrated SAF plant simulation yields a production rate of 32.2 kt/annum for pyruvic acid. This pyruvic acid undergoes decarboxylation in a separate reactor, resulting in the production of approximately 16 kt/annum of acetaldehyde. The decarboxylation reactor releases 678 kg/h of dry cell weight (DCW) produced from the gas fermentation bioreactor.

Further in the process, an aldol-condensation reaction of acetaldehyde generates 12.4 kt/annum of crotonaldehyde. The subsequent hydrogenation of crotonaldehyde leads to the production of 12.1 t/annum of distilled butanol, which is suitable for sale on its own if not used for SAF production. Additionally, the plant produces approximately 8 kt/annum of 2-ethyl-hexanol.

The simulated C_2 heat-integrated SAF plant yields an annual output of 7.7 kt/annum of C_{16} fraction and 0.05 kt/annum of C_{24} fraction. The C_{24} fraction is marketed as a diesel component. In terms of renewable energy, the plant contributes significantly, generating a total of 153.1 Gwh/annum of electricity from sustainable sources. The plant requires 148 kt/annum of cooling water is required across the plant units. The annual electricity requirement of the plant stands at 197 Gwh whereas the plant generates 356.66 Gwh/annum. Table 3.11 shows the summary of plant units electricity requirements while Table 3.12 summarises the production rates of intermediate and major products from the plant.

Table 3.11. Electricity requirements of the C_2 heat integrated SAF plant.

Unit	**Power required (Gwh/annum)**
High-pressure pump (PC2-1)	36.07
Vapour recompression (KC2-1)	26.04
Turbo-expander (KC2-2)	98.93
Compressor (KC2-3)	36.04

Table 3.12. Summary of C_2 heat-integrated production rates of intermediate and major products.

Intermediate and major products	**Production rates**		**Product mass purity**	
	Value	**unit**	**Value**	
Pyruvic acid	32.2	[kt/annum]		
Acetaldehyde	16	[kt/annum]		
Crotonaldehyde	12.4	[kt/annum]		
Butanol	12.1	[kt/annum]	98.9	[%] (w/w)
2-ethyl-hexanol	8	[kt/annum]	97.9	[%] (w/w)
SAF (C_{16} fraction)	7.7	[kt/annum]	99.8	[%] (w/w)
Diesel (C_{24} fraction)	0.05	[t/annum]	99.8	[%] (w/w)
Electricity (KC2-2)	208.208	[Gwh/annum]		
Electricity (TC2-1)	148.45	[Gwh/annum]		

In comparison to the next best alternative utilization of black liquor, Table 3.13 presents a summary of the electricity generated and utilized by a steam turbine electricity generation plant employing black liquor (modelled as guaiacol) with a mass flow rate of 23,725 kg/h. This comparison will be further discussed in Section 3.4.4.

Table 3.13. Summary of the electricity generated and consumed in an electricity generating plant utilizing black liquor.

Unit	**Value (GWh/annum)**
Electricity consumed	
Feed Pump Duty (Black liquor feed)	0.60
Feed Pump Duty(steam generation)	5.27
Mechanical vapour recompression duty	29
Electricity generated	
Steam turbine	172.87

3.4.3 Overall costs of C_2 heat-integrated SAF Plant

To estimate the total capital investment cost of the C_2 SAF plant, three methods already mentioned in section 3.3.1 and specified in Table 3.7 were employed, and the summary of the results is presented in Figure 3.7.

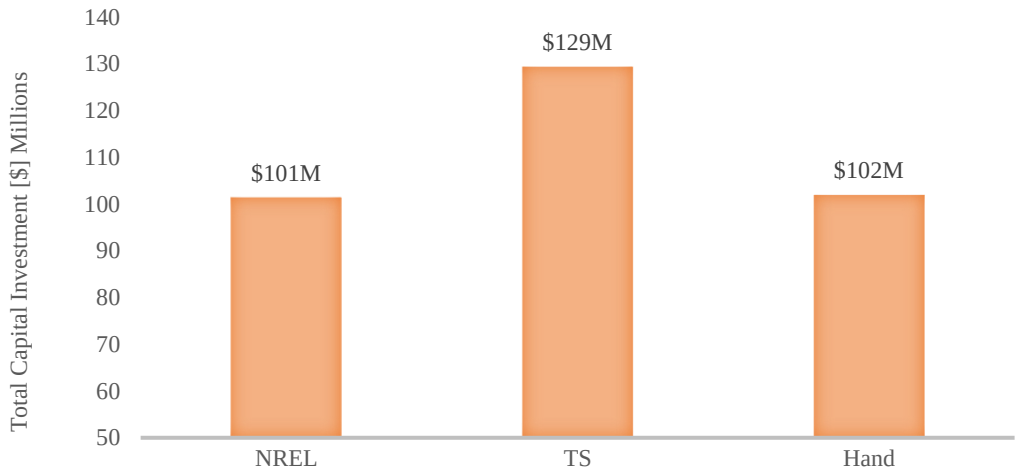

Figure 3.7. Three estimates for TCI for C_2 SAF plant were compared using the Hand, NREL, and TS methods. The Hand and NREL methods produced similar results, and the Hand method estimate was selected for use in the investment analyses.

Detailed data regarding the TCI estimation can be found in section A.4.1 located in Appendix 4. The calculations revealed a negligible difference between the NREL and Hands methods, with estimates of $101MM and $102MM, respectively (as shown in Figure 3.7). Due to its simplicity and close alignment with the NREL method, the hand method was selected as the basis for TCI calculations. Capital cost estimates for traditional renewable electricity generation can be found in a detailed breakdown within section A.4.2 located in Appendix 4. As can be seen from Figure 3.8, the gasification and electricity production section accounts for about 77% of the total fixed capital cost. This is primarily because of the cost of the heat pump compressor and the turbo-expander for electricity generation. This is followed by the fermentation section which has the second overall capital expenditure.

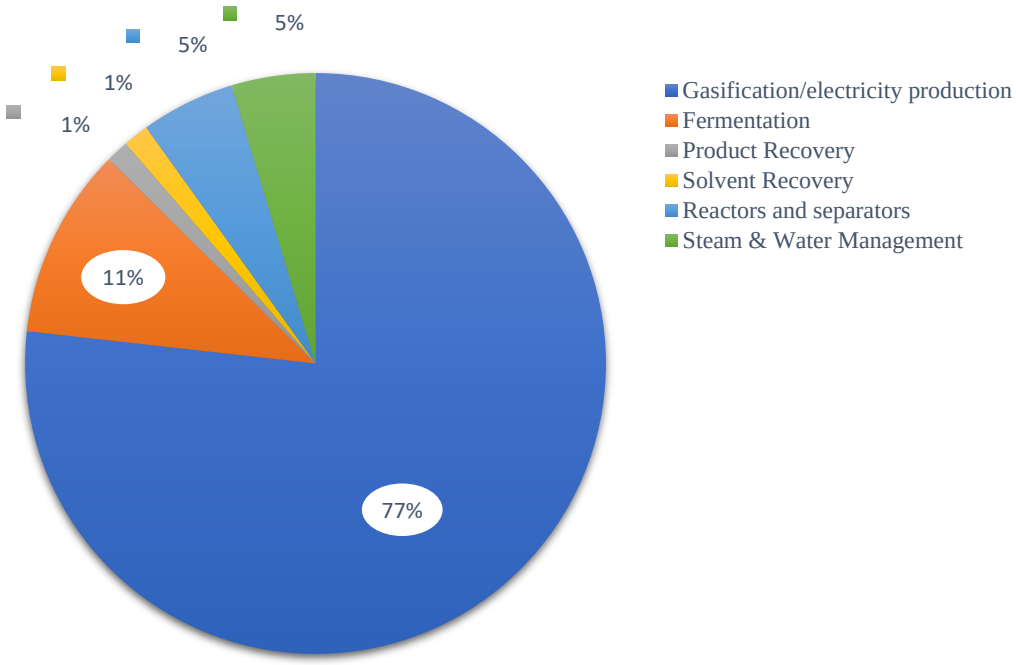

Figure 3.8. This shows the percentage share of each section of the plant on the fixed capital investment. The Gasification/electricity production section which includes the combustion chamber and turbo expander accounts for about 77% of the fixed capital cost (Hand method)

Figure 3.9 summarizes the three FOC calculation of the plant using the three methods already stated in Table 3.8, with the associated data for these costs available in Appendix 4 (Table A.18 - Table A.20). It is noteworthy that while the TS method and the Coulson & Richardson method originate from the same author, they employ different calculation strategies as already mentioned in section 3.3.2. However, their results exhibit a thin-margin agreement of $6.42MM and $6.87MM, respectively (Figure 3.9). The NREL method produced an estimate that was significantly lower and was thus disregarded. Consequently, the TS method estimate was adopted as the basis for fixed operating costs. Additionally, details of fixed operating costs for generating only electricity using black liquor through conventional means are provided in Appendix 4 (Table A.23).

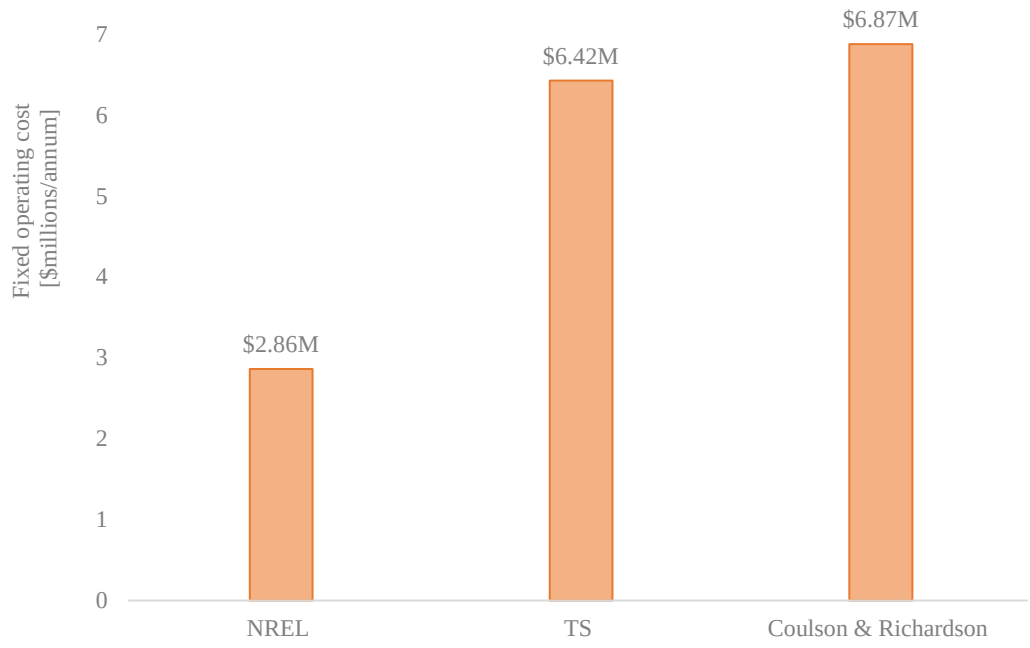

Figure 3.9. Estimations of the fixed operating costs for the C_2 route bio-jet plant were assessed through three methodologies. The CS and TS approaches yielded comparable results, exhibiting a close alignment between the estimates. Consequently, the investment analysis relied on the cost projections provided by the TS method.

C_2 heat-integrated incurred an annual VOC of about $1.76M. Figure 3.10 illustrates that cooling water cost, nutrient cost, and H_2 cost contribute to the variable costs in the proposed SAF plant. Nutrients and H_2 costs represent the majority of the variable costs, accounting for 36% and 23%, respectively. The nutrient costs was incurred on the gas fermentation feed. The H_2 produced in the SCWG is completely utilized for gas fermentation necessitating an additional H_2 cost for the hydrogenation reaction of crotonaldehyde.

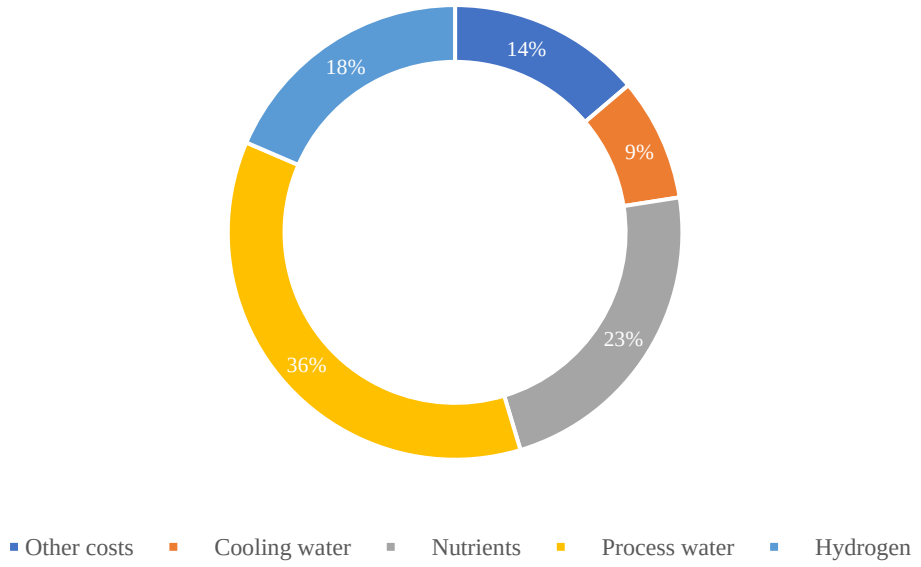

Figure 3.10. A chart showing the percentage share of each variable cost for the proposed plant. Process water and hydrogen costs have the highest share with 36% and 23% respectively.

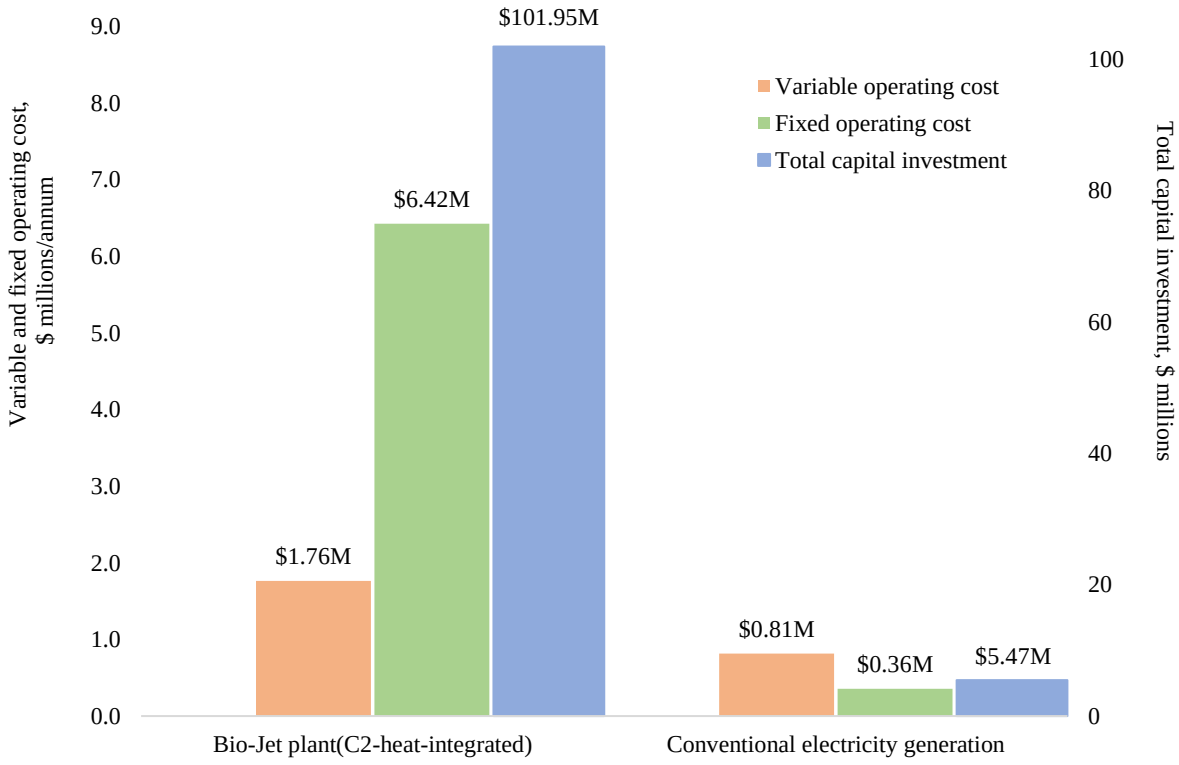

Figure 3.11. This chart compares the TCI, FOC and VOC between the C_2 SAF plant and traditional renewable power production method.

Figure 3.11 depicts a comparison between the TCI, FOC and VOC models of a C_2 route-to-SAF plant and an electricity generation plant that could have utilized black liquor. The variable cost of the conventional electricity generation plant aligns more closely with the variable costs of the proposed SAF plant. Process water cost is the only factor influencing the variable cost in conventional electricity generation. The TCI and FOC of the C_2 heat integrated process are approximately five times greater than the equivalent expenses incurred by a conventional renewable electricity generation plant. Detailed calculations and results for the electricity plant can be found in Appendix 1 and Appendix 4. This is expected as the conventional electricity generation plant only requires steam turbine purchase as opposed to many reactor and separation units required by the proposed C_2 heat-integrated SAF plant. This consequently translates to the high TCI, FOC and VOC.

3.4.4 Investment analysis

The present TEA study outlines production summary of the C_2 heat-integrated route-to-SAF plant that aims to produce both SAF and electricity, as detailed in
Table 3.14 and Figure 3.12. The table highlights the monetary impact of each product towards the overall revenue of the C_2 route-to-SAF plant, with particular emphasis on renewable electricity which emerges as the primary revenue source, highlighting the plant's impressive generation of renewable electricity.

Table 3.14. C_2 heat-integrated route-to-SAF plant production summary.

Products	**Production output**		**Product mass purity**	
	Value	Unit	Value	Unit
SAF fractions	7.7	[kt/annum]	99.8	[%] (w/w)
Net renewable electricity generated	160	[GWh/annum]		

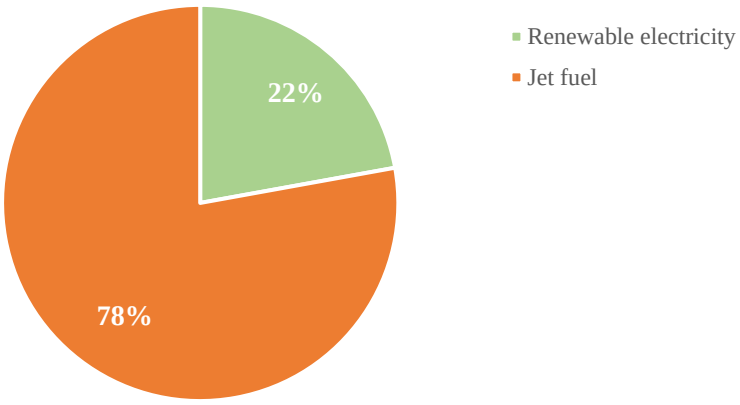

Figure 3.12. Chart showing the share of the two primary income sources of the proposed C_2 heat-integrated route-to-SAF plant.

Renewable electricity accounted for the majority of the income, contributing around 78%. Meanwhile, jet fuel made up the remaining 22% of the plant's income. This is majorly because of the significant amount of electricity produced by the plant.

Investment evaluations for the proposed C_2 heat-integrated route-to-SAF production facility and traditional electricity generation using BL are outlined in section A.4.1 and A.4.2 located in Appendix 4. These assessments align with the financial evaluation criteria provided in Table 3.10.

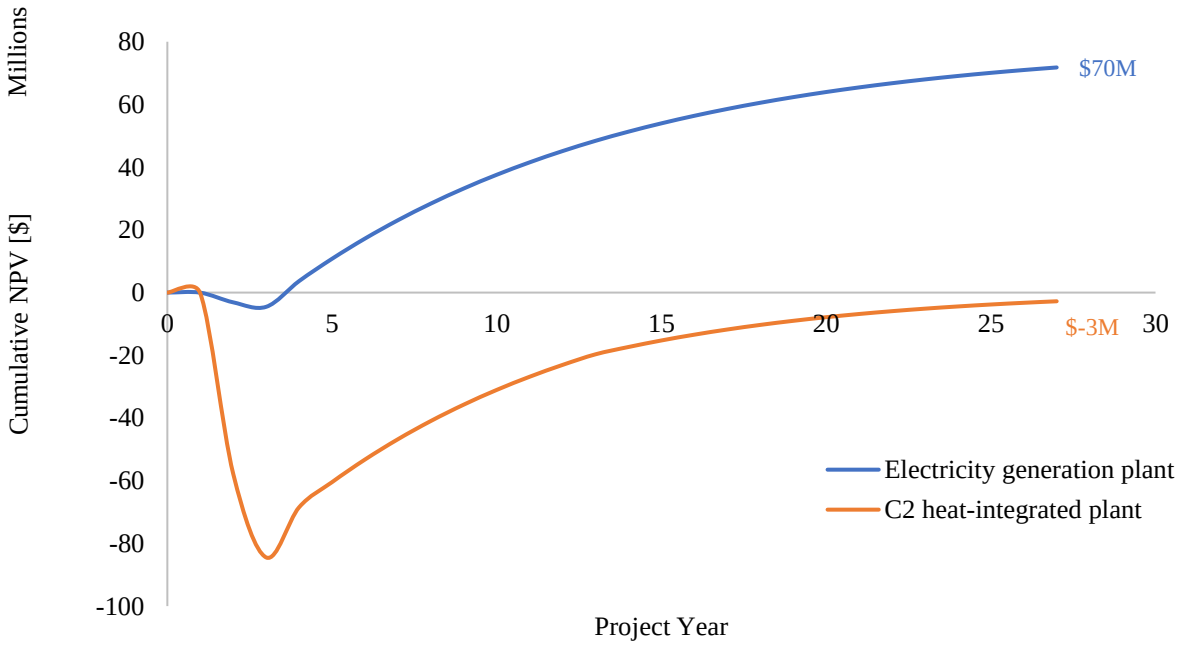

Figure 3.13. The cumulative NPV of the C_2 route-to-SAF plant (excluding the utility value of BL) is compared to that an alternative use of BL in a renewable electricity generation plant.

According to Figure 3.13, investing in an electricity generation plant that employs black liquor would yield a NPV of around $70MM with a payback period of 4 years (electricity selling price at 0.1085 $/KWh). On the other hand, the NPV of the proposed C_2 route bio-jet, disregarding the utility benefit of black liquor, is roughly -$3 million. This discrepancy originates from the fact that utilizing black liquor solely for electricity production incurs capital costs limited to a steam turbine. In contrast, C_2 heat-integrated plants involve multiple equipment requirements, including reactors for converting CO_2 and H_2 into SAF fraction. The considerable contrast in NPV highlights the significant challenges associated with implementing the C_2 heat-integrated plant as an alternative to the conventional approach of generating renewable electricity using black liquor. Despite the negative net cumulative NPV, this technology demonstrates promise and potential for a sustainable pathway to produce bio-jet fuel and other commodity chemicals. Achieving cost and process optimization will be crucial to improve the competitiveness of this technology.

3.4.5 Sensitivity Analysis

As previously stated, a sensitivity analysis was carried out to examine the influence of individual variables on the proposed C_2 heat-integrated bio-jet plant.

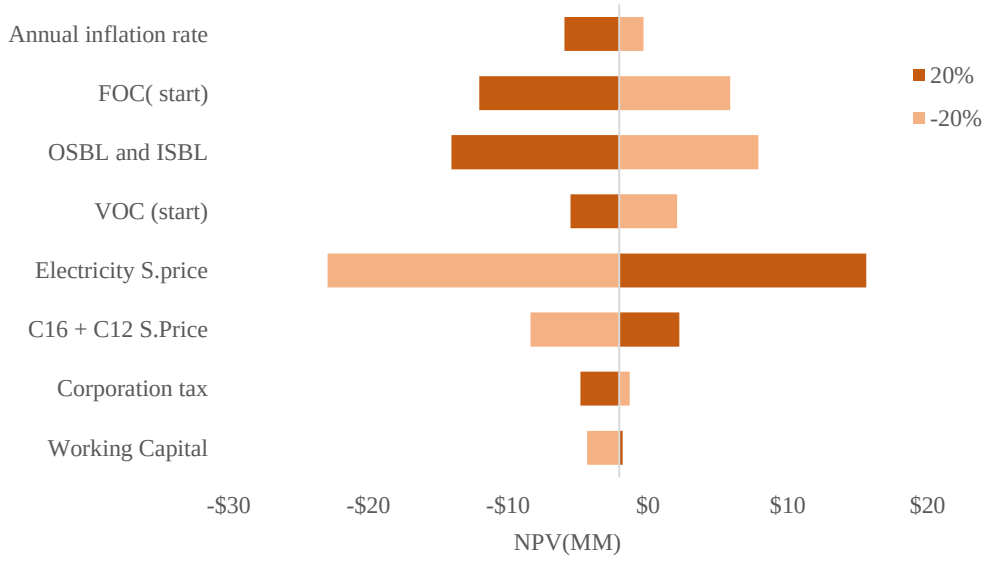

Figure 3.14. Tornado plot showing the effect of varying the values of variables by ±20% on the NPV of the proposed bio-jet plant. The price of renewable electricity has the highest impact on the cumulative NPV.

The analysis was performed using a tornado plot, and the objective was to comprehend the consequences of changes in these variables. A ± 20% variation was introduced in each variable to assess its impact on the plant's NPV, as illustrated in Figure 3.14.

The results indicate that the selling price of renewable electricity has the most significant impact on the NPV of the proposed C_2 heat-integrated plant. This implies that even a minor change in the selling price could significantly affect the plant's profitability. Although the estimated cumulative NPV of the proposed C_2 route-to-SAF plant was -$4 million, a slight 5% increase in the selling price of electricity while assuming that other parameters are constant, could lead to over a 200% increase in the plant's NPV. The nominal calculation in this study employed an electricity price of 0.1085 ($/kwh) to estimate the operational costs and financial viability of the plant. However, a critical observation emerges in the break-even analysis, indicating that the plant achieves equilibrium and covers its operational expenses when electricity is sold at a price of 0.1120 ($/kwh) while the kerosene (C_{12}, C_{16}) price remains $611/ton. This specific threshold serves as a pivotal point in determining the plant's profitability, demonstrating that any electricity sales below this value would result in a deficit, while sales above this threshold generate positive returns. This threshold is easily attainable given the current climate of increased energy prices [187].

Additionally, the fixed operating cost (FOC) had the second-highest overall impact on the plant, as evidenced by Figure 3.14. A 5% reduction in the FOC could result in approximately a 109% increase in the plant's NPV. Furthermore, the jet-fuel price also had a notable impact on the NPV of the plant, with a 5% increase resulting in around a 65% increase in the plant's NPV.

Moreover, changes in corporation tax, annual inflation rate, and variable costs also played a significant role in determining the NPV of the proposed plant. These factors are essential determinants of the overall economic viability of the plant and must be carefully managed to ensure its long-term success. Reducing these costs and optimizing the plant's operations could significantly improve the cumulative NPV of the proposed bio-jet plant, emphasizing the importance of cost-efficient operations.

In conclusion, the sensitivity analysis conducted in this study provides valuable insights into the impact of individual variables on the proposed C_2 heat-integrated bio-jet plant's NPV. The results indicate that the selling price of renewable electricity and FOC had the most significant impact on the plant, while other parameters such as the jet-fuel price, annual inflation rate, VOC, corporation tax, and working capital also played an important role. These findings

emphasize the need for careful management of these factors to ensure the long-term economic viability of the proposed plant.

3.5 Conclusion

In this chapter, a comprehensive study is presented on the utilization of continuous gas fermentation of H_2 and CO_2 to yield acetaldehyde (C_2 route-to-SAF), an intermediate for subsequent SAF production. Additionally, the heat integration of SCW gasification of black liquor and gas fermentation to tackle the energy inefficiency inherent in biological CO2 conversion is demonstrated. This study involved detailed process simulations via ASPEN HYSYS, facilitating a thorough TEA of the entire process. The investigation delves into the economic viability and associated challenges of the proposed C_2 heat-integrated SAF plant. Leveraging Aspen HYSYS for process modelling offered critical insights into equipment sizing, yield projections, and energy output, vital for accurate cost estimations.

The TEA evaluated various methodologies, highlighting differences between the TCI, FOC, and VOC incurred in the C_2 heat-integrated SAF plant compared to conventional renewable electricity generation using black liquor. The TCI estimates for the proposed C_2 SAF plant using the Hand and NREL methods hovered around $102 million and $101 million, respectively, reflecting marginal differences between these methodologies. This sharply contrasted with the lower capital investment required for utilizing black liquor for traditional renewable electricity generation, primarily reliant on a steam turbine.

Concerning FOC, the TS and Coulson & Richardson methods displayed close approximations, recording estimates of approximately $6.42 million and $6.87 million, respectively. The NREL method's output was notably lower and excluded from consideration, positioning the TS method as the primary basis for FOC calculations due to its alignment with the NREL approach and proximity to Coulson & Richardson's findings.

The VOC assessment outlined specific expenditures crucial for the C_2 heat-integrated SAF plant operation, including cooling water, fermentation nutrients, electricity, ammonia, furfural, and hydrogen essential for hydrogenation reactions. Nutrients and hydrogen constituted substantial portions of the VOC, accounting for 36% and 23%, respectively, shaping the plant's operational expenses.

The investment analyses yielded a negative NPV of approximately -$4 million for the proposed C_2 route-to-SAF plant, contrasting the approximate $70 million NPV derived from investing solely in a conventional renewable electricity generation plant employing black liquor. The

discrepancy between these NPV values stems from the diverse equipment requirements in the C_2 heat-integrated SAF plant compared to the singular steam turbine utilized in the conventional electricity generation plant.

The sensitivity analysis underscored the significance of variables such as the selling price of renewable electricity and Fixed Operating Costs (FOC) on the NPV of the C2 heat-integrated bio-jet plant. Despite the estimated cumulative NPV of -$4 million, a minor 5% increase in electricity selling price, assuming other parameters remain constant, could result in a more than 200% increase in the plant's NPV. The break-even analysis indicated that the plant achieves equilibrium and covers operational expenses when electricity is sold at a price of $0.1120 per kWh. This threshold signifies a pivotal point for profitability, with sales below leading to a deficit and sales above generating positive returns.

Essentially, although the present NPV doesn't indicate immediate financial success for the suggested C_2 heat-integrated route-to-SAF plant, this thorough analysis lays down a blueprint. It outlines possible routes for future improvements, highlighting the crucial need to enhance processes and cut operational expenses to strengthen the competitiveness and economic viability of this sustainable technology.

Moreover, government policies and incentives can play a crucial role in making this proposed technology attractive for investors, a topic that will be further discussed in chapter seven.

CHAPTER 4.

ISOBUTENE OLIGOMERISATION AND HYDROGENATION FOR JET-FUEL: AN EXPERIMENTAL STUDY

In this chapter, an investigation into two crucial upgrading units essential for producing SAF fractions via the C_4 route is presented. The C_4 route-to-SAF involves the initial conversion of CO_2 and H_2 to 2-ketoisovalerate via gas fermentation, ultimately resulting in the production of isobutanol (C_4), which is further processed into SAF fractions. Oligomerisation of isobutene and hydrogenation of oligomerised products constitute two of the major upgrading reaction units in the C_4 route-to-SAF process which is detailed in Chapter 6.

The primary focus of this chapter is an experimental investigation of the oligomerization and hydrogenation reactions to produce SAF fractions (C_{16}). The overall results and data from both experiments will be integrated into the simulation model of the C_4 route process in Chapter 6.

The chapter begins with a literature review covering the theoretical aspects of the oligomerization process of isobutene and the rationale for utilizing isobutene (derived from isobutanol dehydration) as a starting feed. The experimental setups for both oligomerization and hydrogenation reactions are presented. The experimental data from both reactions are analysed and discussed, including kinetic fittings using the experimental data from the hydrogenation of dimers, trimers, and tetramers. Figure 4.1 highlights how this chapter is connected with Chapter 6 and overall relevance for this thesis.

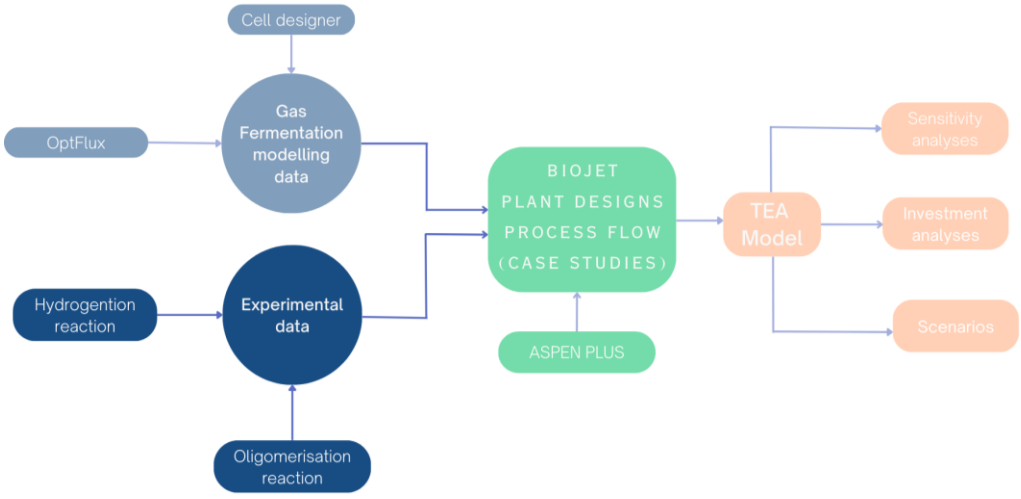

Figure 4.1. Thesis methodology highlighting the connection between the experiments and C_4 route process simulations.

4.1 Literature review – Oligomerisation of isobutene

Olefins are easily accessible, cost-effective, and readily transformable into liquid fuels such as diesel and gasoline, or into chemical commodities for diverse applications such as plastics production [188]. Steam cracking of LNGs can lead to the formation of olefins such as propylene and butene [189]. The industrial significance of olefin oligomerization is attributed to its ability to produce diesel and gasoline fuel-blending stocks, polymer additives, colorants and pigments, emulsifiers and chemical intermediates.

This process involves the synthesis of molecules with comparatively fewer monomer units, in contrast to polymerization, whose products are usually high in mass molecular weights [190]. According to literature data, oligomerization is divided into two parts; higher molecular weight alkene oligomerization, and lower molecular weight alkene (ethylene, propene and butene) oligomerization [191].

Liquid fuel and synthetic lube oils are mostly formed from the oligomerization of lower molecular weight alkenes, while alkenes with high molecular mass lead to diverse lubricating oil varieties. Unsaturated oligomer products are hydrogenated to increase their oxidation resistance or employed as feedstocks for different chemical processes [191].

Most oligomerisation reaction requires the use of a catalyst and there are three main classes of catalysts used for the oligomerization of olefins: cationic, anionic and free radical [189].

Cationic and anionic catalysts are mostly utilized as heterogeneous catalysts whereas the free radical class are homogenous catalysts. Acid and supported nickel catalysts fall under heterogeneous class.

The use of acid as a catalyst for oligomerization dates back to 1930, where it was initially employed in the petroleum industry [191]. Gasoline range iso-olefins (C_6-C_{10}) were obtained by incorporating a type of acid derived from phosphorus into silica clay [192], [193].

However, due to concerns of corrosion, alternative solid acidic catalysts, such as zeolites, were subsequently examined as replacements for the acid-based catalysts [194]. Zeolites, an acidic type of catalyst, are employed in the oligomerization of alkenes, transforming low molecular weight alkenes into high-grade fuels [188].

In contrast to homogeneous systems, zeolitic systems offer several advantages, such as their regenerability and stability over an extensive temperature spectrum, the ability to process feeds that contain a mixture of olefins, and the potential to manipulate product distribution by carefully selecting the catalyst and process parameters [195], [196].

Some research has shown that zeolites' pore structure, as a catalyst, enhances selectivity towards liquid products when oligomerizing alkenes with lower molecular mass [191]. This

led to the MOGD (Mobil olefin to gasoline and distillate) process, which involves using the ZSM-5 class of zeolites to convert alkenes with lower molecular mass into higher molecular weight gasoline and diesel fuels [197], [198].

Supported nickel catalysts are primarily used as dimerization catalysts in the production of feedstocks for various chemical processes by dimerizing ethene, as well as for synthesizing dimer products to create fuels with improved octane ratings. In contrast, homogeneous catalysts are instrumental in converting low molecular weight alkenes into their dimers for use in the petrochemical industry and creating high molecular weight linear alkenes for applications such as detergents and plasticizers [189]. Production of mainly linear products is the noticeable advantage over heterogeneous catalysts; however, the downside consists of complications accompanying catalyst separation. In delving into oligomerisation catalysts, attention now shifts to exploring ion resin exchange catalysts, their evolution, and their applications across various industrial sectors.

4.1.1 Ion exchange resins

Ion exchange resins, such as macro-porous resins, are catalysts that demonstrate adaptability and are employed across a wide range of industrial sectors to synthesize a variety of chemical compounds, including petrochemicals and solvents. Macro-porous ion exchange resins can be traced back as far as the 1960s [199], [200]. Polystyrene resins were formerly utilized before the invention of macro-porous ion exchange resins, unlike macro-porous ion exchange resins, their gels do not have true porosity. Conversely, macro-porous resins possess a well-established, permanent porous structure whose dimensions can be finely tuned through appropriate polymerization conditions [201].

Industrial applications of ion exchange resins have garnered attention over the last decade, especially in the synthesis that involves the replacement of conventional mineral acids with sulfonic acids [202], [203]. For instance, those catalysts have been employed in industrial esterification reactions [202].

Polymeric resins can be modified to incorporate various functional groups that impart desirable properties depending on the intended application. The addition of halogens, such as chlorine, can significantly improve the thermal stability of polymeric resins by serving as electron-withdrawing groups [204]. Resin performance is influenced not only by the monomer's nature, polymerization, and degree of crosslinking, but also by the specific functional groups that have been introduced into the matrix to confer catalytic activity [205]. For instance, copolymers can

be functionalized with sulfonic acid groups by employing alternative chemical approaches [202].

Studies indicate that the catalytic activity of microporous resins is affected by multiple factors, including their chemical composition, surface area, and pore size distribution[206].

Among microporous resins, reticular styrene-divinylbenzene copolymers exhibit the highest degree of microporosity. These copolymers can be synthesized with the assistance of a porogen, such as heptane, which remains inert during monomer reaction and can be easily removed following polymerization, yielding a porous matrix [205]. The extent of structural porosity in reticular styrene-divinylbenzene copolymers is closely related to the type and amount of crosslinking agent employed [207].

A well-known example of a microporous co-divinylbenzene sulfonic polystyrene resin is Amberlyst-15, while nafion, a per-fluorinated sulfonic resin with an alternative polymer backbone structure, is another example [208].

The catalytic potential of macro-porous resins with weak acidic groups, is yet to be fully explored in industrial applications, unlike sulfonic acid resins [205]. In industrial catalysis, microporous sulfonic acid resins have gained significant traction due to their effectiveness in a variety of reactions, including oligomerization [209]–[211]. Table 4.1 highlights the key features of various ion exchange resins that have previously been employed as oligomerization catalysts. In contrast to homogeneous catalysts, microporous resin catalysts, mainly composed of HCl and H_2SO_4, possess several benefits including easy removal from the reaction mixture, the ability to regenerate and reuse for extended periods, and reduced waste generation [[212]–[214]. Moreover, microporous resin catalysts usually result in lower equipment corrosion and higher selectivity [213].

Resins, however, have low thermal stability which imposes temperature limitations (usually up to 423 K [215]) and consequently, regeneration by calcination is hindered. Regeneration of resins catalyst is performed by washing with an appropriate solvent, although the activity is usually lower compared to a fresh resin [216].

However, for commercial applications requiring prolonged efficient resin performance, a more straightforward regeneration process is necessary [217].

Table 4.1. Characteristics of amberlyst and purolite ion-exchange [218] [219][207].

Resin Name	Acid capacity (meq H^+g^{-1})	BET area[a] ($m^2\ g^{-1}$)	Pore volume[b] ($cm^3\ g^{-1}$)	Surface area[c] ($m^2\ g^{-1}$)	Pore Diameter (Å)	Operating temperature[d] (K)max
A-70[e]	3.01	31	0.15	-	195	463
A-48	5.62	44		-	300	
A - 46	0.43	57	0.263	186	192	393
A - 39	5	0.09	0.0003	182	176	403
A - 36	5.4		0.143	147	240	423
A - 35	5.23	29	0.21	166	329	423
A - 16	4.8	1.69	0.013	149	304	403
P - MN500	0.9	900	1 - 1.1	-	-	393
P - CT276	5.2	23	0.21	176	357	408
P - CT275	5.2	28	0.42	183	601	418
P - CT252	5.4	22	0.22	132	394	403
P - CT175	4.98	29	0.48	157	662	418
A - XN1010	3.3	570	-	-	50	

[a] BET (Brunauer Emmett Teller) method.

[b] Adsorption–desorption of N2 at 77 K.

[c] Swelling in water (ISEC method).

[d] Manufacturer

[e] Resin with chloride

4.1.2 Dimerization of Isobutene

In the petroleum industry, isobutene is a significant bulk chemical, which constitutes the major component in naphtha C_4 cuts. The substantial reactivity of isobutene compared to other C_4 components allows for its separation through oligomerization [220]. The primary purpose of isobutene oligomerization is to produce dimers like isooctane, which possess a high octane number. This makes it a practical substitute for MTBE synthesis [221]. Moreover, the lower water solubility of di-isobutenes compared to MTBE minimizes the potential for groundwater contamination. The catalysis of isobutene oligomerization, typically accomplished by acid, is an exothermic reaction [222] that is preferentially carried out in the gas phase. Martens et al [223] found that ZSM-57, characterized by its lobate pore structure, exhibits a high level of selectivity and conversion of C_4 olefins to C_4 olefin dimers. They also suggested that ZSM-22 and ZSM-23, which have 1-dimensional channel systems, are capable of decreasing the degree of branching in oligomerization products [224].

Yoon et al reported that dimer selectivity improves when isobutene conversion decreases, regardless of the kind of catalyst used [225].

Isobutene dimerization, shown schematically in Figure 4.2, produces two trimethyl pentene isomers known as α -di-isobutylene and β -di-isobutylene [222].

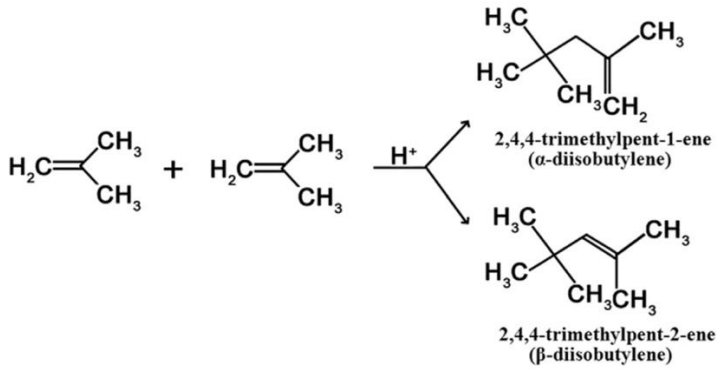

Figure 4.2. A depiction of the formation of two isomers of trimethyl pentene through the acid-catalysed dimerization of isobutylene.

The dimerization of isobutene was investigated using various ion exchange resins in a separate study [207]. The results showed that both selectivity and conversion outcomes for mono-sulfonated (Amberlyst 15,16) and hyper-sulfonated (Amberlyst 35) resins were the same in the presence of TBA [207].

Amberlyst-35 [226] exhibited the highest performance when methanol was used as a selectivity enhancer, while Amberlyst-15 [222] maintained stability and produced superior outcomes without the addition of polar additives. The impact of acidity was explored by Honkela et al. through the deactivation of some active sites in Amberlyst-15 via treatment with sodium hydroxide solutions [207].

Honkela et al. performed additional research on the impact of acidity by treating the ion-exchange resin Amberlyst-15 with sodium hydroxide solutions, resulting in the deactivation of some active sites (with H+ capacity ranging from 2.1 to 4.7 meq/g) [207]. As the acid capacity decreased, the effects of sodium ions and polar additives, referred to as enhancers of specificity, on the catalyst were shown to be distinct. Sodium ions significantly bind to the active sites, reducing proton movement and resin swelling (which increases diffusional limits), and hindering the favourable effects of enhancers of specificity such as tetrabutylammonium on the catalyst [207].

4.1.3 Isobutene Trimerization

Isobutene trimerization has been studied using a variety of cation exchange resins, and the selectivity of trimers rises as the amount of isobutene converted increases [227], regardless of resin type, comparable to the reaction over zeolites.

High isobutene conversion rates can be obtained at high temperatures and low space velocities by utilizing cation exchange resins that have a high concentration of acid groups [228]. The

use of strong acids, such as sulphonic acid, and a high degree of porosity are crucial for maintaining a consistent conversion. Yoon et al work suggested that for a consistent conversion, macro-porosity and a strong acid (sulphonic acid rather than acetic acid) are required. Furthermore, as the acid concentration of the resin catalyst increases, so does the conversion and trimers selectivity [228].

Acid resin catalysts exhibit excellent conversion and selectivity towards trimer formation. Nonetheless, these catalysts pose a challenge in terms of renewability due to their inability to undergo low-temperature drying for organic removal. While the catalysts may be reactivated to their initial activity by washing with hydrocarbons like n-butane, their stability is compromised compared to fresh resin catalysts free from organic residues [216].

Further research into the trimerization of isobutene, catalysed by macro-porous resins with sulfonic acid groups, namely Amberlyst-35 and Amberlyst-15, has revealed that conversion and trimer selectivity are enhanced by a combination of low isobutene concentration, low space velocity, and high acid capacity of the catalyst [229]. Jhung et al suggested that dimerization is favoured at low temperatures, whereas tetramerization is favourable at high temperatures [229]. Jhung et al, also noted that to obtain trimer selectivity above 50%, isobutylene conversion should be higher than 60% [228]. Acid catalysts such as WO_x/ZrO_2 have also been used for trimerization reactions. Over a WO_x/ZrO_2 catalyst produced by calcination at 700 °C, very stable isobutene conversion and good trimer selectivity are achieved [230]. The XRD findings suggest that stable trimerization performance is better achieved with tetragonal ZrO2, whereas monoclinic ZrO2 is unsuitable for consistent trimerization[230]. Several zeolites were investigated for trimerization, and the performance, particularly the stability, was quite low compared to typical zeolites such as mordenite, USY [229], and ZSM-5 [228]. Amberlyst-35 will be used in oligomerisation of isobutene experiment conducted in this thesis.

4.2 Experimental Set-up: Oligomerisation of isobutene

This section presents the design and outcomes of the two experiments conducted in this thesis, aiming to integrate the results into the simulation of the C_4 route SAF plant discussed in Chapter 6. As mentioned earlier, the oligomerisation of isobutene and the subsequent hydrogenation of the products are crucial components in the proposed C_4 route SAF plant's upgrading process. The discussion for each experiment will commence with an overview of the materials and setup, followed by a detailed explanation of the experimental procedures. Finally, the section will conclude with the presentation of results and discussions, including the performed kinetic fittings model for the hydrogenation reaction.

4.2.1 Materials

The oligomerization of isobutene was conducted in a Cambridge Reactor Design (CDR) located inside a fume cupboard. The experimental rig was designed to facilitate the oligomerization of isobutene, a process that involves the combination of small molecules to form larger ones, in this case, the formation of higher molecular weight isobutene oligomers. The experimental rig comprises several key components, including an isobutene cylinder, a fixed-bed reactor, a condenser unit, a product collector, a feedstock thermocouple, and a chiller unit. The isobutene cylinder, which supplies the isobutene feedstock to the reactor, is filled with isobutene gas at slightly above atmospheric pressure.

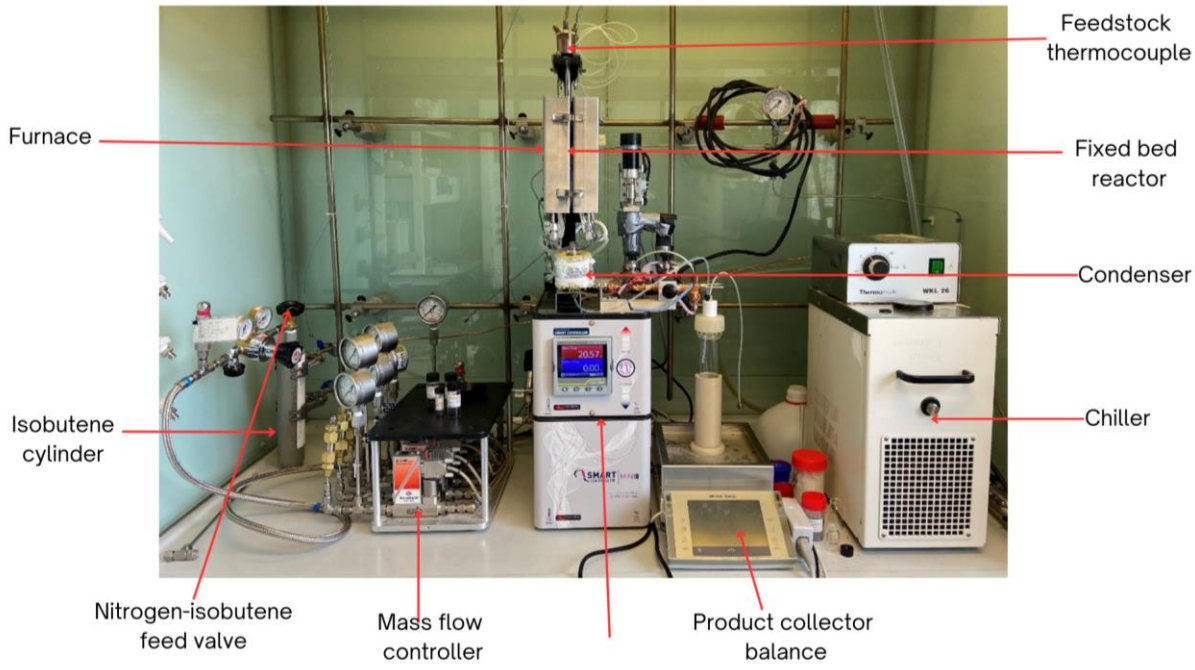

Figure 4.3. Experimental set-up of oligomerisation of isobutene.

Figure 4.3 shows the experimental set up of isobutene oligomerisation carried out. The fixed-bed reactor, where the oligomerization reaction takes place, is a cylindrical vessel made of stainless steel. The reactor is packed with glass wool, silicon carbide, catalyst, and glass beads. The glass beads are used to slow down the movement of isobutene when introduced to the reactor, allowing the isobutene to reach the desired temperature before contact with the catalyst. The glass wool, on the other hand, is used to barricade the top and bottom of the catalytic bed, facilitating easy separation of the glass beads within the reactor. Additionally, silicon carbide, a catalyst diluent, is utilized to dissipate the heat generated by the exothermic reaction.

Underneath the fixed-bed reactor, there is a condenser unit, which serves to condense any products formed during the reaction. The condenser unit is designed to cool the reactor outlet stream, allowing the products to condense and separate from the reactor effluent. The condensed products are then collected in a product collector, which is situated on top of a scale, used to collect and weigh the products resulting from the oligomerization reaction. A feedstock thermocouple is attached to the reactor to regulate the reaction temperature. The thermocouple provides continuous temperature measurement of the reactor content, and the temperature can be regulated by adjusting the flow of coolant through the reactor jacket. The rig also has a chiller unit, which is used to control the reactor temperature and keep the condenser cold. The chiller unit is connected to the reactor and the condenser, and it circulates a coolant through the system to maintain the desired temperature. The various components of the rig work together to provide optimal conditions for the reaction to take place, and to collect and analyse the products formed. The use of glass wool, silicon carbide, glass beads and the thermocouple, all play an important role in maintaining optimal reaction conditions, and in the separation and analysis of the products. Next section presents the catalyst pre-treatment before carrying out the experiment. Amberlyst-35 is chosen due to its superior acidic capacity necessary for the trimerization reaction.

4.2.2 Catalyst pre-treatment

In the oligomerization reaction of isobutene, a commercial catalyst known as Amberlyst-35 was utilized. The catalyst was dried overnight at 110°C and subsequently vacuumed for 3 hours to ensure complete removal of water. Before the initiation of the reaction, the catalyst underwent a pre-treatment in situ at approximately 120°C and 1 bar for 1 hour through the introduction of 10 ml/min of Nitrogen.

The catalyst was used in a specific ratio with silicon carbide, a catalyst diluent. Specifically, 0.7g of Amberlyst-35 and 2.1g of silicon carbide were utilized in the reaction, resulting in a ratio of 1:3 of catalyst to diluent. This ratio is essential for achieving optimal reaction conditions and for the efficient utilization of the catalyst. The use of a catalyst diluent, in this case silicon carbide, helps to dissipate the heat generated by the exothermic reaction and also to increase the stability of the catalyst.

4.2.3 Oligomerisation reaction

The oligomerisation of isobutene was carried out in a gaseous phase using a 300ml fixed bed continuous reactor which is enclosed by a furnace for heating the reactor to the required temperature. Isobutene gas was flashed through the reactor 3 times to discharge any air.

Subsequently, isobutene was constantly fed at the flow rate of 5ml/min to the reactor via the Mass Flow Controller unit (MFC). Nitrogen was used as the carrier gas and introduced at a flow rate of 5ml/min. The reaction temperature and pressure used were 70^{o}C and 1 bar respectively. A constant temperature was maintained by the Cambridge Reactor Design via a thermocouple. The space velocity of isobutene, WHSV(weight-hourly space velocity, g isobutene/g catalyst/h), was maintained at 1.06 h^{-1}.

Reaction products, which underwent condensation via the condenser unit, were collected and weighed periodically to determine the mass balance. The sample of reaction products was analysed with the use of a GC to determine product distribution. Figure 4.8 shows the GC analyses of product samples collected over different intervals of the reaction.

4.3 Experimental Set-up: Hydrogenation of oligomerised alkenes

This section outlines the follow-up hydrogenation experiment conducted, which utilizes the product derived from the oligomerisation of isobutene. Essentially, the product of the oligomerisation reaction is the feedstock of the hydrogenation reaction. This reaction is essential for breaking the double bonds present in dimers, trimers, and tetramers, rendering them suitable for incorporation into SAF drop-in fuels..

4.3.1 Materials

Olefin hydrogenation reaction was performed in a 50ml autoclave which was placed inside a fume hood.

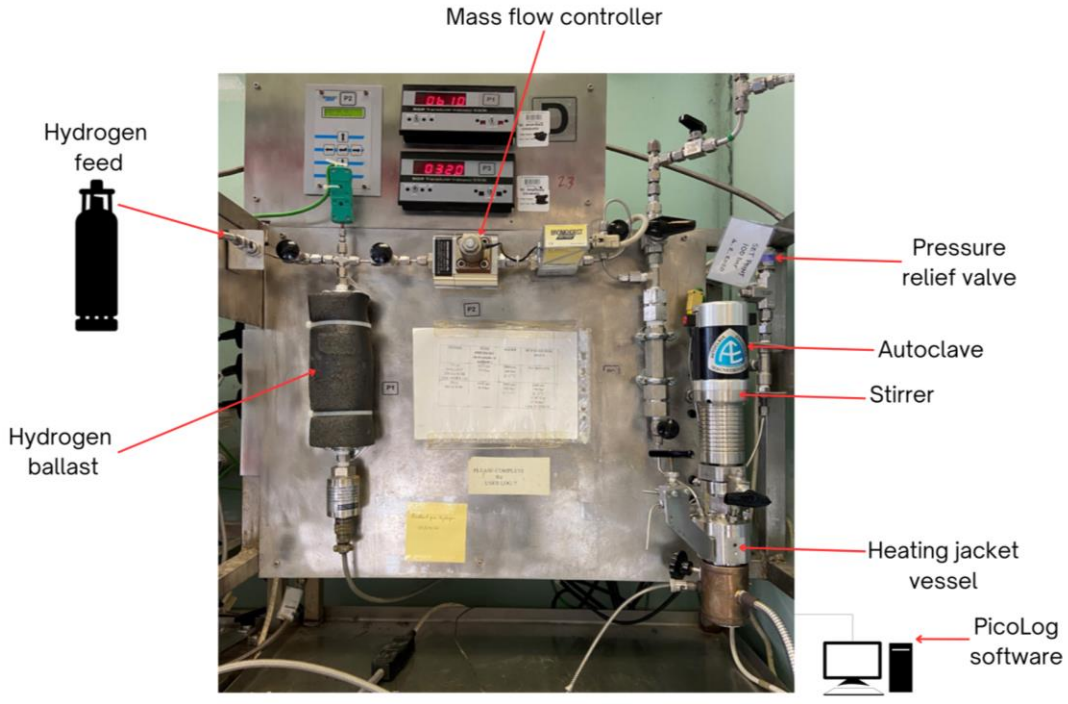

Figure 4.4. Experimental set up rig for the hydrogenation of oligomerised isobutene products

Loading and unloading of reactants and catalysts were performed inside the fume hood to allow evacuation of hydrogen or any other chemical vapour released. Figure 4.4 shows the experimental set-up of the hydrogenation reaction.

A heating jacket was fitted to the vessel to provide heat for the reaction. A mass flow controller together with a hydrogen ballast was utilized to control and maintain the flow of hydrogen into the reactor. 150ml hydrogen ballast located close to the reactor ensured that the pressure of hydrogen remained constant throughout the reaction. A stirrer operating at 1000rpm ensured an even distribution of hydrogen throughout the reaction time. PicoLog software was used to monitor hydrogen uptake and to determine the end of the reaction. Both the ballast and reaction rig are located inside the fume hood. The system has a pressure relief valve which will go off if the pressure within the reactor reaches 100bar.

4.3.2 Hydrogenation reaction

Before the hydrogenation reaction, toluene was introduced into the autoclave to ensure the complete removal of any impurities. Then, the autoclave is heated above the boiling point of the toluene and left for a couple of hours to ensure complete evaporation. The autoclave is sealed and dried overnight. 10g of the oligomerised olefinic mixture was loaded into the vessel. 0.1g of 5 wt.% palladium on aluminium catalyst was also introduced into the reaction vessel and mixed thoroughly with the olefinic product.

Then, the vessel was attached to the autoclave and the sealed system was flushed with hydrogen three times to ensure the removal of air. This was to prevent the deactivation of the catalyst via oxidation. Initially, the system pressure and stirrer are left very low to heat the reaction to the required condition without increasing the pressure in the reactor.

Then, the reactor is allowed to reach 150^{o}C which is the reaction temperature. The desired pressure which was 5 bar was set using the panel control and allowed to fill the autoclave with pure hydrogen. The ballast which was located near the reactor fed hydrogen to the reaction via a mass flow controller while maintaining constant reaction pressure. The initial reaction was allowed to run on 5 bar and was subsequently increased in other reactions. Table 4.2 shows the hydrogenation of oligomerised alkenes in different reaction conditions. PicoLog software was used to determine the end of the reaction via a hydrogen uptake profile. Once the reaction is finished, the heating was stopped, and the system was allowed to cool down to room temperature under stirring.

Table 4.2. Reaction conditions of hydrogenation of oligomerised olefinic mixtures.

	Run 1	Run 2	Run 3
Substrate [g]	10	12.45	15
Catalyst [wt.%]	1	3	1
Temperature [ºC]	150	150	150
Pressure [bar]	5	20	20
Stirrer [rpm]	1000	1000	1000

Once cooled down, hydrogen pressure was released from the vessel. Then, the vessel was unsealed, and the mixture of product and catalysts was transferred to a container to be analysed. The catalyst was allowed to decant to facilitate separation from the product.

4.4 Results and Discussions

4.4.1 Results: Oligomerisation of isobutene reaction

The product distribution trends of isobutene oligomerization over Amberlyst-35 were studied and presented in Figure 4.5. The data shows that the selectivity and conversion were consistent throughout the duration of the oligomerization reaction. Specifically, the selectivity of trimers (C_{12}) was found to constitute a significant portion of the product distribution, with an approximate value of 70%. This was followed by tetramers (C_{16}) which accounted for 20% of the product distribution. On the other hand, the selectivity of dimers (C_8) and pentamers (C_{20}) was relatively low, with a combined average of 7%. The stability of isobutene oligomerization over Amberlyst-35 was determined to be high, as it was found to be maintained for a duration of 234 hours or more. This is attributed to the high concentration of sulphonic acid present in the resin, among the acid resins investigated. However, it is noteworthy that the selectivity of trimers over catalysts such as Amberlyst-31 and WK-40 is comparatively low, while the selectivity of dimers is high. This can be explained by the presence of weak acid sites of carboxylic acid in WK-40 (Diaion) [229].

A mass balance calculation was conducted to determine the conversion of isobutene, which was found to be 100%.

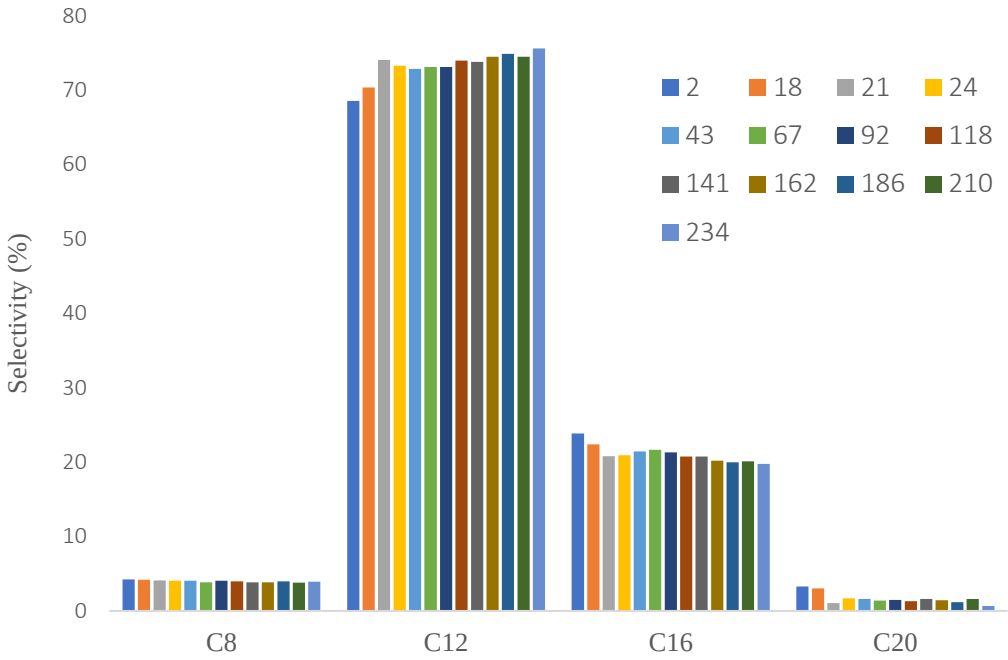

Figure 4.5. Hourly product distribution in the oligomerisation of isobutene over Amberlyst - 35. Temperature - 70^{o}C, Pressure - 1 bar, WHSV – 1h^{-1}. The legend, represented by different colours, indicates the specific hour during the experiment when the product was collected and subsequently analysed.

This calculation was done by comparing the total moles of isobutene fed to the reactor to the moles of isobutene found in the product. The results of the mass balance calculation are presented in Table 4.3. More so, a residence time of 47mins was determined for the reaction. It is also worth mentioning that slight fluctuations were observed in the mass flow controller unit, which may have contributed to the mass balance showing slightly more than 100%. In Figure 4.6, the selectivity of C_{12} - C_{16} (jet-fuel fractions) was found to account for more than 90% of the oligomerization reaction. This aligns well with the objective of producing sustainable jet-fuel drop-ins, as these jet-fuel fractions are of great importance in the aviation industry.

Table 4.3. Showing mass balance of oligomerisation reaction.

Time [h]	Schott bottle (g)	Total fed (g)	Total product(g)	Mass balance (%)
0	247.6			
19	263.0	14.10	15.40	109%
43	265.7	17.81	18.10	102%
67	285.2	35.62	37.60	106%
92	306.5	54.17	58.90	109%
118	328.5	73.46	80.90	110%
141	347.9	90.52	100.30	111%
162	366.8	106.11	119.20	112%
186	387.4	123.91	139.80	113%
210	407.4	141.72	159.80	113%

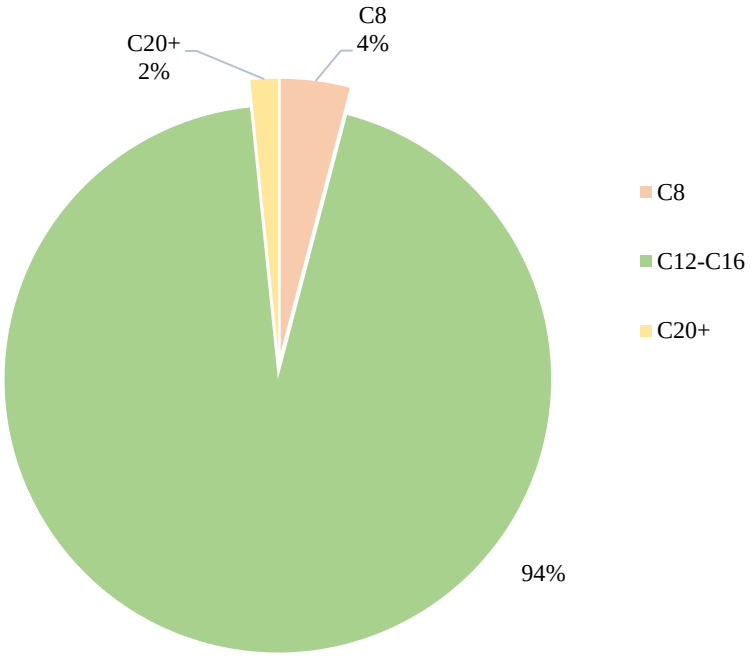

Figure 4.6. shows a typical product selectivity from the isobutene oligomerisation reaction. Selectivity of trimers and tetramers (jet-fuel drop-in fractions) accounts for over 90%.

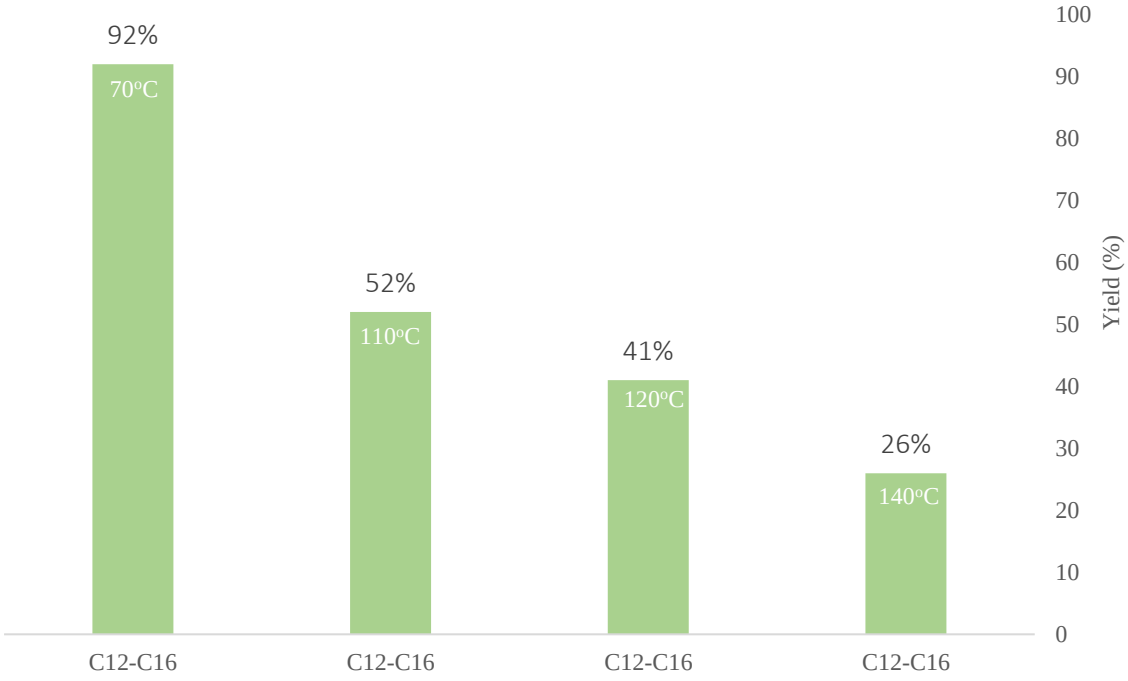

Figure 4.7. The oligomerisation of isobutene in different temperature conditions over Amberlyst - 35. The oligomerisation of isobutene shows the highest yield of trimers and tetramers at 70°C.

The oligomerisation of isobutene was performed in different temperature conditions over Amberlyst – 35, and the effect of temperature on the yield of trimers and tetramers was evaluated. As shown in Figure 4.7, the yield of trimers and tetramers decreased with an increase in temperature. This is due to the fact that the oligomerisation reaction is exothermic, and thus thermodynamically favourable at low temperatures, however, the chain growth is limited kinetically [231]. The oligomerisation of isobutene at 70°C produced the highest yield of trimers and tetramers. Additionally, it was observed that the selectivity of trimers increases with an increase in isobutene conversion, and this can be explained by the successive reaction of oligomerisation via carbenium ions [232]. Overall, the results suggest that temperature plays a crucial role in the oligomerisation of isobutene, and the optimal temperature for the highest yield of trimers and tetramers is 70°C.

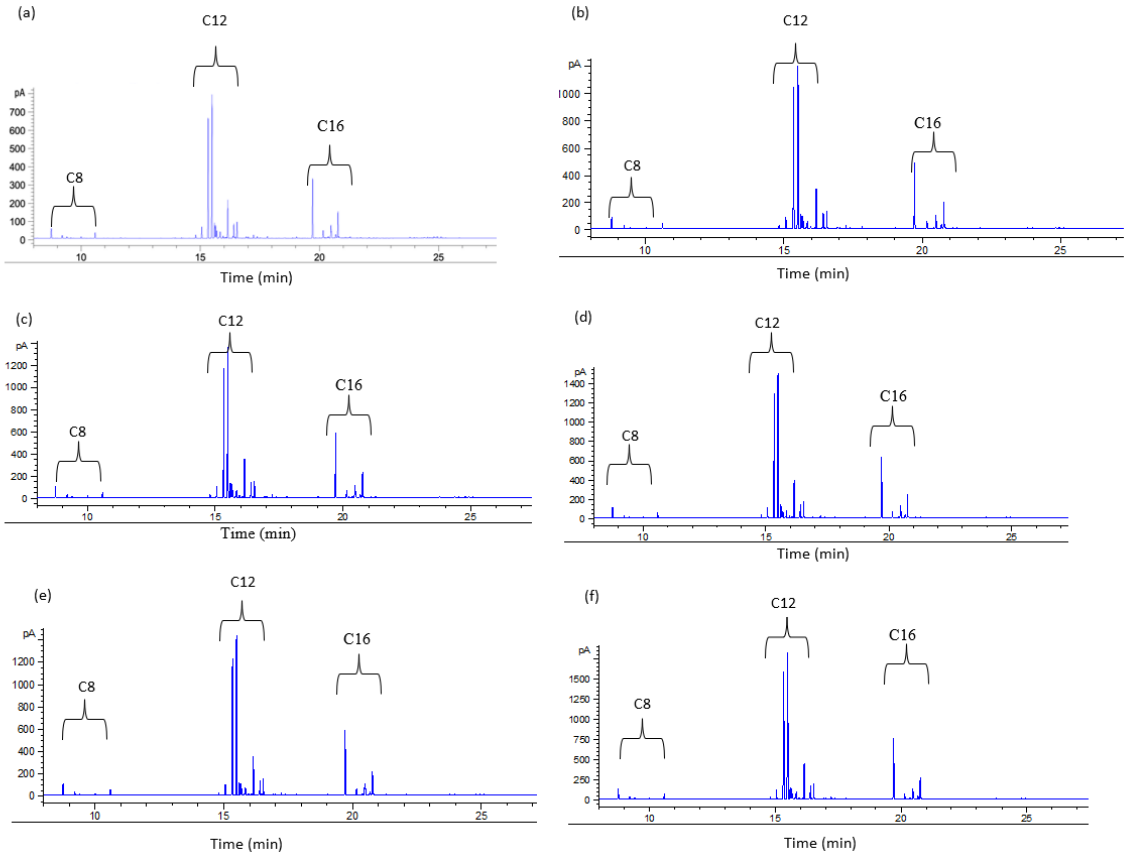

Figure 4.8. Typical GC chromatograph of oligomerisation product at taken and analysed at different reaction times. (a) – (f) corresponds to the GC taken in 2h, 18h, 43h, 67h, 118 and 186h respectively.

4.4.2 Results: Hydrogenation reaction

The hydrogenation of oligomerized alkenes was performed under various conditions and the typical alkane distribution is depicted in Figure 4.9. As expected, the selectivity of trimers and tetramers was found to be the highest, with 69% and 25% respectively. This is due to the fact that hydrogenating alkenes leads to the breaking of the double bonds in the presence of a catalyst, resulting in the production of saturated alkanes. The initial hydrogenation reaction (run 1) was performed at a pressure of 5 bar, a temperature of 150^{o}C and in the presence of 5 wt.% Palladium on aluminium (Pd on Al_2O_3) which resulted in a high yield of alkanes. However, it took more than 45 hours to complete the reaction, as can be seen in Figure 4.10. To investigate the cause of the long reaction time, the hydrogenation reaction was performed under different reaction conditions.

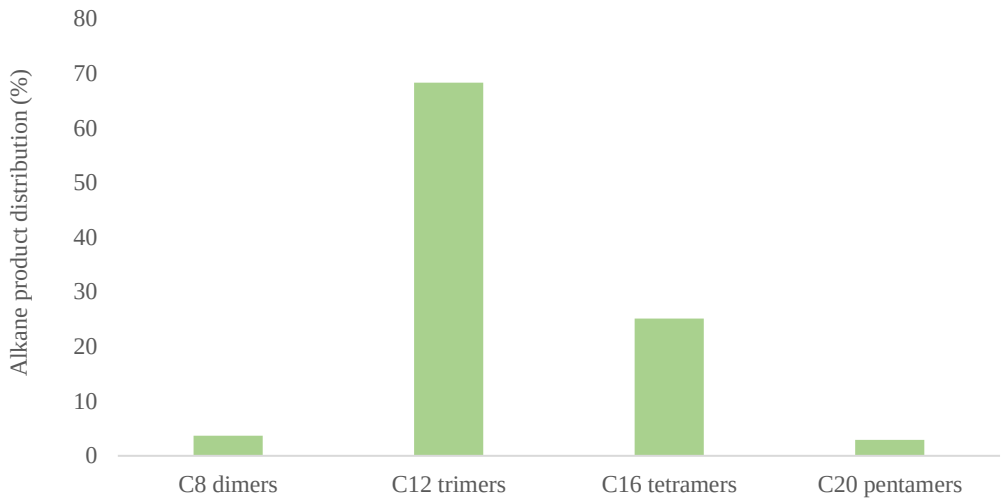

Figure 4.9. Alkane distribution after undergoing hydrogenation reaction.

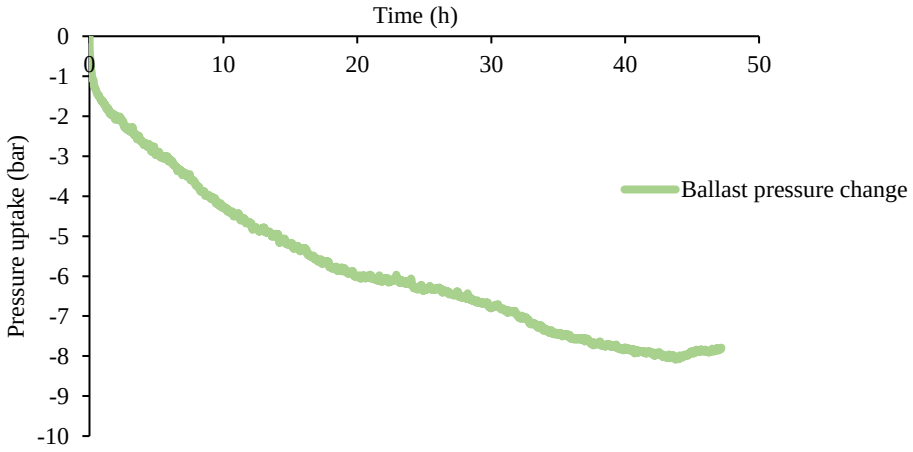

Figure 4.10. Hydrogenation of oligomerised alkenes at 5 bar and under the presence of 5 wt.% Pd on Al_2O_3. The graph shows the pressure uptake via hydrogen ballast with the reaction completion at 45h.

In run 2, the reaction pressure was increased to 20bar, while the catalyst to substrate ratio was maintained at 3:1 with 1wt% Pd on Al_2O_3. A significant change in the reaction rate was observed, as can be seen in Figure 4.11. Unlike run 1 reaction, the reaction was completed much faster. This can be explained by an increased density of hydrogen on the catalyst surface as the pressure increases, thus increasing the hydrogenation reaction rate [233].

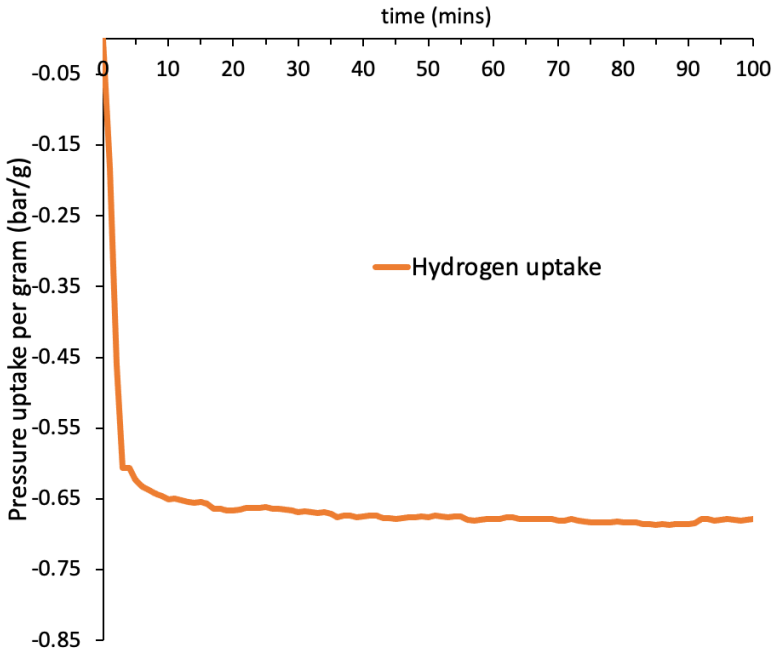

Figure 4.11. Hydrogenation of oligomerised alkenes at 20 bar and under the presence of 5 wt.% Pd on Al_2O_3. The substrate-catalyst ratio was 1:3.

Further investigation was conducted by reducing the catalyst concentration to 1wt% of palladium on aluminium and the catalyst to substrate ratio to 1:1. As can be seen in Figure 4.12, the reaction rate decreased slightly when compared to the previous reaction, however, it was still notably faster than the reaction under 5 bar conditions.

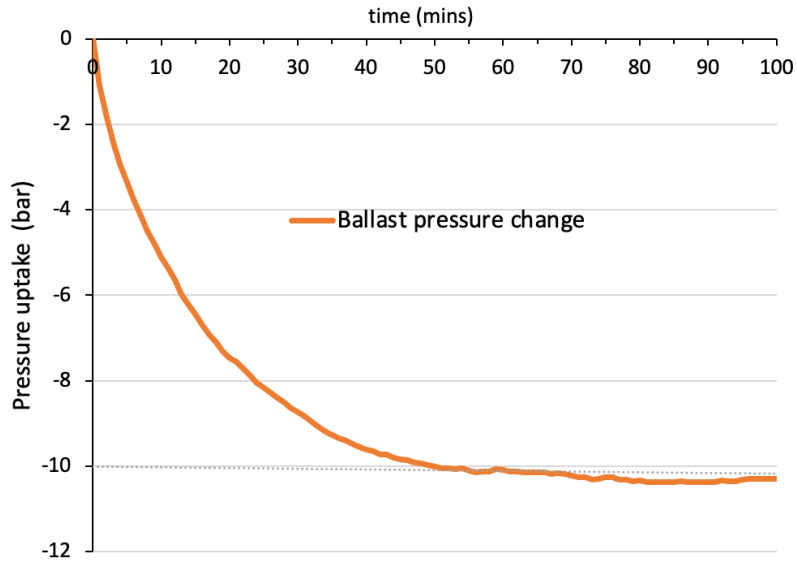

Figure 4.12. Hydrogenation of oligomerised alkenes at 20 bar and under the presence of 1 wt.% Pd on Al_2O_3. The substrate-catalyst ratio was 1:1.

It can be deduced that the catalyst concentration increases the rate of hydrogenation reaction. A graph comparing the three reactions under different conditions can be seen in Figure 4.13.

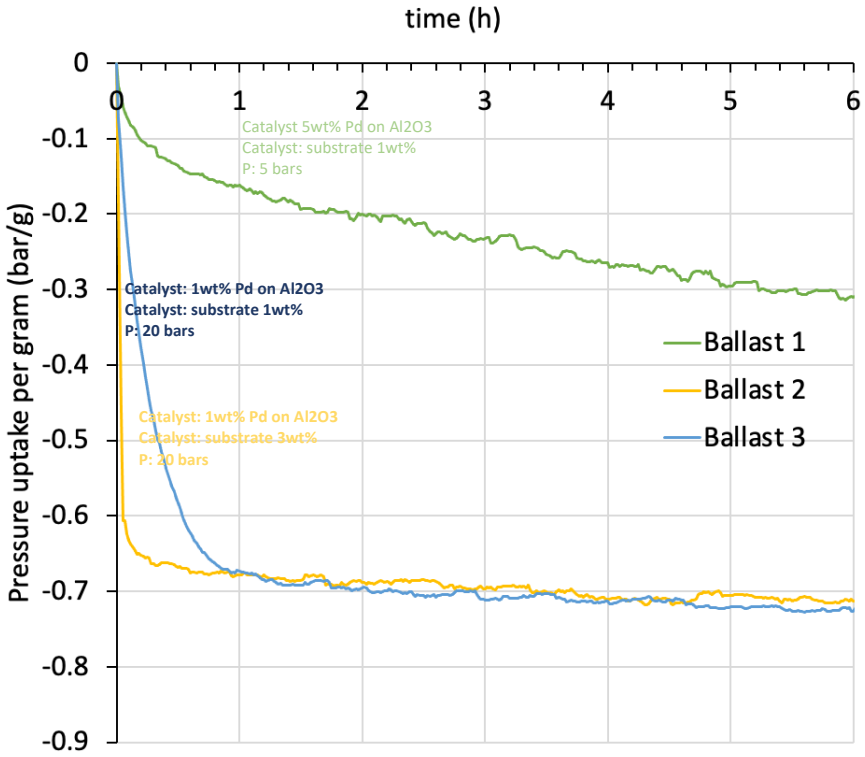

Figure 4.13. Graph comparing three hydrogenation of oligomerised alkenes performed under different conditions. The hydrogen ballast shows the hydrogen uptake profile for the three reactions.

It is crucial to choose the optimal condition for this reaction that would help in cutting costs. Gas chromatography of products from oligomerization and subsequent hydrogenation were compared in Figure 4.14. Notable differences can be seen, especially in the trimers and tetramers region. This can be explained by the formation of other alkane compounds via the breaking of the double bonds in the olefin mixture.

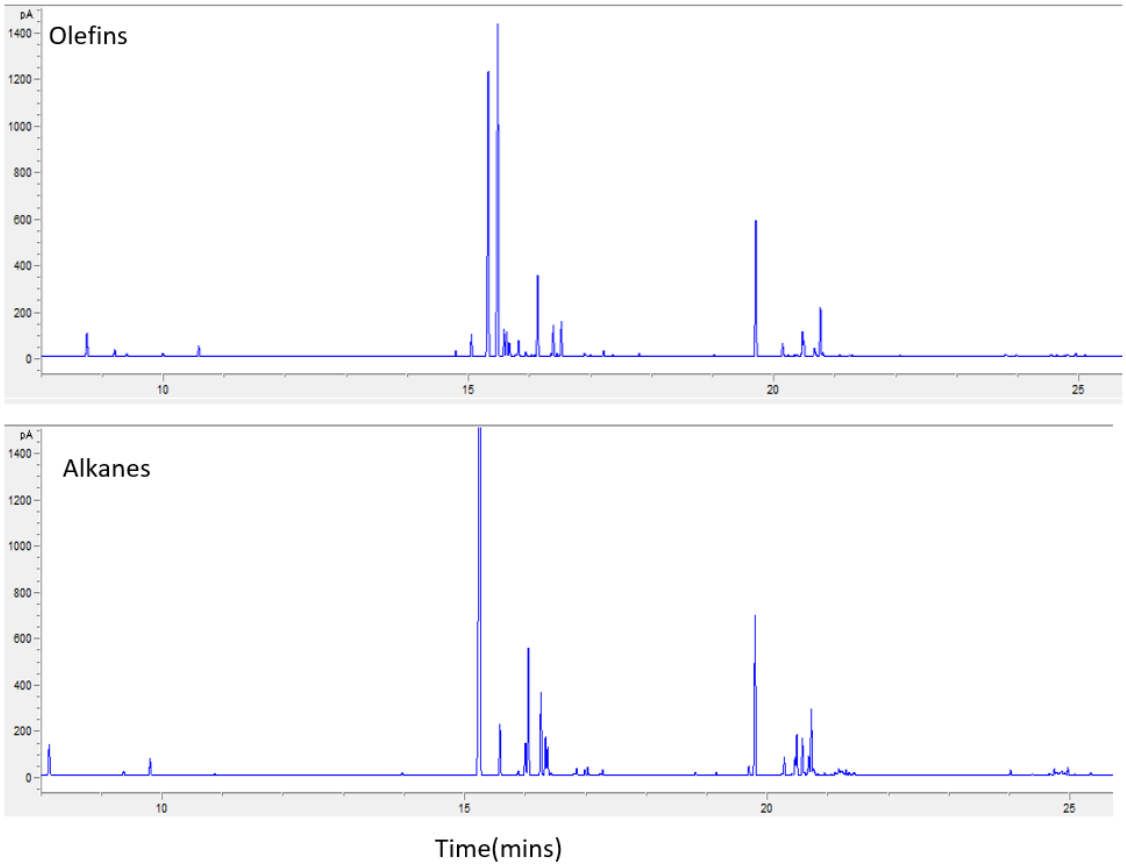

Figure 4.14. GC comparison of oligomerised olefins and hydrogenation olefins.

4.4.3 Reaction kinetics for hydrogenation reaction

To determine the kinetics of the hydrogenation of oligomerised olefins, the kinetic fitting regression modelling method was implemented using the hydrogenation experimental data from run 3. The full details of the data from PicoLog software used to determine this can be found in Appendix 2.

The fitting process involved determining two key model parameters: the kinetic constant "k" and the exponent of the power law, which represents the reaction order "n". By utilizing the Excel solver, the values of "k" and "n" were determined to achieve the best fit by minimizing the sum-squared error of the hydrogen uptake in the reaction. Equation 4.1 shows a simple power law kinetic equation used, where k, C_{AO} and n correspond to reaction rate, the initial concentration of isobutene and reaction order, respectively.

$$\frac{dX}{dt} = k \cdot C_{AO}^{n-1} \cdot (1 - X)^n \qquad \text{Eqn 4.1}$$

$C_{AO} = \frac{M_{substrate}}{V_{reactor}}$, ($gL^{-1}$) Eqn 4.2

where $M_{substrate}$ is the mass of substrate and $V_{reactor}$ denotes the volume of the reactor (300mL). The determined values were: k = 0.008198558 [1/h], n ≈ 2, with a sum error of 31.7.

It was determined that the hydrogenation reaction was second order. Figure 4.15 shows the comparison between the experimental data and the regression kinetic fitting modelling. It can be seen that the kinetic fitting model showed an agreement with the results obtained from the hydrogenation experiment.

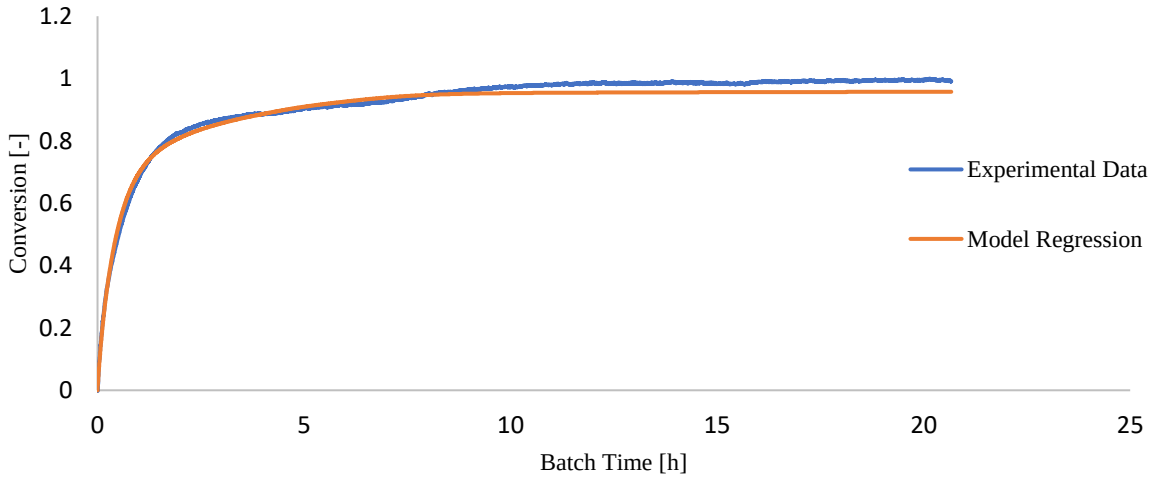

Figure 4.15. Comparison between experimental data and kinetic regression model to determine reaction order.

4.5 Conclusion

In this chapter, two experiments were conducted to integrate their findings into the process simulation of the proposed C_4 route-to-SAF plant, which will be detailed in Chapter 6. These experiments focused on the oligomerization of isobutene and the subsequent hydrogenation of the resulting products, both essential stages in the product upgrading process (isobutanol to SAF fractions) within the C_4 route-to-SAF plant. The materials and setups for both experiments were described, highlighting crucial components such as the reactor, condenser unit, product collector, feedstock thermocouple, and the chiller unit. These elements were necessary in providing optimal conditions for reactions and subsequent product analysis.

In the oligomerization experiment, the examination of isobutene oligomerization over Amberlyst-35 revealed the product distribution. The stability of the oligomerization reaction over Amberlyst-35 was demonstrated for over 234 hours, a critical factor for sustainable jet-fuel drop-ins. The selectivity of trimers (C_{12}) and tetramers (C_{16}), constituting about 90% of the product distribution, stood out as significant SAF fractions. Moreover, the optimal temperature for the highest yield of trimers and tetramers was identified as 70°C.

In the hydrogenation experiment, various reaction conditions were explored to enhance the reaction rate and yield of alkanes from oligomerized alkenes. Initial experimentation (Run 1) at 5 bar pressure, 150°C temperature, and 5 wt.% Palladium on aluminium (Pd on Al_2O_3) yielded high alkanes but took over 45 hours. In Run 2, elevating pressure to 20 bar while maintaining a 3:1 catalyst to substrate ratio with 1 wt.% Pd on Al_2O_3 considerably accelerated the reaction rate. Contrastingly, Run 3, with reduced catalyst concentration to 1 wt.% Pd on Al_2O_3 and a 1:1 ratio, displayed a slightly reduced but notably faster reaction than initial low-pressure conditions. Furthermore, the kinetics of the hydrogenation reaction were determined using regression modelling. The kinetics analysis unveiled the reaction's second-order kinetics, with a kinetic constant "k" of 0.008198558 [1/h] and an approximate reaction order "n" of 2. This model exhibited substantial alignment with experimental data, confirming its reliability in predicting reaction dynamics.

Overall, these experiments provide critical insights into reaction dynamics, temperature optimization, and reaction kinetics. The findings contribute essential groundwork for the efficient integration of these processes into the C_4 route-to-SAF plant discussed in Chapter 6, fostering advancements in SAF production.

CHAPTER 5.

AEROBIC GAS FERMENTATION MODELLING

In this chapter, the focus is placed on the modelling of aerobic gas fermentation as a key unit process within the SAF production plant, encompassing both the C_2 and C_4 routes. The theoretical foundation for gas fermentation has been extensively covered in sections 2.5 of this thesis. Chapter 3 utilized the experimental data from Bommareddy et al. [45] for gas fermentation in the TEA of SAF production via the C_2 heat-integrated route. However, in this chapter, the modelling and simulation of gas fermentation involving CO_2 and H_2 are undertaken to estimate approximate gas uptakes through Flux Balance Analysis (FBA). Two crucial software, Cell Designer and OptFlux, were employed to design the biochemical pathways and execute FBA.

The results contribute to deriving the stoichiometric equation for the aerobic gas fermentation reaction, a critical parameter required in ASPEN HYSYS simulation for a typical conversion reactor modelling. This integration was facilitated by incorporating gas uptake rates from OptFlux simulation into HYSYS and establishing a linkage between HYSYS and EXCEL using Object Linking and Embedding Database (OLE DB). This connection enabled the precise calculation of O_2 uptake rates for the conversion reactor due to the exchange of variable values.

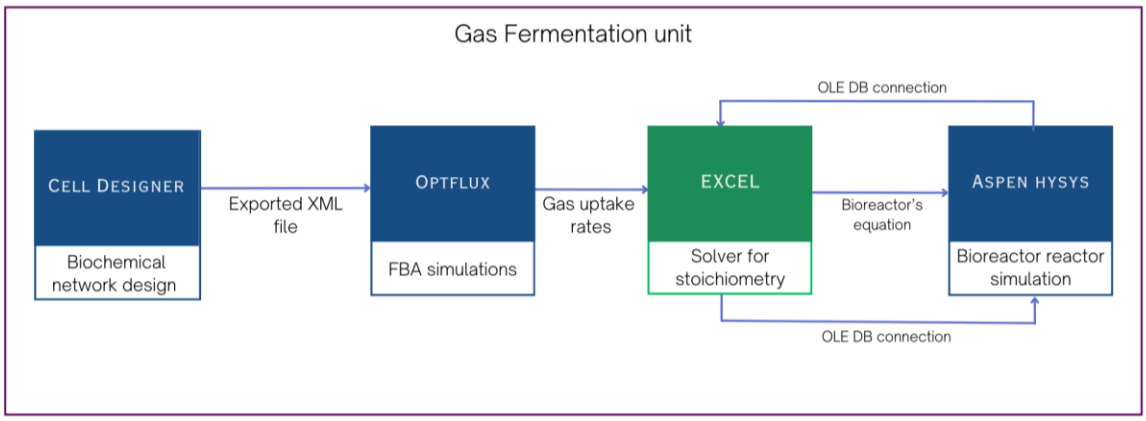

Figure 5.1. Gas fermentation unit demonstrating the integration between Cell Designer, OptFlux, and ASPEN HYSYS in simulating and modelling the bio-reaction between CO_2 and O_2 using Cupriavidus necator as the microbial cell factory.

Figure 5.1 shows how the Cell designer, OptFlux, EXCEL solver and ASPEN HYSYS software were utilized to model the bioreaction that occurred in the aerobic gas fermentation unit operation of C_4 route SAF plant. The reactor sizing and other parameters from ASPEN

HYSYS will ultimately be utilized in the TEA of the overall C_4 route SAF process which is detailed in Chapter 6.

5.1 Gas fermentation

Gas fermentation is a biocatalytic technique that employs biocatalysts to transform gaseous feedstocks such as carbon monoxide (CO), carbon dioxide (CO_2), syngas, methane (CH_4), or biogas into platform chemicals, fuels, polymers, and other products [234].

This method differs from conventional fermentation procedures in that the liquid phase is not supplied to the primary substrates. For numerous years, research has been centred on exploring gas transformation methods, which continue to garner growing attention. The biological conversion of gaseous components encompasses numerous promising routes that align with the concepts of biorefineries. A significant portion of these suggested processes involves utilizing CO_2/CO as an alternate carbon source, aiming to facilitate decarbonization within the energy and materials industries.

Employing microorganisms proficient in assimilating C1 molecules through gas fermentation processes presents a viable approach to reducing reliance on fossil-derived resources. This methodology enables the conversion of gaseous carbon substrates into essential fuels and chemicals, thereby promoting a sustainable alternative to traditional resource consumption. [234].

Section 2.7.2 has established the rationale behind selecting aerobic gas fermentation as a pivotal technology in this thesis for SAF production. The subsequent part of this chapter will delve into modelling aerobic gas fermentation. It will employ Cell Designer and OptFlux, accompanied by a results and discussion section.

5.2 Methods for gas fermentation modelling

5.2.1 Modelling and simulation

A significant problem for systems biology is comprehending the logic and dynamics of gene regulation and metabolic networks. The standardisation of machine-readable formats like models Systems Biology Markup Language (SBML) has helped the creation of complicated biological [235]. We have utilized Cell Designer because it offers diagrammatic interfaces and can translate them into SBML to simplify the modelling of biochemical networks. Unlike HYSYS, which does not consider the full biochemical pathways, cell designing helps to visualize the biochemical pathways and reactions that happen in a typical gas fermentation. Also, an advantage of Cell designer is that stored graphic information about reaction pathways

can be converted into mathematical formulas for analysis and simulation. The main objective of this simulation is to determine the key reaction stoichiometry and coefficients needed for our bioreactor's conversion reactor simulation in ASPEN HYSYS. This in turn will feed into the overall TEA of the C_4 process route to SAF.

5.2.2 Cell Designer Simulation

Cell Designer v4.4 was first used to capture the central metabolism pathways of aerobic gas fermentation where Cupriavidus necator serves as the microbial cell factory using CO_2 as its only source of carbon, H_2 as the electron donor, and O_2 as the electron acceptor [236].

In the context of our gas fermentation modelling, Cell Designer was employed to determine the stoichiometry of the reaction for the conversion reactor modelled in HYSYS and also to visualize the metabolic pathways including glycolysis, the pentose phosphate pathway, the TCA cycle, and oxidative phosphorylation, along with their associated fluxes. The model also visually demonstrate how CO_2 and H_2 are dedicated to biomass and the product of interest (2 keto-isovalerate).

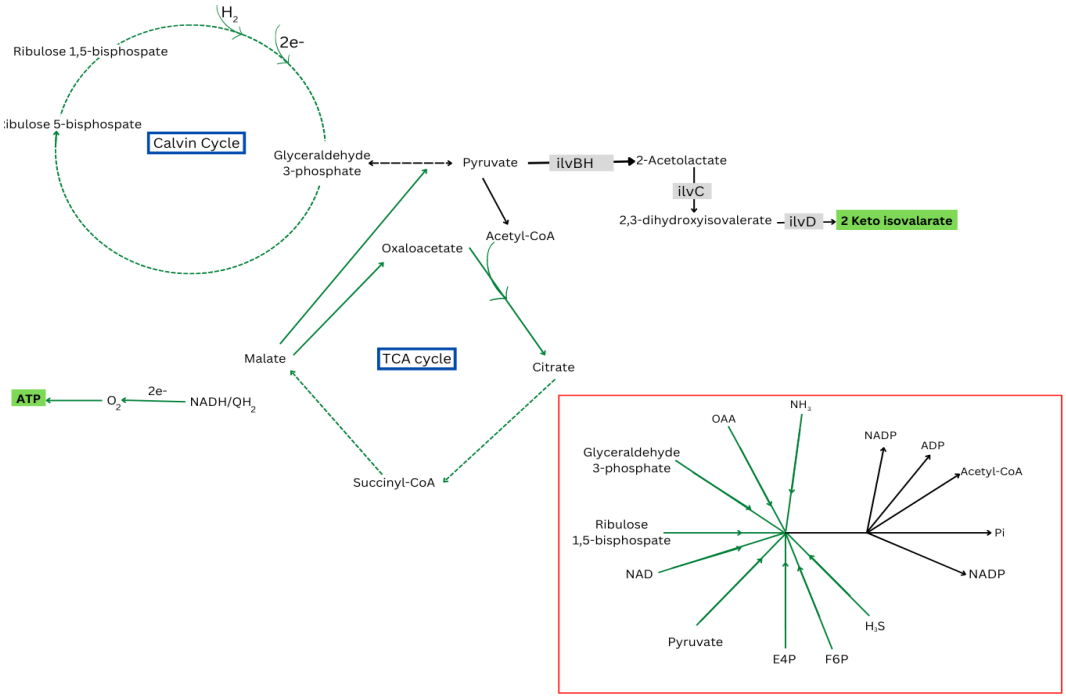

Figure 5.2. A biochemical network displays the production of 2-keto-isovalerate in C. necator H16, a microbial cell factory, by converting CO_2 and H_2 into pyruvate using the Calvin cycle and Krebs cycle and subsequently changing the carbon flow from pyruvate to 2-keto-isovalerate via valine synthesis. The native genes are shown in grey, and the biomass equation is marked in red.

2-ketoisovalerate is an important precursor molecule for biofuel production [237]. 2-ketoisovalerate is produced from pyruvate (from glycolysis) via the valine bio-synthesis pathway [238]. Figure 5.2 illustrates a simplified representation of the production of 2-keto-isovalerate within the microbial cell factory, C. necator.

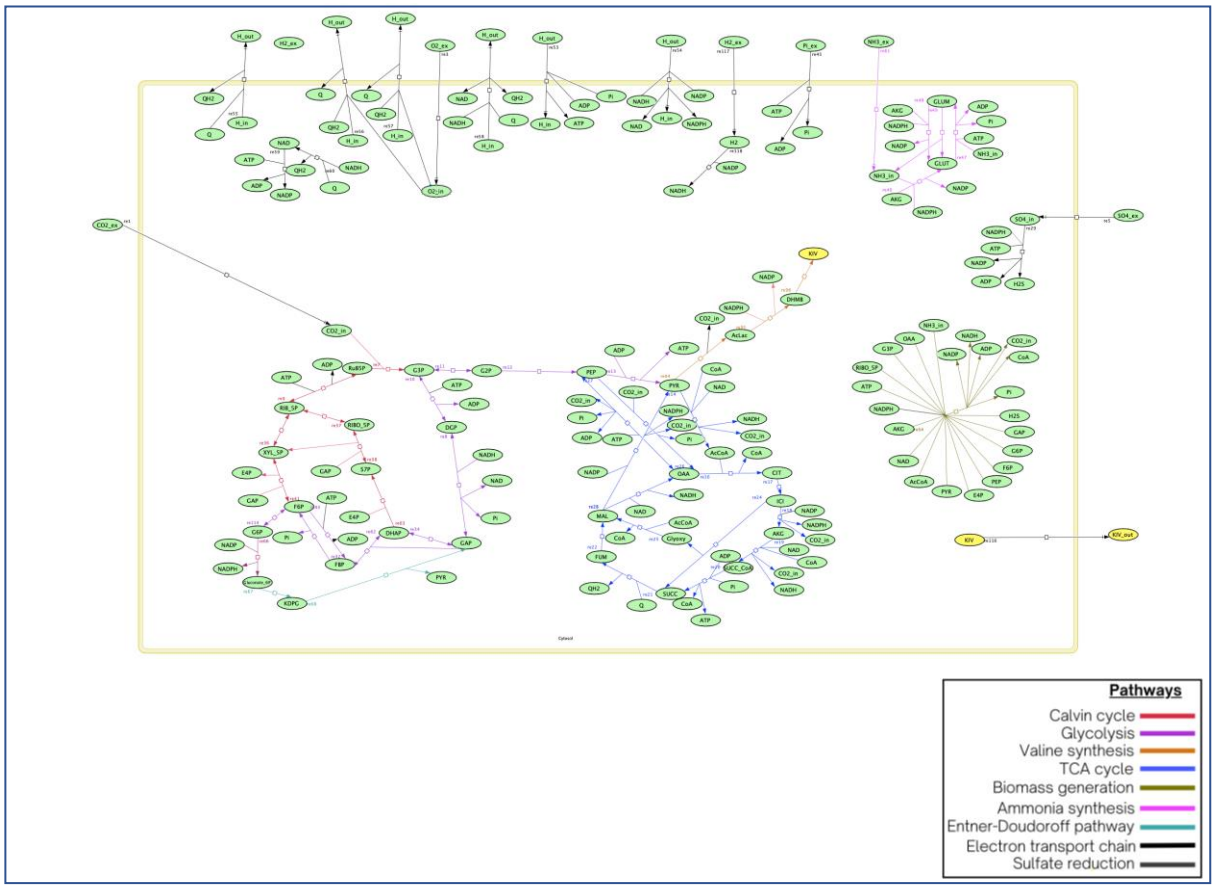

Figure 5.3. Cell Designer simulation of key central metabolism reaction pathways involved in aerobic gas fermentation of H_2 and CO_2 to 2 keto-isovalerate (KIV). The legend indicate the different pathways and how they are connected to each other.

This process involves the conversion of CO_2 and H_2 into pyruvate through the Calvin and Krebs Cycles (already described in sections 2.5.4 – 2.5.8 respectively), subsequently rerouting the carbon flow from pyruvate to 2-keto-isovalerate.

Figure 5.3 depicts central metabolic routes as simulated and designed in Cell Designer software. The full detailed simulation information including nomenclatures can be found in Appendix 3.

The yellow rectangle (cell membrane) denotes that the cells on the outside are extracellular media, whilst everything inside the cell is referred to as the cytosol.

The arrows contain structural information about the reactions which is very useful in the next step of modelling these biochemical reactions in OptFlux to determine the oxygen uptake rates. Lines with arrows at each end indicate a reversible reaction. Transport reactions can also be observed when cell strains move in and out of the microbial cell factory via electron transport chain (already discussed in section 2.5.9). Extra-cellular ammonia, phosphate, oxygen, nitrates, hydrogen and CO_2 are incorporated into the cell to be able to make biomass. In this model, node re64 (gold line) shows the biomass equation which comprises everything needed to build the cell mass defined on the input side of the equation. The products from utilizing the cell mass are defined as the output.

The biomass generated acts as the bio-catalyst for the whole fermentation process. The model in Cell Designer incorporated essential pathways like the TCA cycle (shown in blue), glycolysis (dark purple line), the Calvin cycle (red line), and valine synthesis (orange line), along with their corresponding fluxes. These pathways were covered in Section 2.5.4 to 2.5.9, the cell marked in yellow represents the desired product, KIV, which plays a crucial role in valine synthesis. Within this model, valine synthesis is regulated to conclude at the generation of KIV. Notably, the model shows that KIV is exported from the cell to prevent excessive accumulation, a factor that could impede the overall biochemical process.

5.2.3 OptFlux simulation: Model and applied constraints

The biochemical pathways modelled in Cell Designer were exported as an XML file to be used in OptFlux software. OptFlux is an open-source platform which is used for the computation of metabolic engineering including FBA. OptFlux model was employed to determine the coefficients of the stoichiometry to be used in our conversion reactor in HYSYS which will in turn inform our overall TEA for C_4 heat-integrated process.

All simulations of strains and wild-type models were performed using OptFlux v3.4. The singular carbon source employed was CO_2. The environmental conditions section provides the opportunity to implement simulation constraints. In our simulation, the minimum and maximum uptake rates for CO_2 were set at -1000 mmol $gDCW^{-1}$ h^{-1} and 10000 mmol $gDCW^{-1}$ h^{-1}, respectively. The lower limit for exchange reactions involving other medium components ($NH3^{+}$, $PO4^{3-}$, O_2, and Pi) was established at -1000 mmol $gDCW^{-1}$ h^{-1}, while the upper limit was set at 1000 mmol $gDCW^{-1}$ h^{-1}. The biomass cell equation (re64) as can be seen in Figure 5.3 was maintained at a constant value of 0.05 mmol $gDCW^{-1}$ h^{-1}. These ranges were set to encompass a broad spectrum of potential uptake scenarios. The lower limit was established to account for the minimum feasible uptake of CO_2 for instance by the strains. Conversely, the

upper limit was set to a higher value to allow for the exploration of elevated CO_2 uptake rates that might occur under certain favourable conditions or genetic modifications. This range was aimed at providing a comprehensive view of the potential uptake capabilities and behaviours of the simulated organisms in response to varying environmental conditions.

5.3 Results and discussions

The wild-type model was simulated using parsimonious Flux Balance Analysis (pFBA), which predicts metabolic flux patterns at a steady state using linear programming. pFBA constraints were chosen because it introduces a small improvement over normal FBA according to Lewis et al [239]. The results of the simulation can be seen in Table 5.1.

Table 5.1. Summary of gas fermentation simulation results in Cell Designer.

Metabolite Name	**Values (mmol gDCW^{-1} h^{-1})**
NH_3_ex	0.05
H_2 _ex	49.9
CO_2 _ex	10.9
SO_4_ex	0.05
O_2 _ex	9.7
KIV_ex	4.4

As can be seen from the simulation results, the H_2:CO_2 molar ratio uptake rate is at 5:1 which is in close agreement with experimental findings [240] [45].

Also, the CO_2:O_2 molar uptake ratio is approximately 1:1 which is in close agreement with the reported experimental work [241]. The specific demand for H_2 as an electron donor and O_2 as an electron acceptor is reflected in the molar ratios of H_2 and O_2 intake to CO_2 uptake and O_2 intake to CO_2 uptake.

5.3.1 Mass and energy balance: Oxygen Transfer

In oxygen-dependent biological processes, oxygen transport often presents a significant challenge. Although most nutrients vital for cell development and metabolic actions readily dissolve in water, providing an adequate supply in a thoroughly blended bioreactor, the restricted solubility of oxygen in aqueous solutions renders oxygen transfer a limiting aspect for peak performance and the scaling-up of biological systems. A lack of sufficient oxygen can greatly impact cell growth and hinder overall efficiency [242].

$$\frac{dC_o}{dt} = k_L a(C_o^* - C_o) - Q_o X \qquad \text{Eqn 5.1 [243]}$$

Where dC_o= Change in oxygen concentration over time, dt

k_La = Overall mass transfer coefficient

C_o^* = concentration of saturated O_2

C_o = the concentration of O_2 present in the liquid

C_o is determined by three variables since C_o^* is constant at a set air pressure. These are cell concentration X, the volumetric mass transfer coefficient, k_La, and the specific oxygen absorption rate Qo, which is dictated by the biological system.

In this model, the calculation for k_La was derived through the following expressions:

The equation for k_La is represented as:

$$k_La = \frac{O_2}{LMCD} \quad \text{Eqn 5.2}$$

Here the Log mean concentration difference (LMCD) was determined using:

$$LMCD = \frac{(A-C)-(B-C)}{In(\frac{A-C}{B-C})} \quad \text{Eqn 5.3}$$

where A, B, and C denote O_2 inlet saturation, outlet saturation and broth dissolved O_2 concentration respectively.

Values of A and C were set as 21 (mmol/L) and 0 respectively. And B was calculated with the following formula:

$$B = X \times P \times H, \quad \text{Eqn 5.4}$$

where X, P, and H denote headspace oxygen concentration, back-pressure and Henry's law constant.

In the presence of high cell concentrations, a biological system can face a significant shortage of oxygen. This situation is further aggravated by the reduction of the oxygen transfer coefficient as cell density increases. As the volumetric mass transfer coefficient (k_La) plays a crucial role in providing oxygen to the medium, ensuring an adequately high k_La is a vital aspect of bioreactor design [242].

Several studies have looked at how oxygen transport or concentration affects fermentation process [244]–[246]. The amount of oxygen dissolved in a solution is typically maximized by increasing the oxygen transfer rate (OTR). When the dissolved oxygen level dips beneath the critical threshold, it influences the growth rate and becomes a limiting factor in aerobic fermentation processes. Traditional stirred-tank bioreactors achieve elevated oxygen transfer

rates through intensified mechanical mixing, accelerated gas flow, or the distribution of smaller vapor bubbles [242].

5.3.2 Methods: Mass and energy balance estimations

In the present study, the OptFlux simulation results were utilized to calculate the mass-energy balance of bioreactors, taking into account oxygen transfer limitations. The results of this calculation informed the TEA of a C_4 heat-integrated route conversion reactor.

The simulation took into account various parameters such as oxygen transfer limitations, dilution rate, design O_2 uptake rate, specific uptake rate, CO_2/O_2 Molar Uptake Ratio, H_2/O_2 uptake ratio and Downcomer to Riser Diameter Ratio. These parameters are crucial for the proper functioning of a bioreactor and their inclusion in the simulation ensured that the results obtained were accurate and reliable.

Table *5.2* and Table 5.3 shows the inputs and outputs for the TEA of the gas fermentation. Results from the Cell Designer and OptFlux simulations were utilized as inputs.

Both modelling in Cell Designer and OptFlux simulation resulted to the determination of the following key reaction(including reaction coefficients) which is incorporated in modelling our HYSYS bioreactor conversion reactor:

$$61.876\ CO_2 + 1.684\ NH_3 + 60.39\ 65O_2 + 255.573\ H_2 \rightarrow$$
$$11.028\ C_5H_8O_3 + 1.684\ C_4H_7O_2N + 208.093\ H_2O \qquad \text{Eqn 5.5}$$

More so, for the gas fermentation simulation, a typical $500m^3$ Loop Bioreactor was considered. Beside determining the intensity of our conversion reactor(stoichiometric coefficients) in for HYSYS simulation, the oxygen transfer limitation was also used to determine the number of $500m^3$ fermenters required and subsequently feed in to our C_4 TEA modelling. The use of an Object Linking and Embedding Database (OLE DB) connection between Aspen HYSYS and the EXCEL sheet allowed for an accurate calculation of oxygen uptake rates.

Table 5.2. TEA inputs for bioreactor (C_4 process routes).

Plant Section	Input Parameter	Heat integrated	Non-heat integrated	Unit	Comments
Overall Process	Product Molecular Weight	116.12	116.12	[g/mol]	
	Product Number of Carbons	5	5	[-]	

Plant Section	Input Parameter	Heat integrated	Non-heat integrated	Unit	Comments
	Production Days	350	350	[days]	Two-week annual shutdown
Fermentation	Number of trains	4	1	[-]	Seed + Main Fermenter
	Production Fermenter Vessel Volume	500	500	[m3 vessel volume]	
	Aspect Ratio (Downcomer)	10	10	[-]	
	Downcomer to Riser Diameter Ratio	1.5	1.5	[-]	
	Carbon source Utilisation	95	95	[%]	
	Headspace O_2 Concentration	4	4	[%] (v/v)	
	Design oxygen Uptake Rate (OUR)	250	245	[(mmol O_2)/(L·h)]	
	Specific O_2 Uptake Rate	9.8	9.8	[(mmol O_2)/((g DCW)·h)]	O_2 limiting conditions
	CO_2/O_2 Molar Uptake Ratio	1.102	1.102	[-]	
	H_2/O_2 uptake ratio	5.092	5.092	[-]	
	NH3/O_2 Molar Uptake Ratio	0.005	0.005	[-]	
	Carbon fraction of microorganism on DCW basis	0.480	0.480	[-]	
	Molar Yield				
	Product	0.44	0.44	[(C mol Product)/(mol H_2)]	
	Recirculation Re in Downcomer	2.50E+05	2.50E+05	[-]	Turbulent flow
	Recirculation Overall dP	25	25	[kPa]	Low-pressure drop across structured packing internals
	Turn-around Time	12	12	[h]	
	Approach to pseudo-steady state productivity	24	24	[h]	
	Production Fermenter pseudo-steady state operation	4	4	[weeks]	

Table 5.3. TEA outputs for bioreactor (C_4 process routes).

Plant Section	Output Parameter	Heat-integrated	Non-heat integrated	Unit
	Total Air Compression Duty	4355.42	1073.58	[kW]
Fermentation	$k_{LA}(O_2)$, mass transfer coefficient	329.72	323.13	[1/h]
	Product			
	Productivity	2.78	2.73	[(g Product)/(L·h)]
	Concentration	92.80	90.94	[(g Product)/L]
	Seed fermenter dimensions			
	Downcomer Diameter	1.64	1.64	[m]
	Riser Diameter	1.09	1.09	[m]
	Height	16.40	16.40	[m]
	Heat Transfer Area	42.22	41.38	[m2]
	Production fermenter dimensions			
	Downcomer Diameter	3.53	3.53	[m]
	Riser Diameter	2.35	2.35	[m]
	Height	35.32	35.32	[m]
	Heat Transfer Area	422.22	559.79	[m2]

In addition to the parameters mentioned above, other key variables such as the dilution rate and the design O_2 uptake rate were also taken into account while conducting the simulation. The dilution rate is an important parameter as it determines the rate at which new medium is added to the bioreactor, while the design O_2 uptake rate is used to calculate the amount of oxygen required to sustain the bioreactor.

The specific uptake rate, CO_2/O_2 Molar Uptake Ratio, H_2/O_2 uptake ratio and Downcomer to Riser Diameter Ratio were also used to determine the k_La and the dimensions of the bioreactors. These parameters are crucial for the proper functioning of the bioreactor and their inclusion in the simulation ensured that the results obtained were accurate and reliable.

The oxygen uptake rates for the bioreactor were determined by the difference between the O_2 molar flow rate and off-gas molar rate. The full details of the mass-energy balance for the bioreactor can be found in Appendix 1.

Since a loop bioreactor was assumed, the diameters of the riser and the downcomer sections were calculated in the mass-energy balance. This is crucial for cost estimations of the bioreactor, including capital cost calculations. The riser and downcomer diameters were costed

as towers. This information is important for cost optimization and determining the overall feasibility of the bioreactor design.

5.4 Conclusion

This chapter detailed a modelling and simulation study aimed at comprehending the intricate metabolic networks within aerobic gas fermentation of CO_2 and H_2, utilizing Cupriavidus necator as the cell factory. The focus was on the production of keto-isovalerate, a key intermediate for SAF production, through valine synthesis pathway.

The use of Cell Designer proved invaluable, allowing the translation of diagrammatic representations into SBML and simplifying the modelling of biochemical networks. Unlike ASPEN HYSYS, which lacks consideration of comprehensive biochemical pathways, Cell Designer simulations allowed for detailed modelling of essential biochemical pathways like glycolysis, the pentose phosphate pathway, the TCA cycle, and oxidative phosphorylation.

The exported model from Cell Designer was utilised in the pFBA simulation in OptFlux, providing key insights into metabolic flux patterns in the biochemical networks. The results demonstrated the H_2:CO_2 and CO_2:O_2 molar uptake ratios, aligning closely with reported experimental data. These ratios underscored the specific demands for H_2 as an electron donor and O_2 as an electron acceptor within the simulated biological system.

The study also addressed oxygen uptake associated with the biological processes, presenting equations utilised to calculate the oxygen transfer coefficient (k_{La}) critical for bioreactor design. Mass and energy balance estimations, incorporating OptFlux results, contributed to the overall techno-economic assessment of the C_4 heat-integrated conversion reactor modelled using ASPEN HYSYS.

More so, the simulations enabled the determination of essential parameters for the bioreactor, including key reaction stoichiometry and coefficients. This information, along with oxygen transfer limitations, played a role in estimating the number of fermenters required and subsequent integration into the C_4 route-to-SAF TEA modelling.

Integration of Aspen HYSYS and Excel via OLE DB, facilitated precise oxygen uptake calculations which is pivotal for bioreactor design and cost estimation. The detailed mass and energy balance calculations, including the determination of riser and downcomer diameters, contribute significantly to the feasibility assessment and cost optimization of the bioreactor design.

The modelling and simulation approach, integrating Cell Designer, OptFlux, and Aspen HYSYS, shed light on the complex metabolic networks and oxygen transport dynamics within the aerobic gas fermentation, laying essential groundwork for the overall C_4 route-to-SAF process evaluation. The detailed findings, stoichiometric coefficients, and reactor design parameters will be utilized in simulating the gas fermentation of CO_2 and H_2 conversion reactor in the proposed C_4 route-to-SAF detailed in Chapter 6.

CHAPTER 6.

PROCESS AND TEA MODEL OF BIO JET FUEL PRODUCTION VIA C_4 ROUTE

The C_4 route in this study refers to the utilization of isobutanol as the precursor for SAF production. This chapter will present a comparison of the process and cost between the C_4 heat-integrated and non-heat integrated process routes for SAF production. It will highlight the differences in costs and process performance, comparing the capital investment, FOC, yearly variable costs, and NPV between the two processes. The chapter will also conduct sensitivity analyses on input variables such as ISBL and OSBL costs, electricity price, and price of kerosene, to determine their impact on the NPV of the heat integrated process. The findings will be used to evaluate the potential benefits and drawbacks of heat integration for jet fuel production, and to provide insights for designing and operating a heat-integrated process for this purpose.

6.1 Difference between non-heat and heat-integrated C_4 routes

Process modelling with Aspen HYSYS v12 provided the foundation for the plant's mass and energy equilibrium calculations. Non-heat and heat-integrated C_4 routes were used as case studies.

In the context of this study, the C_4 non-heat-integrated route-to-SAF refers to the process where no heat integration is applied between the bioreactor process streams and SCWG reactor for SAF production, while the heat-integrated C_4 route-to-SAF refers to a process where this heat integration exists between both streams. Both C_4 pathways to SAF share the same process especially in the downstream process, however, the key distinction is that the heat-integrated approach, employs an isopentane-based heat pump to connect the low-temperature exothermic gas fermentation and high-temperature endothermic SCWG, as proposed in [45]. This integration reduces the cooling water cost for the bioreactor in the C_4 heat-integrated route. In contrast, this heat-integration approach is absent in the non-heat integrated C_4 route to SAF production. In effect to that, the non-heat integrated process entails the additional costs of bio-reactor cooling duty and also the air compression. As for the C_4 heat-integrated process, it is able to fully compensate for the compressor duty by utilizing the electricity generated from the high-pressure gas product of the SCWG reactor. As a result, this increases the overall energy efficiency of the process. Figure 6.1 and Figure 6.2 highlight these major differences focusing on the bio-reactors HYSYS simulation section of both processes.

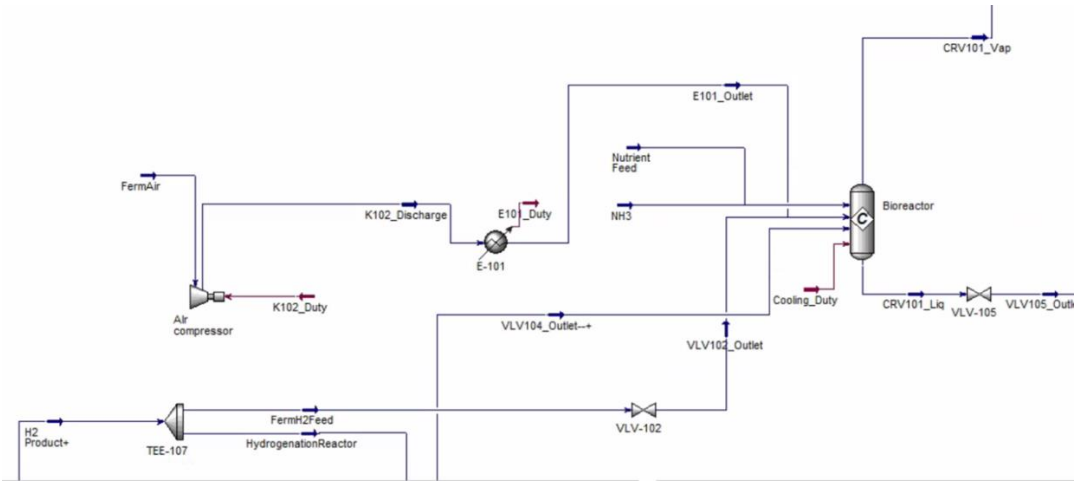

Figure 6.1. C_4 non-heat integrated bioreactor HYSYS simulation section displaying the air compressor duty and cooling duty.

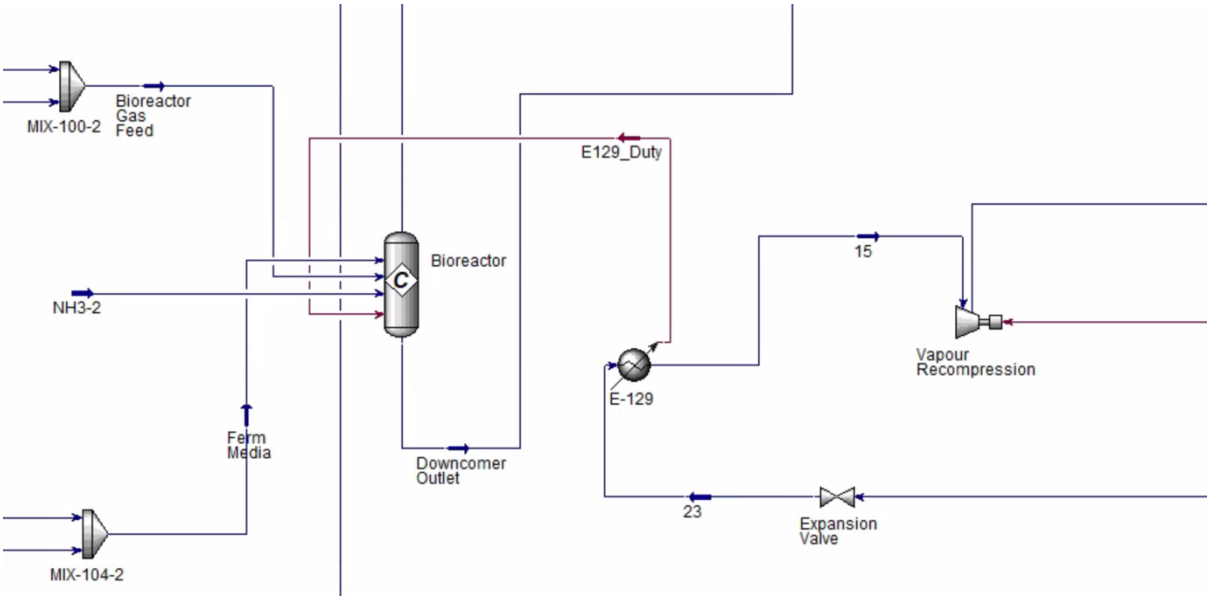

Figure 6.2. C_4 heat integrated bioreactor HYSYS simulation section showing the use of vapour recompression for heat-integration between the bioreactor and methanation reactor.

6.2 Simulation approach and study for both C_4 routes

The modelling and simulation approach is similar to that of C_2 route-to-SAF process already discussed in section 3.1. The primary distinction lies in the utilization of pot ale draft, instead of black liquor, as feed for the supercritical water gasification to produce CO_2 and H_2 required in the aerobic gas fermentation reaction. Pot ale draft, a by-product from Scotch whisky

distillation, is preferred due to its availability stemming from the substantial whisky production in the UK, where both proposed C_4 route-to-SAF plants are assumed to be situated [247].

For both C_4 routes-to-SAF, the stoichiometric equation derived from the gas fermentation modelling in chapter 5 will be applied to simulate the bioreactor using ASPEN HYSYS. Both the upstream and downstream processes of both routes will be examined. It is important to note that the downstream processes for both C_4 routes are identical.

Figure 6.3 presents a general simplified flow diagram of SAF (C_{16}) production via both C_4 routes, highlighting the various sections of the SAF plant. Full details of the HYSYS simulation process flow can be seen in Appendix 1 including the mass-energy balance. A summary of the different operating units associated with the plant modelling is presented in Table 6.1.

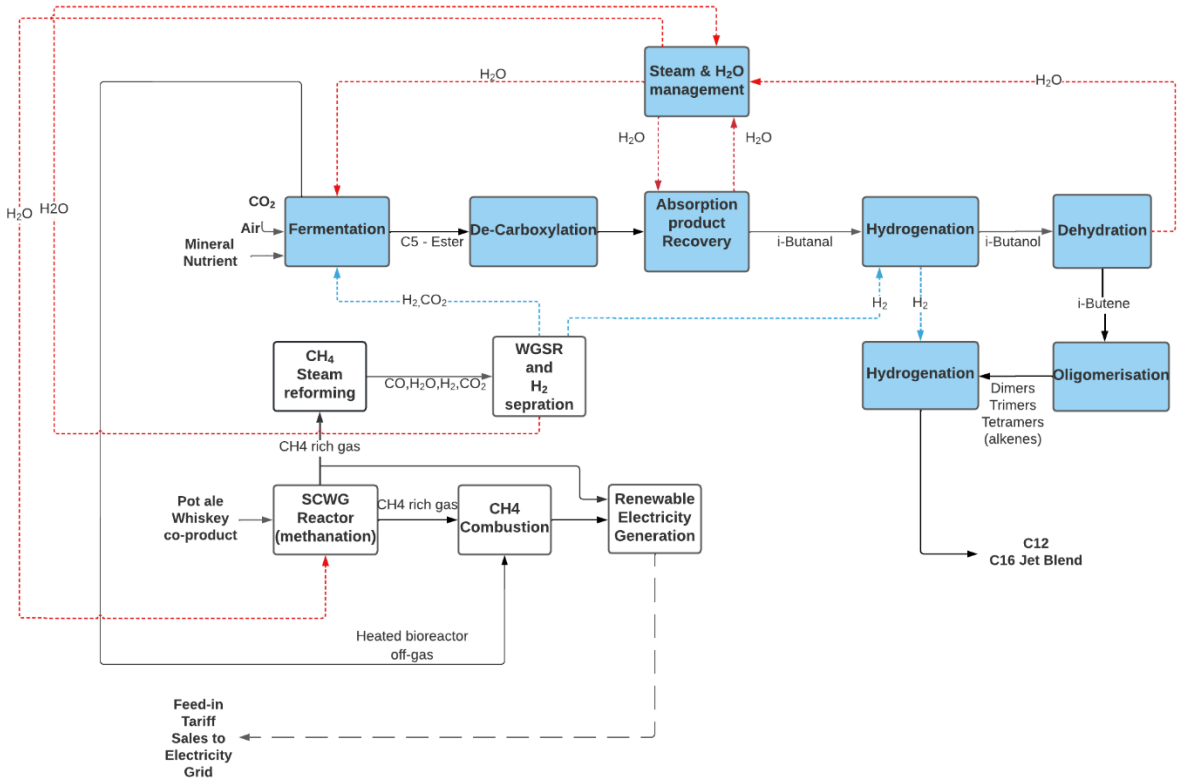

Figure 6.3. A simplified C_4 process flow for the production of renewable C_{16} jet-fuel blend and C_{24} diesel blend.

Table 6.1. Plant section unit operations – C_4 heat and non-heat-integrated route-to-SAF.

Plant division	**Operating units**	**HYSYS package used**
Preliminary processing of feed materials	Supercritical water gas reactor, Combustion chamber and turbine, heat pump condenser and compressor.	LKP
Gas fermentation	A centrifuge, pumps, seed bioreactors, and production bioreactors employed in the bioreactor system.	LKP
Reaction sections	Iso-butanal hydrogenation reactor, Iso-butanol dehydrogenation reactor, isobutene oligomerisation and hydrogenation reactors.	UNIFAC
Product recovery	Iso-butanal recovery, water stripper and removal columns, distillation columns	UNIFAC
Steam and water management	Mechanical vapour compressors, water and steam heat exchangers	LKP

6.2.1 Non-heat-integrated C_4 route-to-SAF: Upstream process simulation

Figure 6.4 illustrates the downstream process of the non-heat-integrated route-to-SAF process. Just like in the C_2 route-to-SAF process simulation, Lee-Kesler-Plocker equation of state was used to model the thermodynamic properties of the process fluids due to its accuracy for high-pressure gases [160] in ASPEN HYSYS.

The simulation begins with wet draft pot ale draft at 20^{o}C and water make-up, which are mixed together. Pot ale draft was represented and modelled as glycerol ($C_3H_8O_3$) in ASPEN HYSYS and fed at 14,000 kg/h at atmospheric pressure and diluted with about 21,000 kg/h of make-up water. The glycerol stream is then pressurized to about 24 MPa by a high pressure pump (PC4-16). This stream is then heated to 376^{o}C by several heat exchangers before entering the SCWG reactor (RC4-10). The SCWG uses the same biomass conversion as the C_2 route-to-SAF process simulation, but the reaction is modified for methanation in the C_4 case. This is achieved by assuming a nickel-based catalyst and lowering the reaction temperature [248]. It is worth noting that methanation reactions typically occur between 200^{o}C and 550^{o}C [249]. The reactor was simulated as a horizontal plug-flow reactor in HYSYS. The SCWG of glycerol produces methane, CO_2 and water, as shown in equation 6.1.

$$4C_3H_8O_3 \rightarrow 7CH_4 + 5CO_2 + 2H_2O \quad \Delta H° = -1.6e^5 KJ/Kgmole \qquad \text{Eqn 6.1}$$

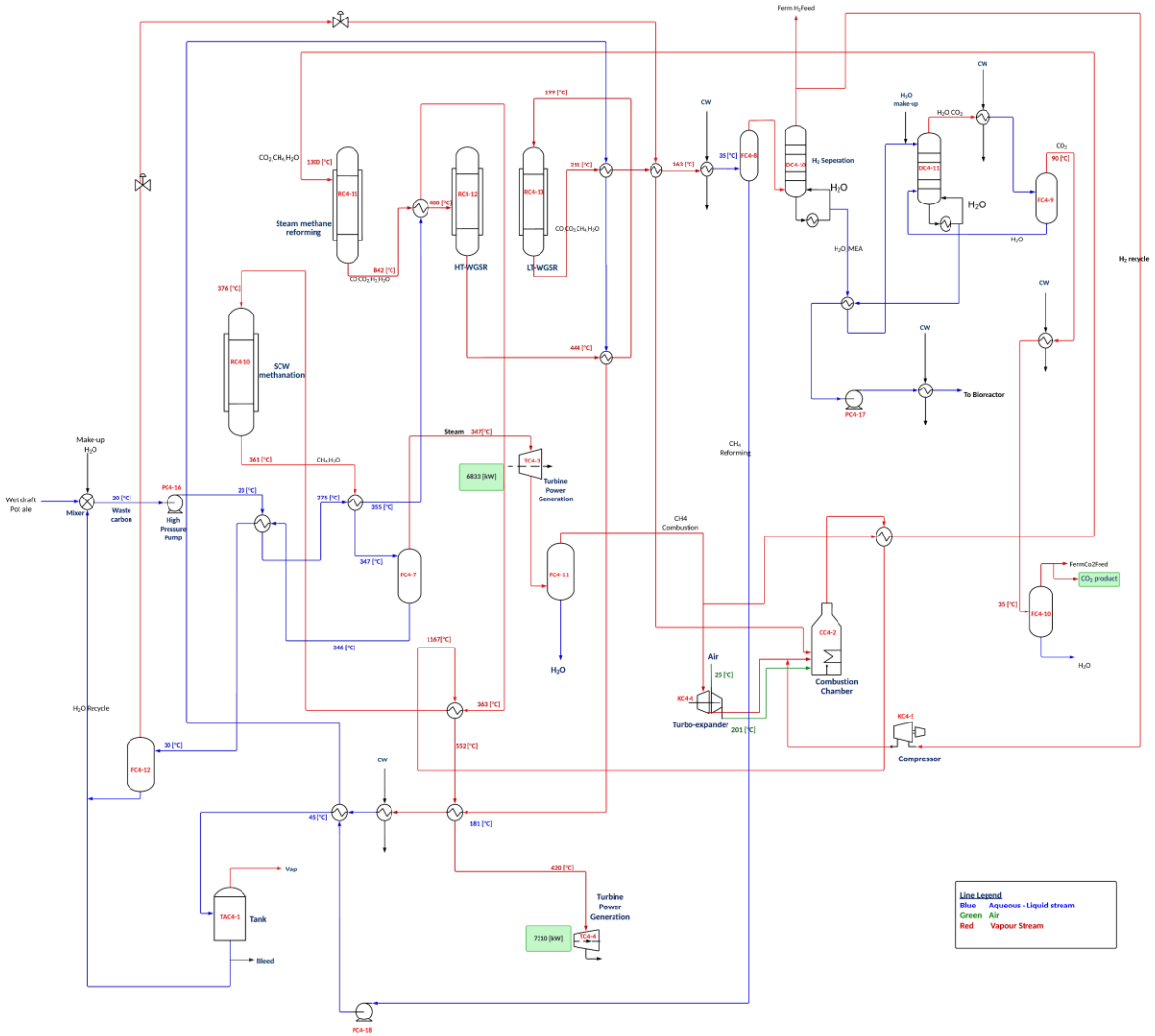

Figure 6.4. Conceptual upstream C_4 non-heat-integrated route-to-SAF process route: Showing the SCWG of pot ale draft for H_2 and CO_2 production required for aerobic gas fermentation. Also showcases the generation of renewable electricity within the SAF plant.

The products exit RC4-10 at 361°C and go to a flash drum (FC4-7) where water is separated and recycled to be used as water make-up for pot ale draft. Methane and CO_2 leave the top of FC4-7 at 347°C and 24 MPa and generate about 6833 kW of electricity through a gas turbine (TC4-3). The gas stream leaves the turbine at a lower temperature of 167°C and water is removed from it by a flash drum (FC4-11). The gas stream from the top of FC4-11 is split into two streams. One stream is sent to a turbo-expander (KC4-4) for CH_4 combustion. The combustion occurs in a combustion chamber, which was simulated as a conversion reactor with the following equations:

$$CH_4 + 2O_2 \rightarrow CO_2 + 2H_2O \qquad \Delta H° = -1.8e^5 KJ/Kgmole \qquad \text{Eqn 6.2}$$

The combustion products leave the reactor at 1390°C and 379 kPa and are cooled to up to 420°C by a network of heat exchangers. This stream is then used to generate additional 7310 kW of electricity in a gas turbine. The other stream containing mostly CH_4 from FC4-11 is directed to a methane reforming reactor (RC4-11) for syngas production. The methane reforming reactor was simulated as a plug-flow reactor operating at 1300°C and 1000 kPa. The reactions used to simulate these are as follows:

Methane reforming:

$$CH_{4(g)} + H_2O_{(g)} \rightarrow 3H_{2(g)} + CO_{(g)} \qquad \Delta H° = 2.06e^5 \text{ KJ/Kgmole} \qquad \text{Eqn 6.3}$$

$$CO_{(g)} + H_2O_{(g)} \rightarrow H_{2(g)} + CO_{2(g)} \qquad \Delta H° = -4.1e^4 \text{ KJ/Kgmole} \qquad \text{Eqn 6.4}$$

$$CH_{4(g)} + 2H_2O_{(g)} \rightarrow 4H_{2(g)} + CO_{2(g)} \qquad \Delta H° = 1.6e^5 \text{ KJ/Kgmole} \qquad \text{Eqn 6.5}$$

The water gas shift reaction (WGSR) is a moderately exothermic reaction involving an equimolar mixture of steam and carbon monoxide and is a critical step in the reformation process as it promotes the production of H_2 gas, which is necessary for the overall process. WGSR along with the reformation reactions was simulated with two additional plug-flow reactors: High-temperature (HT) and Low-temperature (LT) WGSR. The product stream from methane-reforming leaves the reactor (RC4-11) at 842°C and is cooled to 400°C before entering RC4-12 for the HT-WGSR. HT-WGSR is used to adjust the H_2 : CO ratio by converting more CO to CO_2 and thus lowering the CO content in syngas [250]. Equation 6.6 shows the reaction used to simulate HT-WGSR in a plug-flow reactor.

H-T WGSR at 400°C:

$$CO_{(g)} + H_2O_{(g)} \rightarrow H_{2(g)} + CO_{2(g)} \quad \Delta H° = -4.14e^4\ KJ/Kgmole \qquad \text{Eqn 6.6}$$

The product stream from HT-WGSR is cooled down to about 199°C and enters RC4-13 for a LT-WGSR. LT-WGSR is used to further reduce the CO content in syn gas and for high H_2 selectivity [250]. Equation 6.7 shows the reaction used to simulate LT-WGSR in a plug-flow reactor.

L-T WGSR at 198°C:

$$CO_{(g)} + H_2O_{(g)} \rightarrow H_{2(g)} + CO_{2(g)} \quad \Delta H° = -4.14e^4\ KJ/Kgmole \qquad \text{Eqn 6.7}$$

The product stream from RC4-13 at 211°C is cooled to about 35°C and water is removed by a flash drum (FC4-8). The water is then recycled to the water make-up mixer. The vapour stream of H_2 and CO_2 from the top of FC4-8 is sent to an absorber column (DC4-10) where H_2 is separated from the top and used as fermentation feed for the bioreactor. Some of the H_2 is also recycled and sent to the combustion chamber by a compressor (KC4-5). The bottom of DC4-10 contains water and monoethanolamine (MEA) [251], which is used to separate H_2 from CO_2. The MEA solution from the bottom of the column is taken to another reboiler absorber (DC4-11) column for regeneration and then recycled back to the H_2 gas separation column after removing the CO_2 gas by a separation tank (FC4-9). The reboiler absorber also uses column water makeup. The CO_2 stream from FC4-9 is cooled from 90°C to 35°C and goes to another flash drum (FC4-10) where CO_2 product is obtained and used as a feed for the fermentation. The fermentation process simulation is the same as the heat-integrated C_4 route-to-SAF case as will be presented in section 6.2.2.

6.2.2 Heat-integrated C_4 route-to-SAF: Upstream process simulation

Figure 6.5 shows the upstream process simulation of the C_4 heat-integrated route-to-SAF.

The thermodynamic properties of the process fluids were modelled using the Lee-Kesler-Plocker equation of state, which is known for its accuracy in modelling high-pressure gases [160].

The U-loop bioreactor (BC4-1) is modelled as a conversion reactor using CO_2 as the sole carbon source, H_2 as an electron donor, and O_2 as the electron acceptor. CO_2, H_2, air, and nutrient feed (BC4-2) are fed into the bioreactor's conversion reactor at 30°C. The exothermic reaction occurs at approximately 36°C and 400 kPa.

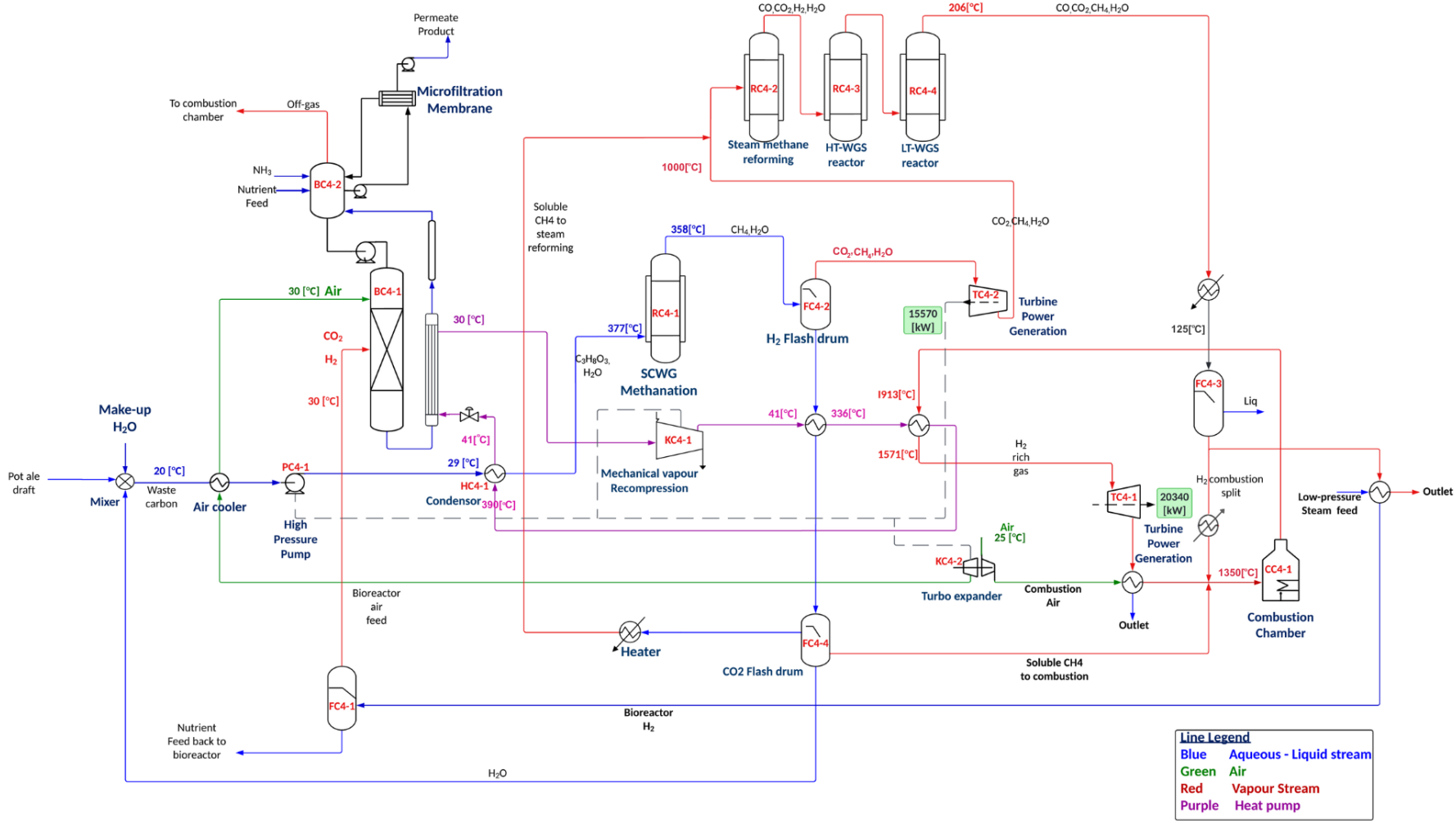

Figure 6.5. Conceptual upstream C_4 heat-integrated route-to-SAF process: Depicting the heat integration between SCWG of pot ale draft and the gas fermentation of CO_2 and H_2. Also showcases the generation of renewable electricity within the C_4 SAF plant.

The bioreactor conversion reaction was modelled based on the following reaction:

$$a\ H_2 + b\ CO_2 + c\ O_2 + d\ NH_3 \rightarrow e\ C_5H_8O_3 + f\ H_2O + g\ DCW \quad \text{Eqn 6.8}$$

Where $C_5H_8O_3$ represents α-keto-isovaleric acid. And a, b, c, d, e, f, g correspond to 255.573, 61.876, 60.397, 1.684, 11.029, 208.093, 1.684 respectively.

DCW (biomass) – $C_{47.5248}H_{6.9307}N_{13.8614}O_{31.6832}$

A portion of the downcomer stream from the bioreactor is recycled back, and heat is absorbed by the evaporator. This heat is then increased to approximately 366°C via a heat pump network for the SCWG reaction. The heat pump network, indicated by a purple line, uses isopentane as the carrier fluid. 10,800 kgmole/h of isopentane with an absorbed temperature of 30°C is introduced into the mechanical vapour recompression pump (KC4-1). It is compressed to about 41°C and further heated to around 390°C through a series of other heat exchangers. The i-pentane stream is then condensed via the condenser (HC4-1) to about 41°C.

Pot ale draft (at 14,000 kg/h), modelled as glycerol, is diluted with makeup water and passed through a high-pressure pump (PC4-1) operating at 27 MPa. This increases the pressure of the glycerol stream from 0.1 MPa to about 27 MPa. The stream is then heated up to about 377°C for the supercritical water gasification reaction via HC4-1. The SCWG uses the same biomass conversion as the C_2 route-to-SAF process simulation, but the reaction is modified for methanation in the C_4 case. This is achieved by assuming a nickel-based catalyst and lowering the reaction temperature [248]. The reactor, simulated as a horizontal plug-flow reactor (RC4-1) in HYSYS, produces methane, CO_2, and water, as already depicted in equation 6.1.

The products exit RC4-1 at 358°C and pass through two flash drums (FC4-2 and FC4-4) where water is separated and recycled for use as water makeup for SCWG feed. Soluble CH_4 from FC4-4 is also recycled back to RC4-2. The CH_4 and CO_2 stream exit the top of FC4-2 at 358°C and 27 MPa, generating approximately 15,570 kW of electricity through a gas turbine (TC4-2). The gas stream, primarily containing CH_4, exits TC4-2 at a lower temperature of 168°C and is heated to 1000°C before being introduced into the steam methane-reforming reactor (RC4-2) for syngas production. The methane reforming reactor is simulated as a plug-flow reactor operating at 1000°C and 1000 kPa, utilizing reactions similar to Equation 6.3 to Equation 6.5. WGSR reactions were simulated with two additional plug-flow reactors: High-temperature and Low-temperature WGSR. The product stream from methane-reforming leaves the reactor (RC4-2) at 632°C and is cooled to 400°C before entering RC4-3 for the HT-WGSR. Equation 6.6 already shows the reaction used to simulate HT-WGSR in a plug-flow reactor.

The product stream from HT-WGSR is cooled down to about 200^{o}C and enters RC4-4 for a LT-WGSR. Equation 6.7 already shows the reaction used to simulate LT-WGSR in a plug-flow reactor just as in the non-heat-integrated case.

The product stream from RC4-4 at 206^{o}C is cooled to about 125^{o}C and introduced to flash drum (FC4-3) for water removal. A portion of the vapour stream of H_2 and CO_2 (H_2 combustion split) from FC4-3 is sent to another flash drum (FC4-1) where H_2 is separated and exits at the top. This is recycled back and used as fermentation feed for the bioreactor. Moreso, the nutrient from the bottom is also fed to the bioreactor.

The remaining portion of the H_2 stream is directed to the combustion chamber (CC4-1) and heated to approximately 1350°C. Moreover, the turbo expander compressor (KC4-2) compresses the air at 25°C and 101 kPa to around 204°C and 400 kPa, also fed into the combustion chamber. The combustion chamber, simulated as a conversion reactor, assumes total conversion of the H_2 and O_2 to H_2O. The product exits the combustion chamber at 2399°C and 0.4 MPa, then cooled to about 1571°C, generating approximately 20,340 kW of electricity via the combustion turbine (TC4-1). This fulfils the plant's electricity needs, with any excess electricity being sold for supplementary income.

6.2.3 Heat and Non-heat integrated C_4 route-to-SAF: Downstream process simulation

As already mentioned in section 6.2, the downstream process of both C_4 cases are the same as can be seen in Figure 6.6 and Figure 6.7. The only difference is that the bioreactor section for the non-heat integrated process is in Figure 6.7.

Figure 6.6 shows the process simulation flow of the upgrading of the bioreactor's product to SAF. The bioreactor broth from BC4-1, which mainly comprises 2-ketoisovalerate, is heated to 85°C and sent to a decarboxylation reactor (RC4-5) via a pump (PC4-2). Typically, 2-ketoisovalerate generated by this pathway is decarboxylated into iso-butanal, an intermediate product, and subsequently transformed to isobutanol through alcohol dehydrogenase [155]. Haojie et al [236] also engineered Cupriviadus necator for isobutanol production via 2-ketoisovalorate.

RC4-5 is modelled as a plug flow reactor in ASPEN HYSYS operating at 85°C and 400 kPa.

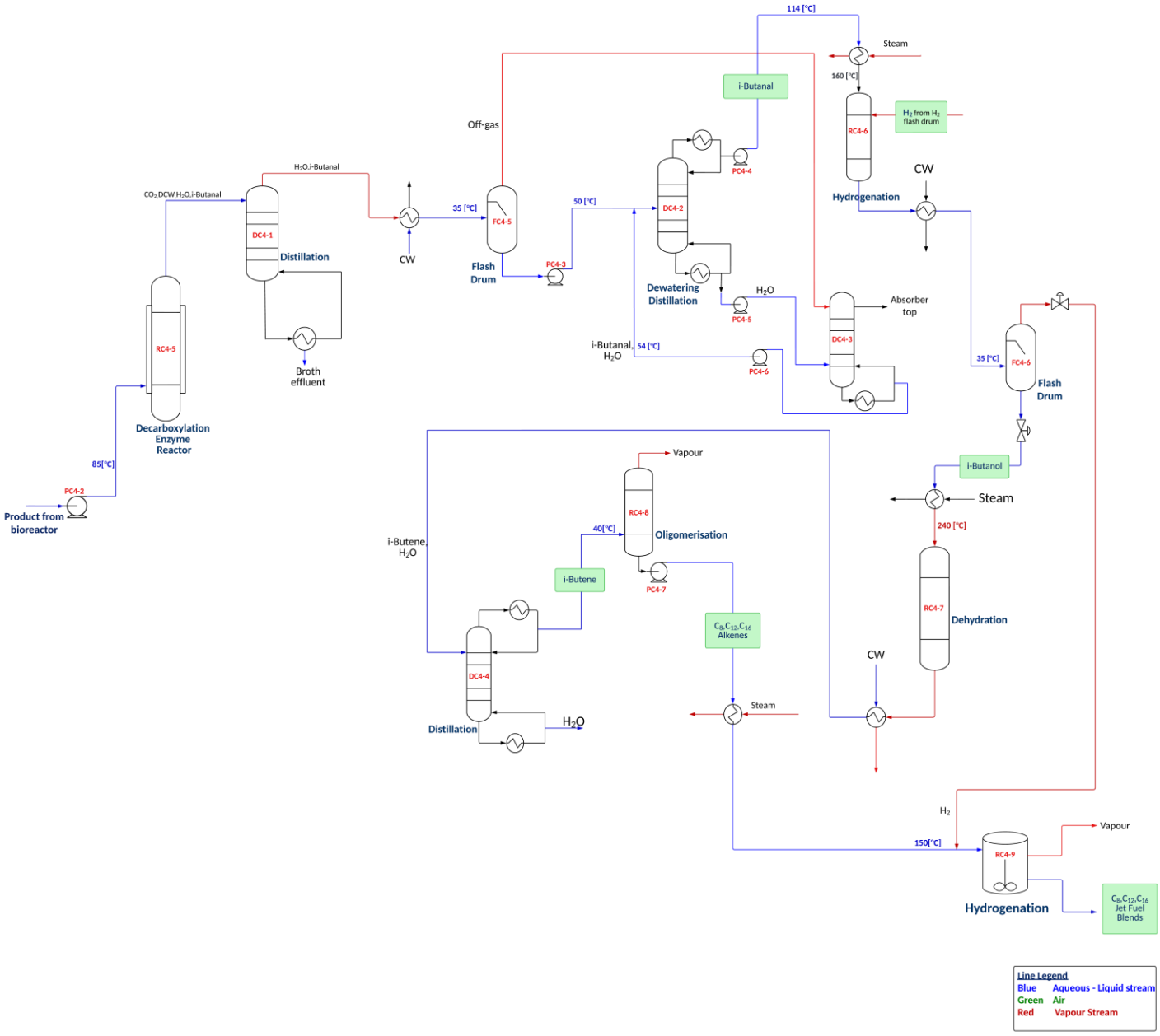

Figure 6.6. Conceptual downstream C_4 heat-integrated route-to-SAF process: showing the upgrading of aerobic gas fermentation product to C_{16} jet blend.

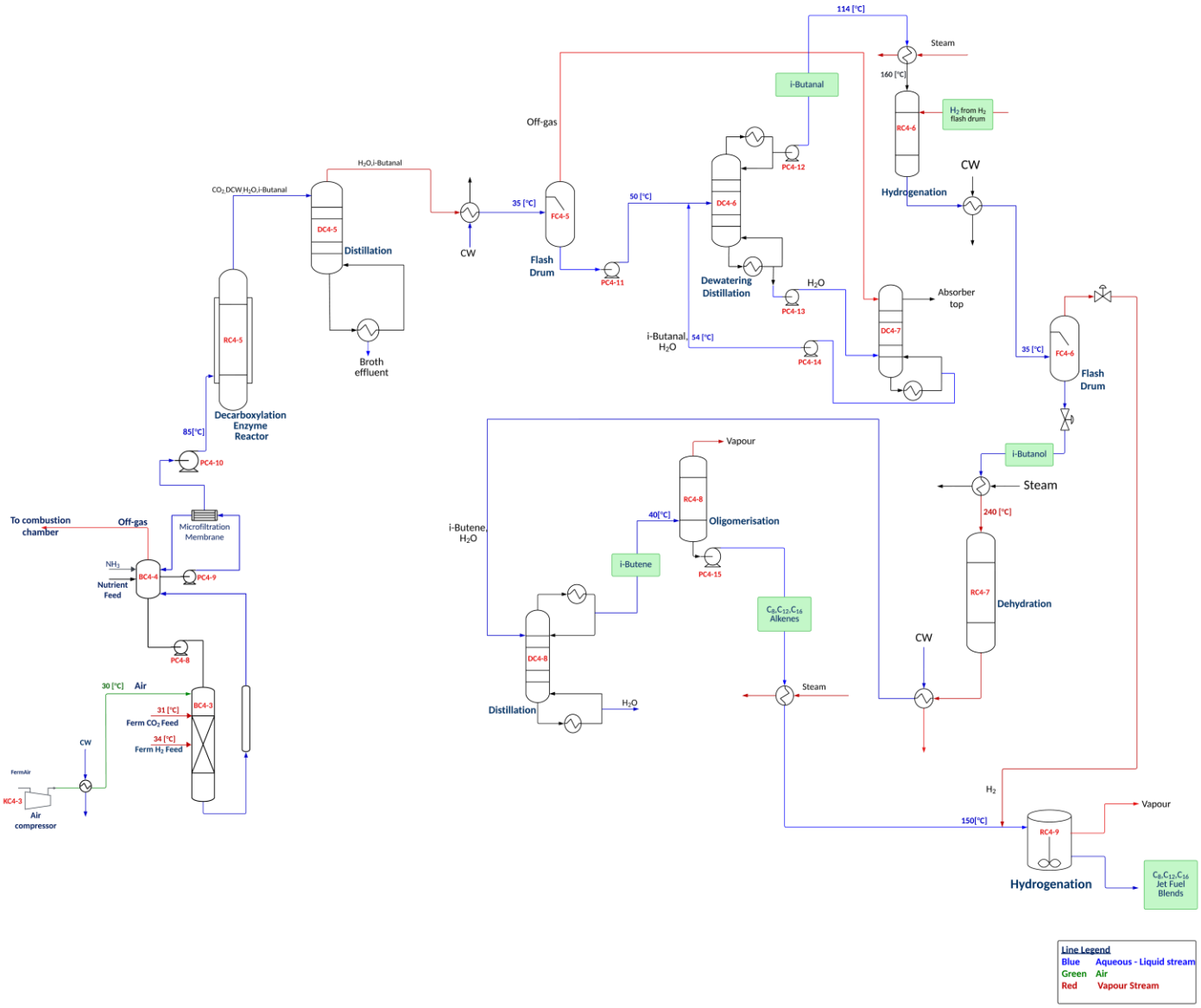

Figure 6.7. Conceptual downstream C_4 non-heat-integrated route-to-SAF process: showing the upgrading of aerobic gas fermentation product to C_{16} jet blend.

Equation 6.9 shows the reaction that was modelled in HYSYS for the decarboxylation of 2-ketoisovalerate:

$$C_5H_8O_3 \rightarrow C_4H_8O + CO_2 \qquad \Delta H° = -2.1e^4\ KJ/Kgmole \qquad \text{Eqn 6.9}$$

The resulting aqueous solution, comprising iso-butanal, CO_2, and residual biomass, exits RC4-5. Dewatering occurs via a reboiler absorber (DC4-1), separating the remaining effluent broth. The iso-butanal solution, exiting DC4-1 at 95°C, undergoes cooling to 35°C before entering a

separator tank (FC4-5) for further water and gas removal. To obtain a purer form of iso-butanal, a distillation column (DC4-2) is employed for separation. At 68°C, approximately 90% pure iso-butanal is obtained as the top product of the column and is subsequently pushed via a pump (PC4-4) to increase the pressure from 1.4 bar to 20 bar, thus matching the pressure of the hydrogen stream for the hydrogenation reaction. The downcomer from DC4-2, containing mostly water and unreacted 2-keto-isovalerate, is sent to an absorber column (DC4-3) together with the stream leaving FC4-5 (containing isobutanal and CO_2). CO_2 is removed from the top, and from the bottom leaves solution isobutanal that is recycled to DC4-2.

The hydrogenation process breaks double bonds in iso-butanal to form isobutanol. The iso-butanal stream is heated to 160°C before entering a continuous stirred tank (CSTR) hydrogenation reactor, achieving a 97% conversion to isobutanol. The reaction's kinetics are based on Saeid et al.'s report [252].

The hydrogenation reaction can be seen below:

$$C_3H_8O_{3(l)} + H_{2(g)} \rightarrow C_4H_{10}O_{(aq)} \quad \Delta H° = -6.8e^4\ KJ/Kgmole \qquad \text{Eqn 6.10}$$

The resulting aqueous isobutanol stream is cooled to 35°C, treated in a separation tank (FC4-6) to remove unused H_2 and impurities, then directed to a dehydration reaction (RC4-7) modelled as a plug flow reactor operating at 240°C and 5 bar. RC4-7 removes a mole of water, forming isobutene (C_4H_8), as per Equation 6.11. The reaction kinetics was obtained from the work of Khan et al [253].

$$C_4H_{10}O_{(g)} \rightarrow C_4H_{8(g)} + H_2O_{(g)} \quad \Delta H° = 2.5e^4\ KJ/Kgmole \qquad \text{Eqn 6.11}$$

The subsequent distillation column (DC4-4) separates isobutene from impurities like ammonia gas, CO_2, and water. Nearly pure isobutene exits at 99% purity and 40°C, forwarded to the oligomerisation reactor (RC4-8) modelled as a conversion reactor. Equations 6.12 to 6.14 depict the reactions modelling isobutene oligomerization:

Isobutene dimers:

$$2C_4H_8 \rightarrow C_8H_{16} \quad \Delta H° = -3.4e^4\ KJ/Kgmole \qquad \text{Eqn 6.12}$$

Isobutene trimers:

$$3C_4H_8 \rightarrow C_{12}H_{24} \quad \Delta H° = -8.6e^4\ KJ/Kgmole \qquad \text{Eqn 6.13}$$

Isobutene tetramers:

$$4C_4H_8 \rightarrow C_{16}H_{32} \qquad \Delta H° = -8.6e^4\ KJ/Kgmole \qquad \text{Eqn 6.14}$$

The experiment in section 4.2 and data from section 4.4.1 provided the conversion rates for each oligomer: 5% for dimers, 90% for trimers, and 5% for tetramers.

The product stream from the RC4-8 is then raised from 5 bar to 10 bar using a pump (PC4-7) for a subsequent hydrogenation step. In line with the hydrogenation experimental results already outlined in section 4.4.2, the stream is further heated from 45°C to 150°C to promote hydrogenation. The hydrogenation reactor (RC4-9) was designed as a CSTR at 150°C and 20 bar. This hydrogenation reaction of the oligomers from the oligomerisation experiment uses excess and leftover H_2 gas from the previous iso-butanal hydrogenation.

To make paraffinic C_{16} fractions, isobutene dimers, trimers, and tetramers are hydrogenated by breaking the double bonds. The reactions as modelled in ASPEN HYSYS are as follows:

Dimers:

$$C_8H_{16} + H_{2(g)} \rightarrow C_8H_{18} \qquad \Delta H° = -1.2e^5\ KJ/Kgmole \qquad \text{Eqn 6.12}$$

Trimers:

$$C_{12}H_{24} + H_{2(g)} \rightarrow C_{12}H_{26} \qquad \Delta H° = -3.7e^3\ KJ/Kgmole \qquad \text{Eqn 6.13}$$

Tetramers:

$$C_{12}H_{24} + H_{2(g)} \rightarrow C_{12}H_{26} \qquad \Delta H° = -3.7e^3\ KJ/Kgmole \qquad \text{Eqn 6.13}$$

6.3 Results and discussions

6.3.1 Production rate and yields of C_4 route-to-SAF Plant

Table 6.2 highlights significant electricity demands and generation within both C_4 cases. In the simulated scenario, both the heat-integrated and non-heat-integrated plants exhibit variations in electricity requirements across different units. Notably, the heat-integrated case showcases specific units such as vapour recompression and turbo expander compressors demanding substantial power inputs. Conversely, the non-heat-integrated case reveals varied energy demands with units like high-pressure pumps and additional compressors, totalling significant power demand, including 19.95 GWh/annum for high-pressure pump (PC4-16) and 36.66 GWh/annum for compressor (KC4-5).

While both C_4 cases demonstrate diverse energy consumption profiles, the power generation aspect presents a contrast. The heat-integrated approach primarily leverages combustion and turbo-expander turbines, contributing to substantial power outputs, with values such as 170,88 GWh/annum and 130.80 GWh/annum respectively.

Table 6.2. Summary of the power consumed and generated by both C_4 route-to-SAF plant cases.

Power consumed (GWh) per year		
Units	**Heat-integrated**	**Non-heat integrated**
Pump (PC4-5)	0.001	
Pump (PC4-4)	0.0019	
Pump (PC4-7)	0.0036	
Vapour recompression (KC4-1)	30.40	
Turbo expander compressor (KC4-2)	87.44	
High pressure pump (PC4-1)	41.34	
High pressure pump (PC4-16)		19.94
Compressor (KC4-5)		36.65
Pump (PC4-17)		0.05
Pump (PC4-18)		0.005
Additional compressor		0.23
Power Generated (GWh) per year		
Combustion turbine (TC4-1)	170.88	
TE Turbine (TC4-2)	130.80	
TE Turbine (TC4-3)		57.40
Turbine power generation (TC4-4)		61.40

In contrast, the non-heat-integrated scenario demonstrates notable power generation through turbines (TC4-3) and turbine (TC4-4), yielding 57.40 GWh/annum and 61.40 GWh/annum, signifying a distinctive emphasis on turbine-driven electricity generation in this case.

The summary of the production rates for both C_4 cases is shown in Table 6.3. In the non-heat integrated process, production rates stand notably lower for all intermediate and major products compared to the heat-integrated counterpart. For instance, the production rate of 2-keto isovalerate in the non-heat integrated case remains at 11.2 kt/annum, whereas in the heat-integrated system, it is 56.8 kt/annum, signifying a substantial increase. Similarly, other key products like isobutanal, isobutanol, isobutene, and SAF (C_{16} fraction) shows substantial production rate disparities between the non-heat integrated and heat-integrated approaches.. Notably, SAF (C_{16} fraction) also experiences a significant surge in production rates,

emphasizing the advantageous impact of the heat-integrated approach on the output of the final SAF product.

Table 6.3. Summary of both C_4 route-to-SAF production rates of intermediate and major products.

Intermediate and major products	**Production rates**		
	Non-heat integrated	**Heat integrated**	**Unit**
2 keto isovalerate	11.2	56.8	[kt/annum]
Isobutanal	6.9	18.7	[kt/annum]
Isobutanol	7.1	19.2	[kt/annum]
Isobutene	5.4	14.5	[kt/annum]
SAF (C_{16} fraction)	5.3	12.9	[kt/annum]

6.3.2 Total Capital Investment (TCI)

Conducting a thorough mass and energy balance simulation, as demonstrated with the C_2 model, is essential for accurately gauging capital expenditures, fixed operational expenses, and variable operational costs. The models proposed by Seider et al. were utilized in predicting the capital costs for major equipment [172]. The calculations for the major equipment in the C4 cases are the same as already presented in section 3.4.1. The Hand method, previously defined and adopted in a section 3.4.3 for the calculation of TCI for the C_2 heat-integrated route, was employed for the computation of TCI for both C_4 routes (heat and non-heat integrated). In Table 6.4 the underlying principles for the Hand method's calculations are presented.

The costs of all machinery were updated to reflect 2019 values using a cost index of 607.5 from Chemical Engineering Plant [177]. Additionally, the location factor of 1.04 for the United Kingdom, as reported by IHIS Markit [254], was taken into consideration during the calculation process.

The calculation of Inside Battery Limit (ISBL) installed costs involves the application of an installation factor to the determined equipment purchase prices. The Hand method utilizes installation factors that are based on the type of equipment. The costs of all machinery were updated to reflect 2019 values using a cost index of 607.5 from Chemical Engineering Plant [177]. Additionally, the location factor of 1.04 for the United Kingdom, as reported by IHIS Markit [254], was taken into consideration during the calculation process.

Table 6.4. Capital investment cost model used for computing TEA for C_4 route-to-SAF plant.

Hand method	
Year basis	2019
Year of production	8110 hours (bioreactor cycle time)
Installation factor (multiplied by equipment cost) – Inside battery limits (ISBL)	Table A.17 (Appendix 4)
Outside battery limits (OSBL)	25% of ISBL
Commissioning costs	5% of ISBL
Fixed capital investments (FCI)	ISBL + OSBL + Commissioning cost
Working Capital	10% of FCI
Total capital investment (TCI)	FCI + Working capital

Detailed calculation results for the TCI for both heat and non-heat-integrated cases can be found in Appendix 4.

Overall, the total capital investment required for the C_4 heat-integrated process is almost twice higher than that of the C_4 non-heat-integrated process, as indicated in Figure 6.8. This is due to the additional infrastructure and equipment utilised in the heat integration. For instance, the cost of vapour recompression equipment was incurred in the heat-integrated process, but not in the non-heat-integrated process.

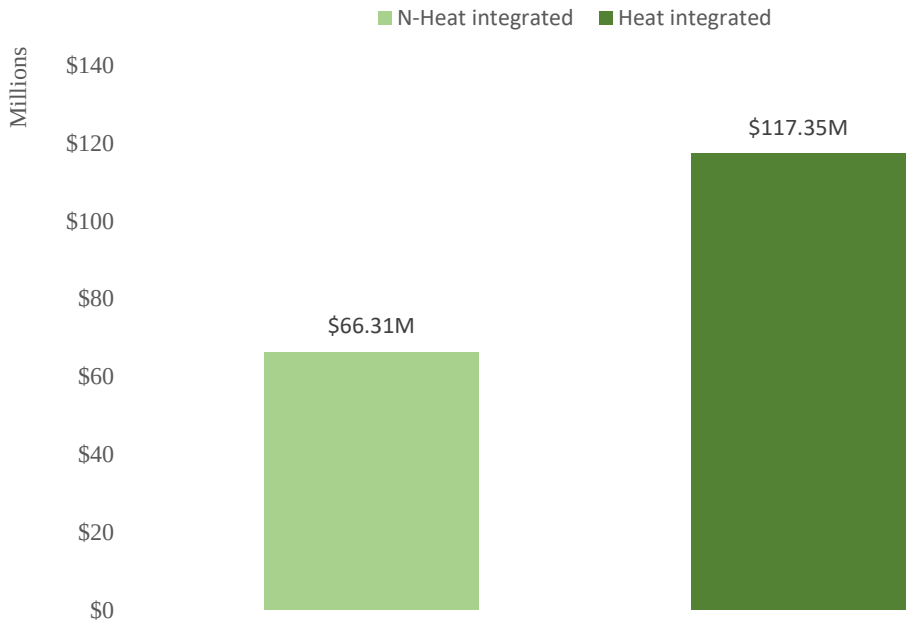

Figure 6.8. Comparison of TCI in both C_4 heat and non-heat integrated processes.

By looking at Figure 6.9, one can observe the comparison between the primary equipment that makes up most of the capital investment costs in both C_4 route-to-SAF processes. For instance, the cost of a combustion chamber in the heat-integrated process is thrice higher, due to the higher temperature feed gas required in this process compared to the non-heat-integrated process.

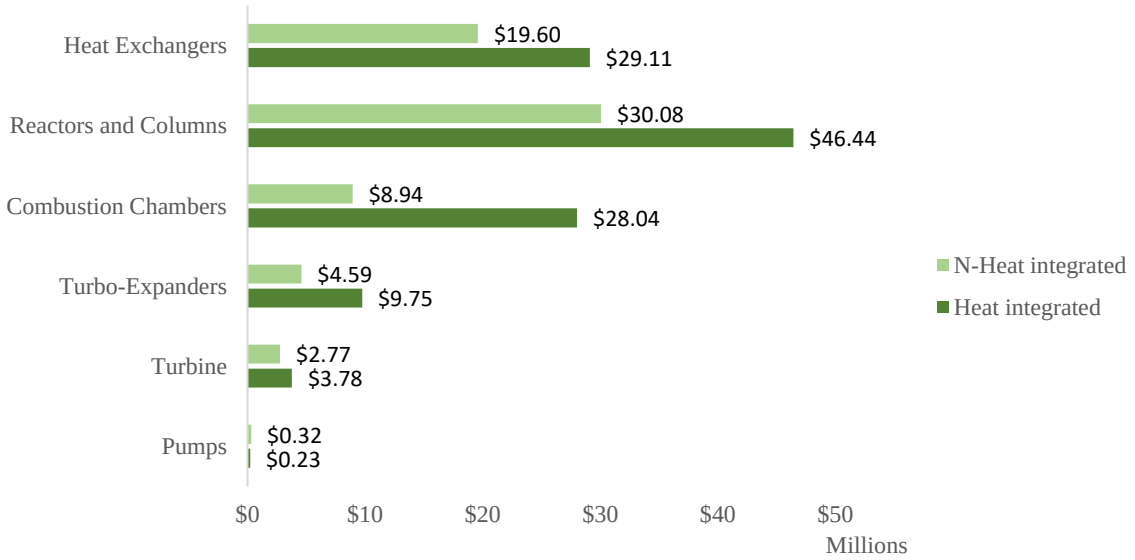

Figure 6.9. Comparison of the breakdown of the primary equipment cost contributing to the overall TCI for both C_4 route-to-SAF cases.

More so, the use of heat exchangers and other heat transfer equipment in the heat-integrated process can result in increased pressure drops and pumping costs, leading to higher operating costs. In the heat-integrated process, the expenses for columns and reactors were approximately 53% higher compared to the non-heat-integrated approach. This was due to the use of five bioreactor trains in the heat-integrated bioreactor modelling, compared to only one in the non-heat-integrated modelling. This significantly increased the size and cost of the process. The number of bioreactor trains was determined using the OLE DB linkage between HYSYS conversion reactor (bioreactor) and EXCEL, utilizing outputs from OptFlux. The seed fermenter and product fermenter were modelled as columns.

Additionally, as can be seen in Figure 6.10, the heat-integrated process generated more electricity compared to the non-heat-integrated process, yet the ratio of electricity generated to usage was relatively constant between the two processes. This highlights that while the heat-integrated process produced a larger amount of electricity, it also consumed a larger amount of energy. This was majorly due to the amount of pumps and compressor used in C_4 heat-integrated process.

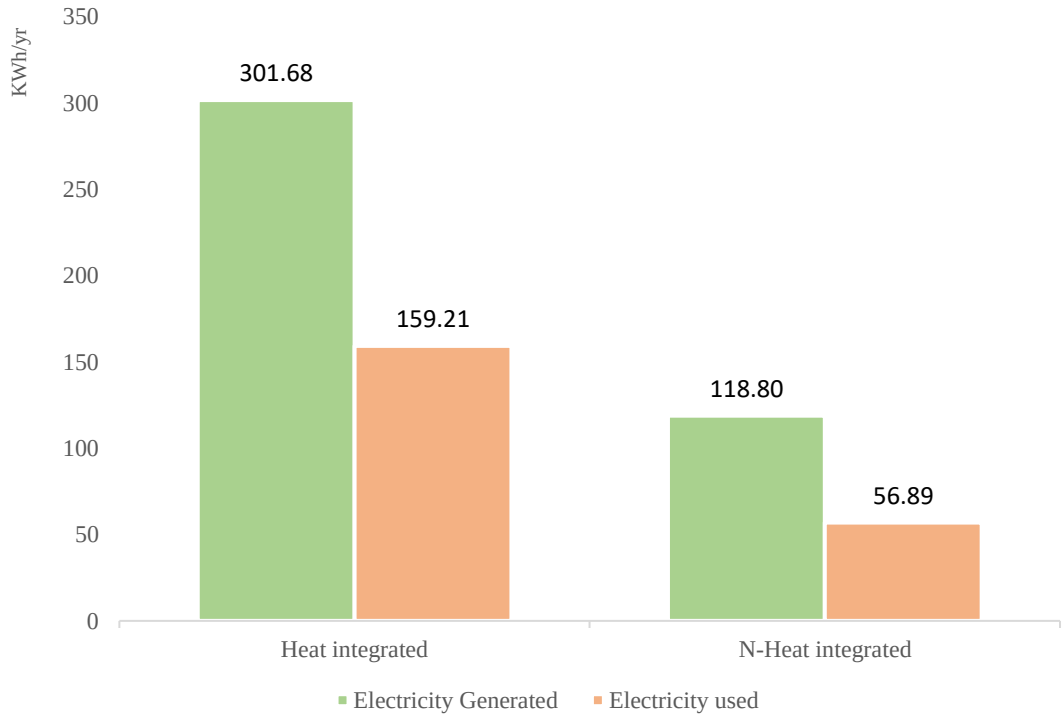

Figure 6.10. Graph comparing the yearly electricity generated and usage (KWh/yr) for both heat and non-heat integrated processes.

When comparing the capital investment in turbo-expanders between the two processes, it can be seen that the investment in the non-heat-integrated process is almost half of what is required

in the heat-integrated process, as depicted in Figure 6.11. Despite the lower capital investment in turbo-expanders in the non-heat-integrated process, this translated to lower revenue generated from renewable electricity production via the turbine in this process, as demonstrated in Figure 6.11.

It is important to consider all these factors when making a decision on the best approach for a particular process and facility. While the higher capital investment in the heat-integrated process may seem disadvantageous, it can lead to substantial energy savings over the lifetime of the process and result in a lower overall cost of operation as can be seen in the investment case.

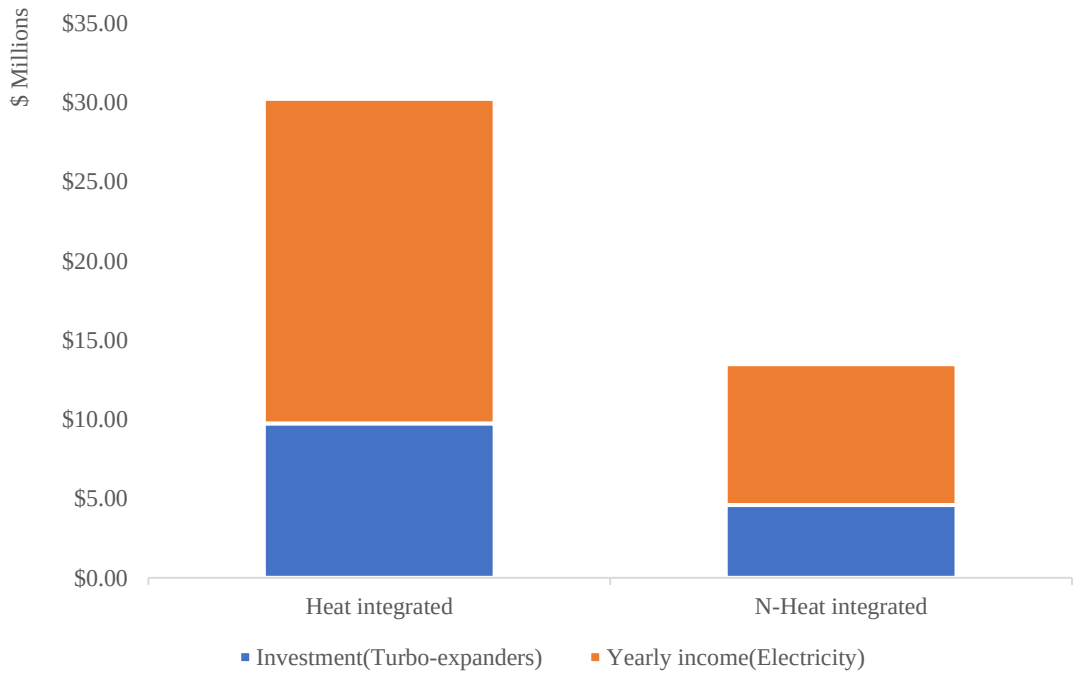

Figure 6.11. Graph comparing the capital investment on Turbo-expanders vs the yearly revenue generated in both heat and non-heat integrated processes.

6.3.3 Fixed Operating Cost

As previously demonstrated with the C_2 model in section 3.4.3, the TS method was selected as the basis for calculating the FOC of both C_4 heat-integrated and non-heat integrated processes. The TS method and parameters used are presented in Table 6.5. Detailed calculation results for the FOC for both heat and non-heat-integrated cases can be found in Appendix 4.

A comparison of the FOC for the heat-integrated and non-heat integrated processes can be observed in Figure 6.12. As depicted in Figure 6.12, the estimation of the FOC for the heat-integrated process was calculated to be 7.35 million dollars. This value represents an increase

compared to the FOC of a non-heat integrated process, which was determined to be 6.50 million dollars. The source of this difference in cost can be attributed to the additional infrastructure and equipment required for the implementation of heat integration.

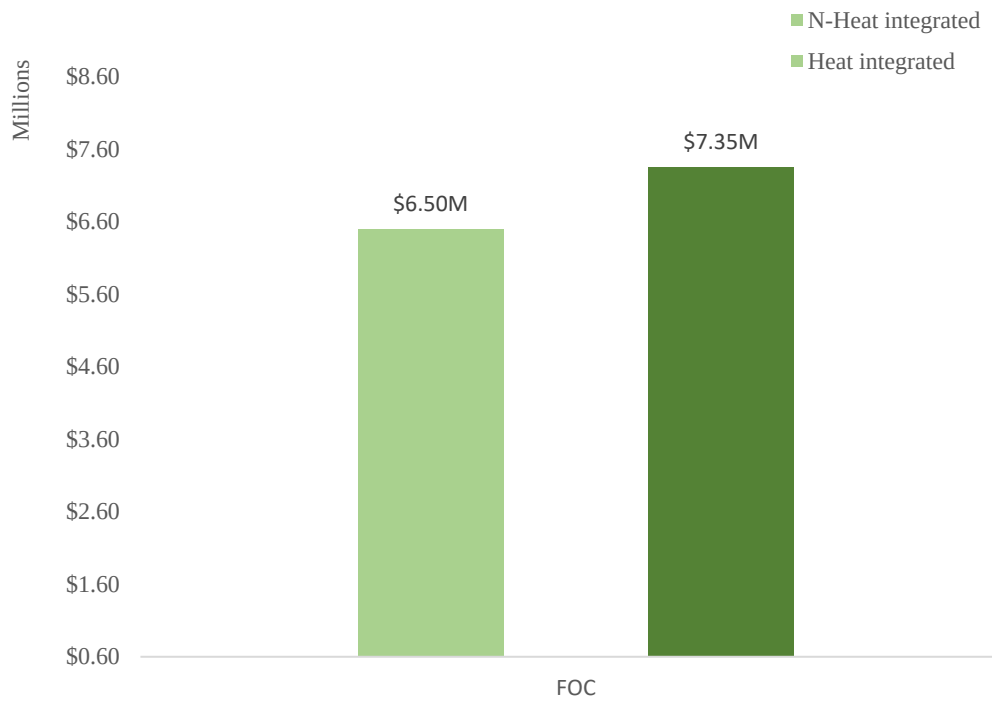

Figure 6.12. The graph presented illustrates a comparative analysis of the annual FOC between C_4 heat-integrated and non-heat integrated processes for SAF production.

Table 6.5. Fixed operating cost model (TS method) [178].

Parameters	**TS Method**
Operating Labour	Salary estimates obtained from salaryexpert.com 3 process operators per shift. 4 shift teams
Supervisory Labour	25% of operating Labour
Direct Salary Overhead	50% of Operating and Supervisory Labour
Maintenance	3% of ISBL
Property Taxes and Insurance	1% of ISBL
Rent of Land	1% of FCI
General Plant Overhead	65% of Total Labour and Maintenance
Allocated Environmental Charges	1% of FCI

One of the key factors contributing to the higher FOC for the heat-integrated process is the significantly higher allocated environmental charges estimation in comparison to the non-heat integrated process. This can be attributed to the higher total costs of both Outside and Inside Battery Limits of Plant (OSBL and ISBL), which were used in the estimation of environmental charges. The higher cost of these components leads to a proportionally higher allocation of environmental charges to the heat-integrated process, resulting in a higher FOC overall.

While heat integration offers the potential for reduced energy consumption and costs across a plant, it is also crucial to consider the maintenance costs associated with a heat-integrated process. As shown in Figure 6.13, the maintenance costs for a heat-integrated process were higher than for a non-heat integrated process.

Additionally, other fixed costs such as plant overhead, land rent, property taxes, and labour are comparatively higher for the heat-integrated process in comparison to the non-heat integrated process, as can be expected. Overall, the difference in the fixed operating costs between the two processes is not substantial.

It is important to recognize that while the initial FOC for a heat-integrated process may be higher, the long-term benefits in terms of energy savings can offset this increase and result in a reduced overall cost of operation.

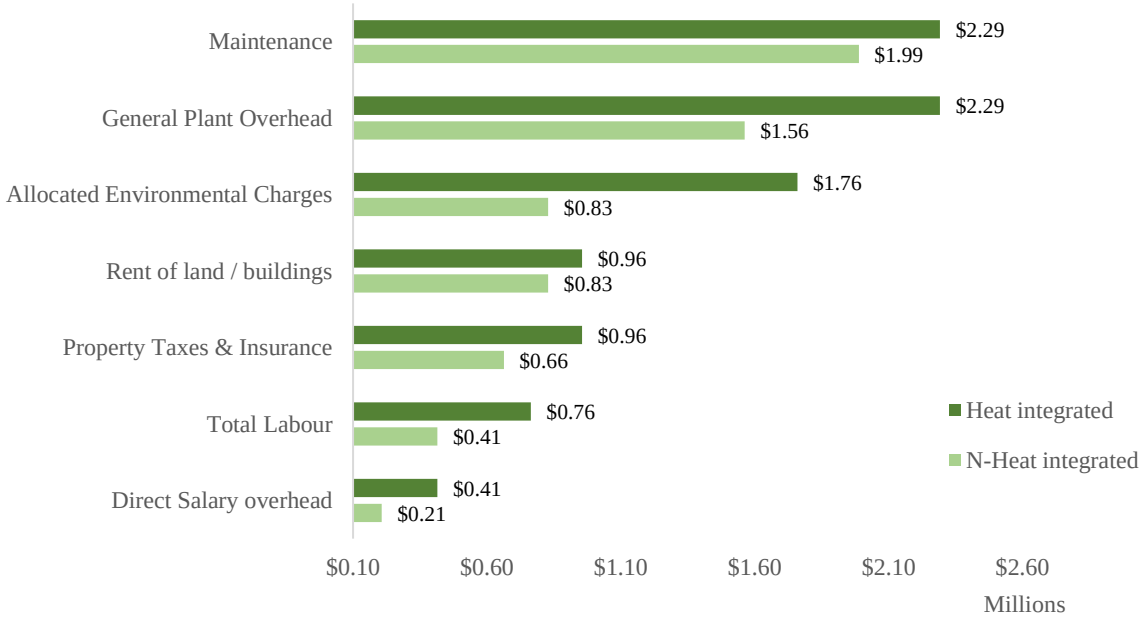

Figure 6.13. Comparison of the breakdown of the annual FOC for both C_4 route-to-SAF cases.

6.3.4 Variable Operating Cost (VOC)

Figure 6.14 shows the comparison between the yearly VOC for C_4 non-heat and heat-integrated route-to-SAF cases. It can be seen that the yearly variable costs for non-heat integrated was about 40 % higher when compared to the heat-integrated case.

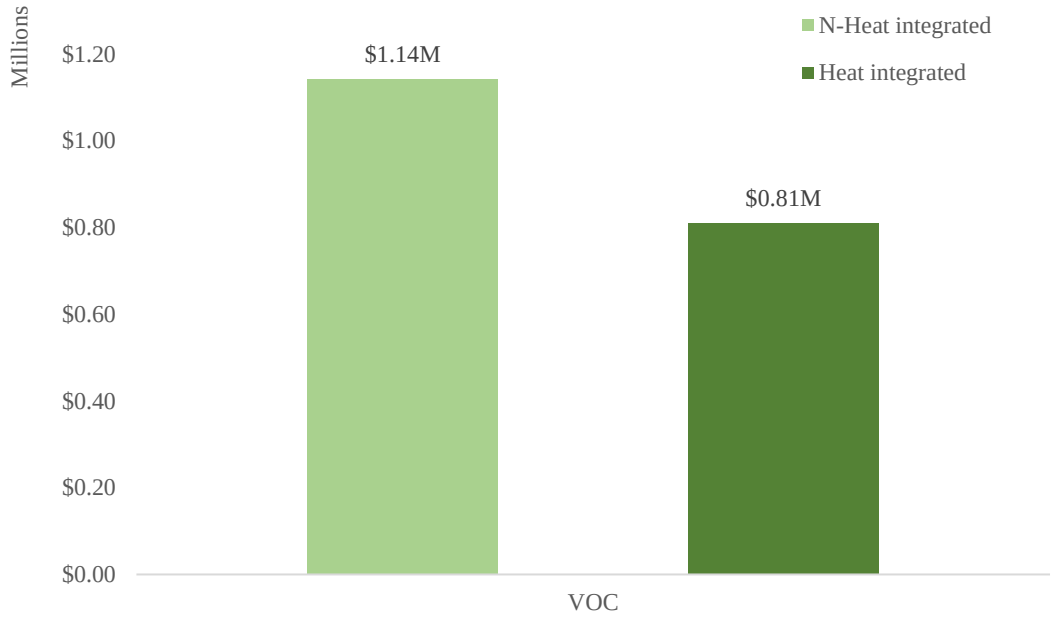

Figure 6.14. Comparison of the annual VOC for both C_4 non-heat-integrated and heat-integrated route-to-SAF.

Figure 6.15 illustrates that the annual variable cost of process water in a heat-integrated process is slightly higher compared to a non-heat integrated process. This increase in cost is due to the higher usage of dilution water and treatment costs in the heat integrated process. Moreover, the cost of process water is higher in a heat-integrated process as it is used for heat transfer purposes, which may require additional treatment to maintain the necessary purity level and prevent scaling, fouling or corrosion of heat transfer surfaces.

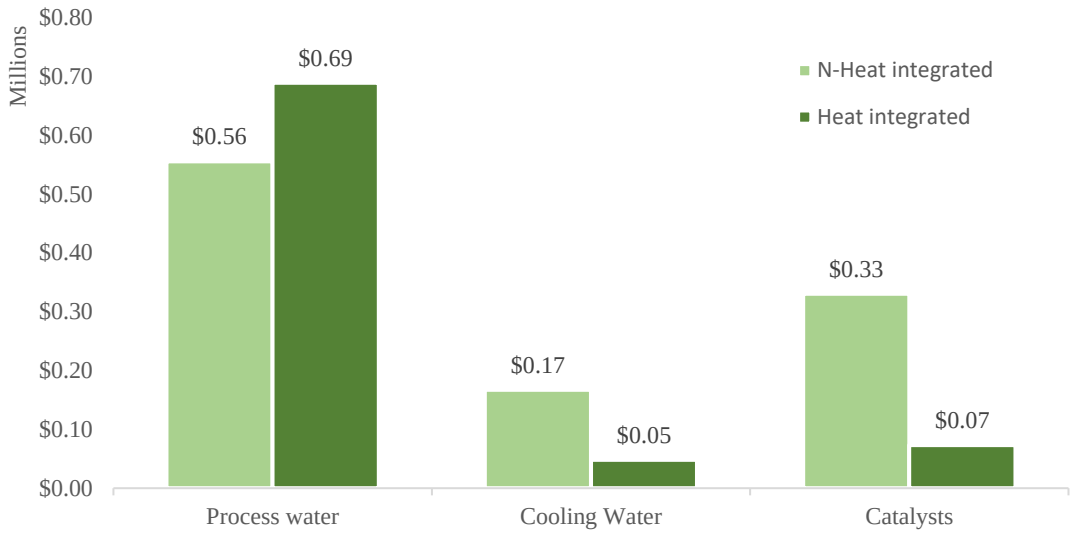

Figure 6.15. The chart displays a comparison of the major variable costs associated with both the C_4 heat-integrated and non-heat integrated processes. It can be observed that the cost of catalyst and cooling water in the non-heat integrated process was found to be notably higher than that of the heat-integrated process.

In contrast, the cost of cooling water in a heat-integrated process is thrice lower than in a non-heat integrated process. The major reason for the higher cost of cooling water in the non-heat integrated process is attributed to the cooling duty of the bioreactor, which is not required in a heat-integrated process. The disparity in cost is due to the improved efficiency of water management in the heat-integrated process.

Additionally, heat recovery and transfer systems can be used to recover heat from the cooling water and reuse it in other parts of the process, leading to further energy savings and reduced cooling water demand. These benefits contribute to the lower cost of cooling water in a heat-integrated process.

Furthermore, as can also be seen in Figure 6.15, the cost of catalysts for a heat-integrated process is approximately five times lower than the cost of catalysts for a non-heat integrated process. The reactor volumes and reaction types were the parameters considered in estimating this cost. The reactor volumes in the non-heat integrated process were higher, thus incurring more catalyst cost. The use of heat exchangers and other heat transfer equipment in a heat-integrated process can help to maintain consistent and controlled process temperatures, reducing the risk of thermal degradation and catalyst poisoning. Consequently, this leads to reduced catalyst degradation and, in turn, lower catalyst costs in the heat-integrated process.

6.3.5 Investment analyses

Investment analysis for both C_4 cases utilised the same calculation methods already presented in section 3.3.4. Calculation results for the investment analysis for both heat and non-heat-integrated cases can be found in Appendix 4.

As can be seen in Figure 6.16, during the initial five-year period, the NPV analysis of the heat-integrated process reveals a lower value compared to the non-heat integrated process, with both indicating a negative cash flow. This can be attributed to the higher capital expenditures associated with the installation and commissioning costs in heat integrated process as compared to the non-heat integrated process.

However, over time, the NPV of the heat integrated process exhibits a more pronounced trend and indicates a greater positive cash flow. This phenomenon implies that, as the process matures and operates over an extended period, it generates more substantial returns and generates higher positive cash flows than the non-heat integrated process. process. In contrast the NPV of the non-heat integrated C_4 process remained negative during the entire 25-year plant period.

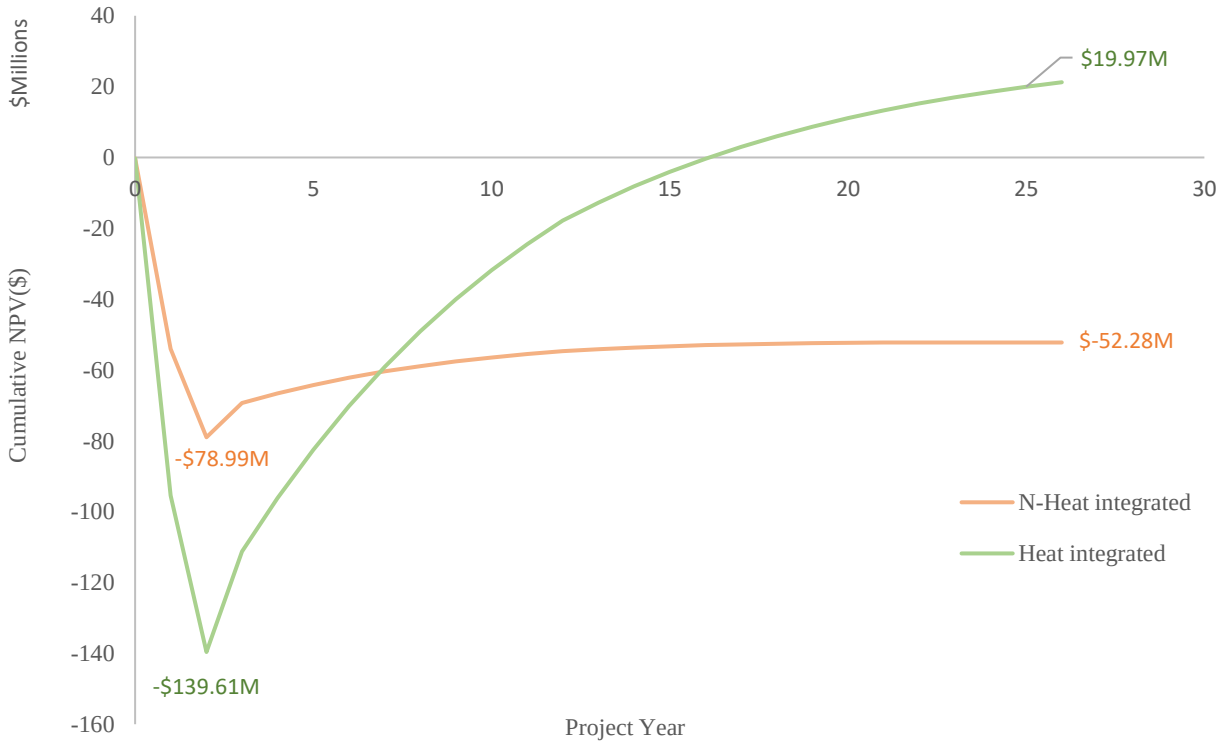

Figure 6.16. The graph displays the cumulative NPV of both C_4 processes, indicating that the heat-integrated process generated a significantly higher positive NPV compared to the non-heat integrated process.

This outcome can be attributed to the enhanced efficiency and potential cost savings conferred by the heat-integrated. When compared to non-heat integrated case, this finding advocates for the implementation of a heat-integrated C_4 process, which has a payback period of 16 years even though the plant is expected to operate for about 25 years as can be seen in Figure 6.16.

From an investor's perspective, the delayed payback period could be a concern. It may impact the plant's short-to-medium-term financial outlook. But, in the context of the growing SAF industry, this delay might align with long-term market projections and evolving regulatory landscapes supporting sustainable aviation initiatives.

Investors who care about sustainability and forward-looking markets might see the delayed payback as a strategic investment. They may recognize the significance of SAF in addressing environmental concerns in the aviation industry. Considering the mounting demand for sustainable alternatives in aviation fuel and the potential for increased adoption over the plant's operational life, the delayed payback might be viewed as a calculated risk for long-term gains and market positioning.

6.3.6 Sensitivity analyses

In this study, a sensitivity analysis was performed on the two C_4 processes to investigate the impact of changes in various input variables on the NPV of the processes. The input variables considered in the analysis include operating costs, taxes, inflation, and electricity prices. The purpose of the analysis was to identify the critical variables that have the most significant effect on the NPV of the processes and to enable better decision-making and risk management.

The sensitivity analysis was conducted by varying the input variables between -20% and 20% and measuring the resulting impact on the NPV of both the heat-integrated and non-heat integrated processes. The results of the analysis were represented visually in Figure 6.17 and Figure 6.18, respectively.

The sensitivity analysis revealed that in the heat integrated process, the ISBL and OSBL costs, electricity price, and price of biofuel are the most sensitive input variables. An increase in these costs would have a substantial effect on the NPV of the process, as depicted by the higher sensitivity of the graph to changes in these variables. In contrast, the non-heat integrated process was found to be less sensitive to changes in the electricity prices, indicating that their impact on the NPV of the process is relatively small. This is due to the less amount of electricity generated by the C_4 non-heat-integrated plant as compared to the heat-integrated counterpart.

The nominal calculation used for both C_4 case studies employed an electricity price of 0.1438 ($/kwh) to estimate the operational costs and financial viability of the plant. However, a critical

observation emerges in the break-even analysis for the heat-integrated case, indicating that the plant achieves equilibrium and covers its operational expenses when electricity is sold at a price of 0.123 ($/kwh) while the kerosene price remains at $611/ton. Contrasting this to the non-heat integrated scenario, the break-even occurs when electricity price is sold for 0.241 ($/kwh) while the kerosene (C_{12}, C_{16}) price remains $611/ton. This indicates ~95 % increase of the electricity selling price when compared with the heat-integrated case.

The terms ISBL and OSBL costs refer to the costs associated with the design, construction, and operation of the process units that are within or outside the boundaries of the process, respectively. The sensitivity analysis demonstrated that changes in these costs can have a significant impact on the financial performance of the heat integrated process.

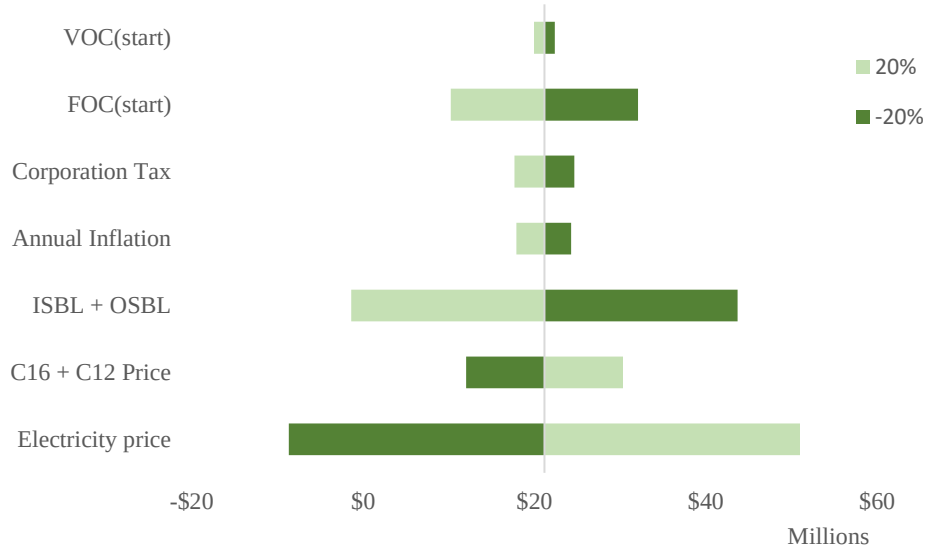

Figure 6.17. The graphical representation illustrates the sensitivity analyses of the C_4 heat-integrated process, revealing the NPV of the process is more significantly affected by variations in the price of electricity, ISBL, and OSBL costs, relative to other parameters.

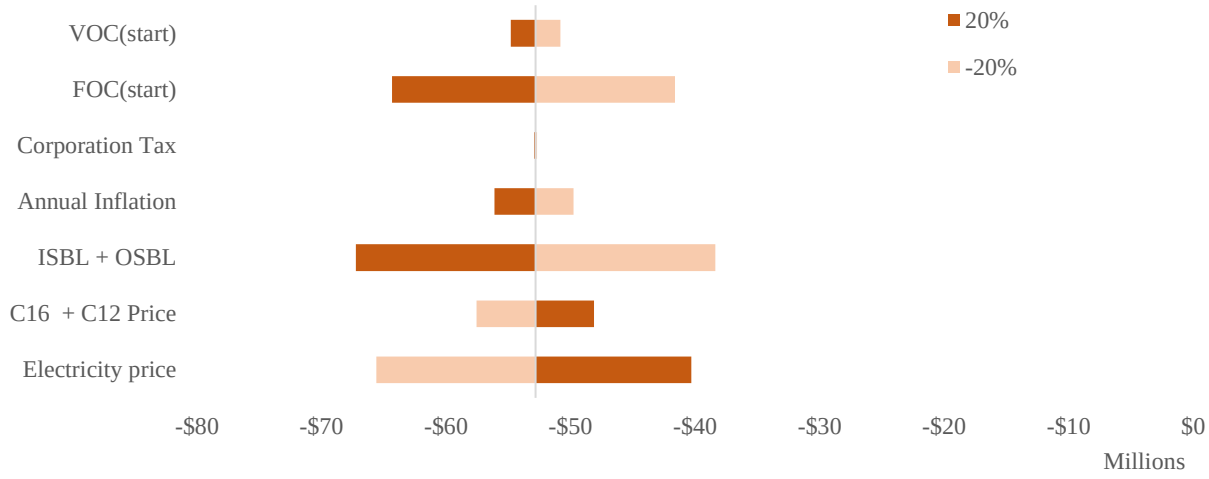

Figure 6.18. The presented graph depicts the sensitivity analysis of the non-heat integrated process and reveals that the NPV of the process is predominantly influenced by variations in fixed operating costs, electricity prices, and ISBL and OSBL capital costs, relative to other factors.

6.4 Conclusion

In conclusion, the process and cost comparison between the C_4 heat-integrated and non-heat integrated process routes for jet fuel production presented in this chapter reveals several key differences in costs performance.

The comparison of capital investment between C_4 heat-integrated (at $117.35M) and C_4 non-heat-integrated ($66.31M) processes indicates that the former requires a about twice investment due to the additional infrastructure and equipment needed for heat integration. The cost of vapour recompression equipment and the quantity of bioreactor trains contribute to the higher investment in the heat-integrated process.

The FOC for the heat-integrated process (at $7.35M) was found to be higher due to the additional infrastructure and equipment required for heat integration when compared to the FOC for the C_4 non-heat-integrated process (at $6.5M). The higher cost is attributed to higher environmental charges, maintenance costs, and other fixed costs such as plant overhead, land rent, property taxes, and labour. Despite this, the difference in FOC between the two processes is not substantial.

In addition, the cost of process water needed is thrice higher in the C_4 heat integrated process (at $690,000) compared to the C_4 non-heat integrated process (at $560,000), however, the non-heat integrated process incurs higher yearly variable costs mainly due to cooling costs which

stands at $50,000 and $170,000 for the C_4 heat-integrated and C_4 non-heat-integrated processes respectively. More so, C_4 heat-integrated process boasts a low yearly catalyst cost requirement of $70,000 compared to $330,000 required by the counterpart. These findings highlight the potential for significant energy savings and improved process efficiency through heat integration.

The initial comparison of NPV between the two C_4 processes suggests that the C_4 heat-integrated process has a significant lower NPV (-$139.61M) compared to the non-heat counterpart (-$78.99M) at the second year, which may be attributed to the higher costs associated with setting up the process. However, as the process matures and operates over a longer period, the NPV (~$20M) of the C_4 heat-integrated process becomes steeper and shows a higher positive cash flow at the 25^{th} year, indicating that it is becoming more profitable compared to the non-heat-integrated counterpart. Although it has a delayed payback period of 16 years which might not make it very attractive to investors.

Furthermore, the sensitivity analysis of input variables such as ISBL and OSBL costs, electricity price, and price of kerosene indicates that these variables have a significant impact on the NPV of the heat integrated process, while the non-heat integrated process is less affected by these changes. This is due to the lower amount of electricity generated by the non-heat-integrated plant when compared to the heat-integrated SAF plant. A notable finding in the break-even analysis for the heat-integrated case reveals that the plant achieves equilibrium and covers operational expenses at an electricity selling price of 0.123 ($/kWh), with a constant kerosene price of $611/ton. In contrast, the non-heat integrated scenario requires an electricity price of 0.241 ($/kWh) to break even, maintaining the kerosene price at $611/ton. This highlights a significant ~95% increase in the electricity selling price compared to the heat-integrated case.

Overall, the findings suggest that while heat integration offers potential energy savings and improved process efficiency, the higher investment and fixed operating costs associated with the heat-integrated process must be carefully evaluated against potential long-term benefits.

CHAPTER 7.

COMPARISON OF C_2 AND C_4 ROUTE-TO-SAF PROCESSES: POLICY IMPLICATIONS

This chapter delves into a comprehensive TEA comparing the C_2 (heat-integrated) and C_4 (non-heat and heat-integrated) pathways for SAF production. Through Monte Carlo simulations addressing uncertainties, a probability distribution for the NPV of the proposed C_4 heat-integrated plant is revealed. The break-even price analysis for the three cases were also presented.

While the investment analysis leans towards favouring the heat-integrated processes of both C_2 and C_4 route-to-SAF, a comparison highlights a shortfall in the proposed heat-integrated technologies when pitted against the alternative use of raw material (black liquor) for renewable electricity generation.

This chapter concludes by evaluating the economic viability of the proposed route-to-SAF plant. It takes into account varying SAF prices and navigates the potential impacts of policies on SAF production within the UK context. This holistic exploration offers comprehensive insights into the economic landscape and policy implications, shedding light on the feasibility and potential challenges of implementing SAF production within the UK aviation sector.

7.1 Techno-economic assessment comparison of C_2 and C_4 route-to-SAF processes

This section assesses the processes and the TEA of SAF production employing both C_2 heat-integrated and C_4 pathways (non-heat-integrated and heat-integrated routes). The C_2 process employed black liquor gasification with the proposed plant located in China. In contrast, the C_4 process considers pot ale draft gasification, assuming the plant is situated in the UK. Acetaldehyde and isobutene, obtained from gas fermentation, served as fundamental building blocks for the C_2 and C_4 routes, respectively. Both routes resulted in the production of SAF and renewable electricity. The C_2 route was initially examined, using acetaldehyde as a precursor for bio-jet fuel synthesis. This route was advantageous from a gas fermentation standpoint, as acetaldehyde is a volatile compound, facilitating its easy removal from the fermenter. Nevertheless, the C_2 route exhibited a significant drawback, as it consisted of numerous operational units, as already presented in Figure 3.1 to Figure 3.3, rendering it capital-intensive.

7.1.1 Total capital investment - C_2 versus C_4 cases

Figure 7.1 display graph comparing the TCI C_2 and both C_4 pathways. Analysing the TCI, the C_4 heat integrated route-to-SAF configuration incurs approximately 15% higher costs than the C_2 heat integrated, whereas the C_4 non-heat integrated shows TCI approximately 54% higher than the C_2 heat integrated scenario.

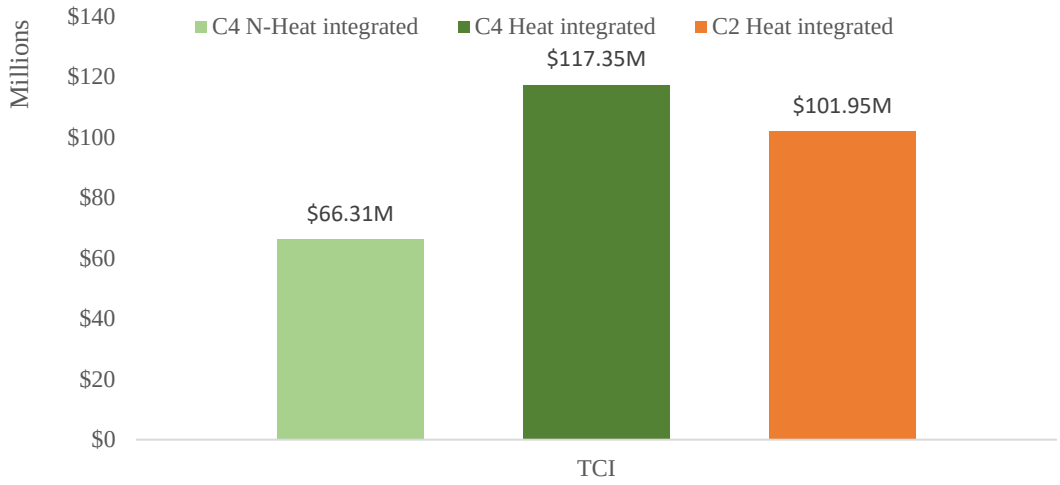

Figure 7.1. Chart comparing TCI of proposed C_2 and both C_4 route-to-SAF plants.

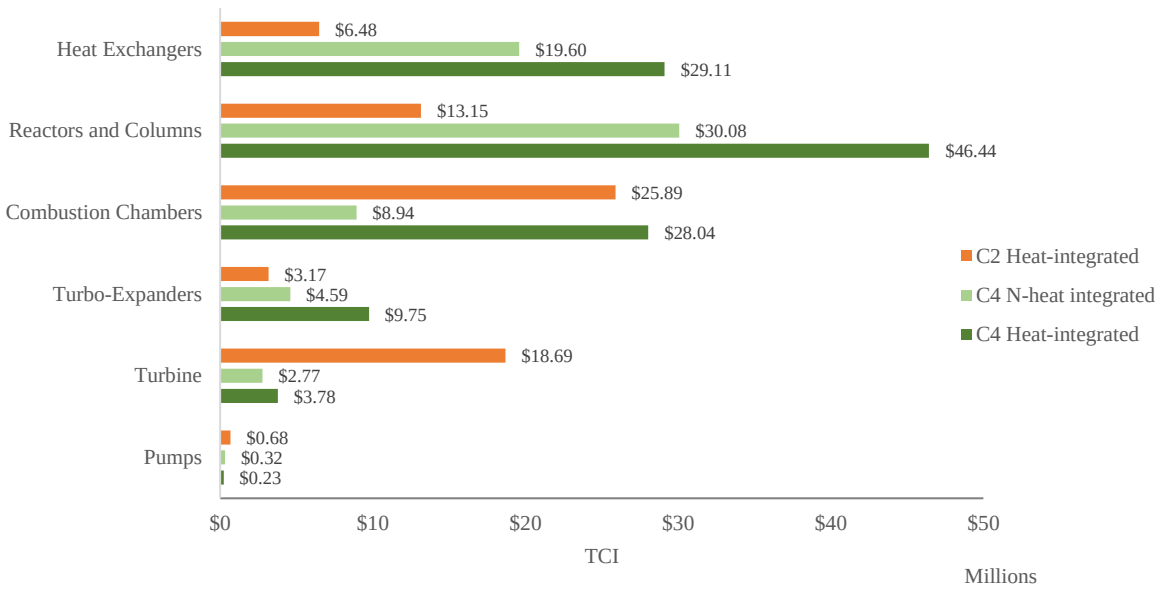

Figure 7.2. Chart showing the breakdown of the TCI of proposed C_2 and both C_4 route-to-SAF plants.

The breakdown of the TCI for the three cases can be seen in Figure 7.2. In the C_2 heat-integrated case, pump costs were higher than in both the C_4 cases. These can be attributed to more units in C_2 case requiring more pump investments.

Regarding turbines, the C_2 heat integrated case shows an outstanding 79% surge in investment compared to the C_4 heat Integrated. However, the C_4 non-heat integrated route exhibited the lowest cost compared to other counterpart.

On the other hand, turbo-expanders cost was the highest in C_4 heat-integrated case, which is twice the cost in the C_4 non-integrated case. The lowest cost for turbo expanders was incurred in the C_2 heat-integrated case. This was because only one turbo expander was utilized in the C_2 case. For combustion chambers, both C_4 heat-integrated and C_2 heat-integrated cases incurred substantial costs, being about 64 % expensive than the C_4 non-heat-integrated case.

In reactors and columns, the C_2 heat-integrated case boasts the lowest cost when compared to the C_4 counterparts. This is mainly due to the less amount of bioreactor trains required in the C_2 case. Also, the cost of the heat exchanger in the C_2 heat-integrated was the lowest when compared with the C_4 cases.

7.1.2 Fixed operating costs - C_2 versus C_4 cases

In Figure 7.3 the comparison of FOC among the three cases demonstrates a nearly uniform cost distribution.

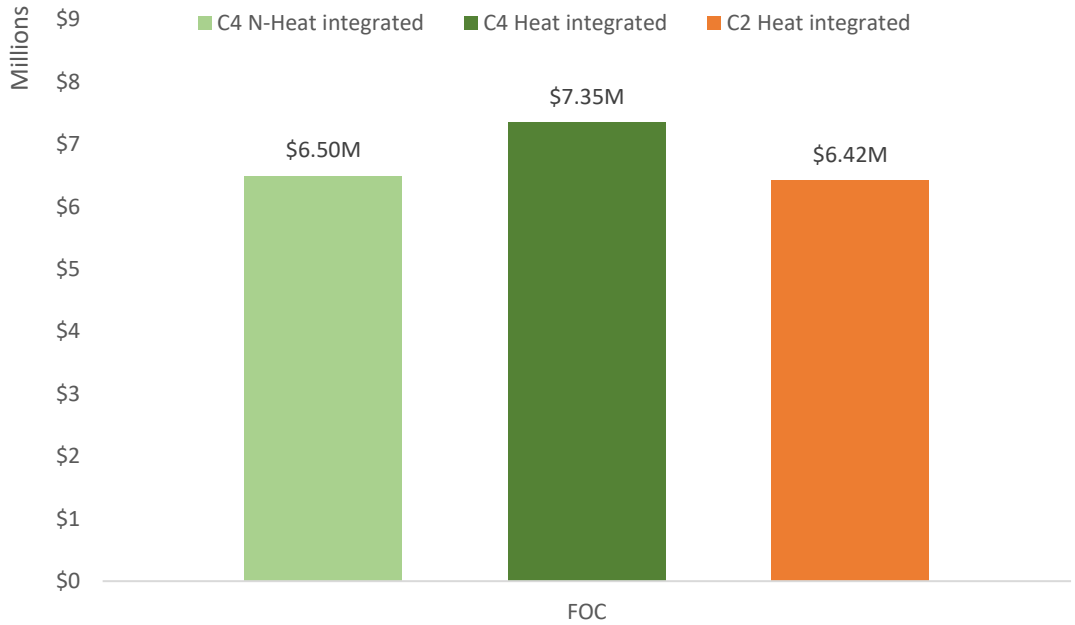

Figure 7.3. Chart comparing FOC of proposed C_2 and both C_4 route-to-SAF plants.

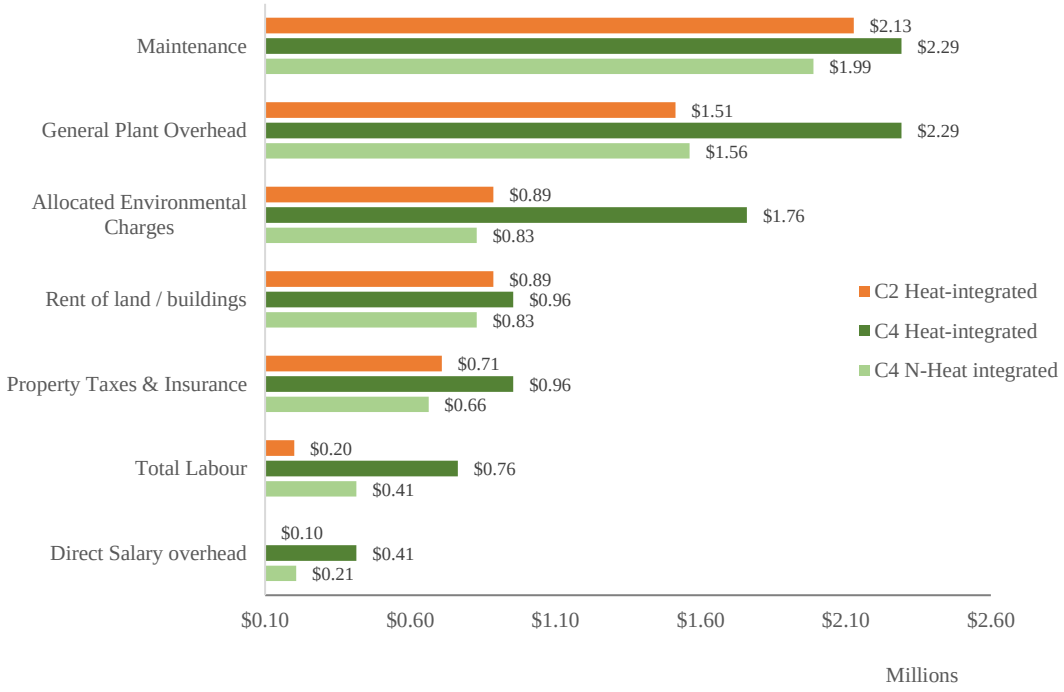

Figure 7.4. Bar chart comparing the estimated yearly FOC of the C_2 and both C_4 route-to-SAF plants.

However, the C_4 heat-integrated case stands out as approximately 11% more expensive than the other cases.

Figure 7.4 provides a detailed breakdown of these costs, revealing that the C_4 heat-integrated scenario incurred higher expenses, particularly in the maintenance and general overhead categories. These high FOC levels in the C_4 heat-integrated cases are primarily attributed to its correlation with TCI, as evident from its calculation.

7.1.3 Variable costs - C_2 versus C_4 cases

Figure 7.5 shows that the C_4 heat-integrated exhibits around 55% lower costs than the C_2 heat-integrated, whereas the C_4 non-heat-integrated demonstrates VOC approximately 30% lower than the C_2 heat-integrated.

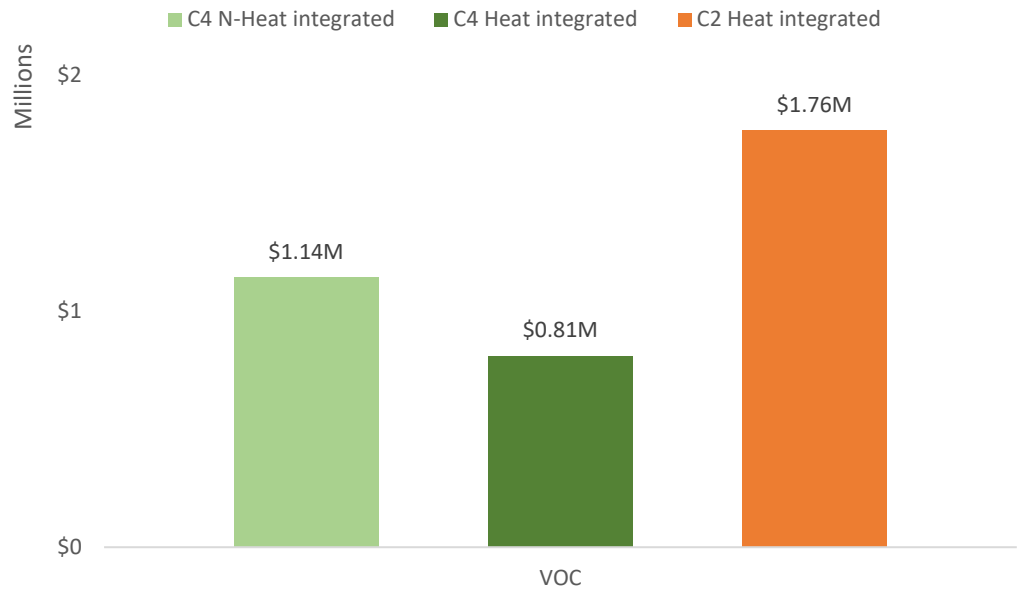

Figure 7.5. Chart comparing VOC of proposed C_2 and both C_4 route-to-SAF plants.

This is mainly due to the absence of the need for cooling water in the heat-integrated cases as can be seen in Figure 7.6. On the other hand, the process water costs for C_4 heat-integrated process is the most expensive when compared to the other counterparts. C_2 heat-integrated process also incurred a significant process water costs. This is mainly due to important role of water in the heat integration configurations of the plants.

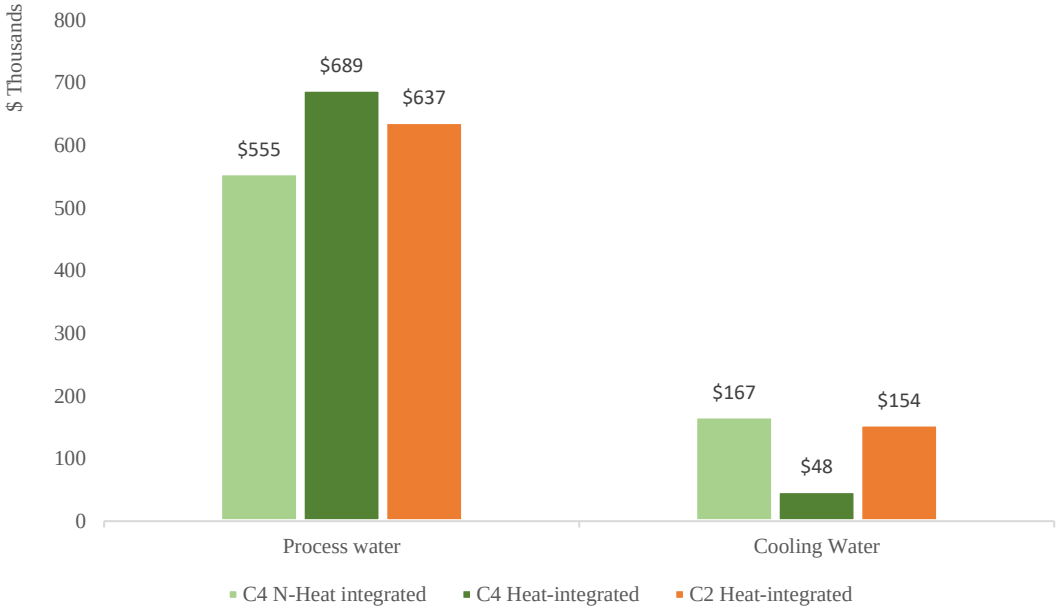

Figure 7.6. Chart comparing process and cooling water costs for both proposed C_2 and C_4 process routes for SAF production.

7.1.4 Investment analysis – C_2 versus C_4

Figure 7.7 illustrates the NPV comparison among the three cases. Notably, both the C_2 heat-integrated and C_4 non-heat-integrated scenarios concluded with negative NPVs, standing at -$4.43M and -$52.20M respectively, after 25 years of plant operations. In contrast, only the C_4 heat-integrated case exhibited a positive NPV, reaching approximately $16.98M and achieving break-even around the 15th year of operations.

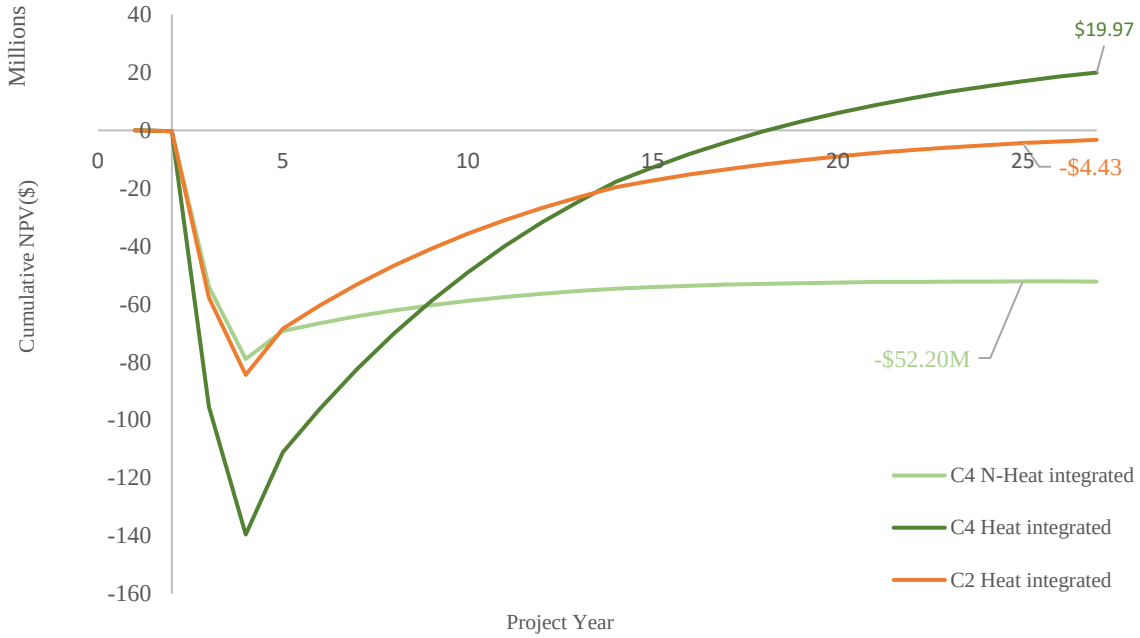

Figure 7.7. A comparison of the NPV for the C_2 heat-integrated route and the C_4 routes, including both non-heat-integrated and heat-integrated cases. The C_4 heat-integrated route demonstrates the most favourable NPV outcome, with an estimated value of approximately $20 million.

The nominal selling price of SAF utilized for determining the NPV of both C_2 and C_4 cases was $611/ton. The electricity selling prices utilized were 0.1083 (kwh/$) and 0.1438 (kwh/$) for C_2 and C_4 cases respectively.

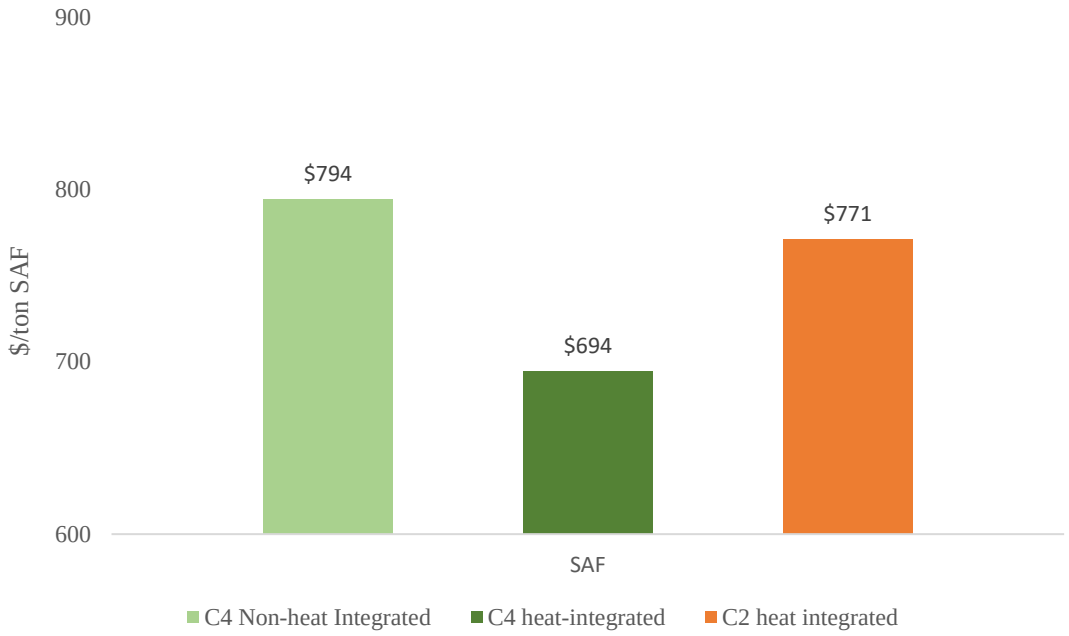

Figure 7.8. Chart comparing the selling prices of SAF necessary to achieve break-even in the 12th year of plant operations across all three cases.

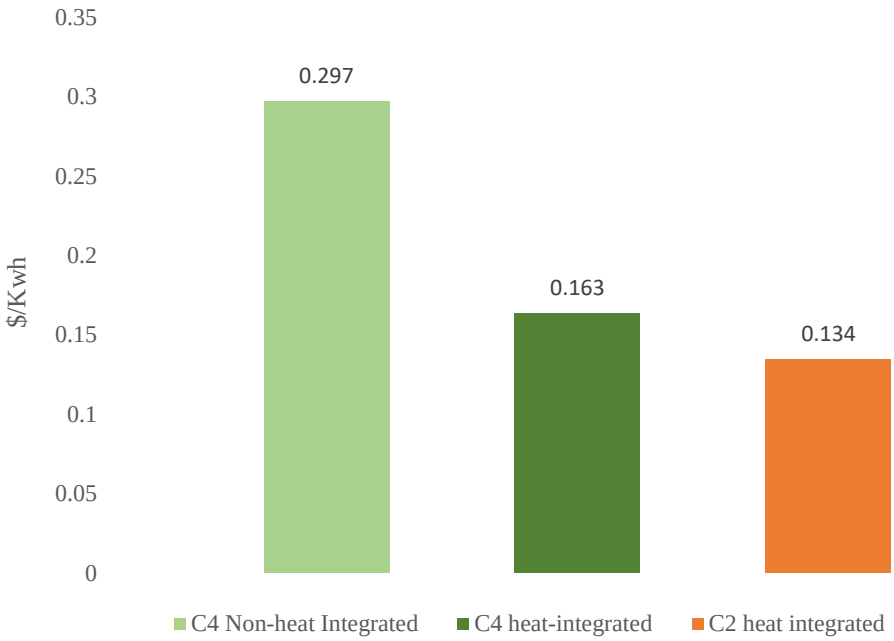

Figure 7.9. Chart comparing the selling prices of electricity necessary to achieve break-even in the 12th year of plant operations across all three cases.

Figure 7.8 and Figure 7.9 presents a comparative analysis of the selling prices of both SAF and electricity required for the proposed C_2 and C_4 SAF plants to break-even in the 12th year of plant operations. It is crucial to emphasize that meeting both conditions, specifically achieving

the target selling prices for electricity and SAF, is needed for the proposed plants to break-even in the 12th year. The C_2 heat-integrated case requires SAF and electricity selling prices of $771 and 0.134 kwh/$, respectively. However, notably, the C_4 heat-integrated route-to-SAF case illustrates the lowest required selling prices for SAF ($694.65/ton) and electricity (0.163 kwh/$), resulting in an earlier break-even compared to other cases proposed. These results indicate that the C_4 heat-integrated process plant has the best potential from an investment perspective. Consequently, C_4 heat-integrated route was selected for further evaluation.

While the C_2 case directly involves the SCWG of black liquor to produce feed for gas fermentation, however C_4 heat-integrated was used to compare the NPV of the alternative use of black liquor for renewable electricity generation as can be seen in Figure 7.10. The C_4 heat-integrated case, despite not incorporating black liquor as a direct feed source, shares commonalities in infrastructure, resources, and operational processes that closely resemble those utilized in the C_2 heat-integrated case.

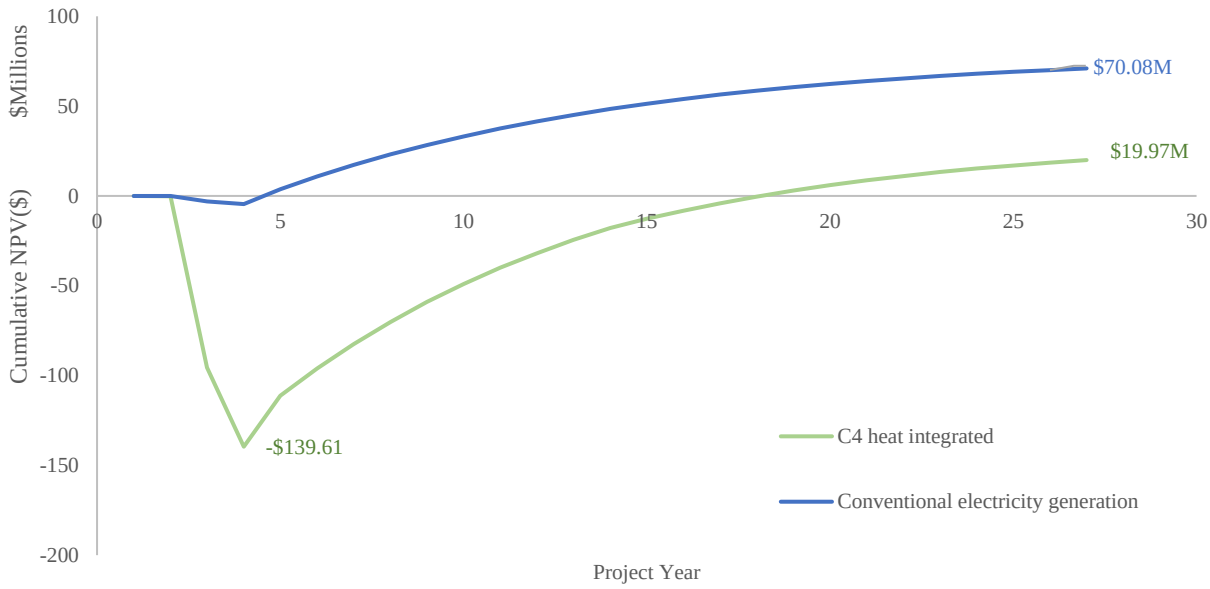

Figure 7.10. The investment analysis of the C_4 heat integrated route-to-SAF is compared to that of a conventional renewable electricity generation plant. Based on the standard TEA model parameters, the plant has a cumulative NPV of approximately $20MM, while the alternative use has an NPV of $70MM.

Additionally, contrasting the alternative use of black liquor for electricity generation against the best economic outcome in the C_4 heat-integrated case allows for a more holistic evaluation.

Although the C_4 heat-integrated process plant (nominal) displayed a positive NPV of approximately $20 million, it still falls behind when compared to the alternative use of black liquor for electricity generation, which boasts an NPV of around $70 million, as shown in Figure 7.10.

7.1.5 Sensitivity analysis

Sections 3.4.5 and 6.3.6 already discussed the selectivity analysis of the C_2 case and both C_4 cases, respectively. Given the recognition of the C_4 heat-integrated case as the most favourable, as already highlighted in section 7.1.4, a Monte Carlo simulation has been conducted to address uncertainties associated with achieving the NPV calculated. The simulation, executed using EXCEL, employed the average of expected values for all variables influencing the NPV result. An initial standard deviation range of 5% - 10% was assigned, as detailed in Table 7.1.

Table 7.1. Input for Monte Carlo simulations showing the expected amount and initial standard deviation utilised.

Parameters	**Expected value**	**Initial standard deviation**
Discounted Rate of Return	10%	0.5
Corporation Tax	20%	1
Annual Inflation	2%	0.1
Installed Equipment Cost	$146,693,164.48	$5,867,726.58
Commissioning Cost	$7,334,658.22	$366,732.91
Working Capital	$14,669,316.45	$1173545.316
TCI	$168,697,139.15	$13495771.13
FOC (start)	$7,348,807.87	$587904.62
VOC (start)	$810,396.92	$64831.75375
Renewable Electricity SP	0.1438 (kwh/$)	0.011504
SAF Forecast price	611($/ton)	48.88
Electricity produced	142.47 (GWh/annum)	107.89

To conduct the simulations, the NORM function in EXCEL was utilized. This function requires three inputs: a random input, the mean value (in this case, the expected value), and the standard deviation value. By running a probability analysis, the simulation generated potential outcomes

for a variety of scenarios, each time yielding a different NPV value. A 1000-trial simulation was executed, showcasing the NPV across a range of scenarios with dynamic input variables, facilitated by the "what-if" function in EXCEL.

The results were plotted using a histogram, illustrating the distribution of 1000 NPV values for the C_4 heat-integrated case (Figure 7.11). The probability distribution indicates that there is approximately a 69% chance that the C_4 heat-integrated case will achieve a net cumulative NPV between $5MM and $65MM.

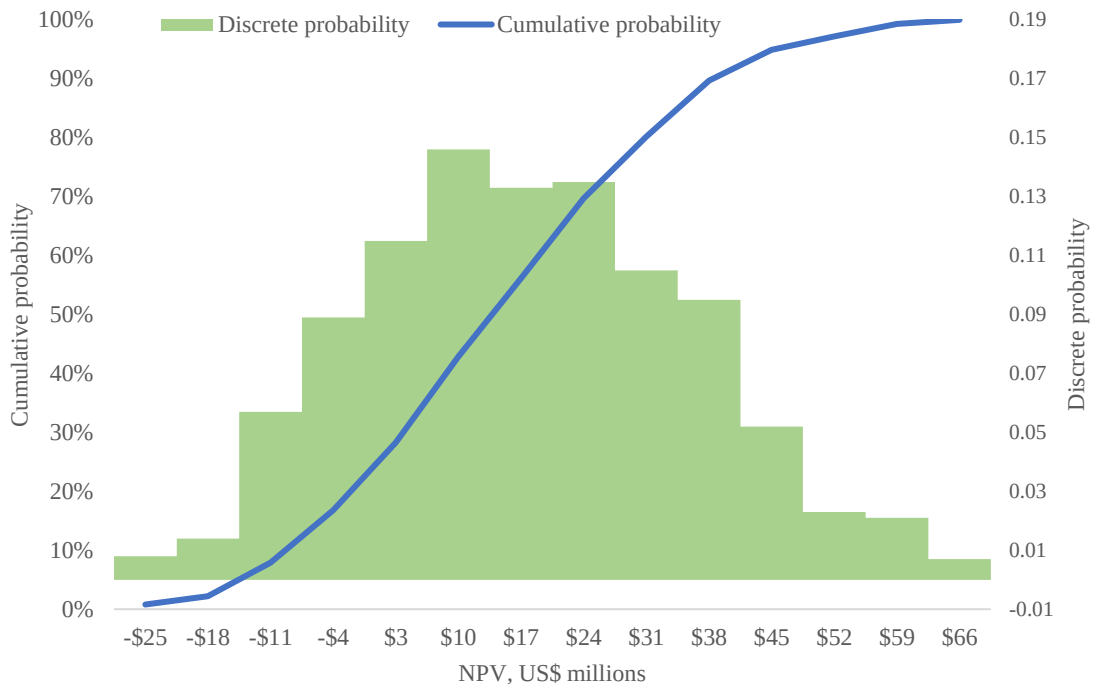

Figure 7.11. Utilizing the Monte Carlo technique to evaluate the potential trade-offs related to the C_4 heat-integrated biobased jet fuel facility.

Table 7.2 consolidates the outcomes from the 1000 simulated scenarios, indicating the risk of loss, which is calculated at 11% in this case. This risk percentage was determined by averaging all negative NPV values from the 1000 scenarios and dividing by 1000. . Understanding this risk of loss is pivotal for risk management strategies specific to the proposed C_4 heat-integrated SAF plant. It provides crucial insight into the probability of scenarios where the project might underperform financially, allowing stakeholders to gauge the potential impact of unfavourable outcomes.

Table 7.2. Monte Carlo simulation output for C_4 heat-integrated route plant's NPV.

Parameter	**Value**
Mean	$21,472,982.96
Standard deviation	$18,154,135.43
Minimum value	-$29,705,991.03
Maximum value	$67,554,977.07
Skewness	0.03
Kurtosis	-0.32
Risk of loss of value	11.50%

7.1.6 Internal Rate of Return (IRR)

In the process of evaluating investments, financial professionals often utilize a variety of tools and techniques, with an internal rate of return (IRR) being a widely used and powerful metric. The IRR is a financial principle that allows investors and companies to assess the prospective profitability of investments by factoring in the monetary value over time. In essence, IRR calculates the expected yearly return of an investment, taking into account the money's time value, which enables investors to evaluate and compare various investment options by quantifying their potential earnings.

As already mentioned, it was evident that the C_4 heat-integrated process outperformed its counterpart, leading to its selection. Although the IRR for the C_4 heat-integrated process was found to be approximately 12% (discounted rate of return was 10%), it falls short of the generally recommended range of 18-20% [255] . It is important to note, however, that our TEA studies employed a conservative price of kerosene at about $611/ton which is about $0.4 per litre tax-free [256]. There is substantial evidence suggesting that the price of SAF has been sold for two or five times this amount, which could potentially impact the investment's profitability and IRR [257]–[261].

In Figure 7.12, various scenarios are presented to examine the effects of doubling and tripling the cost of SAF on our calculations. When the selling price per ton rises from $611 to $1222, the NPV increases by $65 million, and the IRR is 16% with a payback period of 10 years. Furthermore, tripling the selling price results in a significant rise in the NPV ($110 million) and an IRR of 20 % with a shortened payback period of 8 years. In this final scenario, the NPV of a traditional electricity plant ($70 million) is almost the same as that of the C_4 heat-integrated plant as can be seen in Figure 7.12. This highlights the potential and competitiveness of the

suggested heat-integrated SAF plant. In the policy section of this chapter, we will also explore another scenario in the UK SAF policy arena and the impact it could have on the proposed SAF plant.

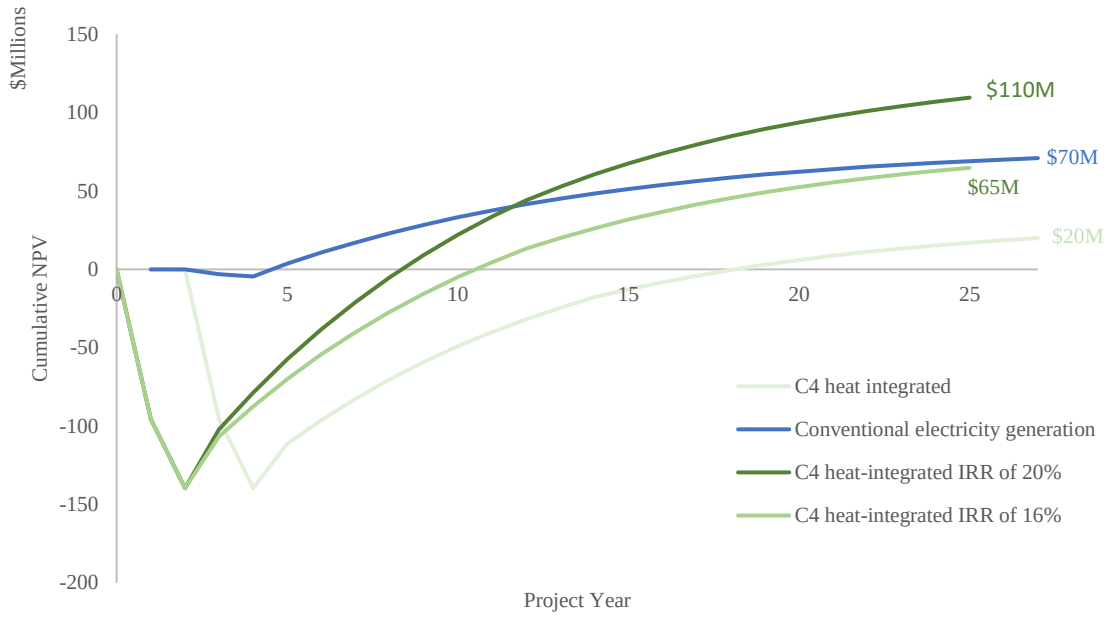

Figure 7.12. A comparative analysis of the NPV for two different applications of black liquor: 1) electricity generation, and 2) supercritical water gasification for C_4 heat-integrated route-to-SAF plant. The first scenario considers a nominal SAF price of $611 per ton, while the second and third scenarios examine the effects of doubling and tripling the price, resulting in IRR of 16 % and 20 %, respectively.

7.1.7 UK policy impact on proposed C_4 heat-integrated route-to-SAF case

Established in 2020, the Jet Zero Council represents a collaborative effort involving the UK government, the aviation sector, and various other parties, with the objective of expediting the growth and market penetration of SAF. By centring on technological advancements, policy formulation, and financial backing, the Council strives to attain net-zero emissions in the aviation industry by the year 2050 [262]. Additionally, they strive to achieve transatlantic flights with zero emissions within a single generation. To accomplish these objectives, the JZC promotes the development of ground-breaking technologies and pioneering methods to significantly reduce the environmental impact of air travel. The UK government has committed to supporting various initiatives under the Jet Zero Council, such as funding for SAF production facilities, research and development projects, and collaborations with international partners to create a global market for SAF.

More recently, in March 2023, the UK Sustainable Aviation Fuel mandate policy was proposed [263]. The proposed SAF mandate by the UK government mandates jet fuel suppliers to blend SAF into aviation fuel starting from 2025. This initiative aims to significantly reduce CO_2 emissions within the aviation industry. The mandate outlines a progressive trajectory for SAF integration in the UK, aiming for a minimum of 10% of jet fuel to be sourced from sustainable feedstocks by 2030. To meet sustainability criteria, SAF must demonstrate at least a 50% reduction in greenhouse gas emissions compared to fossil jet fuel. Additionally, there are specific caps on SAF derived from hydro-processed esters and fatty acids, with the introduction of a PtL sub-target to encourage the development of vital SAF pathways. The scheme incentivizes SAF production through tradable certificates carrying monetary value. This mandate includes an ambitious plan to witness the construction of at least five commercial-scale SAF plants in the UK by 2025.

This mandate policy plays a crucial role in promoting the production and use of SAF, including bio-jet fuels derived from lignocellulosic biomass, which is the focus of this thesis. By setting annual obligations for fuel suppliers, the policy creates a market and demand for SAF, encouraging the development and commercialization of lignocellulosic biomass conversion technologies. The SAF mandate scheme provides price support, helping to make bio-jet fuels more competitive and attractive to investors and fuel suppliers. The buy-out mechanism offers an alternative way for suppliers to discharge their obligation while protecting consumers from high costs, ensuring the overall acceptance and implementation of the SAF mandate. In addition, the policy sends a long-term signal to investors, promoting investment in SAF production technologies, and aims to address barriers to investment in the industry, including revenue certainty. To demonstrate the impact of the SAF Mandate on the economics of bio-jet fuel production, we have utilized the proposed SAF buy-out price (£2567/tonne) in our C_4 route TEA model.

As can be seen in Figure 7.13, NPV (at $210M) of the proposed C_4 heat-integrated route-to-SAF production plant is approximately three times higher than that of an alternative use of black liquor for conventional electricity generation.

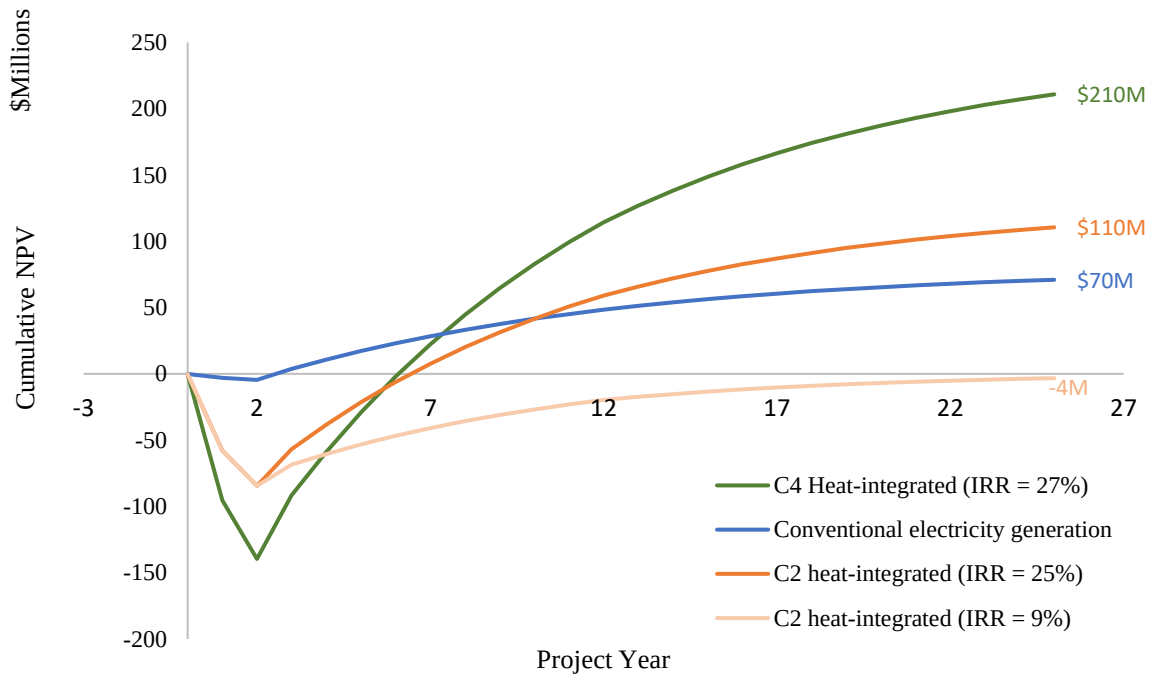

Figure 7.13. Comparison of the NPV between a conventional renewable energy generation plant and the two heat-integrated cases at a buy-out price of £2567/tonne.

Notably, this comparison showcases a substantial increase in the IRR, increasing from the prior 12% to 27%, alongside a shortened payback period of 6 years.

Furthermore, the C_2 heat-integrated case reveals an impressive outlook from its nominal -$4M valuation (based on SAF at $611/ton) to a promising $110M when considering the buy-out price of SAF proposed in the mandate. This shift is accompanied by an increase in IRR, rising to 25% from 9%, and a reduced payback period of approximately 7 years. These findings underscore the potential impact of the UK SAF Mandate policy to the proposed heat-integrated route-to-SAF plants thus stimulating the adoption of lignocellulosic biomass-derived SAF fuels. This policy not only demonstrates potential economic viability but also contributes significantly to curtailing greenhouse gas emissions in the aviation sector.

7.2 Other global policies supporting SAF production

The implementation of policies that support the adoption and use of SAF is crucial in accelerating its market penetration and driving the aviation sector towards a more sustainable future. To promote the development, production, and adoption of SAF, governments and

aviation organizations around the world have implemented various policies and incentives. This section will explore some of these initiatives.

Renewable Fuel Standards (RFS)

Nations such as the United States and the European Union have introduced regulations mandating a certain proportion of renewable fuels, like SAF, to be incorporated into conventional fossil fuels. This strategy fosters the growth of advanced biofuels and encourages their adoption in the transportation industry.

1. The US Renewable Fuel Standard (RFS) Program, which was initiated by the Energy Policy Act of 2005 and broadened by the Energy Independence and Security Act of 2007, sets yearly goals for the volume of renewable fuels to be incorporated into transportation fuels like gasoline and diesel. The program promotes the usage of advanced biofuels, including cellulosic biofuel, biomass-based diesel, and other advanced biofuels[264].

2. The European Union's Renewable Energy Directive (RED) was established in 2009 and later revised in 2018 as RED II. It mandates EU member states to attain a minimum of 32% of renewable energy in their total energy consumption by 2030 [8]. The directive sets specific targets for the use of renewable fuels in the transportation sector, promoting the development and use of advanced biofuels and other renewable fuels.

Refuel - EU Aviation initiative

The European Commission unveiled a comprehensive suite of proposals on July 14, 2021, targeting amendments to the EU's approach to climate, energy, land use, transport, and taxation. With the objective of attaining at least a 55% net decrease in greenhouse gas emissions by 2030 relative to 1990 levels, this compilation of proposals is often referred to as the "Fit for 55" package [265].

One significant aspect of this package is the Refuel - EU aviation initiative, which seeks to foster sustainable air travel by creating a fair competitive environment. The draft regulation contains provisions obligating fuel suppliers to gradually increase the distribution of SAF, such as synthetic aviation fuels or e-fuels. This is intended to promote SAF adoption among airlines and consequently decrease emissions associated with aviation.

Furthermore, the proposal mandates that airlines carry only the amount of jet fuel necessary for secure flight operations when departing from EU airports. This aims to maintain a fair competitive landscape for airlines and airports while minimizing additional emissions resulting from excess fuel weight.

China's SAF Policies

In a recent policy announcement, the Civil Aviation Administration of China (CAAC) outlined ambitious goals for the adoption of SAF in the country[266]. The CAAC aims to increase SAF consumption to over 20,000 tons by 2025, with a cumulative target of 50,000 tons during the 14th Five-Year Plan period.

Furthermore, the CAAC has established aggressive objectives to reduce fuel usage and carbon emissions in China's air transport sector. They intend to decrease fuel consumption per ton-kilometre for the air transportation fleet to 0.293 kg, as well as bring down CO_2 emissions per ton-kilometre to 0.886 kg. The policy announcement reflects China's commitment to a greener future in aviation and emphasizes the importance of adopting sustainable practices in the industry.

Financial Incentives

The United Kingdom, Australia, Canada, Japan, China, India, and South Korea are all actively supporting the development and use of sustainable aviation fuel (SAF) in their efforts to reduce greenhouse gas emissions and achieve their climate goals. To drive these initiatives, these countries are implementing various financial incentives, such as tax credits, subsidies, public-private partnerships (PPPs), loan guarantees, and grants.

In the United Kingdom, the government has set a target of net-zero greenhouse gas emissions by 2050 and has pledged around £110 million in investment towards SAF production and infrastructure [267]. Similarly, Qantas(Australia) has committed to investing $50 million in SAF production and infrastructure[268]. In 2021, Air Canada announced investments of $50 million and established goals to reduce aviation-related emissions by 50% by 2050 [269].

In addition to these national efforts, financial incentives such as tax credits and subsidies are offered in many countries, including the United States. The Renewable Fuel Standard (RFS) provides Renewable Identification Numbers (RINs) to fuel producers, which can be sold to meet regulatory requirements. Moreover, the Blender's Tax Credit offers a $1.00 per gallon credit for blending SAF with conventional jet fuel[270].

Public-private partnerships (PPPs) also play a crucial role in the development and commercialization of SAF technologies. Governments can partner with private entities to secure funding, share risks, and accelerate the production and adoption of SAF. For instance, the U.S. Department of Energy (DOE) has partnered with private companies and research institutions through the Bioenergy Technologies Office (BETO) to develop advanced biofuel technologies.

Finally, loan guarantees and grants can be provided to support the construction and operation of SAF production facilities. By offering financial instruments, governments can bridge the financing gap for new technologies, lower investment risks, and attract private investors. An example of such support is the U.S. Department of Agriculture's (USDA) Biorefinery[271], Renewable Chemical, and Biobased Product Manufacturing Assistance Program, which offers loan guarantees and grants for advanced biofuel production facilities.

7.3 Conclusion

This chapter carried out a comparative analysis between the C_2 (heat-integrated) and C_4 (non-heat-integrated and heat-integrated) routes-to-SAF production, producing crucial insights regarding economic viability and policy implications.

The TEA involved a comprehensive evaluation of TCI, FOC, VOC, NPV, and IRR. Notably, the C_4 heat-integrated route displayed the most promising NPV, surpassing both the C_2 heat-integrated and C_4 non-heat-integrated scenarios. This outcome was supported by break-even analysis, showcasing that the C_4 heat-integrated route necessitated the lowest selling prices for both SAF and electricity to break-even in the 12th year of operations, with required selling prices for SAF at $694.65/ton and electricity at 0.163 kwh/$. This indicates its favourable investment potential compared to the other cases.

Sensitivity analyses, including Monte Carlo simulations, provided a detailed insight of the uncertainties in NPV calculations. The simulation for the C_4 heat-integrated case revealed a probability distribution, indicating a 69% likelihood of achieving a net cumulative NPV between $5MM and $65MM, alongside an 11% calculated risk of loss. These analyses underscore the importance of risk management strategies in mitigating financial uncertainties.

Although the C_4 heat-integrated process showed economic potential with an initial IRR of 12%, indicating a relatively modest value, sensitivity analyses revealed a notable trend. Doubling or tripling SAF prices substantially boosted both NPV and IRR, aligning the C_4 heat-integrated route more closely in competitiveness with the alternative use of black liquor for traditional electricity generation.

More so, the impact of employing the SAF buy-out price ((£2567/tonne) stipulated by the UK SAF mandate policy on SAF production from lignocellulosic biomass proved pivotal. The NPV of the proposed C_4 heat-integrated route-to-SAF production plant increased to $210M from $21M (based on SAF at $611/ton), approximately three times higher than that of an alternative use of black liquor for conventional electricity generation. This comparison showcased a substantial increase in the IRR of the C_4 heat-integrated plant, rising from the initial 12% to 27%, alongside a shortened payback period of 6 years. Likewise, the C_2 heat-integrated case demonstrated significant improvement, transitioning from a nominal -$4M valuation (based on SAF at $611/ton) to a promising $110M NPV when considering the buy-out price stipulated in the mandate. This transformation was accompanied by an increase in IRR, rising to 25% from 9%, and a reduced payback period of approximately 7 years. These findings underscore the potential impact of the UK SAF Mandate policy on the proposed heat-integrated route-to-SAF plants, stimulating the adoption of lignocellulosic biomass-derived SAF fuels.

CHAPTER 8.

CONCLUSION AND RECOMMENDATIONS

This chapter provides a summary of the key findings from each result chapter of the thesis. It presents the conclusions of these findings for the proposed technology and offers policy recommendations based on the research. It also concludes by underscoring the importance of the research and outlining recommendations for future research directions.

8.1 Overview of thesis

This research demonstrated the potential of continuous gas fermentation of H_2 and CO_2 for SAF production. The use of SCW gasification addressed energy inefficiency challenges associated with biological CO_2 conversion. This was demonstrated through a detailed process simulation using ASPEN HYSYS, which included a TEA of the entire process.

The heat integration of SCWG of black liquor (in C_2 route-to-SAF) and pot ale draft (in C_4 route-to-SAF) incorporates an isopentane heat pump to utilize low-temperature heat generated during aerobic gas fermentation for heating the SCWG reactor feed. This integration eliminates the need for cooling water in the bioreactors in heat-integrated cases for both C_2 and C_4 routes, resulting in a notable reduction in cooling water costs.

Additionally, the pressurized gaseous output from the SCWG reactor not only meets the energy requirements of the bioreactor's compressor but also generates substantial income for the plant through renewable electricity generation.

This study also includes experimentation on two crucial upgrading units present in the proposed C_4 route-to-SAF plants: the oligomerisation of isobutene and subsequent hydrogenation reaction of oligomerised alkenes. Key findings from these experiments were integrated into the simulation of the C_4 route-to-SAF plant.

8.2 Conclusions: Summary of results

Chapter 3

1. **TEA methodologies and investment estimations**
    - The TCI for the C_2 heat-integrated route-to-SAF plant falls between \$101-102 million.
    - FOC estimates ranging from \$6.42 to \$6.87 million using TS and Coulson & Richardson methods.
    - VOC analysis for the C_2 heat-integrated process was estimated to be \$1.76M.

2. **Comparative analysis and NPV estimations**
    - C_2 heat-integrated plant achieved a net of 160 Gwh/annum of electricity.
    - The next best alternative use of black liquor in an electricity generation plant using a steam turbine achieved a net of 138 GWh per annum. However, the C_2 heat-integrated plant incurred about 17 times the operational cost compared to the steam turbine plant.
    - At the end of the 25-year operational span, the cumulative NPV for the C_2 heat-integrated route-to-SAF plant amounted to approximately -$3M, reflecting a negative value.
    - In contrast, the alternative use of black liquor in a conventional electricity generation plant yielded a positive cumulative NPV of $70 million, with a payback period of 4 years (electricity selling price at 0.1085 $/kWh).
3. **Sensitivity and break-even analysis results**
    - 5% increase in electricity price could lead to a 200%+ increase in NPV.
    - Break-even point occurs when electricity is sold at $0.1120 per kWh at the 25^{th} year.

Chapter 4

1. **Oligomerization Experiment**
    - Identified trimers (C_{12}) and tetramers (C_{16}) as significant SAF fractions, constituting approximately 90% of the product distribution.
    - Demonstrated stability of the oligomerization reaction over Amberlyst-35 for over 234 hours, critical for sustainable jet-fuel drop-ins.
    - Established 70°C as the optimal temperature for the highest yield of trimers and tetramers.
    - Residence time of 47mins determined fore the reaction.
    - Demonstrated the feasibility of Amberlyst-35 in achieving desired product distributions.

2. **Hydrogenation Experiment**
    - Run 1: 5 bar pressure, 150°C temperature, and 5 wt.% Pd on Al_2O_3 resulted in high alkanes but with an extended reaction time (~45 hours).

- Run 2: Increased pressure to 20 bar with a 3:1 catalyst to substrate ratio (1 wt.% Pd on Al_2O_3) significantly accelerated the reaction rate.
- Run 3: Reduced catalyst concentration to 1 wt.% Pd on Al_2O_3 and a 1:1 ratio showed a slightly reduced but notably faster reaction than initial low-pressure conditions.
- Identified second-order kinetics for the hydrogenation reaction.
- Determined a kinetic constant "k" of 0.008198558 [1/h] and an approximate reaction order "n" of 2, showcasing alignment with experimental data.

3. **Insights and contributions**
    - Detailed insights into reaction dynamics, temperature optimization, and kinetics.
    - Crucial groundwork for efficient integration into the C_4 route-to-SAF plant (Chapter 6).

Chapter 5

1. **Modelling and simulation tools**
    - Utilized Cell Designer for detailed modelling of biochemical pathways.
    - Translated diagrammatic representations into SBML for OptFlux pFBA simulation.
2. **Metabolic insights and FBA**
    - pFBA Simulation revealed H_2:CO_2 (5:1) and CO_2 : O_2 (1:1) molar uptake ratios aligning with experimental data.
    - Highlighted specific demands: 255.573 moles of H_2 and 60.3965 moles of O_2 for keto-isovalerate production.
3. **Key bioreactor design results and platform integration**
    - Integrated Aspen HYSYS and Excel for precise oxygen uptake calculations.
    - Calculated oxygen transfer coefficients (K_{LA}): 323.13 [1/h] (heat-integrated) and 329.72 [1/h] (non-heat-integrated).
    - Used mass and energy balance for techno-economic assessment; determined key reaction stoichiometry:
      $61.876\ CO_2 + 1.684\ NH_3 + 60.3965\ O_2 + 255.573\ H_2 \rightarrow 11.028\ C_5H_8O_3 + 1.684\ C_4H_7O_2N + 208.093\ H_2O$.
    - For the non-heat-integrated C_4 case, one fermentation train was determined, while for the C_4 heat-integrated case, four fermentation trains were calculated.

4. **Overall contribution**
    - Provided insights into the modelling of metabolic networks in and oxygen dynamics for the C_4 route-to-SAF process.
    - Uniquely linked systems biology to a typical chemical engineering process simulation through the stoichiometry of gas fermentation.
    - Findings, coefficients, and design parameters applied in simulating the gas fermentation of CO_2 and H_2 conversion reactor simulation in HYSYS.

Chapter 6

1. **TCI**
    - The C_4 heat-integrated route-to-SAF process requires a more substantial initial investment of $117.35M compared to $66.31M for the C_4 non-heat-integrated route-to-SAF process. This increase is primarily due to the need for extra bioreactor trains required in the heat-integrated case.
2. **FOC**
    - FOC for the C_4 heat-integrated route-to-SAF process stands at $7.35M, slightly higher than the $6.5M for the C_4 non-heat-integrated process. This increase is attributed to the capital investment costs, environmental charges, maintenance, and other fixed expenses such as plant overhead and labour.
3. **VOC**
    - The C_4 heat-integrated route-to-SAF process requires significantly more process water, costing $690,000 compared to $560,000 in the C_4 non-heat-integrated process.
    - The C_4 heat-integrated process incurs lower yearly catalyst costs ($70,000) compared to the non-heat-integrated process ($330,000) and, additionally, features lower cooling costs ($50,000 vs. $170,000).
    - In the overall comparison of VOC, the heat-integrated case amounted to $810,000, while the non-heat-integrated case totalled $1.14M.
4. **NPV**
    - The C_4 heat-integrated plant generated a net electricity output of 142.47 GWh/annum, while the C_4 non-heat-integrated plant produced a net of 61.90 GWh/annum.

- Initially, C_4 heat-integrated process shows a lower cumulative NPV (-$139.61M) compared to the non-heat-integrated process (-$78.99M) at the second year. However, over time, the NPV of the heat-integrated process increases to approximately $20M by the 25th year, indicating improved profitability while the non-heat-integrated counterpart remains at -$52.28M by the 25th year.
- The heat-integrated process exhibits a longer payback period of 16 years, potentially affecting investor attractiveness.

5. **Sensitivity analysis**
    - Changes in input variables such as ISBL, OSBL costs, electricity price, and SAF price significantly impact the NPV of the heat-integrated process, while the non-heat-integrated process is less sensitive due to its lower electricity generation.
    - The heat-integrated scenario achieves break-even at an electricity selling price of $0.123/kWh, assuming a constant SAF price of $611/ton. In contrast, the non-heat-integrated scenario requires a much higher electricity price of $0.241/kWh to break even while maintaining the same SAF price, representing a substantial 95% increase in electricity selling price.

Chapter 7

1. **NPV and break-even analysis**
    - C_4 heat-integrated route showcased the most promising NPV, surpassing both C_2 heat-integrated and C_4 non-heat-integrated scenarios.
    - Break-even analysis indicated lowest required selling prices for SAF ($694.65/ton) and electricity (0.163 kwh/$) in the 12th year for the C_4 heat-integrated route.
2. **Sensitivity analyses and risk management**
    - Monte Carlo simulations revealed uncertainties in NPV calculations.
    - C_4 heat-integrated case showed a 69% likelihood of achieving a net cumulative NPV between $5MM and $65MM with an 11% risk of loss.
3. **Impact of price variations on NPV and IRR**
    - Initial IRR of 12% for C_4 heat-integrated process when SAF price is $611/ton.
    - Doubling SAF price ($611 to $1222/ton) raises NPV by $65 million with a 16% IRR and a 10-year payback.

- Tripling SAF price ($611 to $1833/ton) boosts NPV by $110 million, achieving a 20% IRR and an 8-year payback, nearing traditional electricity plant NPV.

4. **Impact of UK SAF mandate policy**
    - The UK SAF mandate price (£2567/tonne) significantly affected NPV and IRR.
    - For the C_4 heat-integrated route plant, NPV increased from $21M to $210M (based on $611/ton SAF), elevating IRR to 27% and reducing payback to 6 years.
    - Implementing the SAF buy-out price also improved C_2 heat-integrated case with NPV reaching $110M from -$3M, IRR at 25%, and a shortened payback period to 7 years.

In conclusion, the heat-integrated approaches, especially the C_4 heat-integrated route-to-SAF, emerged as the most economically viable option for SAF production. Outperforming both C_2 heat-integrated and C_4 non-heat-integrated scenarios, the C_4 route exhibited promising NPV and minimal selling price requirements. Despite uncertainties revealed in sensitivity analyses, doubling and tripling SAF prices notably enhanced competitiveness.

The implementation of the SAF buy-out price from the UK SAF mandate policy significantly bolstered the economic prospects for both C_4 and C_2 heat-integrated routes, distinctly increasing their NPV and IRR.

The study underscores the potential of heat integration to generate higher revenue streams and bolster profitability within the SAF production process. However, these advantages need careful consideration against the backdrop of higher initial investment and fixed operating costs associated with heat integration. The longer payback period and sensitivity to input variables emphasize the need for a balanced evaluation of these benefits.

Moving forward, incentivizing investments and fostering the development and implementation of SAF production processes becomes crucial, especially considering the demonstrated positive impact within the C_4 and C_2 heat-integrated processes. Governments can provide tax incentives, grants, and partnerships to support SAF plant development. Tailored incentives for sustainable feedstock production, strategic use of green bonds, and multilateral support from organizations like the World Bank are crucial.

Public procurement policies, gradually increasing blending mandates, awareness campaigns, and incentives for choosing SAF-powered flights can stimulate demand for SAF. Essential incentives for emerging SAF technologies and robust infrastructure investment are vital for the seamless integration of SAF into existing supply chains.

These policy recommendations offer a holistic approach to overcoming barriers and fostering SAF adoption, encompassing incentives, partnerships, procurement policies, and infrastructure development.

8.3 Recommendations for future works

The findings presented in this thesis lead to the following recommendations:

- The use of various experimental kinetic data in ASPEN HYSYS for reactor modelling can be further improved by exploring additional experimental investigations. This enhancement aims to refine reaction mechanisms for Guerbet reactions, dimerization, and aldol-condensation within the C_2 heat-integrated scenario, thereby increasing predictive accuracy.
- Process optimisation was not considered in this study. Future studies can engage thorough process optimization efforts aimed at reducing major equipment costs and as a result the TCI, especially in the heat-integrated cases. Based on the presented models and simulations, delve deeper into specific areas of the process that contribute significantly to TCI, seeking innovative solutions or design modifications to achieve cost reductions while maintaining efficiency.
- All the SAF plants proposed in this study consume a significant amount of electricity. Exploring optimization strategies to directly address high electricity consumption within the plants can be beneficial. Identifying and rectifying energy utilization inefficiencies through equipment upgrades, process redesigns, or alternative energy sources can minimize electricity demands.
- Expand research beyond SCWG of black liquor and pot ale draft by examining additional waste carbon sources. Further research can leverage on the modelling and simulations of SCWG to evaluate the feasibility and advantages of utilizing diverse carbon sources, focusing on their impact on SAF production efficiency and sustainability.
- Moving beyond one-way and two-way sensitivity analyses, conducting advanced multi-dimensional sensitivity and uncertainty analyses for proposed routes using existing data can offer a more accurate representation of potential outcomes and risks.
- Experimenting with alternative catalysts for oligomerization based on previous insights could optimize the process for improved SAF yields by enhancing reaction rates and selectivity.

- The isobutene oligomerization reaction was conducted, but unlike the hydrogenation reaction, a kinetic fitting model was not carried out. Subsequent research efforts can concentrate on developing kinetic models through fitting for the oligomerization reaction within the C_4 scenario. By building upon existing experimental data as a foundation, conducting additional experiments, and adjusting the model, a more precise representation of reaction kinetics in the C_4 route can be achieved.
- Wild-card simulation was used in the pFBA bioreactor simulation. Future research can expand the scope of pFBA simulations beyond biomass optimization, exploring various objective functions aligned with desired product outcomes identified from previous modelling, analysing how altering objectives influences metabolic pathways and SAF production efficiency.
- Investigate additional modelling tools such as VirtualCell, NetBuilder, and Cellerator to expand bioreactor reaction pathway simulations beyond those previously employed. Compare and integrate the functionalities of these tools to broaden the understanding of aerobic gas fermentation processes.
- Explore alternative sources of bioreactor feed beyond SCWG, utilizing existing data to evaluate their potential viability. Conduct comparative analyses to assess the impact of different feed sources on SAF yields and production efficiency.
- Future studies can conduct a comprehensive Life Cycle Assessment (LCA) comparing carbon savings between C_2 and C_4 scenarios, integrating additional data and refining methodologies for a more accurate evaluation.
- Future studies can explore the economic potential of producing intermediates like iso-butanol and 2-ethylhexanol from proposed SAF plants, integrating detailed cost analyses and market feasibility studies.
- Investigation into unexplored pathways beyond previous research, considering alternative biochemical routes and reactions for SAF production for potential novel insights and discovery.

REFERENCES

[1] T.Thrasher, J.Hupe, "ICAO review: Sustainable alternative fuels for aviation," ICAO.

[2] S. Duvvuri, "Sustainable fuels The Airbus approach," EU.

[3] IATA, "IATA Fuel factsheet," *https://www.iata.org/contentassets/25e5377cf53c4e48bbaa49d252f3ab03/fact-sheet-fuel.pdf*, 2019.

[4] OECD/IEA, "Key World Energy Statistics 2016, International Energy Agency, Peris," *International Energy Agency, Peris*, 2016.

[5] EPA, "Causes of Climate Change," https://www.epa.gov/climate-change-science/causes-climate-change.

[6] "Biofuels issues and trends," in *Biofuels in the United States: Developments and Trends*, 2013.

[7] European Union, *Directive 2009/28/EC of the European Parliament and of the Council of 23 April 2009 on the promotion of the use of energy from renewable sources and amending and subsequently repealing Directives 2001/77/EC and 2003/30/EC*. EU, 2009.

[8] EU, "Renewable Energy – Recast to 2030 (RED II)," 2023. Accessed: Apr. 23, 2023. [Online]. Available: https://joint-research-centre.ec.europa.eu/welcome-jec-website/reference-regulatory-framework/renewable-energy-recast-2030-red-ii_en#:~:text=The%20RED%20II%20defines%20a,financial%20support%20by%20public%20authorities.

[9] IEA, "Technology Roadmap - Biofuels for Transport," Paris, 2011.

[10] A. Demirbaş, "Political, economic and environmental impacts of biofuels: A review," *Appl Energy*, vol. 86, Nov. 2009, doi: 10.1016/j.apenergy.2009.04.036.

[11] U.S. Energy Information Administration (EIA), "July 2020 Monthly Energy Review," May 2020.

[12] UKRI, "New competition to support Sustainable Aviation Fuel development launched," UKRI.

[13] ATAG, "Beginner's guide to aviation Biofuels," IAA.

[14] M. Köpke, C. Mihalcea, J. C. Bromley, and S. D. Simpson, "Fermentative production of ethanol from carbon monoxide," *Curr Opin Biotechnol*, vol. 22, no. 3, pp. 320–325, Jun. 2011, doi: 10.1016/j.copbio.2011.01.005.

[15] R. H. Natelson, W.-C. Wang, W. L. Roberts, and K. D. Zering, “Technoeconomic analysis of jet fuel production from hydrolysis, decarboxylation, and reforming of camelina oil,” *Biomass Bioenergy*, vol. 75, pp. 23–34, Apr. 2015, doi: 10.1016/j.biombioe.2015.02.001.

[16] E. Martinez-Hernandez, L. F. Ramírez-Verduzco, M. A. Amezcua-Allieri, and J. Aburto, “Process simulation and techno-economic analysis of bio-jet fuel and green diesel production — Minimum selling prices,” *Chemical Engineering Research and Design*, vol. 146, pp. 60–70, Jun. 2019, doi: 10.1016/j.cherd.2019.03.042.

[17] N. R. Baral *et al.*, “Techno-economic analysis and life-cycle greenhouse gas mitigation cost of five routes to bio-jet fuel blendstocks,” *Energy Environ Sci*, vol. 12, no. 3, pp. 807–824, 2019, doi: 10.1039/C8EE03266A.

[18] S. H. Mousavi-Avval and A. Shah, “Techno-economic analysis of hydroprocessed renewable jet fuel production from pennycress oilseed,” *Renewable and Sustainable Energy Reviews*, vol. 149, p. 111340, Oct. 2021, doi: 10.1016/j.rser.2021.111340.

[19] G. W. Diederichs, M. Ali Mandegari, S. Farzad, and J. F. Görgens, “Techno-economic comparison of biojet fuel production from lignocellulose, vegetable oil and sugar cane juice,” *Bioresour Technol*, vol. 216, pp. 331–339, Sep. 2016, doi: 10.1016/j.biortech.2016.05.090.

[20] K. M. Zech, S. Dietrich, M. Reichmuth, W. Weindorf, and F. Müller-Langer, “Techno-economic assessment of a renewable bio-jet-fuel production using power-to-gas,” *Appl Energy*, vol. 231, pp. 997–1006, Dec. 2018, doi: 10.1016/j.apenergy.2018.09.169.

[21] L. Tao, J. N. Markham, Z. Haq, and M. J. Biddy, “Techno-economic analysis for upgrading the biomass-derived ethanol-to-jet blendstocks,” *Green Chemistry*, vol. 19, no. 4, pp. 1082–1101, 2017, doi: 10.1039/C6GC02800D.

[22] S. N. Naik, V. v. Goud, P. K. Rout, and A. K. Dalai, “Production of first and second generation biofuels: A comprehensive review,” *Renewable and Sustainable Energy Reviews*, vol. 14, no. 2, pp. 578–597, Feb. 2010, doi: 10.1016/j.rser.2009.10.003.

[23] R. Bailey, *Another Inconvenient Truth: How Biofuel Policies are Deepening Poverty and Accelerating Climate Change*. 2008.

[24] R. L. Naylor *et al.*, “The Ripple Effect: Biofuels, Food Security, and the Environment,” *Environment: Science and Policy for Sustainable Development*, vol. 49, no. 9, pp. 30–43, Nov. 2007, doi: 10.3200/ENVT.49.9.30-43.

[25] D. Mitchel, *A Note On Rising Food Prices*. The World Bank, 2008. doi: 10.1596/1813-9450-4682.

[26] S. Axon and D. James, “The UN Sustainable Development Goals: How can sustainable chemistry contribute? A view from the chemical industry,” *Curr Opin Green Sustain Chem*, vol. 13, pp. 140–145, Oct. 2018, doi: 10.1016/j.cogsc.2018.04.010.

[27] Y. Sun and J. Cheng, “Hydrolysis of lignocellulosic materials for ethanol production: a review,” *Bioresour Technol*, vol. 83, no. 1, pp. 1–11, May 2002, doi: 10.1016/S0960-8524(01)00212-7.

[28] M. Naqvi, J. Yan, and E. Dahlquist, “Black liquor gasification integrated in pulp and paper mills: A critical review,” *Bioresour Technol*, vol. 101, no. 21, pp. 8001–8015, Nov. 2010, doi: 10.1016/j.biortech.2010.05.013.

[29] Eric D. Larson, Stefano Consonni, and Ryan E. Katofsky, “A Cost-Benefit Assessment of Biomass Gasification Power Generation in the Pulp and Paper Industry ,” Milan, 2003.

[30] G. Giner-Santonja *et al.*, “Best Available Techniques (BAT) Reference Document for the Production of Pulp, Paper and Board.” Jun. 2015. doi: 10.2791/370629.

[31] E. Ahmetović, Z. Kravanja, N. Ibrić, and I. Grossmann, *A review of recent developments of water and energy optimisation methods applied to Kraft pulp and paper mills*. 2020.

[32] A. Kruse, “Hydrothermal biomass gasification,” *J Supercrit Fluids*, vol. 47, no. 3, pp. 391–399, Jan. 2009, doi: 10.1016/j.supflu.2008.10.009.

[33] Y. Guo, S. Z. Wang, D. H. Xu, Y. M. Gong, H. H. Ma, and X. Y. Tang, “Review of catalytic supercritical water gasification for hydrogen production from biomass,” *Renewable and Sustainable Energy Reviews*, vol. 14, no. 1. 2010. doi: 10.1016/j.rser.2009.08.012.

[34] S. N. Reddy, S. Nanda, A. K. Dalai, and J. A. Kozinski, “Supercritical water gasification of biomass for hydrogen production,” *International Journal of Hydrogen Energy*, vol. 39, no. 13. 2014. doi: 10.1016/j.ijhydene.2014.02.125.

[35] M. Kumar, A. Olajire Oyedun, and A. Kumar, “A review on the current status of various hydrothermal technologies on biomass feedstock,” *Renewable and Sustainable Energy Reviews*, vol. 81, pp. 1742–1770, Jan. 2018, doi: 10.1016/j.rser.2017.05.270.

[36] A. Demirbas, “Biorefineries: Current activities and future developments,” *Energy Convers Manag*, vol. 50, no. 11, 2009, doi: 10.1016/j.enconman.2009.06.035.

[37] M. Mohammadi, G. D. Najafpour, H. Younesi, P. Lahijani, M. H. Uzir, and A. R. Mohamed, “Bioconversion of synthesis gas to second generation biofuels: A review,”

Renewable and Sustainable Energy Reviews, vol. 15, no. 9, pp. 4255–4273, Dec. 2011, doi: 10.1016/j.rser.2011.07.124.

[38] J. Daniell, M. Köpke, and S. Simpson, "Commercial Biomass Syngas Fermentation," *Energies (Basel)*, vol. 5, no. 12, pp. 5372–5417, Dec. 2012, doi: 10.3390/en5125372.

[39] Lanzatech, "World's First Commercial Waste Gas to Ethanol Plant Starts Up," https://www.lanzatech.com/2018/06/08/worlds-first-commercial-waste-gas-ethanol-plant-starts/ .

[40] Nina Parker, Mark Schneegurt, Anh-Hue Thi Tu, Philip Lister, and Brian M. Forster, "Fermentation," in *Microbiology*, Texas: OpenStax, 2016. Accessed: Nov. 25, 2023. [Online]. Available: https://openstax.org/books/microbiology/pages/1-introduction

[41] B. Molitor, E. Marcellin, and L. T. Angenent, "Overcoming the energetic limitations of syngas fermentation," *Curr Opin Chem Biol*, vol. 41, pp. 84–92, Dec. 2017, doi: 10.1016/j.cbpa.2017.10.003.

[42] C. M. Humphreys and N. P. Minton, "Advances in metabolic engineering in the microbial production of fuels and chemicals from C1 gas," *Curr Opin Biotechnol*, vol. 50, pp. 174–181, Apr. 2018, doi: 10.1016/j.copbio.2017.12.023.

[43] T. Nevzorova and V. Kutcherov, "Barriers to the wider implementation of biogas as a source of energy: A state-of-the-art review," *Energy Strategy Reviews*, vol. 26, p. 100414, 2019, doi: https://doi.org/10.1016/j.esr.2019.100414.

[44] R. Takors *et al.*, "Using gas mixtures of CO, CO_2 and H_2 as microbial substrates: the do's and don'ts of successful technology transfer from laboratory to production scale," *Microb Biotechnol*, vol. 11, no. 4, pp. 606–625, Jul. 2018, doi: 10.1111/1751-7915.13270.

[45] R. R. Bommareddy *et al.*, "A Sustainable Chemicals Manufacturing Paradigm Using CO2 and Renewable H2," *iScience*, vol. 23, no. 6, p. 101218, Jun. 2020, doi: 10.1016/j.isci.2020.101218.

[46] Q. Yan *et al.*, "Catalytic conversion wood syngas to synthetic aviation turbine fuels over a multifunctional catalyst," *Bioresour Technol*, vol. 127, pp. 281–290, Jan. 2013, doi: 10.1016/j.biortech.2012.09.069.

[47] S. Blakey, L. Rye, and C. W. Wilson, "Aviation gas turbine alternative fuels: A review," *Proceedings of the Combustion Institute*, vol. 33, no. 2, pp. 2863–2885, Jan. 2011, doi: 10.1016/j.proci.2010.09.011.

[48] Ausilio Bauen, Jo Howes, Luca Bertuccioli, and Claire Chudziak, "Review of the potential for biofuels in aviation," 2009.

[49] American Society for Testing and Materials, “Standard Specification for Aviation Turbine Fuels ASTM D1655-21c,” *American National Standard Institute*, 2021.

[50] N. Carter, R. Stratton, M. Bredehoeft, and J. Hileman, “Energy and Environmental Viability of Select Alternative Jet Fuel Pathways,” *47th AIAA/ASME/SAE/ASEE Joint Propulsion Conference and Exhibit 2011*, Jul. 2011, doi: 10.2514/6.2011-5968.

[51] ATAG, “Facts and figures,” http://www.atag.org/facts-andfigures.html.

[52] E. Gazis, B. Mawhood, R. Slade, S. d. Jong, and R. Hoefnagels, “Stakeholder analysis of the renewable jet fuels innovation system: Climate KIC RenJet project,” 2016.

[53] Jonathan Bosch, Sierk de Jong, Dr. Ric Hoefnagels, and Dr. Raphael Slade, “Aviation biofuels: strategically important, technically achievable, tough to deliver,” https://www.imperial.ac.uk/media/imperial-college/grantham-institute/public/publications/briefing-papers/BP-23-Aviation-Biofuels.pdf.

[54] US Department of Energy, “Alternative Aviation Fuels: Overview of Challenges, Opportunities, and Next Steps,” https://www.energy.gov/eere/bioenergy/downloads/alternative-aviation-fuels-overview-challenges-opportunities-and-next-steps.

[55] C. Gutiérrez-Antonio, F. I. Gómez-Castro, J. A. de Lira-Flores, and S. Hernández, “A review on the production processes of renewable jet fuel,” *Renewable and Sustainable Energy Reviews*, vol. 79, pp. 709–729, Nov. 2017, doi: 10.1016/j.rser.2017.05.108.

[56] C. Gutiérrez-Antonio, A. G. Romero-Izquierdo, F. I. Gómez-Castro, S. Hernández, and A. Briones-Ramírez, “Simultaneous energy integration and intensification of the hydrotreating process to produce biojet fuel from jatropha curcas,” *Chemical Engineering and Processing: Process Intensification*, vol. 110, pp. 134–145, Dec. 2016, doi: 10.1016/j.cep.2016.10.007.

[57] S. Maity, “Opportunities, recent trends and challenges of integrated biorefinery: Part I,” *Renewable and Sustainable Energy Reviews*, vol. 43, pp. 1427–1445, Jan. 2015, doi: 10.1016/j.rser.2014.11.092.

[58] W.-C. Wang *et al.*, “Review of Biojet Fuel Conversion Technologies,” Golden, CO (United States), Jul. 2016. doi: 10.2172/1278318.

[59] Roswitha Krautgartner, Lucile Lefebvre, Leif Erik Rehder, Mila Boshnakova, and Monica Dobrescu, “Oilseeds and Products Annual Decreasing Production of Oilseeds, Except for Soybeans,” 2015.

[60] M. L. Ghirardi *et al.*, “Microalgae: A green source of renewable H2,” *Trends in Biotechnology*, vol. 18, no. 12. 2000. doi: 10.1016/S0167-7799(00)01511-0.

[61] P. T. Pienkos and A. Darzins, “The promise and challenges of microalgal-derived biofuels,” *Biofuels, Bioproducts and Biorefining*, vol. 3, no. 4, 2009, doi: 10.1002/bbb.159.

[62] L. Brennan and P. Owende, “Biofuels from microalgae-A review of technologies for production, processing, and extractions of biofuels and co-products,” *Renewable and Sustainable Energy Reviews*, vol. 14, no. 2. 2010. doi: 10.1016/j.rser.2009.10.009.

[63] S. B. Jones *et al.*, “Production of Gasoline and Diesel from Biomass via Fast Pyrolysis, Hydrotreating and Hydrocracking: A Design Case,” Richland, WA, Feb. 2009. doi: 10.2172/950728.

[64] E. M. Grima, A. R. Medina, A. G. Giménez, J. A. Sánchez Pérez, F. G. Camacho, and J. L. García Sánchez, “Comparison between extraction of lipids and fatty acids from microalgal biomass,” *J Am Oil Chem Soc*, vol. 71, no. 9, pp. 955–959, Sep. 1994, doi: 10.1007/BF02542261.

[65] W.-C. Wang *et al.*, “Review of Biojet Fuel Conversion Technologies,” Golden, CO (United States), Jul. 2016. doi: 10.2172/1278318.

[66] ETIP Bioenergy, “European Technology and innovation platform,” *ETIP Bioenergy*, 2023. Accessed: Nov. 18, 2023. [Online]. Available: https://www.etipbioenergy.eu/value-chains/products-end-use/products/hvo-hefa

[67] JetBlue, “JetBlue Accelerates Transition to Sustainable Aviation Fuel (SAF) With Plans for the Largest-Ever Supply of SAF in New York Airports for a Commercial Airline,” *JetBlue Corporate Communications*, Sep. 2021.

[68] C. Gutiérrez-Antonio, F. I. Gómez-Castro, J. A. de Lira-Flores, and S. Hernández, “A review on the production processes of renewable jet fuel,” *Renewable and Sustainable Energy Reviews*, vol. 79, pp. 709–729, Nov. 2017, doi: 10.1016/j.rser.2017.05.108.

[69] T. N. Kalnes, M. M. McCall, and D. R. Shonnard, “Chapter 18. Renewable Diesel and Jet-Fuel Production from Fats and Oils,” 2010, pp. 468–495. doi: 10.1039/9781849732260-00468.

[70] W. C. Wang, N. Thapaliya, A. Campos, L. F. Stikeleather, and W. L. Roberts, “Hydrocarbon fuels from vegetable oils via hydrolysis and thermo-catalytic decarboxylation,” *Fuel*, vol. 95, 2012, doi: 10.1016/j.fuel.2011.12.041.

[71] F. Yang, M. A. Hanna, and R. Sun, “Value-added uses for crude glycerol--a byproduct of biodiesel production,” *Biotechnol Biofuels*, vol. 5, no. 1, 2012, doi: 10.1186/1754-6834-5-13.

[72] J. Regalbuto, “An NSF perspective on next generation hydrocarbon biorefineries,” *Comput Chem Eng*, vol. 34, no. 9, pp. 1393–1396, Sep. 2010, doi: 10.1016/j.compchemeng.2010.02.025.

[73] L. Li, E. Coppola, J. Rine, J. L. Miller, and D. Walker, “Catalytic hydrothermal conversion of triglycerides to non-ester biofuels,” *Energy and Fuels*, vol. 24, no. 2, 2010, doi: 10.1021/ef901163a.

[74] S. Bezergianni and A. Kalogianni, “Hydrocracking of used cooking oil for biofuels production,” *Bioresour Technol*, vol. 100, no. 17, pp. 3927–3932, Sep. 2009, doi: 10.1016/j.biortech.2009.03.039.

[75] D. Verma, B. S. Rana, R. Kumar, M. G. Sibi, and A. K. Sinha, “Diesel and aviation kerosene with desired aromatics from hydroprocessing of jatropha oil over hydrogenation catalysts supported on hierarchical mesoporous SAPO-11,” *Appl Catal A Gen*, vol. 490, pp. 108–116, Jan. 2015, doi: 10.1016/j.apcata.2014.11.007.

[76] A. K. Sinha, M. G. Sibi, N. Naidu, S. A. Farooqui, M. Anand, and R. Kumar, “Process Intensification for Hydroprocessing of Vegetable Oils: Experimental Study,” *Ind Eng Chem Res*, vol. 53, no. 49, pp. 19062–19070, Dec. 2014, doi: 10.1021/ie502703z.

[77] C. Gutiérrez-Antonio, A. G. Romero-Izquierdo, F. Israel Gómez-Castro, and S. Hernández, “Energy Integration of a Hydrotreatment Process for Sustainable Biojet Fuel Production,” *Ind Eng Chem Res*, vol. 55, no. 29, pp. 8165–8175, Jul. 2016, doi: 10.1021/acs.iecr.6b01439.

[78] C. Gutiérrez-Antonio, A. G. Romero-Izquierdo, F. I. Gómez-Castro, S. Hernández, and A. Briones-Ramírez, “Simultaneous energy integration and intensification of the hydrotreating process to produce biojet fuel from jatropha curcas,” *Chemical Engineering and Processing: Process Intensification*, vol. 110, pp. 134–145, Dec. 2016, doi: 10.1016/j.cep.2016.10.007.

[79] D. C. Elliott and E. G. Baker, “Process for upgrading biomass pyrolyzates,” 1989 [Online]. Available: https://www.osti.gov/biblio/866808

[80] D. C. Elliott, “Transportation fuels from biomass via fast pyrolysis and hydroprocessing,” *Wiley Interdiscip Rev Energy Environ*, vol. 2, no. 5, pp. 525–533, Sep. 2013, doi: 10.1002/wene.74.

[81] Douglas C. Elliott and Gary F. Schiefelbein, *Liquid hydrocarbon fuels from biomass*. 1989.

[82] D. C. Elliott, T. R. Hart, G. G. Neuenschwander, M. D. McKinney, M. V. Norton, and C. W. Abrams, “Environmental impacts of thermochemical biomass conversion. Final report,” Golden, CO, Jun. 1995. doi: 10.2172/71292.

[83] T. R. AULICH, C. A. WOCKEN, R. C. TIMPE, and P. PANSEGRAU, “Fuels derived from biological oils and fats,” WO2009025663, 2009

[84] Ted R. Aulich, Chad A., TimpePaul Pansegrau, and WockenRon C, “Energy efficient process to produce biologically based fuels,” 2009

[85] Yun Bao *et al.*, “Production of renewable fuels,” 2012

[86] G. W. Huber, P. O’Connor, and A. Corma, “Processing biomass in conventional oil refineries: Production of high quality diesel by hydrotreating vegetable oils in heavy vacuum oil mixtures,” *Appl Catal A Gen*, vol. 329, pp. 120–129, Oct. 2007, doi: 10.1016/j.apcata.2007.07.002.

[87] Güell B M, Bugge M, Kempegowda R S, George A, and Paap S M, “Benchmark of conversion and production technologies for synthetic biofuels for aviation,” *SINTEF Energy Research*, 2012.

[88] Ramirez-Corredores MM and Sanchez-Iglesias V, “Production of renewable biofuels,” US 20120216448, Aug. 30, 2012

[89] Parimi K and Nguyen TDT, “Methods of deoxygenation and systems for fuel production,” US 8236999, Aug. 2012

[90] Parimi K and Nguyen TDT, “Systems for fuel production,” US 8597599, Dec. 03, 2013

[91] Frey SJ, Gosling CD, Fichti GW, and Amlani A, “Reforming process for renewable aviation fuel,” US 20140005448, Jan. 02, 2014

[92] Silverman J, Resnick SM, and Mendez M, “Biorefinery system, methods and compositions thereof,” US 20140024872, Jan. 12, 2014

[93] S. Geleynse, K. Brandt, M. Garcia-Perez, M. Wolcott, and X. Zhang, “The Alcohol-to-Jet Conversion Pathway for Drop-In Biofuels: Techno-Economic Evaluation,” *ChemSusChem*, vol. 11, no. 21, pp. 3728–3741, Nov. 2018, doi: 10.1002/cssc.201801690.

[94] J. Daniell, M. Köpke, and S. Simpson, “Commercial Biomass Syngas Fermentation,” *Energies (Basel)*, vol. 5, no. 12, pp. 5372–5417, Dec. 2012, doi: 10.3390/en5125372.

[95] R. Stone and J. Medvedeff, “Emerging Company Research,” Cowen and Company.

[96] A. Milbrandt, C. Kinchin, and R. McCormick, “The Feasibility of Producing and Using Biomass-Based Diesel and Jet Fuel in the United States,” 2014, pp. 55–113.

[97] G. Yao, M. D. Staples, R. Malina, and W. E. Tyner, “Stochastic techno-economic analysis of alcohol-to-jet fuel production,” *Biotechnol Biofuels*, vol. 10, no. 1, p. 18, 2017, doi: 10.1186/s13068-017-0702-7.

[98] K. Kumar, C. N. Dasgupta, B. Nayak, P. Lindblad, and D. Das, “Development of suitable photobioreactors for CO2 sequestration addressing global warming using green algae and cyanobacteria,” *Bioresour Technol*, vol. 102, no. 8, pp. 4945–4953, Apr. 2011, doi: 10.1016/j.biortech.2011.01.054.

[99] M. Diender, A. J. M. Stams, and D. Z. Sousa, “Pathways and Bioenergetics of Anaerobic Carbon Monoxide Fermentation,” *Front Microbiol*, vol. 6, Nov. 2015, doi: 10.3389/fmicb.2015.01275.

[100] D. W. Griffin and M. A. Schultz, “Fuel and chemical products from biomass syngas: A comparison of gas fermentation to thermochemical conversion routes,” *Environ Prog Sustain Energy*, vol. 31, no. 2, pp. 219–224, Jul. 2012, doi: 10.1002/ep.11613.

[101] B. D. Heijstra, C. Leang, and A. Juminaga, “Gas fermentation: cellular engineering possibilities and scale up,” *Microb Cell Fact*, vol. 16, no. 1, p. 60, Dec. 2017, doi: 10.1186/s12934-017-0676-y.

[102] N. Scarlat, J.-F. Dallemand, and F. Fahl, “Biogas: Developments and perspectives in Europe,” *Renew Energy*, vol. 129, pp. 457–472, Dec. 2018, doi: 10.1016/j.renene.2018.03.006.

[103] J. M. Clomburg, A. M. Crumbley, and R. Gonzalez, “Industrial biomanufacturing: The future of chemical production,” *Science (1979)*, vol. 355, no. 6320, Jan. 2017, doi: 10.1126/science.aag0804.

[104] *Dictionary of Energy*. Elsevier, 2015. doi: 10.1016/C2009-0-64490-1.

[105] T. Britannica, “ Tricarboxylic acid cycle. ,” *Encyclopedia Britannica.*, Sep. 02, 2022.

[106] J. D. Enderle, “Chapter 8 - Biochemical Reactions and Enzyme Kinetics,” in *Introduction to Biomedical Engineering (Third Edition)*, J. D. Enderle and J. D. Bronzino, Eds., Boston: Academic Press, 2012, pp. 447–508. doi: https://doi.org/10.1016/B978-0-12-374979-6.00008-3.

[107] S. Holmberg and J. G. Litske Petersen, “Regulation of isoleucine-valine biosynthesis in Saccharomyces cerevisiae,” *Curr Genet*, vol. 13, no. 3, pp. 207–217, Mar. 1988, doi: 10.1007/BF00387766.

[108] T. D. Sharkey, “Discovery of the canonical Calvin–Benson cycle,” *Photosynth Res*, vol. 140, no. 2, pp. 235–252, May 2019, doi: 10.1007/s11120-018-0600-2.

[109] Ahmad M, Wolberg A, and Kahwaji CI, *Biochemistry, Electron Transport Chain.* Treasure Island (FL): StatPearls Publishing, 2023. Accessed: Dec. 17, 2023. [Online]. Available: https://www.ncbi.nlm.nih.gov/books/NBK526105/

[110] M. J. Antal, S. G. Allen, X. Dai, B. Shimizu, M. S. Tam, and M. Grønli, "Attainment of the Theoretical Yield of Carbon from Biomass," *Ind Eng Chem Res*, vol. 39, no. 11, pp. 4024–4031, Nov. 2000, doi: 10.1021/ie000511u.

[111] C. Gutiérrez-Antonio, F. I. Gómez-Castro, J. A. de Lira-Flores, and S. Hernández, "A review on the production processes of renewable jet fuel," *Renewable and Sustainable Energy Reviews*, vol. 79, pp. 709–729, Nov. 2017, doi: 10.1016/j.rser.2017.05.108.

[112] M. Asadullah, "Barriers of commercial power generation using biomass gasification gas: A review," *Renewable and Sustainable Energy Reviews*, vol. 29, pp. 201–215, Jan. 2014, doi: 10.1016/j.rser.2013.08.074.

[113] A. Dutta *et al.*, "Process Design and Economics for Conversion of Lignocellulosic Biomass to Ethanol: Thermochemical Pathway by Indirect Gasification and Mixed Alcohol Synthesis," Golden, CO (United States), May 2011. doi: 10.2172/1015885.

[114] R. Rauch, J. Hrbek, and H. Hofbauer, "Biomass gasification for synthesis gas production and applications of the syngas," *Wiley Interdiscip Rev Energy Environ*, vol. 3, no. 4, pp. 343–362, Jul. 2014, doi: 10.1002/wene.97.

[115] M. A. Hastaoglu and M. S. Hassam, "Application of a general gas-solid reaction model to flash pyrolysis of wood in a circulating fluidized bed," *Fuel*, vol. 74, no. 5, pp. 697–703, May 1995, doi: 10.1016/0016-2361(94)00010-O.

[116] M. L. Hobbs, P. T. Radulovic, and L. D. Smoot, "Modeling fixed-bed coal gasifiers," *AIChE Journal*, vol. 38, no. 5, pp. 681–702, May 1992, doi: 10.1002/aic.690380506.

[117] S. Chopra and A. Jain, "A review of fixed bed gasification systems for biomass," *Agricultural Engineering International: CIGR Journal*, vol. 9, May 2007.

[118] C. Dejtrakulwong and S. Patumsawad, "Four Zones Modeling of the Downdraft Biomass Gasification Process: Effects of Moisture Content and Air to Fuel Ratio," *Energy Procedia*, vol. 52, pp. 142–149, 2014, doi: 10.1016/j.egypro.2014.07.064.

[119] O. Yucel and M. A. Hastaoglu, "Kinetic modeling and simulation of throated downdraft gasifier," *Fuel Processing Technology*, vol. 144, pp. 145–154, Apr. 2016, doi: 10.1016/j.fuproc.2015.12.023.

[120] A. Kruse and A. Gawlik, "Biomass Conversion in Water at 330−410 °C and 30−50 MPa. Identification of Key Compounds for Indicating Different Chemical Reaction

Pathways," *Ind Eng Chem Res*, vol. 42, no. 2, pp. 267–279, Jan. 2003, doi: 10.1021/ie0202773.

[121] A. C. P. Borges *et al.*, "Catalytic supercritical water gasification of eucalyptus wood chips in a batch reactor," *Fuel*, vol. 255, p. 115804, Nov. 2019, doi: 10.1016/j.fuel.2019.115804.

[122] J. A. Okolie, R. Rana, S. Nanda, A. K. Dalai, and J. A. Kozinski, "Supercritical water gasification of biomass: a state-of-the-art review of process parameters, reaction mechanisms and catalysis," *Sustain Energy Fuels*, vol. 3, no. 3, pp. 578–598, 2019, doi: 10.1039/C8SE00565F.

[123] Marc Alvarado, "Methanol," Feb. 2016.

[124] Methanol Institute, "Methanol Gasoline Blends," Washinghton DC, SIngapore, 2016.

[125] X. Xiaoding and J. A. Moulijn, "Mitigation of CO_2 by Chemical Conversion: Plausible Chemical Reactions and Promising Products," *Energy & Fuels*, vol. 10, no. 2, pp. 305–325, Mar. 1996, doi: 10.1021/ef9501511.

[126] Caroline Burgess Clifford, "Fischer-Tropsch Process to Generate Liquid Fuels," https://www.e-education.psu.edu/egee439/node/679.

[127] O. Martin *et al.*, "Indium Oxide as a Superior Catalyst for Methanol Synthesis by CO_2 Hydrogenation," *Angewandte Chemie International Edition*, vol. 55, no. 21, pp. 6261–6265, May 2016, doi: 10.1002/anie.201600943.

[128] M. D. Porosoff, B. Yan, and J. G. Chen, "Catalytic reduction of CO_2 by H_2 for synthesis of CO, methanol and hydrocarbons: challenges and opportunities," *Energy Environ Sci*, vol. 9, no. 1, pp. 62–73, 2016, doi: 10.1039/C5EE02657A.

[129] CRI, "World's Largest CO2 Methanol Plant," www.carbonrecycling.is/george-olah/2016/2/14/worlds-largest-co2-methanol-plant.

[130] W. L. Becker, R. J. Braun, M. Penev, and M. Melaina, "Production of Fischer–Tropsch liquid fuels from high temperature solid oxide co-electrolysis units," *Energy*, vol. 47, no. 1, pp. 99–115, Nov. 2012, doi: 10.1016/j.energy.2012.08.047.

[131] A.A. Avidan in:, D.M. Bibby, C.D. Chang, S. Yurchak, and R.F. Howe, *Methane Conversion*, 36th ed. Elsevier Science, 1988.

[132] Tabak S A, A. A. Avidan, and F. J. Krambeck, "Production of synthetic gasoline and diesel fuel from nonpetroleum resources," Apr. 1986.

[133] G. Liu, B. Yan, and G. Chen, "Technical review on jet fuel production," *Renewable and Sustainable Energy Reviews*, vol. 25, pp. 59–70, Sep. 2013, doi: 10.1016/j.rser.2013.03.025.

[134] British Airways, “GreenSky project prepares to land in Thurrock,” https://www.britishairways.com/en-gb/bamediacentre/newsarticles?ArticleID=20140416080250#. VkTzBHarQdU.

[135] B. C. Folkedahl, A. C. Snyder, J. R. Strege, and S. J. Bjorgaard, “Process development and demonstration of coal and biomass indirect liquefaction to synthetic iso-paraffinic kerosene,” *Fuel Processing Technology*, vol. 92, no. 10, pp. 1939–1945, Oct. 2011, doi: 10.1016/j.fuproc.2011.05.013.

[136] J. A. Okolie, R. Rana, S. Nanda, A. K. Dalai, and J. A. Kozinski, “Supercritical water gasification of biomass: a state-of-the-art review of process parameters, reaction mechanisms and catalysis,” *Sustain Energy Fuels*, vol. 3, no. 3, pp. 578–598, 2019, doi: 10.1039/C8SE00565F.

[137] E. M. Moghaddam, A. Goel, M. Siedlecki, K. Michalska, O. Yakaboylu, and W. de Jong, “Supercritical water gasification of wet biomass residues from farming and food production practices: lab-scale experiments and comparison of different modelling approaches,” *Sustain Energy Fuels*, vol. 5, no. 5, pp. 1521–1537, 2021, doi: 10.1039/D0SE01635G.

[138] H. N. Abubackar, M. C. Veiga, and C. Kennes, “Biological conversion of carbon monoxide: rich syngas or waste gases to bioethanol,” *Biofuels, Bioproducts and Biorefining*, vol. 5, no. 1, pp. 93–114, Jan. 2011, doi: 10.1002/bbb.256.

[139] P. C. Munasinghe and S. K. Khanal, “Biomass-derived syngas fermentation into biofuels: Opportunities and challenges,” *Bioresour Technol*, vol. 101, no. 13, pp. 5013–5022, Jul. 2010, doi: 10.1016/J.BIORTECH.2009.12.098.

[140] J. W. Mirwald and O. R. Inderwildi, “Unraveling the Fischer–Tropsch mechanism: a combined DFT and microkinetic investigation of C–C bond formation on Ru,” *Physical Chemistry Chemical Physics*, vol. 14, no. 19, p. 7028, 2012, doi: 10.1039/c2cp23394k.

[141] B. H. Davis, “Fischer–Tropsch Synthesis: Reaction mechanisms for iron catalysts,” *Catal Today*, vol. 141, no. 1–2, pp. 25–33, Mar. 2009, doi: 10.1016/J.CATTOD.2008.03.005.

[142] M. E. Dry, “The Fischer–Tropsch process: 1950–2000,” *Catal Today*, vol. 71, no. 3–4, pp. 227–241, Jan. 2002, doi: 10.1016/S0920-5861(01)00453-9.

[143] E. van Steen and M. Claeys, “Fischer-Tropsch Catalysts for the Biomass-to-Liquid (BTL)-Process,” *Chem Eng Technol*, vol. 31, no. 5, pp. 655–666, May 2008, doi: 10.1002/ceat.200800067.

[144] Z. J. Wang *et al.*, “Quantitative Policy Analysis for Sustainable Aviation Fuel Production Technologies,” *Front Energy Res*, vol. 9, Dec. 2021, doi: 10.3389/fenrg.2021.751722.

[145] B. P. Sharma, T. E. Yu, B. C. English, and C. N. Boyer, “Economic Analysis of Developing a Sustainable Aviation Fuel Supply Chain Incorporating With Carbon Credits: A Case Study of the Memphis International Airport,” *Front Energy Res*, vol. 9, Dec. 2021, doi: 10.3389/fenrg.2021.775389.

[146] H. Heiskanen, I. Virkajärvi, and L. Viikari, “The effect of syngas composition on the growth and product formation of Butyribacterium methylotrophicum,” *Enzyme Microb Technol*, vol. 41, no. 3, pp. 362–367, Aug. 2007, doi: 10.1016/J.ENZMICTEC.2007.03.004.

[147] J. L. Vega, K. T. Klasson, D. E. Kimmel, E. C. Clausen, and J. L. Gaddy, “Sulfur gas tolerance and toxicity of co-utilizing and methanogenic bacteria,” *Appl Biochem Biotechnol*, vol. 24–25, no. 1, pp. 329–340, Mar. 1990, doi: 10.1007/BF02920257.

[148] W. E. Mabee *et al.*, “Updates on Softwood-to-Ethanol Process Development,” *Appl Biochem Biotechnol*, vol. 129, no. 1–3, pp. 55–70, 2006, doi: 10.1385/ABAB:129:1:55.

[149] E. Almeida Benalcázar, H. Noorman, R. Maciel Filho, and J. A. Posada, “Decarbonizing ethanol production via gas fermentation: Impact of the CO/H2/CO2 mix source on greenhouse gas emissions and production costs,” *Comput Chem Eng*, vol. 159, p. 107670, Mar. 2022, doi: 10.1016/j.compchemeng.2022.107670.

[150] A. Hussain *et al.*, “Advances in microbial metabolic engineering for the production of butanol isomers (isobutanol and 1-butanol) from a various biomass,” *Bioenergy Res*, vol. 15, no. 4, pp. 1854–1871, Dec. 2022, doi: 10.1007/s12155-022-10410-8.

[151] P. Jeevitha, J. Ranjitha, M. Anand, S. Mahboob, and S. Vijayalakshmi, “Production of pyruvic acid into value-added products using genetically modified microbes,” in *Valorization of Biomass to Bioproducts*, Elsevier, 2023, pp. 117–134. doi: 10.1016/B978-0-12-822888-3.00012-8.

[152] J. Panich, B. Fong, and S. W. Singer, “Metabolic Engineering of Cupriavidus necator H16 for Sustainable Biofuels from CO2,” *Trends Biotechnol*, vol. 39, no. 4, pp. 412–424, Apr. 2021, doi: 10.1016/j.tibtech.2021.01.001.

[153] C. Matano, T. M. Meiswinkel, and V. F. Wendisch, “Amino Acid Production from Rice Straw Hydrolyzates,” in *Wheat and Rice in Disease Prevention and Health*, Elsevier, 2014, pp. 493–505. doi: 10.1016/B978-0-12-401716-0.00038-6.

[154] M. Eram and K. Ma, “Decarboxylation of Pyruvate to Acetaldehyde for Ethanol Production by Hyperthermophiles,” *Biomolecules*, vol. 3, no. 4, pp. 578–596, Aug. 2013, doi: 10.3390/biom3030578.

[155] L. A. Hazelwood, J.-M. Daran, A. J. A. van Maris, J. T. Pronk, and J. R. Dickinson, “The Ehrlich Pathway for Fusel Alcohol Production: a Century of Research on *Saccharomyces cerevisiae* Metabolism,” *Appl Environ Microbiol*, vol. 74, no. 8, pp. 2259–2266, Apr. 2008, doi: 10.1128/AEM.02625-07.

[156] M. Magdeldin and M. Järvinen, “Supercritical water gasification of Kraft black liquor: Process design, analysis, pulp mill integration and economic evaluation,” *Appl Energy*, vol. 262, p. 114558, Mar. 2020, doi: 10.1016/j.apenergy.2020.114558.

[157] S. Rodgers *et al.*, “Reconciling the Sustainable Manufacturing of Commodity Chemicals with Feasible Technoeconomic Outcomes : Assessing the investment case for heat integrated aerobic gas fermentation,” *Johnson Matthey Technology Review*, vol. 65, no. 3, pp. 375–394, Jul. 2021, doi: 10.1595/205651321X16137377305390.

[158] Y. Hu, M. Gong, X. Xing, H. Wang, Y. Zeng, and C. C. Xu, “Supercritical water gasification of biomass model compounds: A review,” *Renewable and Sustainable Energy Reviews*, vol. 118, p. 109529, Feb. 2020, doi: 10.1016/j.rser.2019.109529.

[159] J. A. Okolie, R. Rana, S. Nanda, A. K. Dalai, and J. A. Kozinski, “Supercritical water gasification of biomass: a state-of-the-art review of process parameters, reaction mechanisms and catalysis,” *Sustain Energy Fuels*, vol. 3, no. 3, pp. 578–598, 2019, doi: 10.1039/C8SE00565F.

[160] C. Li, W. Jia, and X. Wu, “Application of Lee-Kesler equation of state to calculating compressibility factors of high pressure condensate gas,” *Energy Procedia*, vol. 14, pp. 115–120, 2012, doi: 10.1016/j.egypro.2011.12.904.

[161] G. J. DiLeo, M. E. Neff, and P. E. Savage, “Gasification of Guaiacol and Phenol in Supercritical Water,” *Energy & Fuels*, vol. 21, no. 4, pp. 2340–2345, Jul. 2007, doi: 10.1021/ef070056f.

[162] C. Carlini, A. Macinai, A. M. Raspolli Galletti, and G. Sbrana, “Selective synthesis of 2-ethyl-1-hexanol from n-butanol through the Guerbet reaction by using bifunctional catalysts based on copper or palladium precursors and sodium butoxide,” *J Mol Catal A Chem*, vol. 212, no. 1–2, pp. 65–70, Apr. 2004, doi: 10.1016/j.molcata.2003.10.045.

[163] S. Rodgers *et al.*, “Reconciling the Sustainable Manufacturing of Commodity Chemicals with Feasible Technoeconomic Outcomes : Assessing the investment case

for heat integrated aerobic gas fermentation," *Johnson Matthey Technology Review*, vol. 65, no. 3, pp. 375–394, Jul. 2021, doi: 10.1595/205651321X16137377305390.

[164] Z. D. Young, S. Hanspal, and R. J. Davis, "Aldol Condensation of Acetaldehyde over Titania, Hydroxyapatite, and Magnesia," *ACS Catal*, vol. 6, no. 5, pp. 3193–3202, May 2016, doi: 10.1021/acscatal.6b00264.

[165] M. E. Grass, R. M. Rioux, and G. A. Somorjai, "Dependence of Gas-Phase Crotonaldehyde Hydrogenation Selectivity and Activity on the Size of Pt Nanoparticles (1.7–7.1 nm) Supported on SBA-15," *Catal Letters*, vol. 128, no. 1, pp. 1–8, 2009, doi: 10.1007/s10562-008-9754-4.

[166] X. Han, S. Li, H. An, X. Zhao, and Y. Wang, "Improvement of *n* -butanol Guerbet condensation: a reaction integration of *n* -butanol Guerbet condensation and 1,1-dibutoxybutane hydrolysis," *React Chem Eng*, vol. 6, no. 10, pp. 1845–1853, 2021, doi: 10.1039/D1RE00206F.

[167] D. Jiang, X. Wu, J. Mao, J. Ni, and X. Li, "Continuous catalytic upgrading of ethanol to n-butanol over Cu–CeO_2/AC catalysts," *Chemical Communications*, vol. 52, no. 95, pp. 13749–13752, 2016, doi: 10.1039/C6CC05860D.

[168] X. Han, H. An, X. Zhao, and Y. Wang, "Influence of acid-base properties on the catalytic performance of Ni/hydroxyapatite in n-butanol Guerbet condensation," *Catal Commun*, vol. 146, p. 106130, Nov. 2020, doi: 10.1016/j.catcom.2020.106130.

[169] R. Miller and G. Bennett, "Producing 2-Ethylhexanol by the Guerbet Reaction," *Ind Eng Chem*, vol. 53, no. 1, pp. 33–36, Jan. 1961, doi: 10.1021/ie50613a027.

[170] Drochaid research institute, "Dehydration of 2-ethylhexanol to 2 ethyl-1-hexene," 2021.

[171] Z. Jian *et al.*, "Black liquor increases methane production from excess pulp and paper industry sludge," *Chemosphere*, vol. 280, p. 130665, Oct. 2021, doi: 10.1016/j.chemosphere.2021.130665.

[172] W. D. Seider, *Product and process design principles : synthesis, analysis, and evaluation*. Second edition. New York : Wiley, [2004] ©2004. [Online]. Available: https://search.library.wisc.edu/catalog/999975575102121

[173] G. P. Rangaiah and A. Bonilla-Petriciolet, Eds., *Multi-Objective Optimization in Chemical Engineering*. Oxford, UK: John Wiley & Sons Ltd, 2013. doi: 10.1002/9781118341704.

[174] D. Humbird *et al.*, "Process Design and Economics for Biochemical Conversion of Lignocellulosic Biomass to Ethanol: Dilute-Acid Pretreatment and Enzymatic

Hydrolysis of Corn Stover," Golden, CO (United States), Mar. 2011. doi: 10.2172/1013269.

[175] M. S. Ray, "Coulson and Richardson's Chemical Engineering Volume 6 (Design), 2nd Edition, by R.K. Sinnott, Pergamon Press, Oxford, UK (1993). 954 pages. ISBN 0-08-041865-1.," *Developments in Chemical Engineering and Mineral Processing*, vol. 2, no. 4, pp. 254–255, May 2008, doi: 10.1002/apj.5500020410.

[176] *Sustainable Design Through Process Integration*. Elsevier, 2017. doi: 10.1016/C2015-0-00309-4.

[177] Scott Jenkins, "2019 CHEMICAL ENGINEERING PLANT COST INDEX ANNUAL AVERAGE," Chemical Engineering Online .

[178] *Chemical Engineering Design*. Elsevier, 2013. doi: 10.1016/C2009-0-61216-2.

[179] D. C. Y. Foo *et al.*, *Chemical engineering process simulation*. 2017.

[180] ICIS, "Ammonia Prices, Markets & Analysis," https://www.icis.com/explore/commodities/chemicals/ammonia/.

[181] S. H. Krishna *et al.*, "Oxygenated commodity chemicals from chemo-catalytic conversion of biomass derived heterocycles," *AIChE Journal*, vol. 64, no. 6, pp. 1910–1922, Jun. 2018, doi: 10.1002/aic.16172.

[182] Henry Edwardes-Evans, "Green hydrogen costs need to fall over 50% to be viable: S&P Global Ratings," S & P Global Platts.

[183] Index Mundi, "Jet fuel daily price," *https://www.indexmundi.com/commodities/?commodity=jet-fuel&months=180*.

[184] Z. Ming, L. Ximei, L. Na, and X. Song, "Overall review of renewable energy tariff policy in China: Evolution, implementation, problems and countermeasures," *Renewable and Sustainable Energy Reviews*, vol. 25, pp. 260–271, Sep. 2013, doi: 10.1016/j.rser.2013.04.026.

[185] C. M. Kinchin, "BETO Biofuels TEA Database," BioEnergy - Knowledge Discovery framework.

[186] P. Floquet, L. Pibouleau, and S. Domenech, "Separation sequence synthesis: How to use simulated annealing procedure?," *Comput Chem Eng*, vol. 18, no. 11–12, pp. 1141–1148, Nov. 1994, doi: 10.1016/0098-1354(94)E0023-G.

[187] E. Commission, S. A. and I. Directorate-General for Employment, A. Fulvimari, U. Temursho, A. Vaitkeviciute, and M. Weitzel, *Economic and distributional effects of higher energy prices on households in the EU :* Publications Office of the European Union, 2023. doi: doi/10.2767/49249.

[188] K. Tanabe, “Industrial application of solid acid–base catalysts,” *Appl Catal A Gen*, vol. 181, no. 2, pp. 399–434, May 1999, doi: 10.1016/S0926-860X(98)00397-4.

[189] N. Rahimi and R. Karimzadeh, “Catalytic cracking of hydrocarbons over modified ZSM-5 zeolites to produce light olefins: A review,” *Appl Catal A Gen*, vol. 398, no. 1–2, pp. 1–17, May 2011, doi: 10.1016/j.apcata.2011.03.009.

[190] C. T. O’Connor and M. Kojima, “Alkene oligomerization,” *Catal Today*, vol. 6, no. 3, pp. 329–349, Jan. 1990, doi: 10.1016/0920-5861(90)85008-C.

[191] M. Sanati, C. Hörnell, and S. G. Järäs, “The oligomerization of alkenes by heterogeneous catalysts,” pp. 236–288. doi: 10.1039/9781847553263-00236.

[192] V. N. Ipatieff and G. Egloff, “Oligomerization of olefins over phosphorus acid,” *Oil Gas* , vol. 33, no. 52, pp. 31–35, 1934.

[193] F. C. Whitmore and P. L. Meunier, “The Polymerization of Olefins. VI. [1] The Dimers Obtained from Tetramethylethylene. Preliminary Paper [2],” *J Am Chem Soc*, vol. 63, no. 8, pp. 2197–2199, Aug. 1941, doi: 10.1021/ja01853a048.

[194] F. C. Whitmore, W. S. Ropp, and N. C. Cook, “The Dimerization of Triptene with Sulfuric Acid [1],” *J Am Chem Soc*, vol. 72, no. 4, pp. 1507–1511, Apr. 1950, doi: 10.1021/ja01160a022.

[195] M. Bjørgen, K.-P. Lillerud, U. Olsbye, S. Bordiga, and A. Zecchina, “1-Butene Oligomerization in Brönsted Acidic Zeolites: Mechanistic Insights from Low-Temperature in Situ FTIR Spectroscopy,” *J Phys Chem B*, vol. 108, no. 23, pp. 7862–7870, Jun. 2004, doi: 10.1021/jp0377836.

[196] J. P. van den Berg, J. P. Wolthuizen, A. D. H. Clague, G. R. Hays, R. Huis, and J. H. C. van Hooff, “Low-temperature oligomerization of small olefins on zeolite H-ZSM-5. An investigation with high-resolution solid-state 13C-NMR,” *J Catal*, vol. 80, no. 1, pp. 130–138, Mar. 1983, doi: 10.1016/0021-9517(83)90237-3.

[197] D.D. Eley, H. Pines, and P.B. Weisz, “Advances in Catalysis,” *Academic Press, New York*, vol. 31, p. 34, 1982.

[198] S.A. Tabak, “US Patent ,” 24233, 1981

[199] I. M. Abrams and J. R. Millar, “A history of the origin and development of macroporous ion-exchange resins,” *React Funct Polym*, vol. 35, no. 1–2, pp. 7–22, Dec. 1997, doi: 10.1016/S1381-5148(97)00058-8.

[200] A. Chakrabarti and M. M. Sharma, “Cationic ion exchange resins as catalyst,” *Reactive Polymers*, vol. 20, no. 1–2, pp. 1–45, Jul. 1993, doi: 10.1016/0923-1137(93)90064-M.

[201] V. M. T. M. Silva and A. E. Rodrigues, “Kinetic studies in a batch reactor using ion exchange resin catalysts for oxygenates production: Role of mass transfer mechanisms,” *Chem Eng Sci*, vol. 61, no. 2, pp. 316–331, Jan. 2006, doi: 10.1016/j.ces.2005.07.017.

[202] B. C. Gates, H. K. G. Ertl, F. Schüth, J. Weitkamp, and Verlag Chemie, *Catalysis by Ion-Exchange Resins*, 2nd Edition., vol. Vol. 1. Weinheim, 2008.

[203] F. G. Helfferich, “Ion Exchange: Past, Present, and Future,” in *Ion Exchange: Science and Technology*, Dordrecht: Springer Netherlands, 1986, pp. 23–32. doi: 10.1007/978-94-009-4376-6_2.

[204] D. A. Keyworth, “Process for the oligomerization of propylene,” US 4579990, Apr. 01, 1986

[205] B. C. Gates, “ Catalytic Chemistry,” *John Wiley & Sons, Inc, New York*, 1992.

[206] M. Aslam, G. P. Torrence, and E. G. Zey, “Esterification,” in *Kirk-Othmer Encyclopedia of Chemical Technology*, Hoboken, NJ, USA: John Wiley & Sons, Inc., 2000. doi: 10.1002/0471238961.0519200501191201.a01.

[207] M. L. Honkela, A. Root, M. Lindblad, and A. O. I. Krause, “Comparison of ion-exchange resin catalysts in the dimerisation of isobutene,” *Appl Catal A Gen*, vol. 295, no. 2, pp. 216–223, Nov. 2005, doi: 10.1016/j.apcata.2005.08.023.

[208] E.T. Marquis, L.W. Watts, W.H. Brader, and J.W. Darden, “Oligomerized higher olefins,” GB 2089832, Nov. 13, 1981

[209] M. A. Harmer and Q. Sun, “Solid acid catalysis using ion-exchange resins,” *Appl Catal A Gen*, vol. 221, no. 1–2, pp. 45–62, Nov. 2001, doi: 10.1016/S0926-860X(01)00794-3.

[210] M. di Girolamo and M. Marchionna, “Acidic and basic ion exchange resins for industrial applications,” *J Mol Catal A Chem*, vol. 177, no. 1, pp. 33–40, Dec. 2001, doi: 10.1016/S1381-1169(01)00307-7.

[211] R. P. v. Faria, C. S. M. Pereira, V. M. T. M. Silva, J. M. Loureiro, and A. E. Rodrigues, “Glycerol Valorization as Biofuel: Thermodynamic and Kinetic Study of the Acetalization of Glycerol with Acetaldehyde,” *Ind Eng Chem Res*, vol. 52, no. 4, pp. 1538–1547, Jan. 2013, doi: 10.1021/ie302935w.

[212] K. Suwannakarn, E. Lotero, and J. G. Goodwin, “Solid Brønsted Acid Catalysis in the Gas-Phase Esterification of Acetic Acid,” *Ind Eng Chem Res*, vol. 46, no. 22, pp. 7050–7056, Oct. 2007, doi: 10.1021/ie070536u.

[213] F. dos R. Gonçalves, L. E. P. Borges, and C. P. Borges, “Synthesis of Ethyl Acetate by Coupling a Heterogeneous Catalytic System with a Pervaporation Unit,” *Sep Sci Technol*, vol. 39, no. 7, pp. 1485–1500, Jan. 2005, doi: 10.1081/SS-120030796.

[214] K. C. de S. Figueiredo, V. M. M. Salim, and C. P. Borges, “Synthesis and characterization of a catalytic membrane for pervaporation-assisted esterification reactors,” *Catal Today*, vol. 133–135, pp. 809–814, Apr. 2008, doi: 10.1016/j.cattod.2007.12.088.

[215] M. M. Sharma, “Some novel aspects of cationic ion-exchange resins as catalysts,” *React Funct Polym*, vol. 26, no. 1–3, pp. 3–23, Sep. 1995, doi: 10.1016/1381-5148(95)00029-F.

[216] Y. i-Woong, Jong-San Chang, and Sung-Hwa Jhung, “Trimerization of Isobutene over Solid Acid Catalysts: Comparison between Cation-exchange Resin and Zeolite Catalysts,” *Bull Korean Chem Soc*, vol. 29, no. 2, pp. 339–341, Feb. 2008, doi: 10.5012/bkcs.2008.29.2.339.

[217] Ji-Woong Yoon, Sung-Hwa Jhung, Ji-Sun Lee, and Tae-Jin Kim, “Effect of Butadiene in Catalytic Trimerization of Isobutene Using Commercial C $_4$ Feeds,” *Bull Korean Chem Soc*, vol. 29, no. 1, pp. 57–60, Jan. 2008, doi: 10.5012/bkcs.2008.29.1.057.

[218] M. Cadenas, R. Bringué, C. Fité, E. Ramírez, and F. Cunill, “Liquid-Phase Oligomerization of 1-Hexene Catalyzed by Macroporous Ion-Exchange Resins,” *Top Catal*, vol. 54, no. 13–15, pp. 998–1008, Sep. 2011, doi: 10.1007/s11244-011-9721-y.

[219] M. Granollers *et al.*, “Isoamylene Trimerization in Liquid-Phase over Ion Exchange Resins and Zeolites,” *Ind Eng Chem Res*, vol. 49, no. 8, pp. 3561–3570, Apr. 2010, doi: 10.1021/ie901382p.

[220] G.S. Grover and R.V. Chaudhari, “Selective Dimerization of Isobutene using a cation exchange resin catalyst,” in *Recent Developments in Catalysis: Theory and Practice*, B. Viswanathan and C. N. Pillai, Eds., 1991, pp. 345–355.

[221] A. Kolah, Z. Qi, and S. M. Mahajani, “Dimerized isobutene: An alternative to MTBE - Indirect alkylation produces branched paraffin dimers, providing a viable substitute for MTBE in gasoline.,” *Chemical Innovation*, vol. 31, pp. 15-+, Mar. 2001.

[222] K. Hauge, E. Bergene, D. Chen, G. R. Fredriksen, and A. Holmen, “Oligomerization of isobutene over solid acid catalysts,” *Catal Today*, vol. 100, no. 3–4, pp. 463–466, Feb. 2005, doi: 10.1016/J.CATTOD.2004.08.017.

[223] B. Moermans, W. de Beuckelaer, I. F. J. Vankelecom, R. Ravishankar, J. A. Martens, and P. A. Jacobs, “Incorporation of nano-sized zeolites in membranes,” *Chemical Communications*, no. 24, pp. 2467–2468, 2000, doi: 10.1039/b007435g.

[224] J. A. Martens, W. H. Verrelst, G. M. Mathys, S. H. Brown, and P. A. Jacobs, “Tailored Catalytic Propene Trimerization over Acidic Zeolites with Tubular Pores,” *Angewandte Chemie International Edition*, vol. 44, no. 35, pp. 5687–5690, Sep. 2005, doi: 10.1002/anie.200463045.

[225] J.-W. Yoon, S.-H. Jhung, N.-H. Jang, J.-S. Chang, T.-J. Kim, and H.-D. Lee, “Trimerization of Isobutene over Solid Acid Catalysts under Wide Reaction Conditions,” *Bull Korean Chem Soc*, vol. 28, no. 11, pp. 2075–2078, Nov. 2007, doi: 10.5012/bkcs.2007.28.11.2075.

[226] M. Marchionna, M. di Girolamo, and R. Patrini, “Light olefins dimerization to high quality gasoline components,” *Catal Today*, vol. 65, no. 2–4, pp. 397–403, Feb. 2001, doi: 10.1016/S0920-5861(00)00587-3.

[227] Y. Wang, C. Feng, Z. Jin, J. Zhang, J. Yang, and S. Zhang, “A novel N-doped TiO2 with high visible light photocatalytic activity,” *J Mol Catal A Chem*, vol. 260, pp. 1–3, Dec. 2006, doi: 10.1016/j.molcata.2006.06.044.

[228] S.-H. JHUNG, J.-S. CHANG, J. W. YOON, T.-J. KIM, D. H. CHOO, and H.-D. LEE, “PREPARATION METHOD OF LIGHT OLEFIN TRIMERS AND PRODUCTION OF HEAVY ALKYLATES BY USING THEREOF,” WO/2007/091862, 2007

[229] J. W. Yoon, J. S. Chang, H. du Lee, T. J. Kim, and S. H. Jhung, “Trimerization of isobutene over a zeolite beta catalyst,” *J Catal*, vol. 245, no. 1, pp. 253–256, Jan. 2007, doi: 10.1016/J.JCAT.2006.10.008.

[230] J. S. Lee, J. W. Yoon, S. B. Halligudi, J. S. Chang, and S. H. Jhung, “Trimerization of isobutene over WOx/ZrO2 catalysts,” *Appl Catal A Gen*, vol. 366, no. 2, pp. 299–303, Sep. 2009, doi: 10.1016/J.APCATA.2009.07.016.

[231] S. Peratello, “Olefins oligomerization: thermodynamics and kinetics over a mesoporous silica–alumina,” *Catal Today*, vol. 52, no. 2–3, pp. 271–277, Sep. 1999, doi: 10.1016/S0920-5861(99)00081-4.

[232] R. Alcántara, E. Alcántara, L. Canoira, M. J. Franco, M. Herrera, and A. Navarro, “Trimerization of isobutene over Amberlyst-15 catalyst,” *React Funct Polym*, vol. 45, no. 1, pp. 19–27, Aug. 2000, doi: 10.1016/S1381-5148(00)00004-3.

[233] M. Konkol, W. Wróbel, R. Bicki, and A. Gołębiowski, “The Influence of the Hydrogen Pressure on Kinetics of the Canola Oil Hydrogenation on Industrial Nickel Catalyst,” *Catalysts*, vol. 6, no. 4, p. 55, Apr. 2016, doi: 10.3390/catal6040055.

[234] L. Rachbauer, G. Bochmann, and W. Fuchs, “Chapter 4 Gas fermentation,” in *The Autotrophic Biorefinery*, De Gruyter, 2021, pp. 85–112. doi: 10.1515/9783110550603-004.

[235] M. Hucka *et al.*, “The systems biology markup language (SBML): a medium for representation and exchange of biochemical network models,” *Bioinformatics*, vol. 19, no. 4, pp. 524–531, Mar. 2003, doi: 10.1093/bioinformatics/btg015.

[236] H. Pan, J. Wang, H. Wu, Z. Li, and J. Lian, “Synthetic biology toolkit for engineering Cupriviadus necator H16 as a platform for CO2 valorization,” *Biotechnol Biofuels*, vol. 14, no. 1, p. 212, Dec. 2021, doi: 10.1186/s13068-021-02063-0.

[237] J. Lu, C. J. Brigham, J. K. Plassmeier, and A. J. Sinskey, “Characterization and modification of enzymes in the 2-ketoisovalerate biosynthesis pathway of Ralstonia eutropha H16,” *Appl Microbiol Biotechnol*, vol. 99, no. 2, pp. 761–774, Jan. 2015, doi: 10.1007/s00253-014-5965-3.

[238] J. Lu, C. J. Brigham, J. K. Plassmeier, and A. J. Sinskey, “Characterization and modification of enzymes in the 2-ketoisovalerate biosynthesis pathway of Ralstonia eutropha H16,” *Appl Microbiol Biotechnol*, vol. 99, no. 2, pp. 761–774, Jan. 2015, doi: 10.1007/s00253-014-5965-3.

[239] N. E. Lewis *et al.*, “Omic data from evolved *E. coli* are consistent with computed optimal growth from genome-scale models,” *Mol Syst Biol*, vol. 6, no. 1, p. 390, Jan. 2010, doi: 10.1038/msb.2010.47.

[240] R. Wahid, D. G. Mulat, J. C. Gaby, and S. J. Horn, “Effects of H2:CO2 ratio and H2 supply fluctuation on methane content and microbial community composition during in-situ biological biogas upgrading,” *Biotechnol Biofuels*, vol. 12, no. 1, p. 104, Dec. 2019, doi: 10.1186/s13068-019-1443-6.

[241] J. Yu and P. Munasinghe, “Gas Fermentation Enhancement for Chemolithotrophic Growth of Cupriavidus necator on Carbon Dioxide,” *Fermentation*, vol. 4, no. 3, p. 63, Aug. 2018, doi: 10.3390/fermentation4030063.

[242] S.-J. Wang and J.-J. Zhong, “Bioreactor Engineering,” in *Bioprocessing for Value-Added Products from Renewable Resources*, Elsevier, 2007, pp. 131–161. doi: 10.1016/B978-044452114-9/50007-4.

[243] W.S. Hu, J. Meier, and D.I.C. Wang, “ Biotechnology,” *Bioeng*, vol. 28, p. 122, 1986.

[244] B. Bandyopadhyay, A. E. Humphrey, H. Taguchi, and I. by Govind Rao, “Dynamic measurement of the volumetric oxygen transfer coefficient in fermentation systems,” *Biotechnol Bioeng*, vol. 104, no. 5, pp. 841–853, Dec. 2009, doi: 10.1002/bit.22566.

[245] R. K. Finn and J. E. Nowrey, “A Note on the Stability of Clostridia when Held in Continuous Culture,” *Appl Microbiol*, vol. 7, no. 1, pp. 29–32, Jan. 1959, doi: 10.1128/am.7.1.29-32.1959.

[246] S. Ensari and H. C. Lim, “Apparent effects of operational variables on the continuous culture of Corynebacterium lactofermentum,” *Process Biochemistry*, vol. 38, no. 11, pp. 1531–1538, Jun. 2003, doi: 10.1016/S0032-9592(03)00041-4.

[247] J. S. White, K. L. Stewart, D. L. Maskell, A. Diallo, J. E. Traub-Modinger, and N. A. Willoughby, “Characterization of Pot Ale from a Scottish Malt Whisky Distillery and Potential Applications,” *ACS Omega*, vol. 5, no. 12, pp. 6429–6440, Mar. 2020, doi: 10.1021/acsomega.9b04023.

[248] E. M. Moghaddam, A. Goel, M. Siedlecki, K. Michalska, O. Yakaboylu, and W. de Jong, “Supercritical water gasification of wet biomass residues from farming and food production practices: lab-scale experiments and comparison of different modelling approaches,” *Sustain Energy Fuels*, vol. 5, no. 5, pp. 1521–1537, 2021, doi: 10.1039/D0SE01635G.

[249] T. Schaaf, J. Grünig, M. R. Schuster, T. Rothenfluh, and A. Orth, “Methanation of CO2 - storage of renewable energy in a gas distribution system,” *Energy Sustain Soc*, vol. 4, no. 1, p. 2, Dec. 2014, doi: 10.1186/s13705-014-0029-1.

[250] P. Ebrahimi, A. Kumar, and M. Khraisheh, “A review of recent advances in water-gas shift catalysis for hydrogen production,” *Emergent Mater*, vol. 3, no. 6, pp. 881–917, Dec. 2020, doi: 10.1007/s42247-020-00116-y.

[251] P. Luis, “Use of monoethanolamine (MEA) for CO 2 capture in a global scenario: Consequences and alternatives,” *Desalination*, vol. 380, pp. 93–99, Feb. 2016, doi: 10.1016/j.desal.2015.08.004.

[252] M. Saeid and C. Yee, *Simulation of Butanol Production through Hydrogenation of Butanal: Effects of Different Reactor Schemes and Operating Conditions*. 2020.

[253] Y. Khan, M. Marin, R. Karinen, J. Lehtonen, and J. Kanervo, “1-Butanol dehydration in microchannel reactor: Kinetics and reactor modeling,” *Chem Eng Sci*, vol. 137, pp. 740–751, Dec. 2015, doi: 10.1016/j.ces.2015.07.026.

[254] IHS Markit, “PEP Report 204C - Location factors,” *IHS Markit*, 2016.

[255] R. T. Ruegg and H. E. Marshall, “Internal Rate-of-Return (IRR),” in *Building Economics: Theory and Practice*, R. T. Ruegg and H. E. Marshall, Eds., Boston, MA: Springer US, 1990, pp. 67–78. doi: 10.1007/978-1-4757-4688-4_5.

[256] European Commission, “Proposal for a REGULATION OF THE EUROPEAN PARLIAMENT AND OF THE COUNCIL on ensuring a level playing field for sustainable air transport,” *https://commission.europa.eu/documents_en*, 2021.

[257] U.S. Energy Information Administration (EIA), “Petroleum and Other Liquids: Spot Prices,” Jun. 2022. Accessed: Apr. 21, 2023. [Online]. Available: https://www.eia.gov/dnav/pet/hist/LeafHandler.ashx?n=PET&s=

[258] F. Anmar, ““Sustainable Aviation Fuel Costs More but Consumers Will Be Willing to Pay, IATA Chief Says,” Feb. 2022. Accessed: Apr. 21, 2023. [Online]. Available: https://www.cnbc.com/2022/02/11/sustainable-aviation-fuel-costs-more-but-consumers-willing-to-pay-iata.html

[259] A. Bauen, N. Bitossi, L. German, A. Harris, and K. Leow, “Sustainable Aviation Fuels,” *Johnson Matthey Technology Review*, 2020, doi: 10.1595/205651320X15816756012040.

[260] N. Pavlenko, S. Searle, and A. Chritensen, “The Cost of Supporting Alternative Jet Fuels in the European Union,” *International Council on Clean Transportation (ICCT)*, 2019, Accessed: Apr. 21, 2023. [Online]. Available: https://theicct.org/sites/default/files/publications/Alternative_jet_fuels_cost_EU_2020_06_v3.pdf.

[261] NREL, “Annual Technology Baseline: Jet Fuel,” 2020. Accessed: Apr. 21, 2023. [Online]. Available: https://atb.nrel.gov/

[262] UK Government, “Jet Zero Council,” 2020. Accessed: Apr. 23, 2023. [Online]. Available: https://www.gov.uk/government/groups/jet-zero-council#:~:text=Jet%20Zero%20%E2%80%93%20collective%20term%20used,UK%20removed%20from%20the%20environment.

[263] Department for Transport - UK, “Pathway to net zero aviation: Developing the UK sustainable aviation fuel mandate,” Mar. 2023. Accessed: May 16, 2023. [Online]. Available: https://assets.publishing.service.gov.uk/government/uploads/system/uploads/attachment_data/file/1147350/pathway-to-net-zero-aviation-developing-the-uk-sustainable-aviation-fuel-mandate.pdf

[264] Congressional Research Service, “The Renewable Fuel Standard (RFS): An Overview,” Sep. 2022. Accessed: Apr. 23, 2023. [Online]. Available: https://sgp.fas.org/crs/misc/R43325.pdf

[265] Briefing, “ReFuelEU Aviation initiative: Sustainable aviation fuels and the fit for 55 package,” *Think Tank European Parliament*, Dec. 2022, Accessed: Apr. 16, 2023. [Online]. Available: https://www.europarl.europa.eu/thinktank/en/document/EPRS_BRI(2022)698900

[266] CAAC, “The 14th FYP for Green Civil Aviation Development,” 2021. Accessed: Apr. 24, 2023. [Online]. Available: http://www.gov.cn/zhengce/zhengceku/2022-01/28/5670938/files/c22e012963ce458782eb9cb7fea7e3e3.pdf

[267] UK government, “Over £110 million to unlock zero emission guilt-free flights,” 2023. Accessed: Apr. 25, 2023. [Online]. Available: https://www.gov.uk/government/news/over-110-million-to-unlock-zero-emission-guilt-free-flights

[268] Qantas, “QANTAS GROUP CLIMATE ACTION PLAN,” *Qantas Group*, 2022, Accessed: Apr. 25, 2023. [Online]. Available: https://www.qantas.com/content/dam/qantas/pdfs/about-us/environment/qantas-group-climate-action-plan.pdf

[269] “Air Canada makes significant investment in SAF technology,” *Biofuels International*, Mar. 2021, Accessed: Apr. 25, 2023. [Online]. Available: https://biofuels-news.com/news/air-canada-makes-significant-investment-in-saf-technology/

[270] US Department of Energy, “Biodiesel Production and Blending Tax Credit,” *Alternative Fuels Data Center*, Accessed: Apr. 25, 2023. [Online]. Available: https://afdc.energy.gov/laws/5831

[271] USDA, “Biorefinery, Renewable Chemical, and Biobased Product Manufacturing Assistance Program,” 2023. Accessed: Apr. 24, 2023. [Online]. Available: https://www.rd.usda.gov/programs-services/energy-programs/biorefinery-renewable-chemical-and-biobased-product-manufacturing-assistance-program

APPENDIX

List of Tables

List of Figures

Appendix 1

This appendix provides required supplementary information on the technical assumptions implemented for ASPEN HYSYS modelling and simulation in chapter 3 and chapter 6 and also the mass and energy balance

Section A.1.1

This section shows the technical assumptions utilised for the HYSYS simulations of the C_2 and C_4 route-to-SAF processes in Chapter 3 and Chapter 6. Units are the same as labelled in Figure 3.2 and Figure 3.3 for C_2 heat-integrated route-to-SAF process. Also, unit labels for the C_4 cases can be found in Figure 6.4, Figure 6.5, and Figure 6.6.

Table A.1. Technical assumptions for ASPEN HYSYS simulation for C_2 heat integrated route-to-SAF.

Units and Streams	**Modelled in HYSYS as**	**Temperature (ºC)**	**Pressure (kPa)**	**Other parameters**
PC2-1	Pump	25.5 (in) 28.54 (out)	101 (in) 24,000 (out)	
HC2-1	Heat exchanger	33 (in) 233 (out)	24,000 (in) 24,000 (out)	
BC2-1	Conversion reactor	38 - 40	390 (in) 390 (out)	
HC2-2	Heat exchanger	320 (in) 366 (out)	24,000 (in) 24,000 (out)	
KC2-1	Pump	30 (inlet) 40 (outlet)	109 (in) 160 (out)	
Isopentane stream		30	109	
RC2-1	Plug flow reactor	373.5 (in) 321 (out)	24,000 (in) 24,000 (out)	Volume - 35m3, Tube length – 5m
KC2-2	Expander	313 (in) 87 – 113 (out)	24,000 (in) 390 (out)	Isentropic efficiency – 75%
KC2-2	Compressor	20 (in) 204 (out)	101 (in) 400 (out)	Air as inlet. Adiabatic efficiency – 75%
CC2-1	Conversion reactor	130 (in) 1414 (out)	400 (in) 390 (out)	Volume – 25m^3
TC2-1	Expander	395 (in) 363 (out)	390 (in) 100 (out)	
RC2-2	Plug flow reactor	85	390	Tube length -12m

Units and Streams	Modelled in HYSYS as	Temperature (ºC)	Pressure (kPa)	Other parameters
				Volume – 15m^3
RC2-3	Plug flow reactor	90	80	Tube length – 2m Volume – 1m^3
RC2-4	Plug flow reactor	66	250	Tube length – 2m Volume – 0.5m^3
RC2-5	Conversion reactor	95	250	Conversion – 59%
RC2-6	Plug flow reactor	225	270	Tube length – 2m Volume – 03m^3
RC2-7	Conversion reactor	50	460	
RC2-8	Conversion reactor	120	1000	

Table A.2. Technical assumptions for ASPEN HYSYS simulation for C4 heat integrated route-to-SAF.

Units	Modelled in HYSYS as	Temperature (ºC)	Pressure (kPa)	Other parameters
PC4-1	Pump	25.5 (in) 28.99 (out)	101 (in) 27,500 (out)	
HC4-1	Heat exchanger	29 (in) 377 (out)	27,500 (in) 27,500 (out)	
BC4-1	Conversion reactor	38 - 40	400 (in) 400 (out)	
KC4-1	Pump	30 (inlet) 41 (outlet)	109 (in) 160 (out)	
Isopentane stream		30	109	
RC4-1	Plug flow reactor	377 (in) 358 (out)	27,500 (in) 27,500 (out)	Volume - 10m3, Tube length – 10m
KC4-2	Compressor	20 (in) 204 (out)	101 (in) 400 (out)	Air as inlet. Adiabatic efficiency – 75%
CC4-1	Conversion reactor	1350 (in) 2399 (out)	400 (in) 400 (out)	Volume – 25m^3 100% conversion assumed
TC4-1	Expander	1571 (in) 1359 (out)	400 (in) 175 (out)	

Units	Modelled in HYSYS as	Temperature (ºC)	Pressure (kPa)	Other parameters
TC4-2	Expander	358 (in) 168 (out)	27,500 (in) 1000 (out)	Isentropic efficiency – 75%
RC4-2	Plug flow reactor	1000	1000	Tube length - 5m Volume – $5m^3$
RC4-3	Plug flow reactor	400	1000	Tube length – 5m Volume – $10m^3$
RC4-4	Plug flow reactor	200	1000	Tube length – 5m Volume – $5m^3$
RC4-5	Plug flow reactor	85	400	Volume – $15m^3$ Tube length – 10m
RC4-6	CSTR	160	1000	99% conversion
RC4-7	Plug flow reactor	240	500	Volume – $0.5m^3$ Tube length – 2m
RC4-8	Conversion reactor	45	475	90% for trimers 5% for tetramers 5% for trimers
RC4-9	CSTR	150	1000	90% for trimers 5% for tetramers 5% for trimers

Table A.3. Technical assumptions for ASPEN HYSYS simulation for C4 non-heat integrated route-to-SAF.

Units and Streams	Modelled in HYSYS as	Temperature (ºC)	Pressure (kPa)	Other parameters
PC4-16	Pump	20.26 (in) 23 (out)	101 (in) 24,000 (out)	
BC4-3	Conversion reactor	38 - 40	400 (in) 400 (out)	
RC4-10	Plug flow reactor	376 (in) 361 (out)	24,000 (in) 24,000 (out)	Volume - 5m3, Tube length – 10m
RC4-11	Plug flow reactor	1300	1000	Volume - 5m3, Tube length – 10m
RC4-12	Plug flow reactor	400	1000	Volume - 5m3, Tube length – 5m

Units and Streams	Modelled in HYSYS as	Temperature (ºC)	Pressure (kPa)	Other parameters
RC4-13	Plug flow reactor	198	1000	Volume - 5m3, Tube length – 5m
TC4-3	Expander	347 (in) 168 (out)	24,000 (in) 1000 (out)	Isentropic efficiency – 75%
TC4-4	Expander	420 (in) 280 (out)	375 (in) 101 (out)	Isentropic efficiency – 75%
CC4-2	Conversion reactor	167 (in) 1390 (out)	375 (in) 375 (out)	Volume – $25m^3$ 100% conversion assumed
KC4-4	Pump	30 (inlet) 201 (outlet)	101 (in) 375 (out)	
RC4-5	Plug flow reactor	85	400	Volume – $15m^3$ Tube length – 10m
RC4-6	CSTR	160	1000	99% conversion
RC4-7	Plug flow reactor	240	500	Volume – $0.5m^3$ Tube length – 2m
RC4-8	Conversion reactor	45	475	90% for trimers 5% for tetramers 5% for trimers
RC4-9	CSTR	150	1000	90% for trimers 5% for tetramers 5% for trimers

Section A.1.2

This section shows the mass and energy balance result calculations for the C_2 and C_4 route-to-SAF presented in Chapter 3, Chapter 5 and Chapter 6.

Table A.4. Mass and energy balance for the C_2 heat-integrated route-to-SAF

	Value	Unit	Comments
FEEDSTOCK PRETREATMENT			
Feeds			
Black Liquor			
Total Mass Feed Rate	325000	[kg/h]	
Total Guaiacol Mass Feed Rate	23725	[kg/h]	
H2O			

	Value	Unit	Comments
Total Black Liquor Dilution H2O Mass Make-up	120374.463	[kg/h]	
Number of thermal cycles	1.000	[-]	One per seed fermenter
High Pressure Pump			Gear or Lobe Pump
Volumetric Flow			
Total Volumetric Flow (hour basis)	485.0587732	[m3/h]	
Volumetric Flow per thermal cycle (second basis)	0.134738548	[m3/s]	
Duty			
Total Duty	4293.488748	[kW]	
Duty per thermal cycle	4293.488748	[kW]	
Heat Pump Condensor			
Total Duty (hour basis)	61114447.4	[kJ/h]	
Heat Duty per thermal cycle	169762.3548	[kW]	
Overall heat transfer coefficient	10000	[W/(m2·K)]	
Heat Pump Compressor/Vapour recompression			
Total isopentane Molar Flow	9250	[kmol/h]	
Total isopentane Volumetric Flow Rate (STP)	207203.8342	[m3/h] (STP)	
Isopentane Volumetric Flow Rate (STP) per thermal cycle	207203.834	[m3/h] (STP)	
Mechanical Vapour Recompression Duty			
Total Duty	3099.570624	[kW]	
Duty per thermal cycle	3099.571	[kW]	
Number of 750kW Compressors	5.000	[-]	
scH2O Recovery HE			
Total Duty (hour basis)	10060578.9	[kJ/h]	
Heat Duty per thermal cycle	27946.05024	[kW]	
Overall heat transfer coefficient	10000	[W/(m2·K)]	
scH2O Plug Flow Reactor			
Guaiacol Conversion	99.9996859	[%]	
Total Reactor volume	35	[m3]	
Reactor volume per thermal cycle	35	[m3]	
Vapour Heater			
Total Duty (hour basis)	37237482.8	[kJ/h]	
Heat Duty per thermal cycle	103437.4511	[kW]	
Overall heat transfer coefficient	10000	[W/(m2·K)]	

	Value	Unit	Comments
Heat Pump Recovery Heat Exchanger			
Total Duty (hour basis)	65665291.8	[kJ/h]	
Heat Duty per thermal cycle	18240.35883	[kW]	
Overall heat transfer coefficient	3000	[W/(m2·K)]	
Combustion Heater			
Total Duty (hour basis)	37767223.3	[kJ/h]	
Heat Duty per thermal cycle	104908.9531	[kW]	
Overall heat transfer coefficient	3000	[W/(m2·K)]	
Immersion Heater			
Volumetric Flow Rate (Actual)	370862.3957	[m3/h]	
Total Duty (hour basis)	113366.5167	[kJ/h]	
Heat Duty per thermal cycle	31.49069908	[kW]	May need to be three immersion heaters of 5MW each.
Overall heat transfer coefficient	3000	[W/(m2·K)]	
Heating element surface	600	[°C]	
Isopentane inlet	499.9	[°C]	
Isopentane outlet	500	[°C]	
Supercritical Heater			
Total Duty (hour basis)	35852145.2	[kJ/h]	
Heat Duty per thermal cycle	99589.29228	[kW]	
Overall heat transfer coefficient	3000	[W/(m2·K)]	
Turbo-expander/TE Compressor			
Total Air Molar Feed Rate	7750	[kmol/h]	
Air compression			
Total Air Volumetric Feed Rate (STP)	173603.2124	[m3/h] (STP)	
Air Volumetric Feed Rate (STP) per thermal cycle	173603.2124	[m3/h] (STP)	
Turbo-expander Duty			
Total Duty	11777.41925	[kW]	Modelled as single stage compression. Power supply from expander, i.e. no electricity demand. Extrapolating outside the range, given the maximum is 15 [MW].
Duty per thermal cycle	11777.41925	[kW]	
Number of 5MW Turbo-expanders	3.000	[-]	Spreads risk across a number of turbo-expanders for air delivery.

	Value	Unit	Comments
Air Compression After Cooler/Air Cooler			
Total Cooling Duty (hour basis)	10212837.89	[kJ/h]	
Heat Duty per thermal cycle	2836.899	[kW]	
Overall heat transfer coefficient	3000.000	[W/(m2·K)]	
H2 Bioreactor Cooler			
Total Cooling Duty (hour basis)	11792728 2.5	[kJ/h]	
Heat Duty per thermal cycle	32757.578	[kW]	
Overall heat transfer coefficient	3000.000	[W/(m2·K)]	
Combustion			
Number of Combustion Chambers	1.000	[-]	One per production fermenter
H2 Combustion Feed Heater			
Total Heating Duty (hour basis)	15531709.58	[kJ/h]	
Heat Duty per thermal cycle	4314.364	[kW]	
Overall heat transfer coefficient	3000.000	[W/(m2·K)]	
Bioreactor Off-gas Combustion Feed Heater			
Total Heating Duty (hour basis)	7481051.432	[kJ/h]	
Heat Duty per thermal cycle	2078.070	[kW]	
Overall heat transfer coefficient	3000.000	[W/(m2·K)]	
Combustion Chamber			
Volume	25.000	[m3]	
Dimensions			
Aspect Ratio	3	[-]	
Height	4.152830592	[m]	
Combustion Turbine			
Total Turbine Duty	17672.50239	[kW]	23460.00
Plant draw on turbine duty	23583.832	[kW]	
Excess electricity	-5911.330	[kW]	
TE Turbine			
Total Turbine Duty	24786.66797	[kW]	
Plant draw on turbine duty	0.000	[kW]	
Excess electricity	24786.668	[kW]	
FERMENTATION			
Broth properties			
Density	966.7135086	[kg/m3]	
Viscosity	0.797232415	[mPa·s]	Not estimated, likely owed to solid DCW2.

	Value	Unit	Comments
			Assumed to be as for water.
Total Fermentation Flow Rates			
Total Media	2.74E+04	[kg/h]	
NH3	8.25	[kmol/h]	
Broth Bleed Rate (Aqueous phase)	120374.463	[kg/h]	Dilution flow rate
DCW in Centrate	642.4900147	[kg/h]	
Pyruvic acid			
Aqueous phase	618325.996	[kg/h]	
Vapour phase	15.51720317	[kg/h]	
Total Fermentation Steady State Utilisation			
O2	-288.70	[kmol/h]	288.70
CO2	-152.03	[kmol/h]	152.03
H2	-921.66	[kmol/h]	921.66
NH3	-7.57	[kmol/h]	7.57
Production Fermenter O2 Mass Transfer			
Headspace O2 Concentration	0.033541862	[-] (v/v)	
Design O2 Uptake Rate (OUR)	-241.872	[(mmol O2)/(L·h)]	Ungassed broth volume basis.
Specific O2 Uptake Rate	0.163	[(mmol O2)/((g DCW)·h)]	
Henry's Law Constant (25 [°C])	0.001	[mol/(L·bar)]	
Back-pressure	400.000	[kPa] (a)	
Headspace O2 Concentration	3.354	[%] (v/v)	
Outlet saturation	0.174	[mmol/L]	
Broth dissolved O2 concentration	0.000	[mmol/L]	Oxygen limiting cultivation.
Log mean concentration difference (LMCD)	0.655	[mmol/L]	
kla(O2)	369.121	[1/h]	
Production Fermenter Continuous Cultivation			
O2			
O2 Uptake Rate	-72.175	[kmol/h]	
DCW			
Total internal recirculation mass flow rate	108766.5716	[kg/h]	
Total internal DCW mass flow rate	167301.4621	[kg/h]	
Total Mass Flow Rate in Centrate	160.623	[kg/h]	
DCW Concentration in Bioreactor	1486.970	[(g DCW)/L]	
DCW Concentration in Centrate	5.160	[(g DCW)/L]	
DCW Dilution Rate	0.000	[-]	
DCW Productivity	0.538	[(g DCW)/(L·h)]	

	Value	Unit	Comments
H2O			
Make-up Volumetric Flow Rate	5.820	[m3/h]	
Fluid Dilution Rate	0.104	[1/h]	Liquid phase dilution rate. Cell mass retained via centrifuges within the sterile boundary of each bioreactor.
H2			
H2/O2 Molar Uptake Ratio	3.192	[-]	
Uptake Rate	-772.172	[(mmol H2)/(L·h)]	
Molar Flow Rate	-230.416	[(kmol H2)/h]	
Mass Feed Rate	-460.832	[(kg H2)/h]	
NH3			
NH3/O2 Molar Uptake Ratio	0.026	[-]	
Uptake Rate	-6.343	[(mmol NH3)/(L·h)]	
Molar Flow Rate	-1.893	[(kmol NH3)/h]	
Mass Feed Rate	-32.176	[(kg NH3)/h]	
Pyruvic acid(C3-H4-O3)			
Concentration (Aqueous phase)	4965.706	[g/L]	Below toxicity limit of 15 [g/L] IPA
Productivity (Aqueous + Vapour)			
Molar	1377.644	[kmol/h]	
Mass	154585.378	[(kg PA)/h]	
CO2			
CO2/O2 Molar Uptake Ratio	0.527	[-]	Resipiratory Quotient
Uptake Rate	-127.373	[(mmol CO2)/(L·h)]	
Molar Flow	-38.008	[kmol/h]	
Mass Flow	-1672.360	[(kg CO2)/h]	
Production Fermenters Dimensions			
Downcomer	0.250	[(m3 gas)/(m3 total working volume)]	
Riser gas	0.150	[(m3 gas)/(m3 total working volume)]	
Structured Packing Volume Fraction	0.030	[(m3 packing)/(m3 downcomer working volume)]	
Working Volume Fraction	0.800	[(m3 working volume)/(m3 vessel volume)]	Provides head space for foaming.
Number of fermenters	4.000	[-]	
Vessel Volume	500.000	[m3 vessel volume]	
Aspect Ratio (Downcomer)	10.000	[-]	
Downcomer to Riser Diameter Ratio	2.000	[-]	
Downcomer	3.707	[m]	
Riser	1.853	[m]	
Fermenter Height	37.067	[m]	

	Value	Unit	Comments
Broth Volume			
Downcomer	230.400	[m3]	
Riser	68.000	[m3]	
Total	298.400	[m3]	Ungassed broth volume.
Recirculation Pump			
Recirculation Re in Downcomer	1000000.000	[-]	
Volumetric Flow Rate	2.401	[m3/s]	
Pump efficiency	0.650	[-]	
Duty	92.341	[kW]	
Heat exchanger (Evaporator)			
Heat Duty (hourly basis)	20834705.7	[kJ/h]	
Heat Duty	14468.546	[kW]	Exothermic heat duty.
Overall heat transfer coefficient	3000.000	[W/(m2·K)]	
Heat Transfer Area	17.328	[m2]	
Seed Fermenters Dimensions			
Downcomer	0.250	[(m3 gas)/(m3 total working volume)]	
Riser gas	0.150	[(m3 gas)/(m3 total working volume)]	
Structured Packing Volume Fraction	0.030	[(m3 packing)/(m3 downcomer working volume)]	
Working Volume Fraction	0.800	[(m3 working volume)/(m3 vessel volume)]	Provides head space for foaming.
Number of fermenters	1.000	[-]	Given continuous operation, one seed fermenter provides the innoculum for four production fermenters
Volume Fraction of Production Fermenter	10.000	[%] (v/v)	
Vessel Volume	50.000	[m3 vessel volume]	
Aspect Ratio (Downcomer)	10.000	[-]	
Downcomer to Riser Diameter Ratio	2.000	[-]	
Downcomer	1.721	[m]	
Riser	0.860	[m]	
Fermenter Height	17.205	[m]	
Broth Volume			
Downcomer	23.040	[m3]	
Riser	6.800	[m3]	
Total	29.840	[m3]	
Recirculation Pump			
Recirculation Re in Downcomer	1000000.000	[-]	
Volumetric Flow Rate	1.114	[m3/s]	
Pump efficiency	0.650	[-]	
Duty	42.861	[kW]	

	Value	Unit	Comments
Heat exchanger			
Heat Duty	1446.855	[kW]	Exothermic heat duty
Overall heat transfer coefficient	3000.000	[W/(m2·K)]	
Heat Transfer Area	48.228	[m2]	
Annual Production			
Production Fermenters			
Number of Production Fermenters	4.000	[-]	
Continuous Operation	1008.000	[h]	
Turn-around & Steady State Approach	36.000	[h]	
Total Cycle Time	1044.000	[h]	
Continuous Annual Operation	8110.345	[h]	
Number of Runs	32.000	[Runs/annum]	
Feeds to Production Fermenters			
Total enriched H2 Feed Rate	14950037.108	[kg/annum]	1779.77
Total NH3 Mass Feed Rate	1043831.505	[kg/annum]	
Total H2O Media Feed Rate	188797.452	[m3/annum]	
Feeds to DSP			
Broth Volumetic Flow Rate	1009894.099	[m3/annum]	
DCW	5210.816	[t/annum]	
Pyruvic acid	5014962.893	[t/annum]	
Acetone	#REF!	[t/annum]	
PRODUCT RECOVERY FROM BIOREACTOR			
Pyruvate decarboxylation			
Pyruvic acid Conversion	99.68	[%]	
Total Reactor volume	15	[m3]	
Reactor volume per thermal cycle	15	[m3]	
Acetaldehyde Stripper(Column)			
Control Volume Flow Rates			
Feed Rate from pyruvate decarboxylation reactor	2439	[kmol/h]	
Total Feed Rate	46772.87771	[kg/h]	
Acetaldehyde Feed Rate	1910.887965	[kg/h]	
DCW Feed rate	678.3204779		
Pyruvic acid feed rate	12.64955035	[kg/h]	
Bottoms Flow Rate	42834.30643	[kg/h]	
Bottoms			
H2O flow mass rate	42143.10013		

	Value	Unit	Comments
Pyruvic acid Mass Flow Rate	12.54019201	[kg/h]	
Reboiler			
Reboiler Duty (hourly basis)	7134336.455	[kJ/h]	
Reboiler Duty	1981.760	[kW]	
Overall heat transfer coefficient	10000.000	[W/(m2·K)]	
Bottoms	102.3	[°C]	
Steam	109.9	[°C]	
Heat Transfer Area	26.076	[m2]	
Dimensions			
Maximum Vapour Volumetric Flow Rate	5504.726241	[m3/h]	
Design Vapour Linear Velocity	1.000	[m/s]	
Structured packing HETP	0.750	[m]	
Number of stages	10	[-]	
Column Height	7.500	[m]	
SOLVENT RECOVERY(FULFURAL RECOVERY(T101)			
Feed(from AcH stripper distillate)			
Total Molar Flow Rate	417.180	[kmol/h]	
AcH Molar Flow	43.371	[kmol/h]	
H2O Molar Flow	5.599	[kmol/h]	
CO2 Molar Flow	43.420	[kmol/h]	
furfural molar flow rate	323.900	[kmol/h]	
Bottoms			
Total Molar Flow Rate	373.3457461	[kmol/h]	
Furfural Molar Flow	321.622317	[kmol/h]	
AcH Molar Flow	43.37111827	[kmol/h]	
H2O Molar Flow	7.40482465	[kmol/h]	
CO2 Molar Flow	0.567114164	[kmol/h]	
Ammonia	0.380357707	[kmol/h]	
Distillate			
Total Molar Flow Rate	43.78	[kmol/h]	
Furfural Molar Flow(lost)	30.01439751	kg/hr	
AcH Molar Flow	0	[kmol/h]	
H2O Molar Flow	0.110950624	[kmol/h]	
CO2 Molar Flow	42.853	[kmol/h]	
Ammonia	0.149999087	([kmol L)/(kmol D)]	
Vapour flow rate	2852.179967	[m3/h]	

	Value	Unit	Comments
Dimensions			
Vapour linear velocity	1.000	[m/s]	
Structured packing HETP	0.750	[m]	
Number of stages	12	[-]	
Column Height	9.000	[m]	
AcH and Fulfural CONCENTRATION DISTILLATION(T102)			
Feed			
Bottoms Feed from T101			
Total Molar Flow Rate	373.3457461	[kmol/h]	
Furfural Molar Flow	321.622317	[kmol/h]	
AcH Molar Flow	43.37111827	[kmol/h]	
H2O Molar Flow	7.405	[kmol/h]	
Bottoms			
Total Molar Flow Rate	329.0117152	[kmol/h]	
Furfural Molar Flow	321.622317	[kmol/h]	
H2O Molar Flow	7.39E+00	[kmol/h]	
Reboiler			
Reboiler Duty (hourly basis)	10860325.96	[kJ/h]	
Reboiler Duty	3016.757	[kW]	
Overall heat transfer coefficient	10000.000	[W/(m2·K)]	
Bottoms	152.7998379	[°C]	
Steam	250	[°C]	
Heat Transfer Area	3.104	[m2]	
Distillate			
Total Molar Flow	43.28323913	[kmol/h]	
AcH Molar Flow	42.72055149	[kmol/h]	
CO2 Molar Flow	0.207096889	[kmol/h]	
H2O Molar Flow	1.54E-02	[kmol/h]	
Reflux ratio	3.4	([kmol L)/(kmol D)]	
Vapour flow rate	5534.705888	[m3/h]	
Condensor			
Condensor Duty (hourly basis)	5248537.717	[kJ/h]	
Condensor Duty	1457.927	[kW]	
Overall heat transfer coefficient	3000.000	[W/(m2·K)]	
Distillate	2.904300653	[°C]	
Heat Transfer Area	-18.143	[m2]	

	Value	Unit	Comments
Dimensions			
Vapour linear velocity	1.000	[m/s]	
Structured packing HETP	0.750	[m]	
Number of stages	20	[-]	
Column Height	15.000	[m]	
Furfural recovery column(T103)			
Feed			
Total Molar Flow Rate	328.9135088	[kmol/h]	
Furfural Molar Flow	321.6223129	[kmol/h]	
H2O Molar Flow	7.291178102	[kmol/h]	
Bottoms			
Total Molar Flow Rate	304.156001	[kmol/h]	
Furfural Molar Flow	302.324353	[kmol/h]	Recycled
H2O Molar Flow	1.831635959	[kmol/h]	
Reboiler			
Reboiler Duty (hourly basis)	1634706.507	[kJ/h]	
Reboiler Duty	454.085	[kW]	
Overall heat transfer coefficient	10000.00	[W/(m2·K)]	
Bottoms	162.1495	[°C]	
Steam	18	[°C]	
Heat Transfer Area	250	[m2]	
	0.517		
Distillate			
Total Molar Flow	24.75750779	[kmol/h]	
H2O Molar Flow	5.459542512	[kmol/h]	
Furfural Molar Flow	19.29795984	[kmol/h]	
Column internal			
Reflux ratio	13.8	([kmol L)/(kmol D)]	
Vapour flow rate	871.437183	[m3/h]	
Dimensions			
Vapour linear velocity	1.000	[m/s]	
Column Diameter	0.555	[m]	
Structured packing HETP	0.750	[m]	
Number of stages	10	[-]	
Column Height	7.500	[m]	
Aldo-condensation reaction			
Feed			
Total Molar Flow Rate	42.624	[kmol/h]	
AcH Molar Flow	42.070	[kmol/h]	

	Value	Unit	Comments
H2O Molar Flow	0.113	[kmol/h]	
CO2 Molar flow	0.132	[kmol/h]	
Ammonia Molar Flow	0.308	[kmol/h]	
Plug flow aldo			
AcH Conversion	99.99968 59	[%]	
Total Reactor volume	0.999530 02	[m3]	
Reactor volume per thermal cycle	0.999530 02	[m3]	
SEPARATION TRAIN FOR CROTONALDEHYDE			
1st column			
Feed			
Total Molar Flow Rate	42.29804 524	[kmol/h]	
CrotonAD Molar Flow	20.95454 172	[kmol/h]	
H2O Molar Flow	21.05330 996	[kmol/h]	
Bottoms			
Total Molar Flow Rate	20.42508 118	[kmol/h]	
H2O Molar Flow	20.42523 257	[kmol/h]	
H2O Molar Purity	100.001	[%] (mol/mol)	
Reboiler			
Reboiler Duty (hourly basis)	10002722 .51	[kJ/h]	
Reboiler Duty	2778.534	[kW]	
Overall heat transfer coefficient	10000.00 0	[W/(m2·K)]	
Bottoms	96.71001 094	[°C]	
Steam	109.9	[°C]	
Heat Transfer Area	21.065	[m2]	
Distillate			
Total Molar Flow Rate	194.0635 453	[kmol/h]	
H2O Molar Flow	146.3294 497	[kmol/h]	
Crotonadelhyde Molar Flow	43.09718 815	[kmol/h]	
Column internal			
Reflux ratio	1.026802 383	([kmol L)/(kmol D)]	
Vapour flow rate	3197.566 803	[m3/h]	
Dimensions			
Vapour linear velocity	1.000	[m/s]	
Column Diameter	1.063	[m]	
Structured packing HETP	0.750	[m]	
Number of stages	20	[-]	

	Value	Unit	Comments
Column Height	15.000	[m]	
2nd Column(High pressure column)			
Feed			
Total Molar Flow Rate	74.002	[kmol/h]	
Croton Molar Flow Rate	40.858	[kmol/h]	
H2O Molar Flow	29.621	[kmol/h]	
Bottoms			
Total Molar Flow Rate	20.42508 118	[kmol/h]	
CrotonAld Molar Flow	20.60308 325	[kmol/h]	
H2O Molar flow	0.187	[%] (mol/mol)	
Reboiler			
Reboiler Duty (hourly basis)	3556117. 486	[kJ/h]	
Reboiler Duty	987.810	[kW]	
Overall heat transfer coefficient	10000.00 0	[W/(m2·K)]	
Bottoms	134.9180 619	[°C]	
Steam	250	[°C]	
Heat Transfer Area	0.858	[m2]	
Distillate(recycled back)			
Total Molar Flow Rate	53.21187 976	[kmol/h]	
CrotonAld Molar Flow	20.25465 11	[kmol/h]	
H2O Molar Flow	29.43387 442	[kmol/h]	
Column internal			
Vapour flow rate	768.9504 987	[m3/h]	
Dimensions			
Vapour linear velocity	1.000	[m/s]	
Column Diameter	0.521	[m]	
Structured packing HETP	0.750	[m]	
Number of stages	10	[-]	
Column Height	7.500	[m]	
CROTONALDEHYDE HYDROGEN			
Feed			
Total Molar Flow Rate	60.723	[kmol/h]	
Crotonaldehyde Molar Flow	20.603	[kmol/h]	
H2 Molar Flow	39.933	[kmol/h]	Extra hydrogen introduced to the reactor
H2 Mass flow	80.504	[Kg/hr]	
H2O Molar flow	0.187	[kmol/h]	
CrotonAldehyde Conversion	99.99968 59	[%]	
Total Reactor volume	0.5	[m3]	

	Value	Unit	Comments
Reactor volume per thermal cycle	0.5	[m3]	
Crotonaldehyde and 1-butanol Separation			
Feed			
Bottoms Feed from Croton-hydrogenation reactor			
Total Molar Flow Rate	37.09991 371	[kmol/h]	
1-butanol(rec) Molar flow	11.28	[kmol/h]	
1-Butanol Molar Flow	19.96625 917	[kmol/h]	
Crotonaldehyde Molar Flow(Recycled)	0.233205 697	[kmol/h]	
Crotonaldehyde Molar Flow	0.616772 46	[kmol/h]	
Bottoms			
Total Molar Flow Rate	30	[kmol/h]	
1-Butanol Molar Flow	29.69940 463	[kmol/h]	
Reboiler			
Reboiler Duty (hourly basis)	917289.0 582	[kJ/h]	
Reboiler Duty	254.803	[kW]	
Overall heat transfer coefficient	10000.00 0	[W/(m2·K)]	
Bottoms	148.1592 359	[°C]	
Steam	250	[°C]	
Heat Transfer Area	0.250	[m2]	
Distillate			
Total Molar Flow	7.434	[kmol/h]	
H2O Molar Flow	5.323010 59	[kmol/h]	
Butanol Molar Flow	1.550732 92	[kmol/h]	
Crotonaldehyde Molar Flow	5.51E-01	[kmol/h]	
Column internal			
Reflux ratio	2.319	([kmol L)/(kmol D)]	
Vapour flow rate	400.9135 537	[m3/h]	
Condensor			
Condensor Duty (hourly basis)	754964.8 99	[kJ/h]	
Condensor Duty	209.712	[kW]	
Overall heat transfer coefficient	3000.000	[W/(m2·K)]	
Distillate	116.3234 344	[°C]	
Heat Transfer Area	0.811	[m2]	
Dimensions			
Vapour linear velocity	1.000	[m/s]	
Column Diameter	0.011	[m]	

	Value	Unit	Comments
Structured packing HETP	0.750	[m]	
Number of stages	20	[-]	
Column Height	15.000	[m]	
GUeRBET's REACTION(HYDROGENATION)			
Total H2 Mass flow	20.160	[kg/hr]	
Distillation of butanol and 2 ethyl hexanol			
Feed from conversion reactor			57% conversion of butanol
Total Molar Flow Rate	25.42	[kmol/h]	
1-Butanol Molar Flow	11.48285	[kmol/h]	
2-E-1-C6ol Molar Flow	394	[kmol/h]	
Crotonaldehyde Molar Flow	8.499378	[kmol/h]	
	559	[kmol/h]	
	0.234825	[kmol/h]	
	938	[kmol/h]	
Bottoms			
Total Molar Flow Rate	8.585	[kmol/h]	
2-E-1-C6ol Molar Flow	8.499360	[kmol/h]	
	146	[kmol/h]	
Reboiler			
Reboiler Duty (hourly basis)	3035794.45	[kJ/h]	
Reboiler Duty	843.276	[kW]	
Overall heat transfer coefficient	10000.00	[W/(m2·K)]	
Bottoms	0	[°C]	
Steam	222.6585	[°C]	
	986	[°C]	
	250	[°C]	
Heat Transfer Area	3.084	[m2]	
Distillate			
Total Molar Flow	16.83	[kmol/h]	Recycled back
1-Butanol Molar Flow	11.39703	[kmol/h]	
H2O Molar Flow	339	[kmol/h]	
	5.189288	[kmol/h]	
	816	[kmol/h]	
Column internal			
Reflux ratio	2.5	([kmol L)/(kmol D)]	0.00
Vapour flow rate	580.3466	[m3/h]	
	273	[m3/h]	
Condensor			
Condensor Duty (hourly basis)	1782985.85	[kJ/h]	
Condensor Duty	495.274	[kW]	
Overall heat transfer coefficient	3000.000	[W/(m2·K)]	
Distillate	134.9511	[°C]	
	792	[°C]	
Heat Transfer Area	1.574	[m2]	
Dimensions			
Vapour linear velocity	1.000	[m/s]	
Column Diameter	0.453	[m]	

	Value	Unit	Comments
Structured packing HETP	0.750	[m]	
Number of stages	10	[-]	
Column Height	7.500	[m]	
DEHYDROGENATION REACTION			
Feed			
Total Molar Flow Rate	8.585	[kmol/h]	
2-E-1-C6ol Molar Flow	8.4994	[kmol/h]	
Butanol Molar Flow	0.086	[kmol/h]	
Total Reactor volume	3	[m3]	
Reactor volume per thermal cycle	3	[m3]	
2 -ethyl hexene recovery(Distillation)			
Feed			
Total Molar Flow Rate	11.34	[kmol/h]	
	11.48285		
2-E-1-C6= Molar Flow	394	[kmol/h]	
	0.170535		
Butanol Molar Flow	341	[kmol/h]	
	1.872907		
H2O Molar Flow	447	[kmol/h]	
Bottoms			
	8.587057		
Total Molar Flow Rate	133	[kmol/h]	
	953.9011		
2-E-1-C6= Mass flow	216	Kg/hr	
	8.501186		
2-E-1-C6= Molar Flow	368	[kmol/h]	
	7736.467		
2-E-1-C6= Annual production	027	[t/annum]	
Reboiler			
	250154.1		
Reboiler Duty (hourly basis)	551	[kJ/h]	
Reboiler Duty	69.487	[kW]	
	10000.00		
Overall heat transfer coefficient	0	[W/(m2·K)]	
	157.0656		
Bottoms	257	[°C]	
Steam	250	[°C]	
Heat Transfer Area	0.075	[m2]	
Distillate			
Total Molar Flow	2.753	[kmol/h]	Recycling back
	0.795470		
2-E-1-C6= Molar Flow	064	[kmol/h]	
	1.866260		
H2O Molar Flow	084	[kmol/h]	
Column internal			
Reflux ratio	3	([kmol L)/(kmol D)]	
	51.31500		
Vapour flow rate	802	[m3/h]	
Dimensions			

	Value	Unit	Comments
Vapour linear velocity	1.000	[m/s]	
Column Diameter	0.135	[m]	
Structured packing HETP	0.750	[m]	
Number of stages	10	[-]	
Column Height	7.500	[m]	
STEAM AND WATER MANAGEMENT			
CO2 Flash Drum Steam Heater/E101_2			
Total Duty (hour basis)	76642628.65	[kJ/h]	
Total Heat Duty	21289.619	[kW]	
Overall heat transfer coefficient	3000.000	[W/(m2·K)]	
Heat Transfer Area	20.752	[m2]	
Steam Mechanical Compression/K100			
Total Steam Flow Rate	3190	[kmol/h]	
Compression			
Total Compression Duty	4289.521846	[kW]	Modelled as single stage compression.
Number of Compressors	1	[-]	
AcH cooler to Solvent recovery			
Cooler Duty (hourly basis)	3585343.185	[kJ/h]	
Cooler Duty	995.929	[kW]	
Overall heat transfer coefficient	3000.000	[W/(m2·K)]	
Heat Transfer Area	14.868	[m2]	
CrotonAldehyde cooler to separation train			
Cooler Duty (hourly basis)	2901903.263	[kJ/h]	
Cooler Duty	806.084	[kW]	
Overall heat transfer coefficient	3000.000	[W/(m2·K)]	
Heat Transfer Area	2.791	[m2]	
CrotonAldehyde cooler to Guerbet reaction			
Cooler Duty (hourly basis)	13135899.87	[kJ/h]	
Cooler Duty	3648.861	[kW]	
Overall heat transfer coefficient	3000.000	[W/(m2·K)]	
Heat Transfer Area	46.475	[m2]	
1-butanol cooler (E108)			
Cooler Duty (hourly basis)	129079.0417	[kJ/h]	
Cooler Duty	35.855	[kW]	
Overall heat transfer coefficient	3000.000	[W/(m2·K)]	
Heat Transfer Area	0.657	[m2]	
1-butanol cooler to Guebert reaction(E123)			

	Value	Unit	Comments
	129079.0		
Cooler Duty (hourly basis)	417	[kJ/h]	
Cooler Duty	35.855	[kW]	
Overall heat transfer coefficient	3000.000	[W/(m2·K)]	
Heat Transfer Area	0.657	[m2]	
2EHO cooler(E114)			
	129079.0		
Cooler Duty (hourly basis)	417	[kJ/h]	
Cooler Duty	35.855	[kW]	
Overall heat transfer coefficient	3000.000	[W/(m2·K)]	
Heat Transfer Area	0.428	[m2]	
To 2Ethyl hexene separation cooler(E109)			
	969694.2		
Cooler Duty (hourly basis)	595	[kJ/h]	
Cooler Duty	269.360	[kW]	
Overall heat transfer coefficient	3000.000	[W/(m2·K)]	
Heat Transfer Area	2.383	[m2]	

Table A.5. Mass and energy balance for gas fermentation process(C_4 process routes)

Units and streams	Heat integrated	Non-heat Integrated	Units
COMPRESSION			
Air Compression			
Total Air Feed Rate	56959.83	11391.97	[m3/h] STP
Polytropic compression			
Efficiency	0.75	0.75	[-]
Exponent (Cp/Cv)	1.4	1.4	[-]
Pressure			
Suction	100	100	[kPa] (a)
Discharge	600	600	[kPa] (a)
Temperature			
Suction	293	293	[K]
Total Compression Duty	5367.88	1073.58	[kW]
Number of 3MW Compressors	1	0	[-]
Auxilliary Compressor	2367.88	1073.58	[kW]
FERMENTATION			
Broth properties			
Temperature	30	30	[°C]
Density	1035	1035	[kg/m3]
Viscosity	0.8	0.8	[mPa·s]
Production Fermenter O_2 Mass Transfer			
Headspace O_2 Concentration	4	4	[%] (v/v)

Units and streams	Heat integrated	Non-heat Integrated	Units
Design O_2 Uptake Rate (OUR)	245	245	[(mmol O_2)/(L·h)]
Specific O_2 Uptake Rate	9.8	9.8	[(mmol O_2)/((g DCW)·h)]
Henry's Law Constant (25 [°C])	0.0013	0.0013	[mol/(L·bar)]
Back-pressure	4	4	[bar] (a)
Inlet O_2 concentration	21	21	[%] (v/v)
Inlet O_2 saturation	1.88	1.88	[mmol/L]
Outlet saturation	0.21	0.21	[mmol/L]
Broth dissolved O_2 concentration	0	0	[mmol/L]
Log mean concentration difference (LMCD)	0.76	0.76	[mmol/L]
kla(O_2)	323.13	323.13	[1/h]
Production Fermenter Continuous Cultivation			
Total Off-gas			
Molar Flow Rate	803.74	803.74	[kmol/h]
N2			
Off-gas Molar Flow Rate	508.56	508.56	[kmol/h]
O_2			
Off-gas concentration	4.02	4.02	[%] (v/v)
Oxygen uptake rate	74.48	74.48	[kmol/h]
O_2 Molar Feed Rate	106.8	106.8	[kmol/h]
Air Volumetric Feed Rate	11391.97	11391.97	[m3/h] STP
Off-gas Molar Flow Rate	32.32	32.32	[kmol/h]
CO_2			
CO_2 Molar Off-gas Flow Rate	4.32	4.32	[kmol/h]
DCW			
Dilution Rate	0.03	0.03	[1/h]
DCW Concentration	25	25	[(g DCW)/L]
DCW Productivity	0.75	0.75	[(g DCW)/(L·h)]
Carbon fraction of microorganism on DCW basis	0.48	0.48	[(g C)/(g DCW)]
DCW Carbon Sink	0.36	0.36	[(g C DCW)/(L·h)]
DCW Molar Yield	0.02	0.02	[(C mol DCW)/(C mol glucose)]
H_2O			
Average Volumetric Flow Rate	9.09	9.09	[m3/h]
Make-up Volumetric Flow Rate	9.09	9.09	[m3/h]
CO_2			
CO_2/O_2 Molar Uptake Ratio	1.102	1.102	[-]
Uptake Rate	270	270	[(mmol CO_2)/(L·h)]
Utilisation	95	95	[%]
Molar Flow Rate	86.4	86.4	[(kmol CO_2)/h]

Units and streams	Heat integrated	Non-heat Integrated	Units
Mass Feed Rate	3801.6	3801.6	[(kg CO_2)/h]
Ammonia			
$NH3/O_2$ Molar Uptake Ratio	0.01	0.01	[-]
Uptake Rate	1.25	1.25	[(mmol NH3)/(L·h)]
Utilisation	95	95	[%]
Molar Flow Rate	0.4	0.4	[(kmol NH3)/h]
Mass Feed Rate	6.8	6.8	[(kg NH3)/h]
H2			
Off-gas concentration	32.17	32.17	[%] (v/v)
H_2/O_2 Uptake Ratio	5.092	5.092	[-]
Uptake Rate	1247.5	1247.5	[(mmol H_2)/(L·h)]
Utilisation	59.46	59.46	[%]
Molar Flow Rate	637.78	637.78	[(kmol H_2)/h]
Volumetric Feed Rate	14286.57	14286.57	[(m3 H_2)/h] STP
Off-gas Molar Flow Rate	258.54	258.54	[(kmol H_2)/h]
Volumetric Off-gas Flow Rate	5791.44	5791.44	[(m3 H_2)/h] STP
Product Molar Yields			
Product	0.44	0.44	[(C mol Product)/(mol H_2)]
Productivity			
Product (Volumetric)	2.73	2.73	[(g Product)/(L·h)]
Product (DCW basis)	0.11	0.11	[(g Product)/(gDCW·h)]
Concentration			
Product	90.94	90.94	[g/L]
Production Fermenters Dimensions			
Gas hold-up			
Downcomer	0.25	0.25	[(m3 gas)/(m3 total working volume)]
Riser gas	0.15	0.15	[(m3 gas)/(m3 total working volume)]
Structured Packing Volume Fraction	0.03	0.03	[(m3 packing)/(m3 downcomer working volume)]
Working Volume Fraction	0.8	0.8	[(m3 working volume)/(m3 vessel volume)]
Number of fermenters	5	1	[-]
Vessel Volume	500	500	[m3 vessel volume]
Aspect Ratio (Downcomer)	10	10	[-]
Downcomer to Riser Diameter Ratio	1.5	1.5	[-]
Inner Diameter			
Downcomer	3.53	3.53	[m]
Riser	2.35	2.35	[m]
Fermenter Height	35.32	35.32	[m]
Broth Volume			
Downcomer	199.38	199.38	[m3]

Units and streams	Heat integrated	Non-heat Integrated	Units	
Riser	104.62	104.62	[m3]	
Total	304	304	[m3]	
Dilution				
Bleed Rate	9.12	9.12	[m3/h]	
Recirculation Pump				
Recirculation Re in Downcomer	250000	250000	[-]	
Downcomer linear velocity	0.0545	0.0545	[m/s]	
Volumetric Flow Rate	0.5342	0.5342	[m3/s]	
Differential Pressure	25	25	[kPa]	
Pump efficiency	0.65	0.65	[-]	
Duty	20.55	20.55	[kW]	
Heat exchanger				
Heat of reaction	-541150.05	-541150.05	[kJ/(kmol O_2)]	
Oxygen Uptake Rate	74.48	74.48	[(kmol O_2)/h]	
Heat Duty	11195.79	11195.79	[kW]	
Overall heat transfer coefficient	2000	2000	[W/(m2·K)]	
LMTD	10	10	[K]	
Heat Transfer Area	559.79	559.79	[m2]	
Cooling Water Usage	17.2	17.2	[m3/h]	
Coolin water usage to HYSYS				15
Annual Production				
Production Fermenters				
Number of Production Fermenters	5	1	[-]	
Continuous Operation	672	672	[h]	
Turn-around & Steady State Approach	36	36	[h]	
Total Cycle Time	708	708	[h]	
Continuous Annual Operation	7972.88	7972.88	[h]	
Number of Runs	59	11	[Runs/annum]	
Feeds to Production Fermenters				
Total glucose Molar Feed Rate	3440000	689000	[kmol/annum]	
Total H_2O Media Feed Rate	362000	72400	[m3/annum]	
Total H_2O Make-up Feed Rate	362000	72400	[m3/annum]	
Feeds to DSP				
Broth Volumetic Flow Rate	363563.39	72712.68	[m3/annum]	
DCW	9089.08	1817.82	[t/annum]	
Product	33062.51	6612.5	[t/annum]	
Seed Fermenters Dimensions				
Gas hold-up				
Downcomer	0.25	0.25	[(m3 gas)/(m3 total working volume)]	
Riser gas	0.15	0.15	[(m3 gas)/(m3 total working volume)]	

Units and streams	Heat integrated	Non-heat Integrated	Units
Structured Packing Volume Fraction	0.03	0.03	[(m3 packing)/(m3 downcomer working volume)]
Working Volume Fraction	0.8	0.8	[(m3 working volume)/(m3 vessel volume)]
Number of fermenters	5	1	[-]
Volume Fraction of Production Fermenter	10	10	[%] (v/v)
Vessel Volume	50	50	[m3 vessel volume]
Aspect Ratio (Downcomer)	10	10	[-]
Downcomer to Riser Diameter Ratio	1.5	1.5	[-]
Inner Diameter			
Downcomer	1.64	1.64	[m]
Riser	1.09	1.09	[m]
Fermenter Height	16.4	16.4	[m]
Broth Volume			
Downcomer	19.94	19.94	[m3]
Riser	10.46	10.46	[m3]
Total	30.4	30.4	[m3]
Recirculation Pump			
Recirculation Re in Downcomer	250000	250000	[-]
Downcomer linear velocity	0.1174	0.1174	[m/s]
Volumetric Flow Rate	0.248	0.248	[m3/s]
Differential Pressure	25	25	[kPa]
Pump efficiency	0.65	0.65	[-]
Duty	9.54	9.54	[kW]
Heat exchanger			
Heat of reaction	-400000	-400000	[kJ/(kmol O_2)]
Oxygen Uptake Rate	7.45	7.45	[(kmol O_2)/h]
Heat Duty	827.56	827.56	[kW]
Overall heat transfer coefficient	2000	2000	[W/(m2·K)]
LMTD	10	10	[K]
Heat Transfer Area	41.38	41.38	[m2]
Cooling Water Usage	1.27	1.27	[m3/h]

Table A.6. Mass and energy balance for using black liquor in a steam turbine for electricity generation

MASS & ENERGY BALANCE		
ELECTRICITY GENERATION	Value	Unit
Feeds		
Black Liquor		
Total Mass Feed Rate	325000	[kg/h]

Total Guaiacol Mass Feed Rate	23725	[kg/h]
Feed Pump Duty	72.44949273	[kW]
Air Compressor		
Total Air Molar Flow	8750	[kmol/h]
Total isopentane Volumetric Flow Rate (STP)	196003.6269	[m3/h] (STP)
Pressure		
Suction	100	[kPa] (a)
Discharge	150	[kPa] (a)
Temperature		
Suction	25	[°C]
Discharge	73.49319434	[°C]
Mechanical Vapour Recompression Duty		
Total Duty	3452.092807	[kW]
Combustion Turbine		
Total Turbine Duty	20579.49472	[kW]
Number Turbines	3	[-]
Steam Generation	177611.372	
Purified H2O (mass basis)	183555.9763	[kg/h]
Purified H2O (Volumetric basis)	183.556	[m3/h]
Feed Pump Duty	627.368879	[kW]

Section A.1.3

This section host the links to the HYSYS simulation files of the processes presented in Chapter 3 and Chapter 6.

Figure A.1. ASPEN HYSYS simulation file for C_2 heat-integrated route-to SAF.

Link - C_2 heat-integrated HYSYS file

Figure A.2. ASPEN HYSYS simulation file for C_4 non-heat-integrated route-to SAF.

Link - C_4 non-heat-integrated HYSYS file

Figure A.3. ASPEN HYSYS simulation file for C_4 heat-integrated route-to SAF.

Link - C_4 heat-integrated simulation HYSYS file

Appendix 2

This appendix presents the data and results for the kinetic modelling of the hydrogenation of oligomerised isobutene discussed in Chapter 4.

Section A.2.1

This section shows the experimental data utilized to model the kinetics of the hydrogenation reaction. The initial first columns were obtained using the PicoLog software from the

experiment. Other columns were calculated. Note that this is not the complete table. There is about 8760 rows still remaining. To be provided upon request.

Table A.7. Result data from the kinetic regression modelling for hydrogenation reaction of oligomerised isobutene.

Time Seconds	Time Hours	Ballast pressure D (Bar)	Reactor pressure D (Bar)	time corrected (h)	Uptake/gram feedstock	Conversion	**dX/dt**	**X**	**Absolute Error**
0	0.000	26.72	0.78	0.003	0.001	-0.009	1.219	0.003	0.013
10	0.003	26.72	0.78	0.006	0.001	-0.010	1.221	0.007	0.017
20	0.006	26.73	0.78	0.008	0.001	-0.007	1.213	0.010	0.017
30	0.008	26.75	0.78	0.011	0.000	-0.003	1.204	0.013	0.016
40	0.011	30.83	0.79	0.014	0.000	0.002	1.194	0.017	0.015
50	0.014	39.48	0.77	0.017	-0.001	0.007	1.183	0.020	0.014
60	0.017	39.07	0.79	0.019	-0.001	0.011	1.173	0.023	0.012
70	0.019	38.79	0.79	0.022	-0.002	0.015	1.164	0.027	0.012
80	0.022	38.72	0.79	0.025	-0.002	0.020	1.154	0.030	0.010
90	0.025	38.7	0.8	0.028	-0.003	0.024	1.144	0.033	0.009
100	0.028	38.69	0.81	0.031	-0.004	0.030	1.131	0.036	0.006
110	0.031	38.69	0.82	0.033	-0.005	0.040	1.109	0.039	0.001
120	0.033	38.68	0.82	0.036	-0.005	0.045	1.098	0.042	0.003
130	0.036	38.67	0.84	0.039	-0.005	0.045	1.098	0.045	0.000
140	0.039	38.69	0.84	0.042	-0.005	0.045	1.098	0.048	0.003
150	0.042	38.69	0.86	0.044	-0.006	0.046	1.096	0.052	0.005
160	0.044	38.67	0.86	0.047	-0.006	0.049	1.090	0.055	0.006
170	0.047	38.67	0.88	0.050	-0.006	0.052	1.084	0.058	0.006
180	0.050	38.69	0.89	0.053	-0.007	0.054	1.080	0.061	0.007
190	0.053	38.69	0.9	0.056	-0.007	0.057	1.072	0.064	0.006
200	0.056	38.69	0.9	0.058	-0.007	0.060	1.066	0.067	0.006
210	0.058	38.69	0.93	0.061	-0.008	0.064	1.058	0.070	0.006
220	0.061	38.69	0.94	0.064	-0.008	0.066	1.054	0.072	0.007
230	0.064	38.69	0.95	0.067	-0.009	0.071	1.044	0.075	0.005
240	0.067	38.68	0.96	0.069	-0.009	0.075	1.034	0.078	0.003
250	0.069	38.68	0.98	0.072	-0.009	0.077	1.030	0.081	0.004
260	0.072	38.68	0.98	0.075	-0.010	0.081	1.022	0.084	0.003
270	0.075	38.67	1.01	0.078	-0.010	0.084	1.017	0.087	0.003
280	0.078	38.69	1.02	0.081	-0.011	0.088	1.007	0.090	0.001

Time	Time	Ballast pressure D	Reactor pressure D	time corrected (h)	Uptake/gram feedstock	Conversion	dX/dt	X	Absolute Error
290	0.081	38.68	1.03	0.083	-0.011	0.092	0.999	0.092	0.000
300	0.083	38.68	1.04	0.086	-0.012	0.096	0.991	0.095	0.001
310	0.086	38.68	1.05	0.089	-0.012	0.100	0.984	0.098	0.002
320	0.089	38.69	1.07	0.092	-0.013	0.103	0.976	0.101	0.003
330	0.092	38.69	1.08	0.094	-0.013	0.106	0.970	0.103	0.003
340	0.094	38.7	1.09	0.097	-0.013	0.110	0.962	0.106	0.004
350	0.097	38.7	1.11	0.100	-0.014	0.114	0.955	0.109	0.005
360	0.100	38.69	1.12	0.103	-0.014	0.117	0.949	0.111	0.005
370	0.103	38.69	1.14	0.106	-0.015	0.120	0.942	0.114	0.006
380	0.106	38.7	1.16	0.108	-0.015	0.123	0.936	0.117	0.007
390	0.108	38.69	1.16	0.111	-0.015	0.127	0.928	0.119	0.008
400	0.111	38.69	1.18	0.114	-0.016	0.130	0.923	0.122	0.008
410	0.114	38.7	1.19	0.117	-0.016	0.134	0.915	0.124	0.009
420	0.117	38.68	1.2	0.119	-0.017	0.136	0.910	0.127	0.010
430	0.119	38.7	1.22	0.122	-0.017	0.139	0.904	0.129	0.010
440	0.122	38.7	1.22	0.125	-0.017	0.143	0.897	0.132	0.011
450	0.125	38.69	1.23	0.128	-0.018	0.146	0.891	0.134	0.012
460	0.128	38.69	1.25	0.131	-0.018	0.149	0.886	0.137	0.012
470	0.131	38.7	1.26	0.133	-0.018	0.152	0.878	0.139	0.013
480	0.133	38.7	1.27	0.136	-0.019	0.155	0.873	0.142	0.014
490	0.136	38.69	1.26	0.139	-0.019	0.158	0.867	0.144	0.014
500	0.139	38.69	1.27	0.142	-0.019	0.159	0.865	0.146	0.013
510	0.142	38.7	1.28	0.144	-0.020	0.163	0.858	0.149	0.014
520	0.144	38.71	1.29	0.147	-0.020	0.166	0.853	0.151	0.014
530	0.147	38.7	1.29	0.150	-0.020	0.167	0.849	0.154	0.014
540	0.150	38.7	1.3	0.153	-0.021	0.170	0.844	0.156	0.014
550	0.153	38.72	1.31	0.156	-0.021	0.173	0.838	0.158	0.015
560	0.156	38.71	1.3	0.158	-0.021	0.176	0.833	0.161	0.015
570	0.158	38.71	1.32	0.161	-0.022	0.179	0.828	0.163	0.016
580	0.161	38.7	1.32	0.164	-0.022	0.181	0.824	0.165	0.015
590	0.164	38.7	1.33	0.167	-0.022	0.183	0.819	0.167	0.016
600	0.167	38.7	1.33	0.169	-0.022	0.185	0.815	0.170	0.016
610	0.169	38.7	1.34	0.172	-0.023	0.187	0.812	0.172	0.015
620	0.172	38.7	1.34	0.175	-0.023	0.189	0.808	0.174	0.015
630	0.175	38.69	1.34	0.178	-0.023	0.193	0.801	0.177	0.016
640	0.178	38.68	1.34	0.181	-0.024	0.194	0.799	0.179	0.015
650	0.181	38.67	1.34	0.183	-0.024	0.196	0.796	0.181	0.015
660	0.183	38.68	1.35	0.186	-0.024	0.198	0.791	0.183	0.015

Time	Time	Ballast pressure D	Reactor pressure D	time corrected (h)	Uptake/gram feedstock	Conversion	**dX/dt**	**X**	**Absolute Error**
670	0.186	38.67	1.34	0.189	-0.024	0.199	0.789	0.185	0.014
680	0.189	38.68	1.35	0.192	-0.024	0.201	0.785	0.188	0.014
690	0.192	38.67	1.35	0.194	-0.025	0.204	0.780	0.190	0.014
700	0.194	38.68	1.35	0.197	-0.025	0.206	0.777	0.192	0.014
710	0.197	38.67	1.35	0.200	-0.025	0.208	0.773	0.194	0.014
720	0.200	38.68	1.36	0.203	-0.025	0.210	0.770	0.196	0.014
730	0.203	38.67	1.35	0.206	-0.026	0.211	0.768	0.198	0.012
740	0.206	38.68	1.36	0.208	-0.026	0.213	0.765	0.200	0.012
750	0.208	38.66	1.37	0.211	-0.026	0.214	0.761	0.203	0.012
760	0.211	38.65	1.37	0.214	-0.026	0.217	0.756	0.205	0.013
770	0.214	38.66	1.38	0.217	-0.026	0.218	0.754	0.207	0.011
780	0.217	38.65	1.38	0.219	-0.027	0.220	0.751	0.209	0.011
790	0.219	38.67	1.38	0.222	-0.027	0.222	0.748	0.211	0.011
800	0.222	38.67	1.39	0.225	-0.027	0.224	0.744	0.213	0.011
810	0.225	38.66	1.39	0.228	-0.027	0.227	0.739	0.215	0.012
820	0.228	38.66	1.39	0.231	-0.028	0.228	0.738	0.217	0.011
830	0.231	38.66	1.4	0.233	-0.028	0.230	0.732	0.219	0.011
840	0.233	38.67	1.41	0.236	-0.028	0.232	0.729	0.221	0.011
850	0.236	38.65	1.41	0.239	-0.028	0.234	0.726	0.223	0.011
860	0.239	38.67	1.41	0.242	-0.029	0.235	0.724	0.225	0.010
870	0.242	38.66	1.41	0.244	-0.029	0.237	0.721	0.227	0.010
880	0.244	38.67	1.42	0.247	-0.029	0.240	0.716	0.229	0.011
890	0.247	38.66	1.42	0.250	-0.029	0.243	0.711	0.231	0.012
900	0.250	38.67	1.41	0.253	-0.030	0.246	0.706	0.233	0.012
910	0.253	38.68	1.42	0.256	-0.030	0.247	0.702	0.235	0.012
920	0.256	38.67	1.42	0.258	-0.030	0.249	0.699	0.237	0.012
930	0.258	38.67	1.43	0.261	-0.030	0.251	0.696	0.239	0.012
940	0.261	38.67	1.42	0.264	-0.031	0.254	0.691	0.241	0.013
950	0.264	38.68	1.42	0.267	-0.031	0.255	0.689	0.243	0.012
960	0.267	38.66	1.42	0.269	-0.031	0.257	0.686	0.245	0.012
970	0.269	38.67	1.43	0.272	-0.031	0.260	0.681	0.247	0.013
980	0.272	38.66	1.42	0.275	-0.032	0.261	0.680	0.249	0.012
990	0.275	38.66	1.42	0.278	-0.032	0.261	0.680	0.250	0.010
1000	0.278	38.67	1.43	0.281	-0.032	0.264	0.673	0.252	0.012
1010	0.281	38.67	1.42	0.283	-0.032	0.266	0.670	0.254	0.012
1020	0.283	38.67	1.41	0.286	-0.032	0.267	0.668	0.256	0.011
1030	0.286	38.66	1.42	0.289	-0.033	0.270	0.663	0.258	0.012
1040	0.289	38.66	1.43	0.292	-0.033	0.273	0.659	0.260	0.013

Time	Time	Ballast pressure D	Reactor pressure D	time corrected (h)	Uptake/gram feedstock	Conversion	**dX/dt**	**X**	**Absolute Error**
1050	0.292	38.67	1.42	0.294	-0.033	0.274	0.657	0.262	0.012
1060	0.294	38.68	1.42	0.297	-0.033	0.275	0.655	0.263	0.011
1070	0.297	38.68	1.36	0.300	-0.034	0.277	0.652	0.265	0.011
1080	0.300	35.79	19.35	0.303	-0.034	0.278	0.649	0.267	0.011
1090	0.303	35.06	20.75	0.306	-0.034	0.280	0.646	0.269	0.012
1100	0.306	35.16	20.76	0.308	-0.034	0.281	0.644	0.271	0.011
1110	0.308	35.17	20.76	0.311	-0.034	0.282	0.643	0.272	0.010
1120	0.311	35.13	20.76	0.314	-0.034	0.284	0.640	0.274	0.010
1130	0.314	35.09	20.76	0.317	-0.035	0.286	0.636	0.276	0.010
1140	0.317	35.04	20.76	0.319	-0.035	0.286	0.636	0.278	0.008
1150	0.319	34.99	20.75	0.322	-0.035	0.288	0.633	0.279	0.008
1160	0.322	34.94	20.77	0.325	-0.035	0.290	0.630	0.281	0.009
1170	0.325	34.9	20.76	0.328	-0.035	0.290	0.630	0.283	0.007
1180	0.328	34.85	20.77	0.331	-0.035	0.291	0.629	0.285	0.006
1190	0.331	34.8	20.77	0.333	-0.036	0.294	0.624	0.286	0.007
1200	0.333	34.74	20.75	0.336	-0.036	0.295	0.621	0.288	0.007
1210	0.336	34.63	20.7	0.339	-0.036	0.297	0.618	0.290	0.007
1220	0.339	34.58	20.78	0.342	-0.036	0.298	0.616	0.292	0.007
1230	0.342	34.58	20.78	0.344	-0.036	0.299	0.615	0.293	0.006
1240	0.344	34.58	20.72	0.347	-0.037	0.302	0.610	0.295	0.007
1250	0.347	34.57	20.69	0.350	-0.037	0.305	0.605	0.297	0.008
1260	0.350	34.54	20.69	0.353	-0.037	0.307	0.602	0.298	0.008
1270	0.353	34.51	20.69	0.356	-0.037	0.308	0.601	0.300	0.008
1280	0.356	34.49	20.69	0.358	-0.038	0.310	0.598	0.302	0.008
1290	0.358	34.45	20.68	0.361	-0.038	0.311	0.595	0.303	0.008
1300	0.361	34.42	20.68	0.364	-0.038	0.313	0.592	0.305	0.008
1310	0.364	34.38	20.68	0.367	-0.038	0.316	0.587	0.307	0.009
1320	0.367	34.36	20.69	0.369	-0.038	0.317	0.585	0.308	0.009
1330	0.369	34.31	20.68	0.372	-0.039	0.318	0.584	0.310	0.008
1340	0.372	34.26	20.68	0.375	-0.039	0.320	0.581	0.312	0.008
1350	0.375	34.24	20.68	0.378	-0.039	0.322	0.578	0.313	0.009
1360	0.378	34.2	20.68	0.381	-0.039	0.323	0.576	0.315	0.008
1370	0.381	34.17	20.67	0.383	-0.039	0.325	0.573	0.316	0.008

Appendix 3

This appendix provides required supplementary information on the Cell designer and OptFlux simulations as presented in Chapter 5.

Section A.3.1

This section shows the simulation information utilized in Cell Designer and OptFlux for the aerobic gas fermentation of H_2 and CO_2 as relating to C_4 case. This section provides the metabolites nomenclatures presented in Figure 5.3.

Table A.8. Metabolite id and nomenclature showing shadow prices

Metabolite id	Metabolite Name	Shadow Prices
ADP	Adenosine Diphosphate	0
AKG	Alpha-Ketoglutarate	165.5
ATP	Adenosine Triphosphate	9.75
AcCoA	Acetyl Coenzyme A	79.75
AcLac	Acetyl Lactate	82.75
CIT	Citrate	170.25
CO_2_ex	Carbon Dioxide (extracellular)	1
CO_2_in	Carbon Dioxide (intracellular)	2
CoA	Coenzyme A	0
DGP	Dolichyl Diphosphate	101.25
DHAP	Dihydroxyacetone Phosphate	100.5
DHMB	Dihydromethylbutyrate	88.5
E4P	Erythrose 4-Phosphate	130.5
F6P	Fructose 6-Phosphate	196.25
FBP	Fructose 1,6-Bisphosphate	201
FUM	Fumarate	90.5
G2P	Glucose 2-Phosphate	91.5
G3P	Glycerol 3-Phosphate	90.5
G6P	Glucose 6-Phosphate	197.25
GAP	Glyceraldehyde 3-Phosphate	99.5
GLUM	Glutamate	5
GLUT	Glutathione	0
Gluconate_6P	6-Phosphogluconate	193.5
Glyoxy	Glyoxylate	11.75
H2S	Hydrogen Sulfide	56.25
H2_ex	Hydrogen ions (intracellular)	1
H2_in	Hydrogen ions (extracellular)	2
H_in	Hydrogen ions (intracellular)	-0.75
H_out	Hydrogen ions (extracellular)	0
ICI	Isocitrate	171.25
K2BUT	2-Ketobutyrate	-4
KDPG	2-Keto-3-Deoxy-6-Phosphogluconate	193.5
KIV	α-Ketoisovalerate	-2
MAL	Malate	91.5
NAD	Nicotinamide Adenine Dinucleotide Phosphate (reduced)	-10.75
NADH	Nicotinamide Adenine Dinucleotide (reduced)	-7.75
NADP	Nicotinamide Adenine Dinucleotide Phosphate	0
NADPH	Nicotinamide Adenine Dinucleotide Phosphate (reduced)	4.75
NH3_ex	Ammonia (extracellular)	1
NH3_in	Ammonia (intracellular)	2
O_2_ex	Oxygen (extracellular)	1
O_2_in	Oxygen (intracellular)	2
OAA	Oxaloacetate	89.5

Metabolite id	Metabolite Name	Shadow Prices
PEP	Phosphoenolpyruvate	92.5
PYR	Pyruvate	83.75
Pi	Inorganic Phosphate	5.75
Pi_ex	Inorganic Phosphate (extracellular)	0.75
Q	Ubiquinone	-1
QH2	Ubiquinol	0
RIBO_5P	Ribose 5-Phosphate	166.25
RIB_5P	Ribulose 5-Phosphate	167.25
RuB5P	Ribulose 1,5-Bisphosphate	178
S7P	Sedoheptulose 7-Phosphate	232
SO4_ex	Sulfate (extracellular)	1
SO4_in	Sulfate (intracellular)	2
SUCC	Succinate	90.5
SUCC_CoA	Succinyl Coenzyme A	160.5
TMA	Trimethylamine	0
XYL_5P	Xylulose 5-Phosphate	166.25
s58	α-Ketoisovalerate (extracellular)	-1

Table A.9. Variable extra simulation information

Reaction id	Reduced Costs	Reaction id	Reduced Costs	Reaction id	Reduced Costs
R_EX_CO_2_ex_	0	re20	66	re58	0
R_EX_H2_ex_	0	re21	0	re59	0
R_EX_H_out_	0	re22	0	re60	2
R_EX_NH3_ex_	0	re23	0	re61	0
R_EX_O_2_ex_	0	re24	69	re62	0
R_EX_Pi_ex_	0	re25	0	re63	4.26E-14
R_EX_SO4_ex_	0	re26	0	re64	1454.25
R_EX_s58_	0	re27	0	re65	0
re1	0	re28	0	re66	0
re10	0	re29	0	re67	0
re11	0	re3	0	re68	10.25
re12	0	re32	0	re69	0
re13	0	re34	0	re7	0
re14	0	re36	0	re71	0
re16	0	re37	-2.84E-14	re72	0
re17	0	re38	1.42E-14	re73	0
re18	0	re41	-1.42E-14	re74	0

Reaction id	Reduced Costs	Reaction id	Reduced Costs	Reaction id	Reduced Costs
re19	0	re45	0	re75	0
re2	0	re46	172.25	re8	0
re53	0	re47	0	re9	0
re54	0	re48	175.25		
re55	0.5	re49	4		
re56	0	re5	0		
re57	0.5	re50	0		

Section A.3.2

This section shows the simulation results and solutions utilized in Cell Designer and OptFlux for the aerobic gas fermentation of H_2 and CO_2 as relating to C_4 case. Also shows the reaction of the conversion bioreactor derived.

Table A.10. pFBA OptFlux simulations solutions.

Metabolite ID	Metabolite Name	Uptake Values(mmol gDCW−1 h−1)
Consumption		
NH3_ex	Ammonia (extracellular)	0.05
H2_ex	Hydrogen gas (extracellular)	49.999576
CO_2_ex	Carbon Dioxide (extracellular)	10.858887
SO4_ex	Sulfate (extracellular)	0.05
O_2_ex	Oxygen (extracellular)	9.8614569
Production		
s58	KIV_ex - α-Ketoisovalerate (extracellular)	4.3544437

Table A.11. Drain reaction values from pFBA simulations

Flux id	Flux name	Flux values
R_EX_CO_2_ex_	Drain to CO_2_ex	-10.858887
R_EX_H_out_	Drain to H_out	0
R_EX_SO4_ex_	Drain to SO4_ex	-0.05
R_EX_H2_ex_	Drain to H2_ex	-49.999576
R_EX_NH3_ex_	Drain to NH3_ex	-0.05
R_EX_Pi_ex_	Drain to Pi_ex	0
R_EX_O_2_ex_	Drain to O_2_ex	-9.8614569
R_EX_s58_	Drain to KIV_ex	4.35444378

Table A.12. Internal transport reaction values from pFBA simulation.

Flux id	Flux values	Flux id	Flux values	Flux id	Flux values	Flux id	Flux values
re24	0	re60	0	re19	0	re75	4.354444
re68	0	re62	5.254444	re18	0.05	re7	15.31333
re23	5.754444	re61	0.05	re50	49.99958	re74	4.354444
re67	0	re13	10.25889	re46	0	re9	15.31333
re26	5.654444	re57	0	re45	0	re32	5.254444
re25	0	re12	4.654444	re48	0	re38	5.104444
re69	0	re56	19.72291	re47	0	re71	0
re20	0	re59	0	re41	5.154444	re73	4.354444
re64	0.05	re14	0.1	re49	0	re72	4.354444
re63	5.104444	re58	19.72291	re2	49.99958		
re22	0	re53	36.88111	re1	10.85889		
re66	0	re11	4.654444	re3	9.861457		
re21	0	re55	0	re34	-10.3589		
re65	0.05	re10	25.92222	re37	5.054444		
re28	-5.75444	re54	10.25889	re5	0.05		
re27	0	re17	0.05	re36	10.25889		
re29	0.05	re16	0.05	re8	25.92222		

Table A.13. The coefficients for the conversion reactor calculated

		C	H	O	N
NH_3	-1.684		-5.052		-1.684
CO_2	-61.876	-61.876		-123.752	
O_2	-60.3965			-120.793	
H2	-255.573		-511.146		
C_5H8O_3	11.028	55.14	88.224	33.084	
$C_4H_7O_2N$	1.684	6.736	11.788	3.368	1.684
H_2O	208.093		416.186	208.093	
		0	0	0	0

Appendix 4

This appendix provides a breakdown of the TEA results for Chapter 3 and Chapter 6.

Section A.4.1

This section provides the breakdown of the TEA results of the C_2 heat-integrated route-to-SAF.

Table A.14. Estimation of TCI for C_2 heat-integrated route-to-SAF (NREL Method).

Plant section	Major ISBL Equipment item	Quantity	Item Cost [$]	Purchase cost correction factor [-]	Purchase cost [$]	ISBL Installed Cost Cran factor	Installed cost (2006) [$]	CE cost Index adjustment to 2019	Location Factor	Total Installed Cost [$]	Total Plant section [$]
	scH_2O Gasification Thermal Cycle										
	High Pressure Pump	1	$87,955.77	1	$87,955.77	2.30	$202,298.27	$245,792.40	0.51	$125,125.55	
	Heat Pump Condensor	1	$36,570.07	1	$36,570.07	2.20	$80,454.15	$97,751.80	0.51	$49,762.51	
	Heat Pump Compressor	1	$1,537,949.75	1	$1,537,949.75	1.60	$2,460,719.61	$2,989,774.32	0.51	$1,522,004.56	
	scH_2O Recovery HE	1	$99,112.26	1	$99,112.26	2.20	$218,046.97	$264,927.07	0.51	$134,866.44	
	scH_2O Plug Flow Reactor	1	$183,150.60	1	$183,150.60	1.50	$274,725.90	$333,791.97	0.51	$169,923.49	
	Vapour Heater	1	$90,005.95	1	$90,005.95	2.20	$198,013.08	$240,585.89	0.51	$122,475.07	
	Heat Pump Recovery HE	1	$7,612.85	1	$7,612.85	2.20	$16,748.26	$20,349.14	0.51	$10,359.14	
	Combustion Chamber	1	########	1	$11,960,755.58	2.20	$26,313,662.27	$31,971,099.66	0.51	$16,275,529.25	$36,843,328.40
Feedstock Pre-treatment	Supercritical Heater	1	$143,351.49	1	$143,351.49	2.20	$315,373.28	$383,178.54	0.51	$195,064.72	
	Turbo-expander/TE Compressor	1	$2,155,665.50	1	$2,155,665.50	1.80	$3,880,197.91	$4,486,524.99	0.51	$2,283,955.49	
	Air Compression After Cooler/Air Cooler	1	$8,541.99	1	$8,541.99	2.20	$18,792.37	$22,832.73	0.51	$11,623.46	
	H_2 Bioreactor Cooler	1	$25,587.82	1	$25,587.82	2.20	$56,293.20	$68,396.23	0.51	$34,818.47	
	Combustion										
	H_2 Combustion Feed Heater	1	$30,448.15	1	$30,448.15	2.20	$66,985.92	$81,387.90	0.51	$41,432.14	
	Bioreactor Off-gas Combustion Feed Heater	1	$23,064.90	1	$23,064.90	2.20	$50,742.78	$61,652.47	0.51	$31,385.43	
	Fired Heater/Combustion heater	1	$2,424,054.14	1	$2,424,054.14	1.80	$4,363,297.46	$4,674,961.56	0.51	$2,379,882.91	
	Combustion Turbine	1	########	1	$10,562,526.94	1.80	$19,012,548.48	$23,100,246.41	0.51	$11,759,643.56	
	TE Turbine	1	$1,522,878.91	1	$1,522,878.91	1.80	$2,741,182.05	$3,330,536.18	0.51	$1,695,476.22	
	Seed Fermenters										
	Seed fermenters	1	$186,818.40	1	$186,818.40	2.00	$373,636.80	$453,968.71	0.51	$231,101.87	
	Seed fermenter Recirculation Pumps	1	$24,783.01	1	$24,783.01	2.30	$57,000.93	$69,256.13	0.51	$35,256.22	
Fermentation	Seed fermenter Heat Exchangers	1	$27,379.39	1	$27,379.39	2.20	$60,234.65	$73,185.11	0.51	$37,256.35	$3,836,199.68
	Production Fermenters										
	Production fermenters	4	$644,722.99	1	$2,578,891.97	2.00	$5,157,783.94	$6,266,707.49	0.51	$3,190,193.09	
	Production fermenter Recirculation Pumps	4	$40,123.58	1	$160,494.33	2.30	$369,136.95	$448,501.40	0.51	$228,318.63	
	Production Fermenter HE	4	$20,957.93	1	$83,831.72	2.20	$184,429.78	$224,082.19	0.51	$114,073.53	
	Pyruvate decarboxylation										
Product Recovery from Bioreactor Aqueous & Vapour	Pyruvate decarboxylation Plug flow reactor	1	$307,060.57	1	$307,060.57	1.50	$460,590.86	$559,617.89	0.51	$284,884.71	
	Acetaldehyde Stripper(Column)										$363,675.59
	Tower	1	$45,875.04	1	$45,875.04	2.40	$110,100.10	$133,771.62	0.51	$68,099.13	
	Reboiler	1	$7,857.28	1	$7,857.28	2.20	$17,286.03	$21,002.52	0.51	$10,691.75	
	Furfural recovery Distillation										
	Tower	1	$89,638.04	1	$89,638.04	2.40	$215,131.30	$261,384.53	0.51	$133,063.03	
	AcH and Fulfural Concentration distillation										
Solvent Recovery	Tower	1	$174,372.09	1	$174,372.09	2.40	$418,493.01	$508,469.00	0.51	$258,846.34	$609,571.22
	Reboiler	1	$8,212.71	1	$8,212.71	2.20	$18,067.96	$21,952.57	0.51	$11,175.40	
	Furfural recovery Distillation 2										
	Tower	1	$123,473.50	1	$123,473.50	2.40	$296,336.39	$360,048.72	0.51	$183,290.02	
	Reboiler	1	$17,046.87	1	$17,046.87	2.20	$37,503.11	$45,566.28	0.51	$23,196.43	
	Aldo-condensation reaction										
	Aldo-condensation reaction	3	$118,145.46	1	$354,436.39	1.50	$531,654.58	$645,960.32	0.51	$328,839.05	
	LP CrotonAd column										
Crotonaldehyde Production and separation	Tower	3	$123,473.50	1	$370,420.49	2.40	$889,009.18	$1,080,146.16	0.51	$549,870.06	$1,214,895.22
	Reboiler	3	$7,576.60	1	$22,729.79	2.20	$50,005.53	$60,756.72	0.51	$30,929.43	
	HP CrotonAd column										
	Tower	3	$56,575.58	1	$169,726.73	2.40	$407,344.15	$494,923.14	0.51	$251,950.55	
	Reboiler	3	$13,058.08	1	$39,174.25	2.20	$86,183.35	$104,712.78	0.51	$53,306.14	
	Crotonaldehyde Hydrogenation										
	Crotonaldhehyde Hydrogenation	1	$118,145.46	1	$118,145.46	1.50	$177,218.19	$215,320.11	0.51	$109,613.02	
	Crotonaldehyde and 1-butanol Separation										
	Tower	1	$119,437.60	1	$119,437.60	2.40	$286,650.23	$348,280.03	0.51	$177,298.93	
	Reboiler	1	$27,557.73	1	$27,557.73	2.20	$60,627.01	$73,661.82	0.51	$37,499.03	
	Condenser	1	$13,424.86	1	$13,424.86	2.20	$29,534.69	$35,884.65	0.51	$18,267.80	
Crotonaldehyde hydrogenation and Guebert reaction	**2EHO recovery**										
	Tower	1	$51,287.39	1	$51,287.39	2.40	$123,089.74	$149,554.04	0.51	$76,133.48	$697,457.41
	Reboiler	1	$8,263.66	1	$8,263.66	2.20	$18,180.05	$22,088.76	0.51	$11,244.73	
	Condenser	1	$10,091.33	1	$10,091.33	2.20	$22,200.93	$26,974.13	0.51	$13,731.72	
	Dehydrogenation reaction										
	Dehydrogenation reaction	1	$118,145.46	1	$118,145.46	1.50	$177,218.19	$215,320.11	0.51	$109,613.02	
	2EthylHexene recovery										
	Tower	1	$26,777.18	1	$26,777.18	2.40	$64,265.24	$78,082.26	0.51	$39,749.34	
	Reboiler	1	$76,653.89	1	$76,653.89	2.20	$168,638.57	$204,895.86	0.51	$104,306.35	
	CO2 flash drum steam heater	1	$21,628.74	1	$21,628.74	3.50	$75,700.58	$91,976.21	0.51	$46,822.33	
	Steam Mechanical Vapour Compressors	1	$1,994,472.37	1	$1,994,472.37	2.50	$4,986,180.94	$6,058,209.84	0.51	$3,084,053.17	
	AcH cooler to solvent recovery	1	$7,317.70	1	$7,317.70	3.50	$25,611.95	$31,118.52	0.51	$15,841.51	
	CrotonoAldehyde cooler to separattion train	1	$8,460.92	1	$8,460.92	3.50	$29,613.23	$35,980.07	0.51	$18,316.38	
Steam & Water Management	1-butanol cooler	1	$14,974.00	1	$14,974.00	3.50	$52,409.01	$63,676.94	0.51	$32,416.02	$3,310,219.40
	2EHO cooler	1	$19,199.37	1	$19,199.37	3.50	$67,197.80	$81,645.33	0.51	$41,563.19	
	To 2Ethyl hexene separation cooler(E109)	1	$8,825.97	1	$8,825.97	3.50	$30,890.91	$37,532.45	0.51	$19,106.65	
	1-butanol cooler to Guebert reaction	1	$14,974.00	1	$14,974.00	3.50	$52,409.01	$63,676.94	0.51	$32,416.02	
	CrotonoAldehyde cooler to Guebert	1	$9,092.73	1	$9,092.73	3.50	$31,824.55	$38,666.83	0.51	$19,684.12	

Table A.15. Extra capital expense associated with the NREL method for C_2 heat-integrated bio-jet Plant.

Additional Costs for Determining Total Capital Investment (TCI)				
Item	**Description**	**Unit (Basis)**	**[$/annum]**	**Comments**
Additional Direct Costs				
Warehouse	4	equipment]	1,875,014	On-site storage of equipment and supplies.
Development	9	equipment]	4,218,781	drainage, rail system, soil borings, and general paving.
Additional piping	5	equipment]	2,109,391	outside the battery limits.
Indirect Costs				
costs	10	[% of TDC]	5,507,853	the construction contractor.
Field expenses	10	[% of TDC]	5,507,853	services, temporary construction facilities, and field
construction	20	[% of TDC]	11,015,707	construction.
contingency	10	[% of TDC]	5,507,853	construction.
Other costs	10	[% of TDC]	5,507,853	permits, surveys, and fees. Piling, soil
		TOTAL ADDITIONAL COSTS	41,250,305	

Table A.16. Estimation of TCI for C_2 heat-integrated route-to-SAF plant using TS Method.

Plant section	Major ISBL Equipment item	Quantity	Item Cost [$]	Purchase cost correction factor [-]	Purchase cost [$]	ISBL Installed Cost Cran factor	Installed cost (2006) [$]	CE cost Index adjustment to 2019	Location Factor	Total Installed Cost [$]	Total Plant section [$]
	scH$_2$O Gasification Thermal Cycle										
Feedstock Pre-treatment	High Pressure Pump	1	$87,955.77	1	$87,955.77	3.30	$290,254.05	$352,658.67	0.51	$179,527.96	$62,271,558.97
	Heat Pump Condensor	1	$36,570.07	1	$36,570.07	3.30	$120,681.23	$146,627.70	0.51	$74,643.77	
	Heat Pump Compressor	1	$1,537,949.75	1	$1,537,949.75	3.30	$5,075,234.19	$6,166,409.54	0.51	$3,139,134.40	
	scH$_2$O Recovery HE	1	$99,112.26	1	$99,112.26	3.30	$327,070.46	$397,390.61	0.51	$202,299.66	
	scH$_2$O Plug Flow Reactor	1	$183,150.60	1	$183,150.60	3.30	$604,396.97	$734,342.32	0.51	$373,831.68	
	Vapour Heater	1	$90,005.95	1	$90,005.95	3.30	$297,019.62	$360,878.84	0.51	$183,712.61	
	Heat Pump Recovery HE	1	$7,612.85	1	$7,612.85	3.30	$25,122.39	$30,523.71	0.51	$15,538.71	
	Combustion Chamber	1	$11,960,755.58	1	$11,960,755.58	3.30	$39,470,493.41	$47,956,649.49	0.51	$24,413,293.87	
	Supercritical Heater	1	$143,351.49	1	$143,351.49	3.30	$473,059.92	$574,767.81	0.51	$292,597.08	
	Turbo-expander/TE Compressor	1	$2,155,665.50	1	$2,155,665.50	3.30	$7,113,696.16	$8,225,295.81	0.51	$4,187,251.73	
	Air Compression After Cooler/Air Cooler	1	$8,541.99	1	$8,541.99	3.30	$28,188.56	$34,249.10	0.51	$17,435.19	
	H$_2$ Bioreactor Cooler	1	$25,587.82	1	$25,587.82	3.30	$84,439.79	$102,594.35	0.51	$52,227.71	
	Combustion										
	H$_2$ Combustion Feed Heater	1	$30,448.15	1	$30,448.15	3.30	$100,478.89	$122,081.85	0.51	$62,148.21	
	Bioreactor Off-gas Combustion Feed Heater	1	$23,064.90	1	$23,064.90	3.30	$76,114.16	$92,478.71	0.51	$47,078.14	
	Fired Heater/Combustion heater	1	$2,424,054.14	1	$2,424,054.14	3.30	$7,999,378.67	$8,570,762.86	0.51	$4,363,118.66	
	Combustion Turbine	1	$10,562,526.94	1	$10,562,526.94	3.30	$34,856,338.89	$42,350,451.75	0.51	$21,559,346.52	
	TE Turbine	1	$1,522,878.91	1	$1,522,878.91	3.30	$5,025,500.42	$6,105,983.01	0.51	$3,108,373.06	
Fermentation	**Seed Fermenters**										$6,250,304.11
	Seed fermenters	1	$186,818.40	1	$186,818.40	3.30	$616,500.72	$749,048.37	0.51	$381,318.09	
	Seed fermenter Recirculation Pumps	1	$24,783.01	1	$24,783.01	3.30	$81,783.95	$99,367.50	0.51	$50,585.02	
	Seed fermenter Heat Exchangers	1	$27,379.39	1	$27,379.39	3.30	$90,351.98	$109,777.66	0.51	$55,884.52	
	Production Fermenters										
	Production fermenters	4	$644,722.99	1	$2,578,891.97	3.30	$8,510,343.51	$10,340,067.36	0.51	$5,263,818.59	
	Production fermenter Recirculation Pumps	4	$40,123.58	1	$160,494.33	3.30	$529,631.28	$643,502.01	0.51	$327,587.60	
	Production Fermenter HE	4	$20,957.93	1	$83,831.72	3.30	$276,644.67	$336,123.28	0.51	$171,110.29	
Product Recovery from Bioreactor Aqueous & Vapour	**Pyruvate decarboxylation**										$736,420.28
	Pyruvate decarboxylation Plug flow reactor	1	$307,060.57	1	$307,060.57	3.30	$1,013,299.88	$1,231,159.36	0.51	$626,746.35	
	Acetaldehyde Stripper(Column)										
	Tower	1	$45,875.04	1	$45,875.04	3.30	$151,387.64	$183,935.98	0.51	$93,636.30	
	Reboiler	1	$7,857.28	1	$7,857.28	3.30	$25,929.04	$31,503.78	0.51	$16,037.63	
Solvent Recovery	**Furfural recovery Distillation**										$842,456.91
	Tower	1	$89,638.04	1	$89,638.04	3.30	$295,805.53	$359,403.72	0.51	$182,961.67	
	AcH and Fulrural Concentration distillation										
	Tower	1	$174,372.09	1	$174,372.09	3.30	$575,427.89	$699,144.88	0.51	$355,913.72	
	Reboiler	1	$8,212.71	1	$8,212.71	3.30	$27,101.94	$32,928.86	0.51	$16,763.10	
	Furfural recovery Distillation 2										
	Tower	1	$123,473.50	1	$123,473.50	3.30	$407,462.54	$495,066.99	0.51	$252,023.78	
	Reboiler	1	$17,046.87	1	$17,046.87	3.30	$56,254.67	$68,349.42	0.51	$34,794.64	
Crotonaldehyde Production and separation	**Aldo-condensation reaction**										$1,952,302.59
	Aldo-condensation reaction	3	$118,145.46	1	$354,436.39	3.30	$1,169,640.08	$1,421,112.70	0.51	$723,445.91	
	LP CrotonAd column										
	Tower	3	$123,473.50	1	$370,420.49	3.30	$1,222,387.63	$1,485,200.97	0.51	$756,071.33	
	Reboiler	3	$7,576.60	1	$22,729.79	3.30	$75,008.30	$91,135.08	0.51	$46,394.14	
	HP CrotonAd column										
	Tower	3	$56,575.58	1	$169,726.73	3.30	$560,098.21	$680,519.32	0.51	$346,432.00	
	Reboiler	3	$13,058.08	1	$39,174.25	3.30	$129,275.03	$157,069.16	0.51	$79,959.21	
Crotonaldehyde hydrogenation and Guebert reaction	**Crotonaldhehyde Hydrogenation**										$1,162,996.61
	Crotonaldhehyde Hydrogenation	1	$118,145.46	1	$118,145.46	3.30	$389,880.03	$473,704.23	0.51	$241,148.64	
	Crotonaldehyde and 1-butanol Separation										
	Tower	1	$119,437.60	1	$119,437.60	3.30	$394,144.07	$478,885.04	0.51	$243,786.03	
	Reboiler	1	$27,557.73	1	$27,557.73	3.30	$90,940.52	$110,492.73	0.51	$56,248.54	
	Condenser	1	$13,424.86	1	$13,424.86	3.30	$44,302.04	$53,826.97	0.51	$27,401.70	
	2EHO recovery										
	Tower	1	$51,287.39	1	$51,287.39	3.30	$169,248.40	$205,636.80	0.51	$104,683.54	
	Reboiler	1	$8,263.66	1	$8,263.66	3.30	$27,270.07	$33,133.14	0.51	$16,867.09	
	Condenser	1	$10,091.33	1	$10,091.33	3.30	$33,301.39	$40,461.19	0.51	$20,597.58	
	Dehydrogenation reaction										
	Dehydrogenation reaction	1	$118,145.46	1	$118,145.46	3.30	$389,880.03	$473,704.23	0.51	$241,148.64	
	2EthylHexene recovery										
	Tower	1	$26,777.18	1	$26,777.18	3.30	$88,364.70	$107,363.11	0.51	$54,655.34	
	Reboiler	1	$76,653.89	1	$76,653.89	3.30	$252,957.85	$307,343.79	0.51	$156,459.52	
Steam & Water Management	CO2 flash drum steam heater	1	$21,628.74	1	$21,628.74	3.50	$75,700.58	$91,976.21	0.51	$46,822.33	$3,310,219.40
	Steam Mechanical Vapour Compressors	1	$1,994,472.37	1	$1,994,472.37	2.50	$4,986,180.94	$6,058,209.84	0.51	$3,084,053.17	
	AcH cooler to solvent recovery	1	$7,317.70	1	$7,317.70	3.50	$25,611.95	$31,118.52	0.51	$15,841.51	
	CrotonoAldehyde cooler to separattion train	1	$8,460.92	1	$8,460.92	3.50	$29,613.23	$35,980.07	0.51	$18,316.38	
	1-butanol cooler	1	$14,974.00	1	$14,974.00	3.50	$52,409.01	$63,676.94	0.51	$32,416.02	
	2EHO cooler	1	$19,199.37	1	$19,199.37	3.50	$67,197.80	$81,645.33	0.51	$41,563.19	
	To 2Ethyl hexene separation cooler(E109)	1	$8,825.97	1	$8,825.97	3.50	$30,890.91	$37,532.45	0.51	$19,106.65	
	1-butanol cooler to Guebert reaction	1	$14,974.00	1	$14,974.00	3.50	$52,409.01	$63,676.94	0.51	$32,416.02	
	CrotonoAldehyde cooler to Guebert	1	$9,092.73	1	$9,092.73	3.50	$31,824.55	$38,666.83	0.51	$19,684.12	

Table A.17. Estimation of TCI for C_2 heat-integrated route-to-SAF plant using Hand Method.

Plant section	Major ISBL Equipment item	Quantity	Item Cost [$]	Purchase cost correction factor [-]	Purchase cost [$]	Comments	ISBL Installed Cost Hand factor	Installed cost (2006) [$]	Purchase cost CE Index (2006)	CE cost Index adjustment to 2019	Location Factor	Total Installed Cost [$]	Total Plant section [$]
Feedstock Pre-treatment	**scH2O Gasification Thermal Cycle**												54451k
	High Pressure Pump	1	88k	1	88k		4.00	352k	500	427k	0.51	218k	
	Heat Pump Condensor	1	37k	1	37k		3.50	128k	500	156k	0.51	79k	
	Heat Pump Compressor	1	1538k	1	1538k		2.50	3845k	500	4672k	0.51	2378k	
	scH2O Recovery HE	1	99k	1	99k		3.50	347k	500	421k	0.51	215k	
	scH2O Plug Flow Reactor	1	183k	1	183k		4.00	733k	500	890k	0.51	453k	
	Vapour Heater	1	90k	1	90k		3.50	315k	500	383k	0.51	195k	
	Heat Pump Recovery HE	1	8k	1	8k		3.50	27k	500	32k	0.51	16k	
	Combustion Chamber	1	11961k	1	11961k		3.50	41863k	500	50863k	0.51	25893k	
	Supercritical Heater	1	143k	1	143k		3.50	502k	500	610k	0.51	310k	
	Turbo-expander/TE Compressor	1	2156k	1	2156k		2.50	5389k	525	6231k	0.51	3172k	
	Air Compression After Cooler/Air Cooler	1	9k	1	9k		3.50	30k	500	36k	0.51	18k	
	H2 Bioreactor Cooler	1	26k	1	26k		3.50	90k	500	109k	0.51	55k	
	Combustion												
	H2 Combustion Feed Heater	1	30k	1	30k		3.50	107k	500	129k	0.51	66k	
	Bioreactor Off-gas Combustion Feed Heater	1	23k	1	23k		3.50	81k	500	98k	0.51	50k	
	Fired Heater/Combustion heater	1	2424k	1	2424k		2.00	4848k	567	5194k	0.51	2644k	
	Combustion Turbine	1	10563k	1	10563k		2.50	26406k	500	32084k	0.51	16333k	
	TE Turbine	1	1523k	1	1523k		2.50	3807k	500	4626k	0.51	2355k	
Fermentation	**Seed Fermenters**												7542k
	Seed fermenters	1	187k	1	187k		4.00	747k	500	908k	0.51	462k	
	Seed fermenter Recirculation Pumps	1	25k	1	25k		4.00	99k	500	120k	0.51	61k	
	Seed fermenter Heat Exchangers	1	27k	1	27k		3.50	96k	500	116k	0.51	59k	
	Production Fermenters												
	Production fermenters	4	645k	1	2579k		4.00	10316k	500	12533k	0.51	6380k	
	Production fermenter Recirculation Pumps	4	40k	1	160k		4.00	642k	500	780k	0.51	397k	
	Production Fermenter HE	4	21k	1	84k		3.50	293k	500	356k	0.51	181k	
Product Recovery from Bioreactor Aqueous & Vapour	**Pyruvate decarboxylation**												890k
	Pyruvate decarboxylation Plug flow reactor	1	307k	1	307k		4.00	1228k	500	1492k	0.51	760k	
	Acetaldehyde Stripper(Column)												
	Tower	1	46k	1	46k		4.00	184k	500	223k	0.51	113k	
	Reboiler	1	8k	1	8k		3.50	28k	500	33k	0.51	17k	
Solvent Recovery	**Furfural recovery Distillation**												1013k
	Tower	1	90k	1	90k		4.00	359k	500	436k	0.51	222k	
	AcH and Fulfural Concentration distillation												
	Tower	0k	174k	0k	174k		0k	697k	1k	847k	0.51	431k	
	Reboiler	0k	8k	0k	8k		0k	29k	1k	35k	0.51	18k	
	Furfural recovery Distillation 2												
	Tower	1	123k	1	123k		4.00	494k	500	600k	0.51	305k	
	Reboiler	1	17k	1	17k		3.50	60k	500	72k	0.51	37k	
Crotonaldehyde Production and separation	**Aldo-condensation reactor**												2347k
	Aldo-condensation reactor	3	118k	1	354k		4.00	1418k	500	1723k	0.51	877k	
	LP CrotonAd column												
	Tower	3	123k	1	370k		4.00	1482k	500	1800k	0.51	916k	
	Reboiler	3	8k	1	23k		3.50	80k	500	97k	0.51	49k	
	HP CrotonAd column												
	Tower	3	57k	1	170k		4.00	679k	500	825k	0.51	420k	
	Reboiler	3	13k	1	39k		3.50	137k	500	167k	0.51	85k	
Other reactions including(Crotonaldehyde hydrogenation and Guebert reaction)	**Crotonaldhehyde Hydrogenation**												1368k
	Crotonaldhehyde Hydrogenation	1	118k	1	118k		4.00	473k	500	574k	0.51	292k	
	Crotonaldehyde and 1-butanol Separation												
	Tower	1	119k	1	119k		4.00	478k	500	580k	0.51	295k	
	Reboiler	1	28k	1	28k		3.50	96k	500	117k	0.51	60k	
	Condenser	1	13k	1	13k		3.50	47k	500	57k	0.51	29k	
	2EHO recovery												
	Tower	1	51k	1	51k		4.00	205k	500	249k	0.51	127k	
	Reboiler	1	8k	1	8k		3.50	29k	500	35k	0.51	18k	
	Condenser	1	10k	1	10k		3.50	35k	500	43k	0.51	22k	
	Dehydration reaction												
	Dehydration and hydrogenation reactors	1	118k	1	118k		4.00	473k	500	574k	0.51	292k	
	2EthylHexene recovery												
	Tower	1	27k	1	27k		4.00	107k	500	130k	0.51	66k	
	Reboiler	1	77k	1	77k		3.50	268k	500	326k	0.51	166k	
Steam & Water Management	CO2 flash drum steam heater	1	22k	1	22k		3.50	76k	500	92k	0.51	47k	3310k
	Steam Mechanical Vapour Compressors	1	1994k	1	1994k		2.50	4986k	500	6058k	0.51	3084k	
	AcH cooler to solvent recovery	1	7k	1	7k		3.50	26k	500	31k	0.51	16k	
	CrotonoAldehyde cooler to separattion train	1	8k	1	8k		3.50	30k	500	36k	0.51	18k	
	1-butanol cooler	1	15k	1	15k		3.50	52k	500	64k	0.51	32k	
	2EHO cooler	1	19k	1	19k		3.50	67k	500	82k	0.51	42k	
	To 2Ethyl hexene separation cooler(E109)	1	9k	1	9k		3.50	31k	500	38k	0.51	19k	
	1-butanol cooler to Guebert reaction	1	15k	1	15k		3.50	52k	500	64k	0.51	32k	
	CrotonoAldehyde cooler to Guebert	1	9k	1	9k		3.50	32k	500	39k	0.51	20k	

Table A.18. FOC for C_2 heat-integrated route-to-SAF plant (C & R).

Labour & Supervision	Salary [$] (2020)	Number	Cost [$]
Plant manager	29,591	1	29,591
Plant engineer	29,977	1	29,977
Maintenance supervisor	20,406	1	20,406
Maintenance technician	14,968	3	44,903
Lab manager	21,569	1	21,569
Lab technician	14,619	1	14,619
Shift supervisor	15,267	4	61,067
Shift operators	13,373	12	160,470
Yard employees	6,184	4	24,735
Clerks and secretaries	11,488	3	34,464
Total operating and supervisory labour cost			**441,800**

FIXED COSTS			
Fixed Operational Consideration	Assessment Basis	Unit (Basis)	Annual cost [$/annum]
Maintenance	5	[% of FCI]	4,432,590
Operating Labour			274,703
Laboratory Costs	20	[% Operating Labour]	54,941
Supervisory Labour	20	[% Operating Labour]	167,097
Plant overhead	50	[% of operating labour]	137,352
Capital charges	10	[% of FCI]	0
Insurance	1	[% of FCI]	886,518
Local taxes	1	[% of FCI]	886,518
Royalties	1	[% of FCI]	0
FIXED COSTS			**6,839,718**
Sales expense	20	[% of Direct Production Costs]	34,464
General Overheads			
Research & Development			
		TOTAL FIXED OPERATING COSTS	**6,874,182**

Table A.19. FOC for C_2 heat-integrated route-to-SAF plant (NREL).

Labour & Supervision	Salary [$] (2020)	Number	Cost [$]
Plant manager	29,591	1	29,591
Plant engineer	29,977	1	29,977
Maintenance supervisor	20,406	1	20,406
Maintenance technician	14,968	3	44,903
Lab manager	21,569	1	21,569
Lab technician	14,619	1	14,619
Shift supervisor	15,267	4	61,067
Shift operators	13,373	12	160,470
Yard employees	6,184	4	24,735
Clerks and secretaries	11,488	3	34,464
Total salaries			441,800
Labour burden	90 [%] of Total Salaries		397,620
Total labour cost			**839,421**

Other overhead		Annual cost [$]
Maintenance	3 [%] of ISBL	1,406,260
Property insurance	0.7 [%] of FCI	616,880
Total fixed operating cost		**2,862,561**

Table A.20. FOC for C_2 heat-integrated route-to-SAF plant (Sinnot).

Fixed Operational Consideration	Assessment Basis	Unit (Basis)	Annual cost [$/annum]	Comments
Operating Labour	Wage & Salary Cost for shift team members (excl. supervision)	[$/annum]	160,470	
Supervisory Labour	25	[% of Operating labour]	40,118	
Direct Salary Overhead	50	[% of Operating + Supervisory]	100,294	
Maintenance	3	[% of ISBL]	2,295,788	
Property taxes & insurance	1	[% of ISBL]	765,263	
Rent of land/buildings	1	[% of FCI]	994,841	
General plant overhead	65	[% of total labour + maintenance]	1,622,644	
Allocated environmental charges	1	[% of FCI]	994,841	
Interest charges (capital)	0	[% of total capital investment]	0	
		TOTAL FIXED OPERATING COST	6,974,258	[$/annum]

Table A.21. Investment Analysis for C_2 heat-integrated using the Hand method.

Year	Project Life	Detailed design	Fixed Capital Investment	Working Capital	Fixed OPEX	BL Forecast	Variable OPEX	Product Forecast	Plant Income	Depreciation	Corporation Tax	Total Cash Flow	NPV	Cumulative NPV	Comments
		[$]	[$]	[$]	[$]	[$/t]	[$]	[$/ton]	[$]	[$]	[$]	[$]	[$]	[$]	
2019	0	-250,000	0	0	0		0		0	0	0	-250,000	-250,000	-250,000	
2020	1	0	-63,297,382	0	0		0		0	0	0	-63,297,382	-57,543,074	-57,793,074	Plant construction
2021	2	0	-32,281,665	0	0		0		0	0	0	-32,281,665	-26,679,062	-84,472,136	& commissioning
2022	3	0	0	9,407,799	-6,817,335	0.00	-1,872,530	611	21,336,758	-9,557,905	-772,247	21,282,446	15,989,816	-68,482,320	Year 0 for Plant Ope
2023	4	0	0	0	-6,953,682	0.00	-1,909,980	611	21,336,758	-9,557,905	-728,798	11,744,298	8,021,514	-60,460,806	
2024	5	0	0	0	-7,092,756	0.00	-1,948,180	611	21,336,758	-9,557,905	-684,480	11,611,343	7,209,731	-53,251,075	
2025	6	0	0	0	-7,234,611	0.00	-1,987,143	611	21,336,758	-9,557,905	-639,275	11,475,729	6,477,750	-46,773,325	
2026	7	0	0	0	-7,379,303	0.00	-2,026,886	611	21,336,758	-9,557,905	-593,166	11,337,403	5,817,881	-40,955,445	
2027	8	0	0	0	-7,526,889	0.00	-2,067,424	611	21,336,758	-9,557,905	-546,135	11,196,310	5,223,161	-35,732,283	
2028	9	0	0	0	-7,677,427	0.00	-2,108,772	611	21,336,758	-9,557,905	-498,164	11,052,396	4,687,295	-31,044,988	
2029	10	0	0	0	-7,830,975	0.00	-2,150,948	611	21,336,758	-9,557,905	-449,233	10,905,603	4,204,582	-26,840,406	
2030	11	0	0	0	-7,987,594	0.00	-2,193,966	611	21,336,758	-9,557,905	-399,323	10,755,874	3,769,868	-23,070,538	
2031	12	0	0	0	-8,147,346	0.00	-2,237,846	611	21,336,758	-9,557,905	-348,415	10,603,151	3,378,491	-19,692,047	
2032	13	0	0	0	-8,310,293	0.00	-2,282,603	611	21,336,758	0	-2,685,966	8,057,897	2,334,086	-17,357,962	
2033	14	0	0	0	-8,476,499	0.00	-2,328,255	611	21,336,758	0	-2,633,001	7,899,004	2,080,055	-15,277,907	
2034	15	0	0	0	-8,646,029	0.00	-2,374,820	611	21,336,758	0	-2,578,977	7,736,932	1,852,160	-13,425,747	
2035	16	0	0	0	-8,818,949	0.00	-2,422,316	611	21,336,758	0	-2,523,873	7,571,620	1,647,805	-11,777,942	
2036	17	0	0	0	-8,995,328	0.00	-2,470,762	611	21,336,758	0	-2,467,667	7,403,001	1,464,644	-10,313,298	
2037	18	0	0	0	-9,175,235	0.00	-2,520,177	611	21,336,758	0	-2,410,337	7,231,010	1,300,561	-9,012,737	
2038	19	0	0	0	-9,358,739	0.00	-2,570,581	611	21,336,758	0	-2,351,860	7,055,579	1,153,643	-7,859,094	
2039	20	0	0	0	-9,545,914	0.00	-2,621,992	611	21,336,758	0	-2,292,213	6,876,639	1,022,169	-6,836,925	
2040	21	0	0	0	-9,736,832	0.00	-2,674,432	611	21,336,758	0	-2,231,373	6,694,120	904,580	-5,932,345	
2041	22	0	0	0	-9,931,569	0.00	-2,727,921	611	21,336,758	0	-2,169,317	6,507,951	799,476	-5,132,869	
2042	23	0	0	0	-10,130,200	0.00	-2,782,479	611	21,336,758	0	-2,106,020	6,318,059	705,589	-4,427,280	
2043	24	0	0	0	-10,332,804	0.00	-2,838,129	611	21,336,758	0	-2,041,456	6,124,369	621,780	-3,805,500	
2044	25	0	0	0	-10,539,460	0.00	-2,894,891	611	21,336,758	0	-1,975,602	5,926,805	547,020	-3,258,479	
2045	26	0	0	0	-10,750,249	0.00	-2,952,789	611	21,336,758	0	-1,908,430	5,725,290	480,383	-2,778,096	
2046	27	0	0	-9,407,799	-10,965,254	0.00	-3,011,845	611	21,336,758	0	-1,839,915	-3,888,055	-296,572	-3,074,668	

Section A.4.2

This section presents the TEA results of using black liquor to generate electricity in a steam turbine plant.

Table A.22. Estimation of TCI for steam turbine electricity plant (HM).

Plant section	Major ISBL Equipment item	Quantity	Item Cost [$]	Purchase cost correction factor [-]	Purchase cost [$]	ISBL Installed Cost Hand factor	Installed cost (2006) [$]	CE cost Index adjustment to 2019	Location Factor	Total Installed Cost [$]	Total Plant section [$]
Electricity Generation	Steam Turbine	3	$930,651.75	1	$2,791,955	2.50	$6,979,888	$7,478,452	0.51	$3,807,056	$3,807,056

Table A.23. Estimation of FOC for steam turbine electricity plant.

Fixed Operational Consideration	Assessment Basis	Unit (Basis)	Annual cost [$/annum]
Operating Labour	Wage & Salary Cost for shift team members (excl. supervision)	[$/annum]	13,373
Supervisory Labour	25	[% of Operating labour]	3,343
Direct Salary Overhead	50	[% of Operating + Supervisory]	8,358
Maintenance	3	[% of ISBL]	114,212
Property taxes & insurance	1	[% of ISBL]	38,071
Rent of land/buildings	1	[% of FCI]	47,588
General plant overhead	65	[% of total labour + maintenance]	85,103
Allocated environmental charges	1	[% of FCI]	47,588
Interest charges (capital)	0	[% of total capital investment]	0
		TOTAL FIXED OPERATING COST	357,636

Table A.24. Investment analysis result for steam turbine electricity plant (HM).

Year	Project Life	Detailed design	Fixed Capital	Working Capital	Fixed OPEX	BL Forecast	Variable OPEX	Electricity Forecast	Plant Income	Depreciation	Corporation Tax	Total Cash Flow	NPV	Cumulative NPV	Comments
		[$]	[$]	[$]	[$]	[$/t]	[$]	[$/kWh]	[$]	[$]	[$]	[$]	[$]	[$]	
2019	0	-25,000	0	0	0		0		0	0	0	-25,000	-25,000	-25,000	
2020	1	0	-3,397,797	0	0		0		0	0	0	-3,397,797	-3,088,907	-3,113,907	Plant construction & commissioning.
2021	2	0	-1,732,877	0	0		0		0	0	0	-1,732,877	-1,432,129	-4,546,036	
2022	3	0	0	505,010	-379,526	0.00	-864,501	0.1085	14,972,100	-513,067	-3,303,751	10,929,331	8,211,368	3,665,332	Year 0 for Plant Operation
2023	4	0	0	0	-387,117	0.00	-881,791	0.1085	14,972,100	-513,067	-3,297,531	10,405,661	7,107,206	10,772,538	
2024	5	0	0	0	-394,859	0.00	-899,427	0.1085	14,972,100	-513,067	-3,291,187	10,386,627	6,449,278	17,221,817	
2025	6	0	0	0	-402,756	0.00	-917,415	0.1085	14,972,100	-513,067	-3,284,715	10,367,213	5,852,021	23,073,838	
2026	7	0	0	0	-410,812	0.00	-935,763	0.1085	14,972,100	-513,067	-3,278,114	10,347,410	5,309,858	28,383,696	
2027	8	0	0	0	-419,028	0.00	-954,479	0.1085	14,972,100	-513,067	-3,271,381	10,327,212	4,817,720	33,201,416	
2028	9	0	0	0	-427,408	0.00	-973,568	0.1085	14,972,100	-513,067	-3,264,514	10,306,609	4,371,008	37,572,425	
2029	10	0	0	0	-435,956	0.00	-993,040	0.1085	14,972,100	-513,067	-3,257,509	10,285,594	3,965,542	41,537,967	
2030	11	0	0	0	-444,676	0.00	-1,012,900	0.1085	14,972,100	-513,067	-3,250,364	10,264,160	3,597,525	45,135,492	
2031	12	0	0	0	-453,569	0.00	-1,033,158	0.1085	14,972,100	-513,067	-3,243,076	10,242,296	3,263,511	48,399,003	
2032	13	0	0	0	-462,640	0.00	-1,053,822	0.1085	14,972,100	0	-3,363,909	10,091,728	2,923,214	51,322,217	
2033	14	0	0	0	-471,893	0.00	-1,074,898	0.1085	14,972,100	0	-3,356,327	10,068,981	2,651,477	53,973,695	
2034	15	0	0	0	-481,331	0.00	-1,096,396	0.1085	14,972,100	0	-3,348,593	10,045,779	2,404,880	56,378,574	
2035	16	0	0	0	-490,958	0.00	-1,118,324	0.1085	14,972,100	0	-3,340,704	10,022,113	2,181,104	58,559,678	
2036	17	0	0	0	-500,777	0.00	-1,140,690	0.1085	14,972,100	0	-3,332,658	9,997,974	1,978,046	60,537,724	
2037	18	0	0	0	-510,792	0.00	-1,163,504	0.1085	14,972,100	0	-3,324,451	9,973,352	1,793,795	62,331,519	
2038	19	0	0	0	-521,008	0.00	-1,186,774	0.1085	14,972,100	0	-3,316,079	9,948,238	1,626,616	63,958,135	
2039	20	0	0	0	-531,428	0.00	-1,210,510	0.1085	14,972,100	0	-3,307,540	9,922,621	1,474,934	65,433,070	
2040	21	0	0	0	-542,057	0.00	-1,234,720	0.1085	14,972,100	0	-3,298,831	9,896,492	1,337,319	66,770,388	
2041	22	0	0	0	-552,898	0.00	-1,259,414	0.1085	14,972,100	0	-3,289,947	9,869,840	1,212,470	67,982,859	
2042	23	0	0	0	-563,956	0.00	-1,284,603	0.1085	14,972,100	0	-3,280,885	9,842,656	1,099,210	69,082,068	
2043	24	0	0	0	-575,235	0.00	-1,310,295	0.1085	14,972,100	0	-3,271,642	9,814,927	996,466	70,078,535	
2044	25	0	0	0	-586,740	0.00	-1,336,501	0.1085	14,972,100	0	-3,262,215	9,786,644	903,268	70,981,803	
2045	26	0	0	0	-598,475	0.00	-1,363,231	0.1085	14,972,100	0	-3,252,599	9,757,796	818,732	71,800,535	
2046	27	0	0	-505,010	-610,444	0.00	-1,390,495	0.1085	14,972,100	0	-3,242,790	9,223,360	703,537	72,504,072	

Section A.4.3

This section shows the TEA breakdown associated with the C_4 heat and non-heat-integrated routes-to-SAF in chapter 6.

Table A.25. TCI for C_4 heat-integrated route-to-SAF plant.

Equipment Type	CE (Sum of Items)	Hand Factor	ISBL (US)	Location Factor	ISBL (GBR)
Pumps	$55,746.37	4	$222,985.48	1.04	$231,904.90
Turbine	$1,455,295.83	2.5	$3,638,239.58	1.04	$3,783,769.17
Turbo-Expanders	$3,749,265.39	2.5	$9,373,163.48	1.04	$9,748,090.02
Combustion Chambers	$6,739,889.45	4	$26,959,557.81	1.04	$28,037,940.12
Reactors and Columns	$11,163,506.74	4	$44,654,026.94	1.04	$46,440,188.02
Heat Exchangers	$7,997,977.85	3.5	$27,992,922.46	1.04	$29,112,639.36
TOTALS	$31,161,681.63	$	$112,840,895.75	$	$117,354,531.59

Table A.26. FOC for C_4 heat-integrated route-to-SAF plant.

Capital Investment	Unit	Value	Unit2	Adjusted Value	Calculated Value	Uncertainty factor
ISBL Cost			$	$117,354,531.59	117354531.6	1
OSBL Cost	% ISBL	25	$	$29,338,632.90	29338632.9	1
Total FCI		ISBL+OSBL	$	$146,693,164.48	Total installed cost	
Plant Operation						
TOL (days / yr)	d		d	350	to allow shutdown	
TOL (year)	h	TOL (d) x 24	h	8400	continuous operation	
Labour						
Exchange Rate	GBP	1	$	1.3699		
Labour rate per shift wo	GBP/y	30290	$/y	41494.271	https://www.salaryexpert.com/salary/job/c	1
Number of shift teams		4				
Shift team members		2		8		
Operating Labour	GBP/y	242320	$/y	331954.168		
Supervisory Labor	% operating la	25	$/y	82988.542		
Direct Salary overhead	% operating +	50	$/y	207471.355		
Total Labour	Operating + Supervisory lab		$/y	414942.71		
Site Costs						
Maintenance	% ISBL	3	$/y	2292312.796		
Property Taxes & Insura	% ISBL	1	$/y	764104.2653		
Rent of land / buildings	% FCI	1	$/y	955130.3317		
General Plant Overhead	% Total labou	65	$/y	1759716.079		
Allocated Environmental	%FCI	1	$/y	955130.3317		
Interest on Capital	% FCI	0	$/y	0		
		Total FOC	**$/y**	**$7,348,807.87**		

Table A.27. VOC for C_4 heat-integrated route-to-SAF plant.

Item	Cost
Process water	$688,971.81
Cooling Water	$48,211.57
Deionised water	
Catalysts	$73,213.54
Total costs	810396.9219

Table A.28. Investment analysis for C_4 heat-integrated route-to-SAF plant.

Year	Project Life	Detailed Design	FCI	Working Capital	FOC	VOC	co-product Forecast	C16 Forcast		Plant Income	Depreciation	Corporation Tax	Total Cash Flow	NPV	Cumulative NPV
	y	$	$	$	$	$	$/t	$/t		$	$	$	$	$	$
2021	0	-250000	0	0	$0.00	$0.00	0	611	0	$0.00	0.00	0.00	-250,000.00	-$250,000.00	-$250,000.00
2022	1	0	-10473891.9	0	$0.00	$0.00	0	611	0	$0.00	0.00	0.00	-104,738,919.44	-$95,217,199.49	-$95,467,199.49
2023	2	0	-53416848.9	0	$0.00	$0.00	0	611	0	$0.00	0.00	0.00	-53,416,848.91	-$44,146,156.13	-$139,613,355.62
2024	3	0	0	15567195.97	-$7,798,613.70	-$859,999.70	0	611	0	3.25E+07	-1.58E+07	-1.60E+06	3.78E+07	2.84E+07	-1.11E+08
2025	4	0	0	0	-$7,954,585.97	-$877,199.69	0	611	0	3.25E+07	-1.58E+07	-1.57E+06	2.21E+07	1.51E+07	-9.61E+07
2026	5	0	0	0	-$8,113,677.69	-$894,743.68	0	611	0	3.25E+07	-1.58E+07	-1.53E+06	2.19E+07	1.36E+07	-8.25E+07
2027	6	0	0	0	-$8,275,951.25	-$912,638.56	0	611	0	3.25E+07	-1.58E+07	-1.50E+06	2.18E+07	1.23E+07	-7.02E+07
2028	7	0	0	0	-$8,441,470.27	-$930,891.33	0	611	0	3.25E+07	-1.58E+07	-1.46E+06	2.17E+07	1.11E+07	-5.91E+07
2029	8	0	0	0	-$8,610,299.68	-$949,509.16	0	611	0	3.25E+07	-1.58E+07	-1.42E+06	2.15E+07	1.00E+07	-4.91E+07
2030	9	0	0	0	-$8,782,505.67	-$968,499.34	0	611	0	3.25E+07	-1.58E+07	-1.38E+06	2.13E+07	9.05E+06	-4.00E+07
2031	10	0	0	0	-$8,958,155.79	-$987,869.33	0	611	0	3.25E+07	-1.58E+07	-1.34E+06	2.12E+07	8.17E+06	-3.18E+07
2032	11	0	0	0	-$9,137,318.90	-$1,007,626.71	0	611	0	3.25E+07	-1.58E+07	-1.30E+06	2.10E+07	7.37E+06	-2.45E+07
2033	12	0	0	0	-$9,320,065.28	-$1,027,779.25	0	611	0	3.25E+07	-1.58E+07	-1.26E+06	2.09E+07	6.65E+06	-1.78E+07
2034	13	0	0	0	-$9,506,466.58	-$1,048,334.83	0	611	0	3.25E+07	0.00E+00	-4.39E+06	1.75E+07	5.08E+06	-1.27E+07
2035	14	0	0	0	-$9,696,595.92	-$1,069,301.53	0	611	0	3.25E+07	0.00E+00	-4.34E+06	1.74E+07	4.58E+06	-8.16E+06
2036	15	0	0	0	-$9,890,527.83	-$1,090,687.56	0	611	0	3.25E+07	0.00E+00	-4.30E+06	1.72E+07	4.12E+06	-4.05E+06
2037	16	0	0	0	-$10,088,338.39	-$1,112,501.31	0	611	0	3.25E+07	0.00E+00	-4.26E+06	1.70E+07	3.71E+06	-3.41E+05
2038	17	0	0	0	-$10,290,105.16	-$1,134,751.34	0	611	0	3.25E+07	0.00E+00	-4.21E+06	1.68E+07	3.33E+06	2.99E+06
2039	18	0	0	0	-$10,495,907.26	-$1,157,446.36	0	611	0	3.25E+07	0.00E+00	-4.17E+06	1.67E+07	3.00E+06	5.99E+06
2040	19	0	0	0	-$10,705,825.41	-$1,180,595.29	0	611	0	3.25E+07	0.00E+00	-4.12E+06	1.65E+07	2.69E+06	8.68E+06
2041	20	0	0	0	-$10,919,941.92	-$1,204,207.20	0	611	0	3.25E+07	0.00E+00	-4.07E+06	1.63E+07	2.42E+06	1.11E+07
2042	21	0	0	0	-$11,138,340.75	-$1,228,291.34	0	611	0	3.25E+07	0.00E+00	-4.02E+06	1.61E+07	2.17E+06	1.33E+07
2043	22	0	0	0	-$11,361,107.57	-$1,252,857.17	0	611	0	3.25E+07	0.00E+00	-3.97E+06	1.59E+07	1.95E+06	1.52E+07
2044	23	0	0	0	-$11,588,329.72	-$1,277,914.31	0	611	0	3.25E+07	0.00E+00	-3.92E+06	1.57E+07	1.75E+06	1.70E+07
2045	24	0	0	0	-$11,820,096.31	-$1,303,472.60	0	611	0	3.25E+07	0.00E+00	-3.87E+06	1.55E+07	1.57E+06	1.86E+07
2046	25	0	0	0	-$12,056,498.24	-$1,329,542.05	0	611	0	3.25E+07	0.00E+00	-3.82E+06	1.53E+07	1.41E+06	2.00E+07
2047	26	0	0	0	-$12,297,628.21	-$1,356,132.89	0	611	0	3.25E+07	0.00E+00	-3.77E+06	1.51E+07	1.26E+06	2.12E+07
2048	27	0	0	-15567195.97	-$12,543,580.77	-$1,383,255.55	0	611	0	3.25E+07	0.00E+00	-3.71E+06	-$722,360.31	-5.51E+04	21,175,707.02

Parameter	Unit	Value	Comment	Column1	Parameter2	Factor	Unit3	Value4	Comment5
Discounted Rate of Return	%	10			Installed Equipment Cost		$	$146,693,164.48	ISBL + OSBL
Corporation Tax	%	20	In UK		Commissionning Cost	5	$	$7,334,658.22	
Linear Depreciation	y	10			Working Capital	10	$	$14,669,316.45	
Annual Inflation	%	2	Only feedstock / product exempt						
Plant Life	y	25			TOTAL CAPITAL		$	$168,697,139.15	IEC + Comm +WC
Cumulative NPV	$	2.12E+07			FOC (start)		$	$7,348,807.87	
IRR	%				VOC (start)		$	$810,396.92	

Table A.29. Installed capital costs calculations for heat exchanges (C_4 heat-integrated).

Equipment Item	Comments	E-106	E-119	E-122-2	E-123-2	E-124-2	E-126	E-127	E-132	E-135	Condensor	Air Cooler	E-113	E-114	E-115	E-116	E-117	E-1192
Q / kJh-1	Cold Start Duty	1.91E+07	4.45E+06	8.79E+07	1.25E+08	1.09E+07	3.96E+08	5.49E+08	7.76E+07	7.23E+07	9.30E+08	1.34E+07	1.29E+08	1.33E+07	1.37E+06	6.08E+05	3.30E+07	1.61E+06
Q / W	Unit correction	5.32E+06	1.24E+06	2.44E+07	3.49E+07	3.04E+06	1.10E+08	1.52E+08	2.15E+07	2.01E+07	2.58E+08	3.71E+06	3.60E+07	3.69E+06	3.82E+05	1.69E+05	9.16E+06	4.48E+05
U	Assume no phase cha	3.00E+03	3.00E+03	3.00E+03	3.00E+03	3.00E+03	3.00E+03	1.00E+04	1.00E+04	3.00E+03	1.00E+04	3.00E+03	3.00E+03	3.00E+03	3.00E+03	3.00E+03	3.00E+03	3.00E+03
LMTD		2.38E+01	6.96E+01	6.96E+01	1.37E+03	2.06E+01	-4.37E-02	-4.37E-02	9.79E+01	1.67E+01	1.27E+01	5.65E+01	4.21E+02	7.97E+00	1.22E+01	8.69E+01	4.65E+01	3.62E+01
A = Q/(U*LMTD)		7.45E+01	5.92E+00	1.17E+02	8.46E+00	4.92E+01	-8.38E+05	-3.49E+05	2.20E+01	4.00E+02	2.03E+03	2.19E+01	2.85E+01	1.54E+02	1.05E+01	6.47E-01	6.57E+01	4.13E+00
A / ft^2	Unit correction	8.02E+02	6.37E+01	1.26E+03	9.10E+01	5.30E+02	-9.02E+06	-3.75E+06	2.37E+02	4.31E+03	2.19E+04	2.36E+02	3.07E+02	1.66E+03	1.13E+02	6.97E+00	7.08E+02	4.45E+01
Area bounded / ft^2	min 150	8.02E+02	1.50E+02	1.26E+03	1.50E+02	5.30E+02	1.50E+02	1.50E+02	2.37E+02	4.31E+03	2.19E+04	2.36E+02	3.07E+02	1.66E+03	1.50E+02	1.50E+02	7.08E+02	1.50E+02
CB = exp{11.667 - 0.870	Floating Head	2.84E+04	1.77E+04	3.54E+04	1.77E+04	2.40E+04	1.77E+04	1.77E+04	1.90E+04	7.96E+04	3.67E+05	1.90E+04	2.02E+04	4.14E+04	1.77E+04	1.77E+04	2.69E+04	1.77E+04
FM = a + (A/100)^b	Cr-Mo Shell / Cr-Mo	2.88E+00	2.73E+00	2.92E+00	2.73E+00	2.84E+00	2.73E+00	2.73E+00	2.77E+00	3.05E+00	3.24E+00	2.77E+00	2.79E+00	2.95E+00	2.73E+00	2.73E+00	2.87E+00	2.73E+00
FL	Tube length = 20ft	1.00E+00	1.00E+00	1.00E+00	1.00E+00	1.00E+00	1.00E+00	1.00E+00	1.00E+00	1.00E+00	1.00E+00	1.00E+00	1.00E+00	1.00E+00	1.00E+00	1.00E+00	1.00E+00	1.00E+00
P (shell side) / kpa		1.60E+02	1.50E+02	1.00E+03	4.00E+02	1.00E+03	1.75E+02	2.75E+04	1.00E+03	4.00E+02	2.75E+04	4.00E+02	3.75E+02	1.15E+03	1.15E+03	3.75E+02	2.00E+02	1.50E+02
P (shell side) / psig	Unit correction	2.32E+01	2.18E+01	1.45E+02	5.80E+01	1.45E+02	2.54E+01	3.99E+03	1.45E+02	5.80E+01	3.99E+03	5.80E+01	5.44E+01	1.67E+02	1.67E+02	5.44E+01	2.90E+01	2.18E+01
FP = 0.9803 + 0.018(P/100) + 0.0017(P/100)^		9.85E-01	9.84E-01	1.01E+00	9.91E-01	1.01E+00	9.85E-01	4.40E+00	1.01E+00	9.91E-01	4.40E+00	9.91E-01	9.91E-01	1.02E+00	1.02E+00	9.91E-01	9.86E-01	9.84E-01
CP = FP*FM*FL*CB	Capital Purchase cos	8.04E+04	4.75E+04	1.05E+05	4.78E+04	6.88E+04	4.75E+04	2.12E+05	5.32E+04	2.41E+05	5.23E+06	5.22E+04	5.59E+04	1.24E+05	4.90E+04	4.78E+04	7.60E+04	4.75E+04
Ibase (2006)		5.00E+02	5.00E+02	5.00E+02	5.00E+02	5.00E+02	5.00E+02	5.00E+02	5.00E+02	5.00E+02	5.00E+02	5.00E+02	5.00E+02	5.00E+02	5.00E+02	5.00E+02	5.00E+02	5.00E+02
I(2019)		6.08E+02	6.08E+02	6.08E+02	6.08E+02	6.08E+02	6.08E+02	6.08E+02	6.08E+02	6.08E+02	6.08E+02	6.08E+02	6.08E+02	6.08E+02	6.08E+02	6.08E+02	6.08E+02	6.08E+02
CE (adjusted f.o.b) = CP (	Correction for time	9.77E+04	5.77E+04	1.27E+05	5.81E+04	8.36E+04	5.78E+04	2.58E+05	6.47E+04	2.92E+05	6.35E+06	6.34E+04	6.79E+04	1.51E+05	5.95E+04	5.81E+04	9.23E+04	5.77E+04
Total CE (Heat Exchangers)		8.00E+06																

Table A.30. Installed capital costs calculations for reactors and columns(C_4 heat-integrated).

Equipment Item	Unit	Comment	Steam methane reforming reactor	Methanation	HT-WGS Reactor	LT-WGS reactor	Decarboxylation reactor	Isobutanol deh	E-102	E-103	E-104	E-105	Seed fermen	Seed fermen	Production fer	Production fer
Vol. Flow	m3/h								3126.90	4344.43	815.18	904.98				
Di	m	Inner Diameter	1.13	0.36	1.60	1.13	1.38	0.56	1.05	1.24	0.54	0.57	1.64	1.09	3.53	2.35
Di	ft		3.70	1.17	5.24	3.70	4.53	1.85	3.45	4.07	1.76	1.86	5.38	3.58	11.58	7.71
Di	in		44.42	14.05	62.83	44.42	54.41	22.21	41.40	48.85	21.14	22.27	64.57	42.91	138.98	92.52
Length	m	tan-tan tube length	10.00	10.00	10.00	10.00	10.00	10.00					16.40	16.40	35.32	35.32
# Stages		Will need updating							30.00	30.00	30.00	30.00				
Stage Length	ft	Assumption							2.00	2.00	2.00	2.00	2.00	2.00	2.00	2.00
Length	ft		32.81	32.81	32.81	32.81	32.81	32.81	60.00	60.00	60.00	60.00	53.81	53.81	53.81	115.88
Length	in		393.70	393.70	393.70	393.70	393.70	393.70	720.00	720.00	720.00	720.00	645.67	645.67	645.67	1390.55
Po	kPa	Condenser Operating Pressure	1000.00	27500.00	1000.00	1000.00	400.00	500.00	160.00	160.00	137.78	525.00	400.00	400.00	400.00	400.00
Po	bar		10.00	275.00	10.00	10.00	4.00	5.00	1.60	1.60	1.38	5.25	4.00	4.00	4.00	4.00
Po	psig		130.34	3971.85	130.34	130.34	43.32	57.82	8.51	8.51	5.29	61.45	43.32	43.32	43.32	43.32
Pd	psig		164.85	4048.84	164.85	164.85	59.20	77.40	13.13	13.13	8.47	81.99	59.20	59.20	59.20	59.20
Operating T	C	inlet + conservative	632.55	358.38	415.80	206.16	85.00	240.00	111.38	111.54	54.41	150.09	35.72	35.72	35.72	35.72
T	F		1170.59	677.09	780.40	403.09	185.00	464.00	232.48	232.77	129.94	302.17	96.30	96.30	96.30	96.30
Max Stress	psi	#NAME?	15000.00	15000.00	15000.00	15000.00	15000.00	15000.00	15000.00	15000.00	15000.00	15000.00	15000.00	15000.00	15000.00	15000.00
Weld Quality, E			1.00	1.00	1.00	1.00	1.00	1.00	1.00	1.00	1.00	1.00	1.00	1.00	1.00	1.00
tp	in	minimum thickness	0.25	2.20	0.33	0.25	0.11	0.06	0.02	0.02	0.01	0.06	0.13	0.08	0.27	0.18
Do	in	[Do = Di + 2(tp)]	44.92	18.57	63.52	44.92	54.62	22.33	41.44	48.84	21.15	22.40	64.82	43.08	139.53	92.89
tw	in	weather thickness	0.07	0.24	0.09	0.07	0.06	0.18	0.26	0.21	0.67	0.61	0.12	0.20	0.05	0.36
ty	in	ts+tw+1/8	0.28	1.38	0.32	0.28	0.21	0.25	0.27	0.24	0.46	0.46	0.25	0.27	0.29	0.40
ty, actual	in	closest standard size	0.31	0.31	0.32	0.31	0.31	0.31	0.38	0.38	0.38	0.38	0.38	0.38	0.38	0.38
MoC Density	kg/m3	31655 Reference : AZOM	8.89	8.89	8.89	8.89	8.89	8.89	7.87	7.87	7.87	7.87	7.87	7.87	7.87	7.87
MoC Density	lb/in3	PFR C276 at 22 degC: https://www.hightempmetals.com/techdata/hitempHastC276data.php	0.32	0.32	0.32	0.32	0.32	0.32	0.28	0.28	0.28	0.28	0.28	0.28	0.28	0.28
Weight	lb		6054.80	1833.58	8838.32	6054.80	7543.89	2922.34	7446.38	8053.40	6549.66	6917.52	10057.12	7030.33	27037.54	48469.01
V	m3	Internal volume							15.88	22.07	4.14	4.60	34.64	15.30	160.50	153.20
VP	m3	Packing volume = 80%							14.30	19.86	3.73	4.14	31.18	13.77	144.45	137.88
CPK	$/ft3	Packing cost per ft3							70.00	70.00	70.00	70.00	70.00	70.00	70.00	70.00
CPK	$/m3								2472.05	2472.05	2472.05	2472.05	2472.05	2472.05	2472.05	2472.05
VPCPK	$								35340.90	49101.71	9213.39	10228.31	77076.36	34047.60	357094.30	340836.48
Area	m2	cross sect area							0.87	1.21	0.23	0.25	2.11	0.93	9.79	4.34
CDR	$/ft3	Distributor cost							125.00	125.00	125.00	125.00	125.00	125.00	125.00	125.00
CDR	$								1168.68	1623.73	304.68	338.24	2842.24	1255.53	13168.10	5835.92
VPCPK + CDR	$	Cost of structured packing							36509.58	50725.44	9518.06	10566.55	79918.60	35303.13	370262.39	346672.40
CPL	$	Cost of platforms and ladders	11235.63	4795.10	14518.38	11235.63	13053.17	6729.08	17552.89	19478.80	11468.61	11854.37	21310.99	16453.94	34625.98	49498.98
CV = exp(7.2756 + 0.18255)(H/W)		Purchase Factor	31101.05	16023.07	38896.45	31101.05	35391.21	20594.21	45656.97	47832.25	42332.50	43713.54	54663.52	44132.13	101788.56	150043.54
FM		C-276, 316, 316	1.70	3.70	1.70	1.70	1.70	1.70	1.70	1.70	1.70	1.70	1.70	1.70	1.70	1.70
Number of Tubes			1.00	10.00	1.00	1.00	1.00	1.00	1.00	1.00	1.00	1.00	1.00	1.00	1.00	1.00
CP	$	Purchase Cost	64107.42	640804.58	80642.34	64107.42	73218.23	41739.23	131679.31	151519.07	92951.92	96731.94	194157.58	126781.69	577928.92	651245.40
lbase (2006)			500.00	500.00	500.00	500.00	500.00	500.00	500.00	500.00	500.00	500.00	500.00	500.00	500.00	500.00
l (2019)			607.50	607.50	607.50	607.50	607.50	607.50	607.50	607.50	607.50	607.50	607.50	607.50	607.50	607.50
CE	$		7.789E+04	7.786E+05	9.798E+04	7.789E+04	8.896E+04	5.071E+04	1.600E+05	1.841E+05	1.129E+05	1.175E+05	1179507.28	770198.76	3510918.20	3956315.80
Total CE-Col	$			11163506.74												

Table A.31. Installed capital costs calculations for pumps used (C_4 heat-integrated).

Equipment Item	Comment	High pressure pump	P-103	P-104	P-105
Q / m^3 h-1	capacity flow	485.08	31.03	3.23	2.20
Q / gpm	gallons per minute	2135.72	136.61	14.21	9.68
dP	delta P	27399.00	10.00	1860.00	525.00
density	Inlet fluid density	979.23	942.65	707.77	782.29
H / m		2.85	0.00	0.27	0.07
H / ft	Head	9.36	0.00	0.88	0.22
S	Size Factor	6533.24	8.14	13.32	4.59
CB = EXP{9.7171 - 0.6019[ln(S)] + 0.051		4604.31	5903.82	4947.54	7485.23
FT	Assumptions in excel	1.00	1.00	1.00	1.00
FM	Stainless Steel	2.00	2.00	2.00	2.00
CP		9208.62	11807.63	9895.08	14970.45
lbase (2006)		500.00	500.00	500.00	500.00
l (2019)		607.50	607.50	607.50	607.50
CE		11188.48	14346.27	12022.52	18189.10
CE-P Total		55746.37			

Table A.32. Total installed cost for non C_4 heat-integrated route-to-SAF plant.

Equipment Type	CE (Sum of Items)	Hand Factor	ISBL (US)	Location Factor	ISBL (GBR)
Pumps	76833.5115	4	307334.046	1.04	$319,627.41
Turbine	1067300.787	2.5	2668251.97	1.04	$2,774,982.05
Turbo-Expanders	1767026.884	2.5	4417567.21	1.04	$4,594,269.90
Combustion Chambers	2149334.473	4	8597337.89	1.04	$8,941,231.41
Reactors and Columns	7230406.06	4	28921624.2	1.04	$30,078,489.20
Heat Exchangers	5.38E+06	3.5	18845449.8	1.04	$19,599,267.77
TOTALS	17675315.94	$	63757565.1	$	$66,307,867.73

Table A.33. FOC for C_4 non heat-integrated SAF plant.

Capital Investment	Unit	Value	Unit2	Adjusted Value	Calculated Value	Uncertainty factor
ISBL Cost			$	66307867.73	66307867.73	1
OSBL Cost	% ISBL	25	$	16576966.93	16576966.93	1
Total FCI		ISBL+OSBL	$	82884834.67	Total installed cost	
Plant Operation						
TOL (days / yr)	d		d	350	to allow shutdown	
TOL (year)	h	TOL (d) x 24	h	8400	continuous operation	
Labour						
Exchange Rate	GBP	1	$	1.3699		
Labour rate per shift w	GBP/y	30290	$/y	41494.271	https://www.salaryex	1
Number of shift teams		4				
Shift team members		2		8		
Operating Labour	GBP/y	242320	$/y	331954.168		
Supervisory Labor	% operating l	25	$/y	82988.542		
Direct Salary overhead	% operating +	50	$/y	207471.355		
Total Labour	Operating + Supervisory la		$/y	414942.71		
Site Costs						
Maintenance	% ISBL	3	$/y	1989236.032		
Property Taxes & Insu	% ISBL	1	$/y	663078.6773		
Rent of land / buildings	% FCI	1	$/y	828848.3467		
General Plant Overhea	% Total labou	65	$/y	1562716.182		
Allocated Environment	%FCI	1	$/y	828848.3467		
Interest on Capital	% FCI	0	$/y	0		
		Total FOC	$/y	6495141.65		

Table A.34. VOC for C_4 non heat-integrated bio-jet plant.

Item	Cost
Process water	$555,331.16
Deionised Water	$167,163.71
Cooling Water	$330,344.66
Catalysts	$89,195.71
Total costs	$1,142,035.24

Table A.35. Investment analysis for C_4 non heat-integrated SAF plant.

Year	Project Life	Detailed De	FCI	Working Capital	FOC	VOC	C16 Forec	BL forecast	Plant Income	Depreciation	Corporation Tax	Total Cash Flow	NPV	Cumulative NPV
	y	$	$	$	$	$	$/t	$/t	$	$	$	$	$	
2021	0	-250000	0	0	0	0	611	0	0	0	0	-250000	-250000	-250000
2022	1	0	-59179772	0	0	0	611	0	0	0	0	-59179771.95	-53799793	-5.40E+07
2023	2	0	-30181683.7	0	0	0	611	0	0.00E+00	0.00E+00	0.00E+00	-3.02E+07	-24943540	-7.90E+07
2024	3	0	0	8795804.963	-6.893E+06	-1.212E+06	611	0	1.22E+07	-8.94E+06	0.00E+00	1.29E+07	9.70E+06	-6.93E+07
2025	4	0	0	0	-7.031E+06	-1.236E+06	611	0	1.22E+07	-8.94E+06	0.00E+00	3.96E+06	2.70E+06	-6.66E+07
2026	5	0	0	0	-7.171E+06	-1.261E+06	611	0	1.22E+07	-8.94E+06	0.00E+00	3.79E+06	2.36E+06	-6.42E+07
2027	6	0	0	0	-7.315E+06	-1.286E+06	611	0	1.22E+07	-8.94E+06	0.00E+00	3.63E+06	2.05E+06	-6.22E+07
2028	7	0	0	0	-7.461E+06	-1.312E+06	611	0	1.22E+07	-8.94E+06	0.00E+00	3.45E+06	1.77E+06	-6.04E+07
2029	8	0	0	0	-7.610E+06	-1.338E+06	611	0	1.22E+07	-8.94E+06	0.00E+00	3.28E+06	1.53E+06	-5.89E+07
2030	9	0	0	0	-7.762E+06	-1.365E+06	611	0	1.22E+07	-8.94E+06	0.00E+00	3.10E+06	1.31E+06	-5.76E+07
2031	10	0	0	0	-7.918E+06	-1.392E+06	611	0	1.22E+07	-8.94E+06	0.00E+00	2.92E+06	1.12E+06	-5.64E+07
2032	11	0	0	0	-8.076E+06	-1.420E+06	611	0	1.22E+07	-8.94E+06	0.00E+00	2.73E+06	9.57E+05	-5.55E+07
2033	12	0	0	0	-8.237E+06	-1.448E+06	611	0	1.22E+07	-8.94E+06	0.00E+00	2.54E+06	8.09E+05	-5.47E+07
2034	13	0	0	0	-8.402E+06	-1.477E+06	611	0	1.22E+07	0.00E+00	-4.69E+05	1.88E+06	5.44E+05	-5.41E+07
2035	14	0	0	0	-8.570E+06	-1.507E+06	611	0	1.22E+07	0.00E+00	-4.30E+05	1.72E+06	4.53E+05	-5.37E+07
2036	15	0	0	0	-8.742E+06	-1.537E+06	611	0	1.22E+07	0.00E+00	-3.89E+05	1.56E+06	3.73E+05	-5.33E+07
2037	16	0	0	0	-8.916E+06	-1.568E+06	611	0	1.22E+07	0.00E+00	-3.48E+05	1.39E+06	3.03E+05	-5.30E+07
2038	17	0	0	0	-9.095E+06	-1.599E+06	611	0	1.22E+07	0.00E+00	-3.06E+05	1.23E+06	2.42E+05	-5.28E+07
2039	18	0	0	0	-9.277E+06	-1.631E+06	611	0	1.22E+07	0.00E+00	-2.64E+05	1.05E+06	1.90E+05	-5.26E+07
2040	19	0	0	0	-9.462E+06	-1.664E+06	611	0	1.22E+07	0.00E+00	-2.20E+05	8.80E+05	1.44E+05	-5.24E+07
2041	20	0	0	0	-9.651E+06	-1.697E+06	611	0	1.22E+07	0.00E+00	-1.75E+05	7.02E+05	1.04E+05	-5.23E+07
2042	21	0	0	0	-9.844E+06	-1.731E+06	611	0	1.22E+07	0.00E+00	-1.30E+05	5.20E+05	7.03E+04	-5.23E+07
2043	22	0	0	0	-1.004E+07	-1.766E+06	611	0	1.22E+07	0.00E+00	-8.38E+04	3.35E+05	4.12E+04	-5.22E+07
2044	23	0	0	0	-1.024E+07	-1.801E+06	611	0	1.22E+07	0.00E+00	-3.65E+04	1.46E+05	1.63E+04	-5.22E+07
2045	24	0	0	0	-1.045E+07	-1.837E+06	611	0	1.22E+07	0.00E+00	0.00E+00	-5.81E+04	-5.90E+03	-5.22E+07
2046	25	0	0	0	-1.066E+07	-1.874E+06	611	0	1.22E+07	0.00E+00	0.00E+00	-3.04E+05	-2.80E+04	-5.22E+07
2047	26	0	0	0	-1.087E+07	-1.911E+06	611	0	1.22E+07	0.00E+00	0.00E+00	-5.54E+05	-4.65E+04	-5.23E+07
2048	27	0	0	-6129889.418	-1.109E+07	-1.949E+06	611	0	1.22E+07	0.00E+00	0.00E+00	-6.94E+06	-5.29E+05	-5.28E+07